Dr. Nick Gregor and Dr. Linda Al Atik, “Seismic Hazard Analysis for the Pebble Mine Project, Southwest Alaska” (June 2020)

With Cover Letter by Dr. Norm Abrahamson

EXHIBIT B

June 1, 2020

To: Nick Gregor
From: Norm Abrahamson

Subject: Review of "Seismic Hazard Analysis for the Pebble Mine Project, Southwest Alaska", dated May 20, 2020

Overall, the report is a high-quality seismic hazard analysis that provides the deterministic and probabilistic hazard results for the Pebble Mine Project. The methods used in the report follow best practice in seismic hazard analysis. The May 20, 2020 version of the report adequately addresses my comments on earlier drafts of the report. A summary of my review of the final report is given below.

For the seismic source characterization, the models for the crustal faults, background zones, and subduction zone are based on up-to-date data and current methodologies. The seismic hazard is controlled by the slab events which is common for this site/source geometry of the subduction zone. Given that the slab events control the hazard at the site, the results can be sensitive to the modeling of the slab earthquakes in the PSHA. The approach used in this report captures the finite-fault geometries of the slab events and is an improvement over the widely used point-source approach.

The selection of the ground-motion models (GMMs) can have a significant effect on the hazard. For crustal earthquakes, the report uses equal weights for the five NGA-W2 models. For subduction earthquakes, the report uses the three alternative branches of the 2016 BCHydro model and the new Kuehn et al (2020) NGA-SUB model. Most of the weight is given to the BCHydro model. Given that the NGA-SUB models have just been released, and this project is one of the first applications and revisions may still be made to the NGA-SUB models, using a low weight on the new NGA-SUB model is appropriate at this time. As the new NGA_SUB models become stable over the next year, updates to the hazard at the Pebble Mine site should consider larger weights to these new GMMs.

In conclusion, the UHS and deterministic spectra developed in the report are appropriate to use as reference rock spectral for the seismic evaluation of the Pebble Mine sites. As noted in the report, when applying these results, the site conditions at the Pebble Mine project sites should be determined and the hazard results adjusted to the site-specific site condition if needed.

Norman Abrahamson

Seismic Hazard Analysis for the Pebble Mine Project, Southwest Alaska

Prepared for:

K&L Gates

Prepared by:

Nick Gregor and Linda Al Atik

May 20th, 2020

Table of Contents

List of Tables

List of Figures

1. Introduction

A seismic hazard analysis (SHA) study is performed for the Pebble Mine project located in Southwest Alaska. This large proposed surface mining complex is located greater than 300 km southwest of Anchorage and approximately 100 km west of the Cook Inlet. As part of the proposed mining operations, three Tailings Storage Facilities (TSF) are expected to be constructed as shown in Figure 1. The planned heights for these three TSF are 545 feet (Main TSF), 305 – 425 feet (Pyritic TSF) and 300 feet (South TSF) (Pebble Partnership, 2018). For this SHA study, ground motions are estimated for approximate center point locations of the three main TSF locations: Main, Pyritic (Area E), and South, as listed in Table 1. These three site locations are within approximately 8 km of each other and as such the estimated ground motions from these three separate site locations are expected to be similar. A full presentation of the analysis is provided for the Main TSF site location and an abbreviated set of the results is presented for the other two TSF site locations in the report.

Table 1. Selected site locations for the Main, Pyritic and South TSF sites.

TSF	Latitude (North)	Longitude (West)
Main	59.908	-155.417
Pyritic (Area E)	59.897	-155.336
South	59.841	-155.457

Ground motions are developed for the horizontal component of motion based on acceleration response spectra consistent with 5% spectral damping. The development of vertical ground-motion spectra is not included in this study, nor is the development of spectrum compatible time histories. All of the ground-motion estimates are based on an assumed reference site condition of rock material with an average shear wave velocity in the top 30 m (V_{S30}) of 760 m/sec. The selection of this reference rock site condition is based on the limited site-specific material information available for the TSF site locations, the limited applicability of the ground-motion models (GMM) for harder rock site conditions, and the ability to scale ground motions from this common reference site condition to potential hard rock site-specific conditions that might be expected around the Pebble Mine project site. Ground motions developed for reference site conditions with V_{S30} of 760 m/sec can be subsequently adjusted to site-specific conditions through a standard analytical site response study when additional site measurements are obtained. Ground motions in this study are developed for a suite of spectral periods ranging from PGA (0.01 sec) to 10 sec.

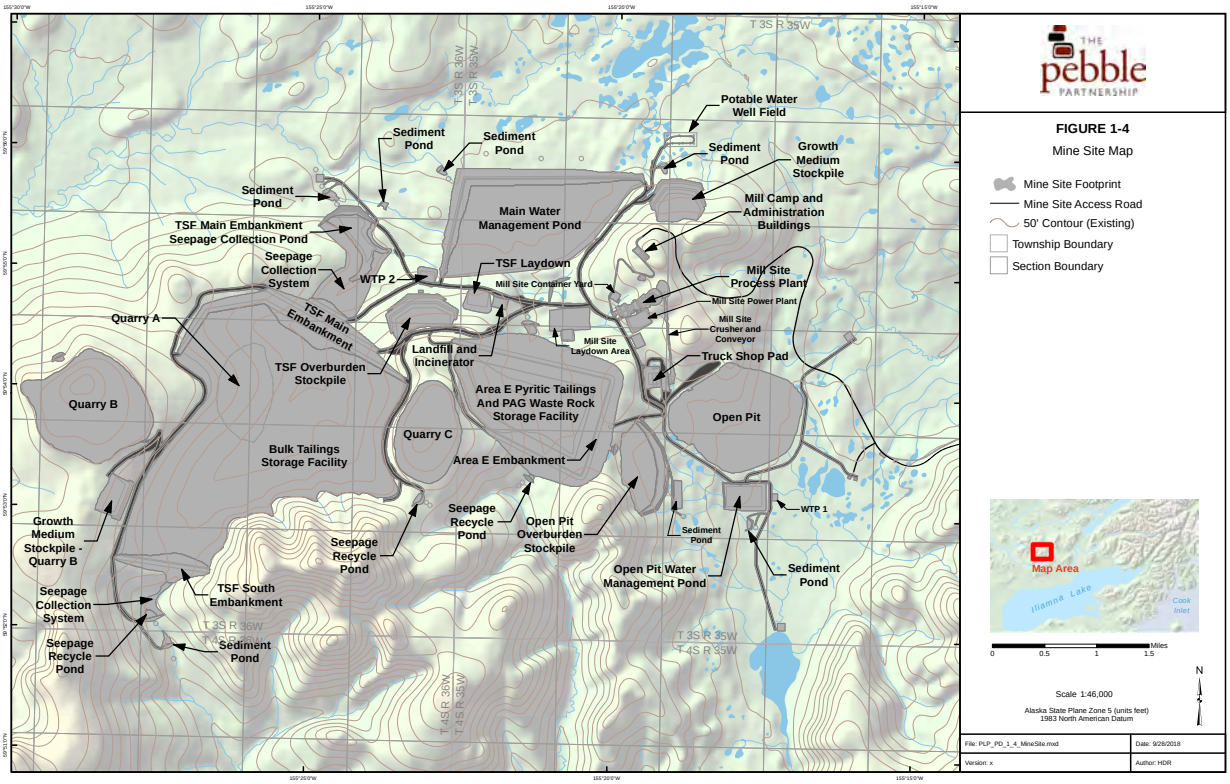

Figure 1. Overview map of the proposed Pebble Mine project in Southwest Alaska. Three TSF embankments are indicated on the map (Main Embankment, Pyritic Area E embankment, and South Embankment). (Source: Pebble Partnership, 2018)

This SHA study follows the current state of practice in performing both a probabilistic seismic hazard analysis (PSHA) and deterministic seismic hazard analysis (DSHA). Following this approach, previous seismic source characterization (SSC) models and as well ground-motion characterization (GMC) models used in previous SHA studies (e.g., Knight-Piesold, 2013, Wesson et al., 2007, 2008) are reviewed and considered in the analysis. In addition, a literature review for both SSC and GMC models is conducted. Note that no field studies are conducted as part of this SHA study.

The basic elements of a SHA are shown in Figure 2 (Earthquake Engineering Research Institute, 1989). The SSC model and the GMC model constitute the input to both the PSHA and DSHA. Note that for the DSHA, the probability density function for magnitude is not required, but rather, the maximum magnitude associated with each seismic source is required. The SSC model defines the earthquake source seismicity and geometry while the GMC model defines the ground-motion scaling as a function of the earthquake source parameters, propagation parameters, and local site conditions.

The primary output of a PSHA study is a set of seismic hazard curves for the ground-motion parameters of interest from which uniform hazard spectra (UHS) are developed using equations given in McGuire (2004) given a specific hazard level (i.e., return period). UHS are developed for

return periods of 475, 1,000, 2,475, 5,000, and 10,000 years for this study. Hazard curves are computed for the mean hazard curves and as well the fractile distribution of hazard curves that allows for the estimate of the uncertainty associated with the mean hazard results. A deaggregation of the seismic hazard using equations given in Bazzurro and Cornell (1999) is used to define controlling events (design earthquake scenarios) and provide an understanding of the controlling seismic sources to the total hazard. These deaggregation results are expected to vary as a function of spectral period and hazard level.

For the DSHA study, the primary output is the response spectrum associated with a given seismic source event consistent with SSC and GMC models. The resulting spectra are computed for the median and 84th percentile cases. Only those scenario events that control the DSHA (i.e., estimate the largest ground motions) are typically considered in a DSHA study.

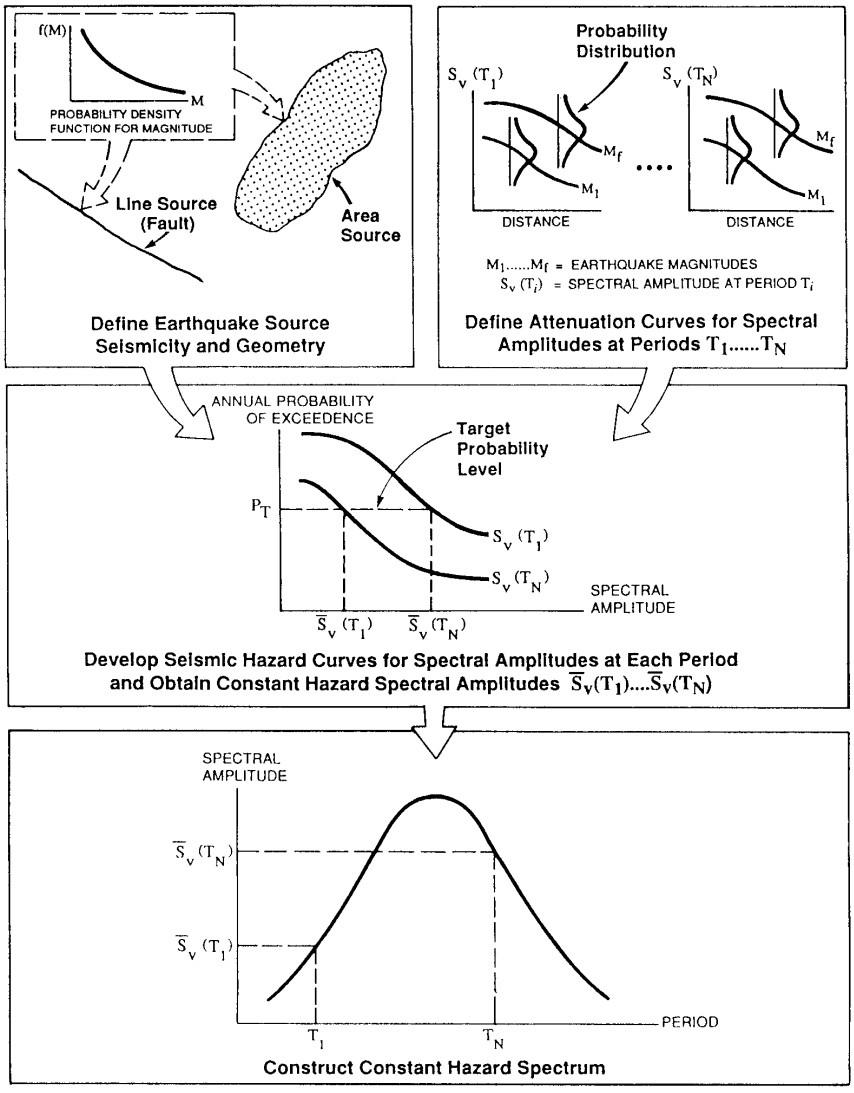

Figure 2. Schematic showing the elements of a probabilistic seismic hazard analysis (Source: Earthquake Engineering Research Institute, 1989).

The PSHA is computed for this study using the HAZ45.2 computer program developed by D. Norm Abrahamson (Abrahamson, 2018). This computer program is validated for calculating seismic hazard by successfully passing the test cases developed as part of the Pacific Earthquake Engineering Research Center (PEER) PSHA code verification project (Hale et al., 2018).

In this report, we present an overview of the SSC and GMC models as developed and implemented in the SHA study. The PSHA results are presented in terms of mean and fractile hazard curves at select spectral periods (i.e., 0.01, 0.2, 0.5, 1.0, and 3.0 sec). Based on the full set of spectral period hazard curves, the uniform hazard spectra (UHS) are presented at a suite of return period levels spanning the range of 475-yr to 10,000-yr. Deaggregation results are also presented in the report for a select suite of spectral periods and hazard levels.

For the DSHA, the computed spectra for the median and 84^{th} percentile cases are provided. These deterministic spectra are calculated for each of the three different seismic sources considered in the analysis: crustal faults, subduction interface events and subduction slab events. In addition, comparisons relative to the UHS spectra are presented in the report.

The resulting PSHA and DSHA ground motions for the reference site condition of rock material with a V_{S30} value of 760 m/sec are presented and compared in this report, however, a recommendation of the applicable design spectra for the TSFs is not included as part of the scope of this report.

1.1 Previous SHA studies

As part of the USGS development of seismic hazard maps for the United States, the most current regional seismic hazard map for the state of Alaska was published in 2007 (Wesson et al., 2007, 2008). Currently the USGS has begun the process of updating this regional map for Alaska, but at this time, any preliminary results based on this update are not available (C. Mueller, personal communication). It is expected that this updating process may require a year of more before it will be completed. Note that the USGS did not perform a DSHA study for the region of Alaska for their 2007 study.

A previous site-specific study by Knight-Piesold (2013) was conducted for the Pebble Mine project. The selected site location used in that study was approximately 2 km west of the selected Pyritic TSF site location, which places it approximately in the center of the Open Pit in Figure 1. This previous study performed both a PSHA and DSHA study for this selected site location. This study relied mainly on the SSC model developed for the USGS 2007 regional seismic hazard map (Wesson et al., 2007) with some additional crustal fault characterizations around the project area (Knight-Piesold, 2013).

For the GMC model, the Knight-Piesold (2013) study employed more current GMMs than those used for the USGS 2007 study. However, these GMMs have subsequently been superseded by more recent GMMs as noted in the technical review of the Knight-Piesold (2013) study

(Parkington, 2018). One of the recommendations from this review was the use of the more current NGA-West2 GMMs for the deterministic analysis of the crustal faults (Parkington, 2018).

In addition to the noted release and suggested use of updated crustal GMMs, more recent subduction GMMs are available and have been used in seismic hazard analysis studies to estimate ground motions from subduction earthquakes than were used in the Knight-Piesold (2013) study.

As part of the development of the SSC and GMC models used in this current SHA study, deviations or differences from this current study and both the USGS (Wesson et al., 2007, 2008) and Knight-Piesold (2013) studies are presented and discussed in the report. In addition, a comparison of the results from these studies is evaluated in the report.

2. Seismic Source Characterization

2.1 Regional Tectonics

The dominant tectonic feature in Southwest Alaska is the seismically active subduction of the Pacific plate beneath the North America plate. This is occurring with a relative plate motion rate of approximate 55 mm/yr (Koehler and Carver, 2018 and references therein) as indicated in Figure 3. Historically, several large interface events have occurred along this approximate 4,000 km Alaska-Aleutian subduction zone with the largest being the 1964 **M**9.2 Great Alaska earthquake. The approximate rupture zones for these large historical interface events are shown in Figure 3. Historical events associated with the deeper part of the subducting slab have also been observed in the region with the two most recent events being the 2016 **M**7.1 Iniskin earthquake (Abers and Mann, 2018) and the 2018 **M**7.1 Anchorage earthquake (Ruppert and Witter, 2020). The earthquake locations of these two deeper and significant slab earthquakes are shown in Figure 4 along with the depth contours for the top of the subducting slab, the approximate rupture area of the 1964 Great Alaska earthquake and regional seismicity. Deep slab events associated with the subducting Pacific plate have been observed down to depths as great as 200 km in the region, although with less frequency than slab events associated with the shallower depths of the subducting plate.

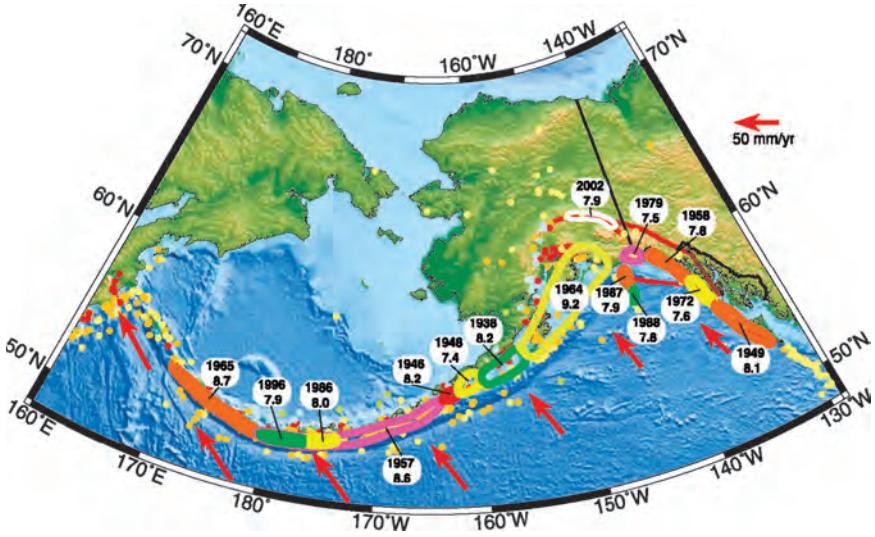

Figure 3. Generalized tectonic environment for Alaska and the approximate rupture zones for the large historical earthquakes associated with the interface subduction zones and major crustal faults (Source: Wesson et al., 2008).

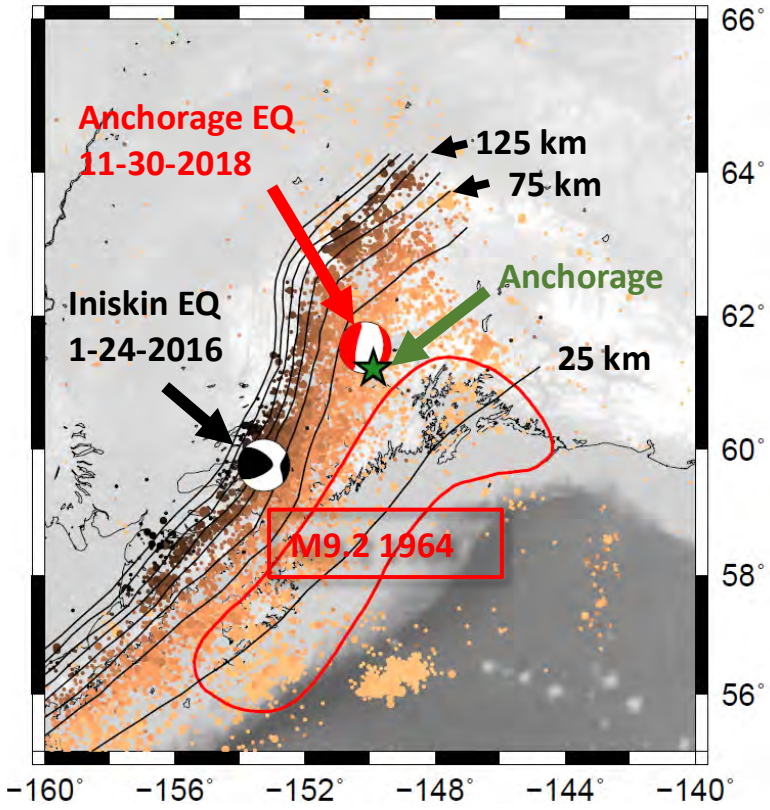

Figure 4. Location of two historical significant slab events crustal faults (Source: Abers and Mann, 2018).

In addition to the subducting plates tectonic feature, several major crustal faults have been identified in Central and Southeast Alaska (Koehler et al., 2012; Koehler et al. 2013, Koehler and Carver, 2018). These crustal faults are common in the backarc region of oblique and rotational plate vector motions as is occurring along the eastern section of the Alaska-Aleutian subduction zone (Elliott and Freymueller, 2018). Specifically, the Denali fault system was the source of the 2002 **M**7.9 Denali earthquake. Given its proximity to the major population centers of Fairbanks and Anchorage and the recent large earthquake, this section of the Denali fault has received more extensive field investigations and studies (e.g., see Haeusler et al., 2016 and references therein) than the extended sections of the fault system to the west which are closer the Pebble project sites. Additional secondary crustal faults have been identified and characterized in the region (Koehler et al., 2012; Koehler et al. 2013, Koehler and Carver, 2018) and are discussed as part of the SSC model development.

2.2 Seismicity

Historically Alaska had recorded a large number of earthquakes given its active tectonic environment. These events are associated with both crustal events and as well both interface and slab subduction events. As part of the USGS regional seismic hazard maps, a compiled historical seismicity catalog was developed which included earthquakes through the end of 2004 (Wesson et al., 2007, 2008). As part of this development, a standard process was applied for the removal of duplicate event listings and the identification of dependent earthquakes. The duplicate removal process followed a ranking of reporting seismicity catalog agencies with the preferred location being selected from the highest ranking reporting catalog agency (Wesson et al., 2007, 2008). For the identification of dependent events, the Gardner and Knopoff (1974) methodology was applied. This USGS seismicity catalog was obtained (C. Mueller, personal communication) and used for events prior to 2005. These events are plotted in Figure 5 for a selected project region between latitudes 52 to 65 degrees north and longitudes -144 to -165 degrees west. The events falling in this project section box are plotted in Figure 5 and are separated based on the depth boundary value of 50 km that was used in the USGS analysis (Wesson et al., 2017, 2018).

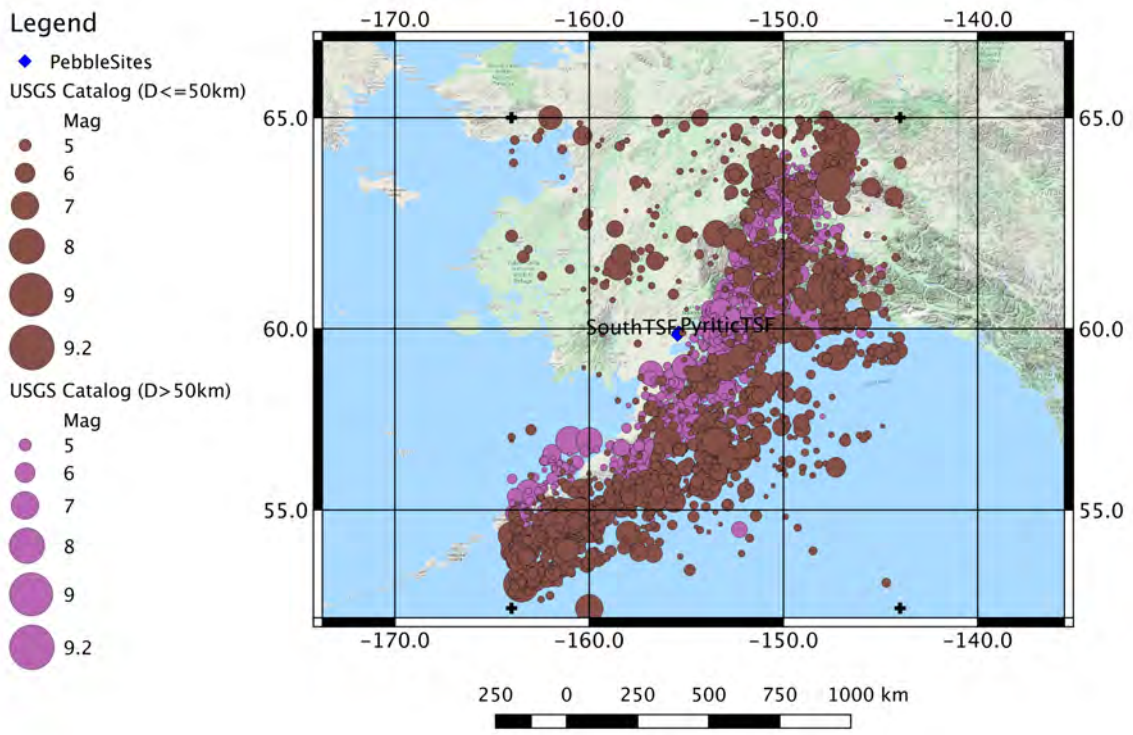

Figure 5. USGS seismicity catalog (through 2004) for events within the project region.

Given the expected occurrence of earthquakes in this region since the end of 2004, a seismicity catalog search from the ANSS Comcat on-line catalog web portal (https://earthquake.usgs.gov/earthquakes/search/) is performed for the bounding project box region starting from January 1, 2005 through to March 27, 2020. This search is not performed for the pre-2005 time based on the recommendation from C. Muller (personal communication) that it should be consistent with the USGS 2007 catalog. Given this recent seismicity catalog search, the various magnitude scales are converted to a common moment magnitude scale following the Sipkin (2003) and Utsu (2002) scaling relationships. These relationships are the same relationships used in a recent SHA study in British Columbia Canada (BC Hydro, 2012).

Following the same approach that was used by the USGS, dependent events are identified based on Gardner and Knopoff (1974). The resulting catalog for events since January 1, 2005 is plotted in Figure 6, again separated by the depth boundary of 50 km.

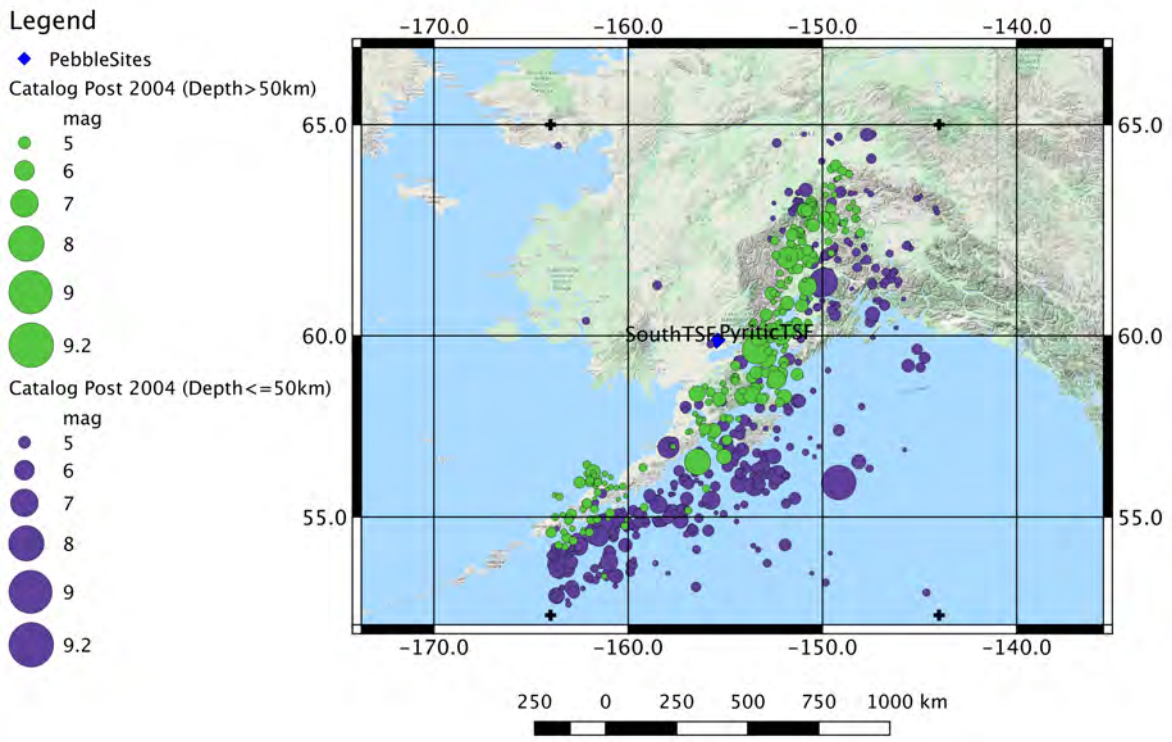

Figure 6. Seismicity catalog (since January 1, 2005) for events within the project region.

Visually for the active subduction zone, the recent events since January 1, 2005 (Figure 6) show a similar activity rate and geographic distribution to the pre 2005 events (Figure 5). For the interior region of Alaska away from the subduction zone, the more recent events are less populace which can be an artificial visual observation given the shorter time period for the recent events when compared to the full USGS catalog.

The first event in the USGS catalog occurred in 1899. A critical input parameter needed for the estimation of recurrence parameters from an earthquake catalog is the period of completeness. This has been observed to be magnitude dependent and is heavily dependent on the seismic network coverage and or historical accounts for a given region. As expected, the limited historical accounts and later installed seismic instruments networks limit the period of completeness for this region of Alaska. The USGS (Wesson et al., 2007, 2008) estimated the period of completeness as listed in Table 2. Similar period of completeness intervals were estimated from the more recent SHA study for Susitna Dam (Furgo, 2012), and for that study, the same USGS intervals were adopted.

Table 2. Period of completeness for USGS earthquake catalog.

Magnitude	Completeness year
4.5 and greater	1964
6.0 and greater	1932
6.9 and greater	1898

Given the updated seismicity catalog developed for this SHA study, recurrence parameters are estimated following the Weichert (1980) methodology for both the USGS catalog and the full updated catalog. The period of completeness intervals listed in Table 2 are applied in the calculation and recurrence parameters are computed for the full catalog and the depth differentiated catalog. The results are shown in Figure 7 – 9. The top plot in each figure shows the calculated cumulative annual recurrence curve from the USGS catalog (orange lines) and the project catalog (blue line). The bottom plot shows the ratio between the project catalog and the USGS catalog. Based on these comparisons of the recurrence curves, the addition of approximately 15 years of more recent seismicity (project catalog) resulted in a reduction of about 10% or less in the overall recurrence rates of earthquakes in the project region for all depths. For the depths less than 50 km the reduction is slightly larger up to about 14% and less and for the deeper events (i.e., greater or equal to 50 km) the reduction is only about 6%.

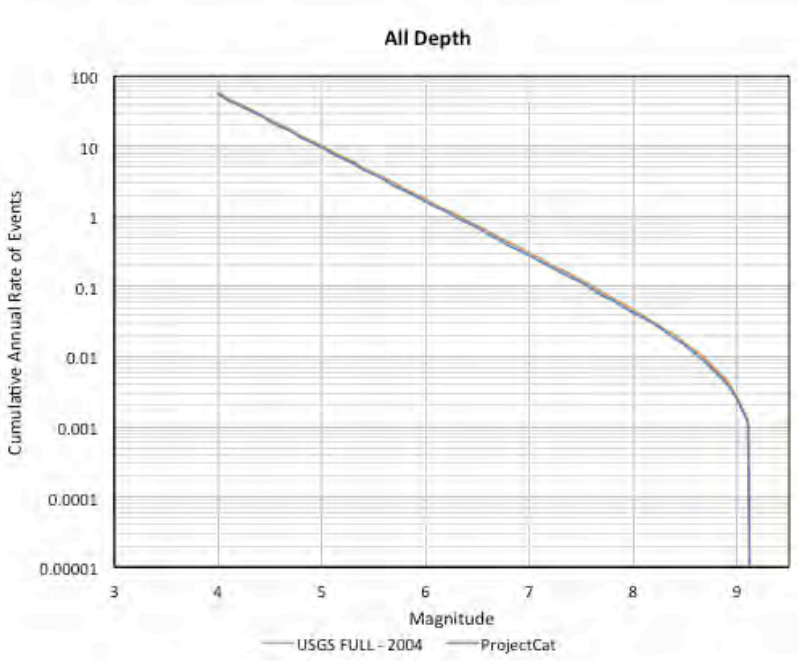

(a)

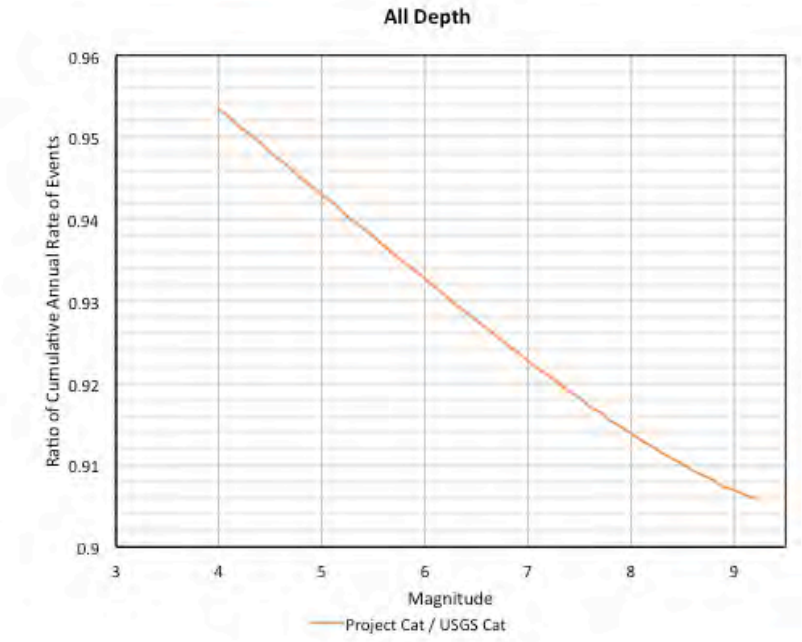

(b)

Figure 7. Calculated recurrence curve for the USGS catalog (orange line) and the updated project catalog (solid blue line) over all depths (a) and ratio of recurrence curves for the project catalog over USGS catalog (b).

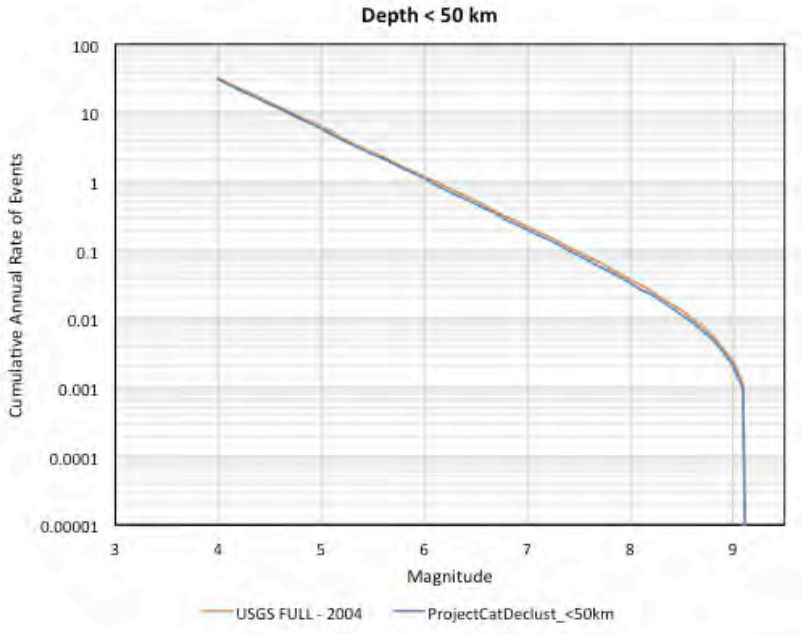

(a)

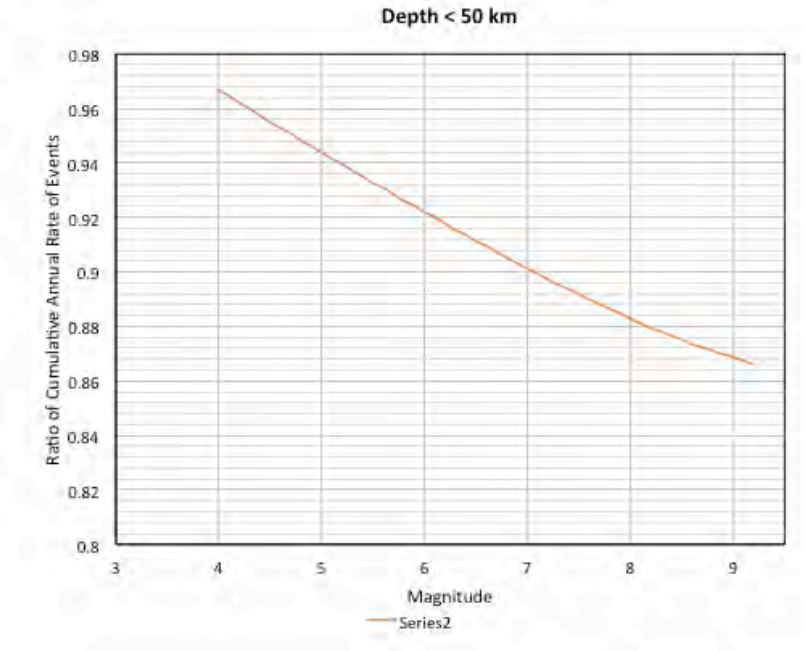

(b)

Figure 8. Calculated recurrence curve for the USGS catalog (orange line) and the updated project catalog (solid blue line) for depths less than 50 km (a) and ratio of recurrence curves for the project catalog over USGS catalog (b).

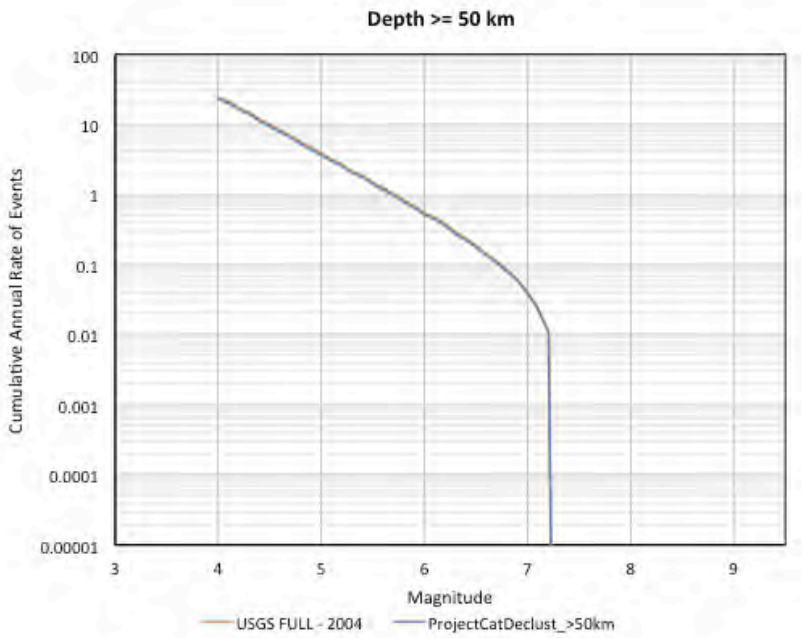

(a)

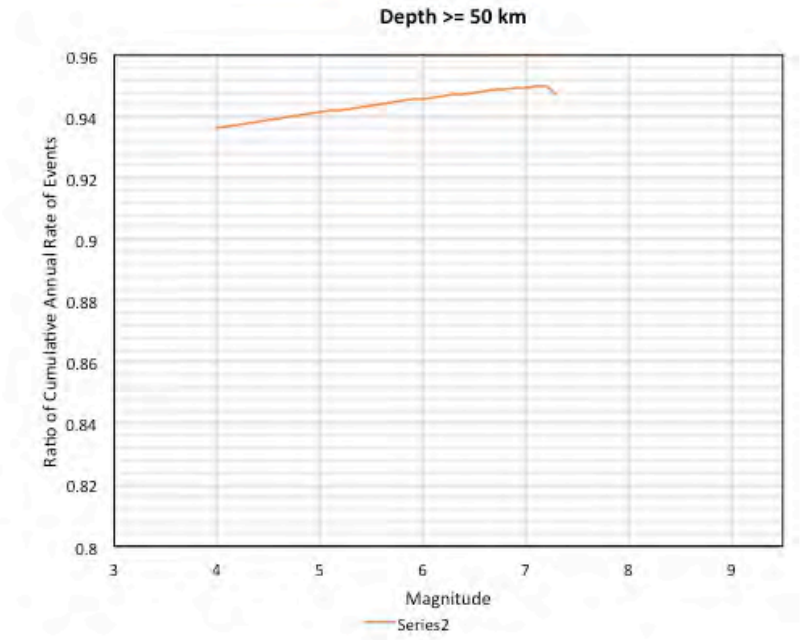

(b)

Figure 9. Calculated recurrence curve for the USGS catalog (orange line) and the updated project catalog (solid blue line) depths greater than or equal to 50 km (a) and ratio of recurrence curves for the project catalog over USGS catalog (b).

2.3 Crustal Fault Sources

Given the overall regional tectonics, several crustal faults have been identified in the project region (Wesson et al., 2007, 2008; Koehler et al., 2012; Koehler et al, 2013; Koehler and Carver, 2018). These faults have been characterized based either on field investigations, field mapping and or inferences from geologic, tectonic and historical studies. As noted earlier, for this seismic hazard study, no new field work is conducted, and the characterization and implementation of the crustal faults for the analysis is based on previous seismic hazard studies in the region and published literature. Future studies, which may lead to the identification and characterization of new faults and or refinement of the current faults used in this analysis, may require a reassessment of the seismic hazard results presented in this study. The crustal fault sources used in this analysis are shown in Figure 10 along with the project site location. Additional crustal faults have been identified and characterized in Southern Alaska, but they are not expected to contribute to the overall seismic hazard at the project site location given their large distance from the project site (Wesson et al., 2007, 2008; Fugro, 2012; Koehler et al., 2012; Koehler et al, 2013; Koehler and Carver, 2018). For each of these faults, a discussion is presented on their characterization used for this SHA. Although the Knight-Piesold (2013) study provides a listing of the faults used in their analysis, their report is lacking on the full specific characterization of these specific crustal faults (e.g., slip rate), and thus an assessment cannot fully be made about potential differences in the characterization of these faults. Discussion is provided, however, when direct comparisons between the Knight-Piesold (2013) study and this current SHA study can be made.

For all of the crustal faults, the Youngs and Coppersmith (1984) magnitude recurrence model is applied. This is selected based on the common state of practice for the modeling of crustal faults. The vertical thickness for each fault is assigned to be 15 km. This value is consistent with the assigned vertical thickness of 15 km for the Castle Mountain fault used by the USGS (Wesson et al., 2007) and is also consistent with the average hypocentral depth of about 12 km for crustal events in the area. Given the relatively small contribution to the total hazard from these crustal faults, no epistemic variability was applied to the vertical thickness. All the crustal faults are assumed to be surface rupturing faults, which to be consistent with the USGS model (Wesson et al., 2007).

The estimate of the maximum magnitudes for the crustal faults is based on the magnitude-area scaling relationship of Wells and Coppersmith (1994). For cases in which variable dip angles are assigned, the best estimate dip angle is used in calculating the maximum magnitude. To capture the epistemic uncertainty, the maximum magnitude is varied by +/-0.2 magnitude units with the weights of 0.185, 0.63 and 0.185 selected to represent the 5^{th}, 50^{th} and 95^{th} percentiles. This range is based on the observed range based on different magnitude-area scaling relationships (e.g., see Appendix E of Field et al., 2013).

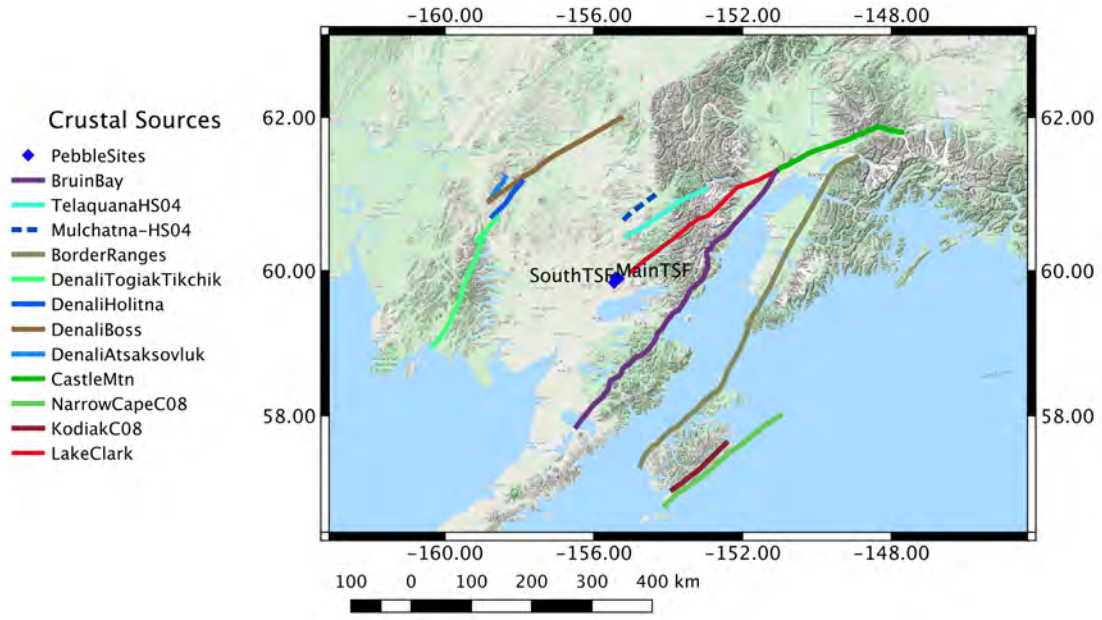

Figure 10. Characterized crustal fault used in the SHA.

Lake Clark Fault

The Lake Clark fault is a right-oblique reverse fault that is mapped from the southwest end of Lake Clark (Haeussler and Saltus, 2004) in a northeasterly direction to the terminus of the western end of the Castle Mountain fault, north of the Cook Inlet. This fault has been identified and mapped in several studies (e.g., Haeussler and Saltus, 2004; Amato et al., 2007; Gillis et al. 2009; Koehler and Reger, 2011), including the Quaternary fault and fold database for Alaska (Koehler et al., 2012). The western trace and terminus of the fault, which is closest to the project site, was refined based on the analysis of aeromagnetic data (Haeussler and Saltus, 2004). In that study, the preferred Lake Clark fault trace was along the northern side of Lake Clark and the end of the fault was approximately located at the southwest end of Lake Clark (Haeussler and Saltus, 2004).

Given the general limited amount of field investigations in this part of Alaska for crustal fault studies due to the remoteness and difficulty in performing such field investigations, there exists a level of uncertainty about the western terminus of the Lake Clark fault. Any western extension of this fault would bring it closer to the project site locations. As noted in the Knight-Piesold (2013) report, personal communications with P. Haeussler indicated that the southwest

extension of the Lake Clark fault was unresolvable given the lack of bedrock exposures in the area but there could be a southern splay towards Iliamna Lake. Two additional field studies (Koehler, 2010; Haeussler and Waythomas, 2011) of the mapped Braid surface scarp south of the project site along the north side of Iliamna Lake concluded that the creation of the scarp was not based on seismic activities. Also noted in the Knight-Piesold (2013) report, a detailed surface geology and geomorphology study was conducted by T. Hamilton for the immediate area around the project site and his findings did not indicate any linear features or disturbance of surficial deposits that would be consistent with seismic fault activity. Based on these studies and conclusions and the acceptance of the Knight-Piesold (2013) characterization, we model the terminus of the Lake Clark fault at the southwest end of Lake Clark, consistent with the findings from Haeussler and Saltus (2004). Any additional future studies which would potentially extend this western terminus of the Lake Clark fault could impact the hazard results provided in this study, and we recommend that a re-analysis be performed in the future based on any updated characterizations of the Lake Clark fault.

Haeussler and Saltus (2004) estimated approximately 26 km of right-lateral offset in the past 34 – 39 Ma for the Lake Clark fault. Previously, Plafker et al. (1975) estimated about 5 km of offset in the last 38.6 Ma and Detterman et al. (1976) estimated about 500 – 1,000 m of vertical uplift of the northwest side of the fault from offset Tertiary strata near the Cook Inlet. These estimates lead to geologic slip rates of 0.67 – 0.76 mm/yr from the Haeussler and Saltus (2004) study and a slower rate of 0.14 mm/yr from the Plafker et al. (1975) study. Koehler and Carver (2018) also note that the Lake Clark fault could be active but with a low slip rate and still remains a poorly characterized fault. To capture this range in the estimated slip rates, four values are assigned. The values of 0.67, 0.715 and 0.76 mm/yr are adopted from the Haeussler and Saltus (2004) study with a total weight of 0.9. The individual weights of 0.27, 0.36, and 0.27 are assigned given the limited data. The central value of 0.715 mm/yr is based on the average of the upper and lower values. The remaining 0.1 weight was assigned to the lower slip rate of 0.14 mm/yr coming from the previous Plafker et al. (1975) study. This assigned 0.1 weight is based on the judgment that the more recent Haeussler and Saltus (2004) study better represented the slip rates than the older study.

The dip angle of this fault is assigned to be 70 degrees with an uncertainty of +/- 15 degrees based on the characterization given in Koehler and Reger (2011). The closest approach of this fault to the Main TSF site location is approximately 25 km with the site being located on the hanging-wall side of this fault.

Based on the mapped length of 262 km, an estimated maximum magnitude of 7.62 is computed based on the Wells and Coppersmith (1994) empirical relationship for magnitude and fault area.

Castle Mountain Fault

The Castle Mountain fault is located northeast of the project site and its western end is at the northeast end of the Lake Clark fault. Given the similar alignment of the fault traces from these

two faults, it has been postulated that these two faults are part of the same system and or connected (Koehler and Reger, 2011); however, no definitive evidence has been shown that this is case. Therefore, for this study, the two faults are treated as separate faults similar to the other seismic hazard studies performed in the region (Fugro, 2012).

The Castle Mountain fault is one of the few crustal faults characterized in the USGS 2007 study for Alaska (Wesson et al., 2007, 2008) in the region around the project site location. Given its relative close location to Anchorage and the observation of recent historical earthquakes associated with this fault, it has received more investigative studies over the years than the other crustal faults in the region (e.g., Labay and Haeussler, 2001; Haeussler et al., 2002; Willis et al., 2007; Koehler and Reger, 2011).

The fault is characterized as an oblique strike-slip fault with a high dip angle that is segmented into eastern and western sections (Willis et al., 2007). The eastern section has a noted dip angle of 75 degrees, dipping to the north, with associated historical events (mb 5.7 and 1984 and magnitude 4.5 in 1996) but no Holocene surface rupture (Willis et al., 2007 and references therein). In contrast, the western section has noted Holocene surface rupture but no associated historical earthquakes (Willis et al., 2007 and references therein).

Preferred slip-rate estimates for the western section of the Castle Mountain fault are 3.0 – 3.2 mm/yr (Willis et al., 2007). The USGS 2007 study (Wesson et al., 2007, 2008) used a slightly lower value of 2.9 mm/yr for the Castle Mountain fault which is a significant increase from the previous state hazard map for Alaska which used an assigned slip rate of 0.5 mm/yr (Wesson et al., 1999). The assigned slip rates for this study are listed in Table 3. The highest and lowest slip rate values of 3.2 and 0.5 mm/yr are selected to capture the range in slip rates each with 50% weight. These are selected given the potential feature that the western section of the Castle Mountain fault is less active (Willis et al., 2007) than the central and eastern section where most of the field work has been performed. This is consistent with the observed decrease in slip rate moving westward along the Denali fault system. Additional variation is not included in the slip rate logic tree for this fault given its distance from the project site and low contribution to the total hazard.

The dip angle of this fault is assigned to be 75 degrees with an uncertainty of +/- 10 degrees. These dip angles are based on general dip angles observed for oblique and strike-slip faults as well as the estimated values from Koehler and Reger (2011) for the Lake Clark fault. The weights for these three values are selected to represent the approximation for the 5^{th}, 50^{th} and 95^{th} percentile distribution. The closest approach for this fault to the Main TSF site location is approximately 286 km. Based on the mapped length of 189 km, an estimated maximum magnitude of 7.47 is computed based on the Wells and Coppersmith (1994) empirical relationship for magnitude and fault area.

Telaquana Fault

The Telaquana fault is mapped parallel to the Lake Clark fault and is located about 35 km to the northwest (Haeussler and Saltus, 2004). Limited information is available for this fault in the published literature and the adopted characterization for this study is based on the characterization from Haeussler and Saltus (2004). This fault is classified as a right-lateral strike-slip fault based on the observed offsets of the magnetic anomalies. Haeussler and Saltus (2004) estimated 10 km (western end) and 11 km (eastern end) of offset in the past 34 – 39 Ma. This translates to a geologic slip rate of between 0.25 – 0.32 mm/yr. The adopted slip rates for the SSC model are listed in Table 3 for the Telaquana fault. These three values are based on the lowest, central, and highest slip rate estimates from the Haeussler and Saltus (2004) study and the assigned weights are selected to represent the 10^{th}, 50^{th}, and 90^{th} percentile given the limited amount of data.

The closest distance from this fault to the Main TSF site location is approximately 63 km. Based on the mapped length of 135 km, an estimated maximum magnitude of 7.31 was computed based on the Wells and Coopersmith (1994) empirical relationship.

Mulchatna Fault

The Mulchatna fault is located north of the Telaquana fault and maps along a similar fault trace azimuth (see Figure 10). This mapped section of the fault is contained in the Plafker et al. (1994) neotectonic map for Alaska (Koehler et al., 2013) database but is not included in the Quaternary fault and fold database (Koehler et al., 2012). Plafker et al. (1994) had this fault identified as being pre-Quaternary. Decker et al. (1994) describe the characterization of the Mulchatna fault as being based on a pronounced aeromagnetic discontinuity.

As part of the Knight-Piesold (2013) study, the Mulchatna fault was included, however, the report does not present the full characterization of this fault which would be needed for a PSHA study (e.g., slip rate or recurrence interval estimates). Given the lack of knowledge for this fault either from the Knight-Piesold (2013) study, published literature (e.g., this fault is not described in the Koehler and Carver, 2018 study), the apparent lack of Quaternary seismic activity, and the expected minimal contribution to the seismic hazard for the project site, this crustal fault source is not included in the analysis. Future studies may provide the opportunity to include this potential crustal seismic source in future seismic hazard studies.

Bruin Bay Fault

The Bruin Bay fault is an identified fault which starts in the southwest of Becharof Lake and is mapped in a northeasterly direction to the approximate location of the Lake Clark and Castle Mountain faults in the northern Cook Inlet area (see Figure 10). This fault represents the northwestern tectonic boundary of the Cook Inlet forearc basin (Betka et al., 2017). Hartsock (1954) first identified the presence of this fault on the Iniskin Peninsula. The fault has been characterized as a reverse fault with variable dip angles ranging between 45 – 80 degrees

dipping to the northwest (Stevens and Craw, 2003 and references therein). Detterman and Reed (1980) noted that the Bruin Bay fault is not defined by a single plane, but rather is observed to be defined by a series of steeply dipping faults which span a range of 6 – 8 km. This is consistent with the Plafker et al. (1994) fault database provided in Koehler et al., (2013). For this seismic study, a singular fault plane is approximated based on these mapped fault traces and other assumed singular fault traces for the Bruin Bay fault (e.g., see Stevens and Craw, 2003; Haeussler and Saltus, 2011; Betka et al., 2017). To capture the uncertainty in the dip of the fault, three dip angles of 50, 65, and 80 degrees were assigned to this fault with the weights of 0.185, 0.63, 0.185 (see Table 3). The dip angles are based on a representative dip angle of 65 degrees for a reverse fault from the Stevens and Craw (2003) study and the range of +/-15 degrees from the Koehler and Reger (2011) study for the Lake Clark fault. The assigned weights are selected to represent the 5^{th}, 50^{th}, and 95^{th} percentile. The closest approach for this fault to the Main TSF site location is approximately 99 km.

Estimates for the slip rate of the Bruin Bay fault are limited and based on long-term geologic offsets. A historical study for the northeastern end of the fault (Barnes, 1966) indicated that the fault is buried under Quaternary deposits except where it is exposed. Schmoll and Yehle (1987) concluded that there is no geologic evidence of activity within the last ~120,000 years (i.e., during the late Pleistocene or Holocene time period). Haeussler et al. (2000) postulate that the northern end of the fault may be associated with Quaternary deformation. More recently, Betka et al. (2017) postulated that the hanging-wall uplift rate associated with the Bruin Bay fault system could be in the range of 0.2 – 0.4 mm/yr based on the offset during the last 31 – 37 Ma. Koehler and Carver (2018) suggest that this fault could be reactivated given the modern stress field in the region. The assigned slip rates of 0.2, 0.3, and 0.4 mm/yr are selected given the estimated range from Betka et al. (2017). The assigned weights of 0.3, 0.4, and 0.3 are selected given the limited data to represent the 10^{th}, 50^{th} and 90^{th} percentile.

Previous seismic hazard studies in the region (Woodward Clyde, 1978) have associated the November 3, 1943 crustal earthquake M_w=7.2 as potentially being associated with the Bruin Bay fault. The epicenter location of this event is located about 40 – 50 km north of the Castle Mountain fault and further away from the Bruin Bay fault. A more recent reanalysis of this event and other historical events in the Cook Inlet area (Silwal et al., 2018) does not support this association of the 1943 historical earthquake with the Bruin Bay fault system.

The total mapped length of the Bruin Bay fault is 509.6 km would translate to a maximum magnitude of 7.9. However, given the potential discontinuous nature of the sections of the Bruin Bay fault as mapped in the region, judgment is applied to reduce this total mapped fault length for the calculation of the maximum magnitude. The maximum magnitude is calculated based on the rupture length being equal to ½ of the total fault length and has a value of 7.6.

Border Ranges Fault

The Border Ranges fault represents the arc-forearc boundary of the Alaskan-Aleutian arc (Haeussler and Saltus, 2011; Pavlis and Roeske, 2007) and has been mapped on a large regional

scale as a single structure for over 1,300 km from Kodiak Island eastwards to Baranof Island (e.g., see Figure 1 of Pavlis and Roeske, 2007). On a more focused site-specific area scale, the Border Ranges fault consists of several shorter mapped segments (Plafker et al., 1994) similar to the other mapped faults in the project region. For this seismic hazard study, a single fault plane is selected to approximate the location of the Border Ranges fault (see Figure 10) due to the large distance to the site region.

Field investigations and general studies of this fault are variable along the sections with an increased emphasis and focus on the sections closer to Anchorage (Pavlis and Roeske, 2007 and references therein). Additional studies have also been conducted on the northwest side of Kodiak Island where the fault is exposed (Pavlis and Roeske, 2007 and references therein). This section is the closest to the project site at an approximate distance of 213 km. The fault is characterized as a vertically dipping strike-slip fault consistent with the tectonic evolution of this boundary fault (Stevens and Craw, 2003; Haeussler and Saltus, 2011).

Estimates of the fault activity of the Border Ranges fault have been limited especially in the region around the project site and has been noted to vary significantly along strike (Pavlis and Roeske, 2007). In the Stuart Creek region, which is located east of Anchorage, Pavlis and Roeske (2007) postulate that up to 130 km of displacement has occurred over the last 65 Ma. This would translate to a geologic slip rate of 2 mm/yr. For this seismic analysis, this estimated slip rate of 2 mm/yr is adopted as the central slip rate for the Border Ranges fault. In the region around Kodiak Island, Caver et al. (2008) estimate an overall southwest movement of 3 – 5 mm/yr for the Bering Block and a general regional tectonic GPS movement of 5 – 15 mm/yr. These estimates would be accommodated by the Border Ranges, Kodiak Island, and Narrow Cape faults. The upper and lower slip rates of 1 and 3 mm/yr are selected in combination with the upper and lower slip rates for the Kodiak Island and Narrow Cape faults to approximate the range of values from Carver et al. (2008). The range in total slip rates from the three faults is 3.25 – 11.6 mm/yr, which is slightly lower than the GPS regional range of 5 – 15 mm/yr from Carver et al. (2008) but more consistent with the Bering block specific range of 3 – 5 mm/yr from Carver et al. (2008). The assigned weights of 0.3, 0.4 and 0.3 are judged to be representative of the 10^{th}, 50^{th}, and 90^{th} percentile based on the uncertainty in the data for this source.

Based on the mapped length of approximately 589 km, a maximum magnitude of 7.9 is estimated. However, consistent with the reduction applied for the Bruin Bay fault, the maximum magnitude assigned to the Border Range fault is computed based on the judgment of using ½ of the total mapped fault length. This maximum magnitude is 7.6.

Kodiak Island and Narrow Cape Faults

The Kodiak Island and Narrow Cape faults represent a series of sub-parallel faults around the area of Kodiak Island (Plafker et al., 1994; Koehler et al., 2013). These faults are azimuthally in alignment with the Border Ranges fault and the trench of the Aleutian Subduction zone (see Figure 10). These faults are believed to accommodate compression and flexure of the upper

plate given the on-going subduction tectonic process (Koehler and Caver, 2018). These faults were characterized to be vertically dipping strike-slip faults with the vertical thicknesses of 15 km (Carver et al., 2008).

GPS measurements across Kodiak Island indicate left-lateral displacements on the order of 5 – 15 mm/yr (Carver et al., 2008). This total would be accommodated by the Border Ranges, Kodiak Island and Narrow Cape faults. In addition, Carver et al. (2008) estimated an individual slip rate of 3.3 mm/yr for the Narrow Cape fault. In the USGS 2007 model, the Kodiak Island fault is assigned a slip rate of 1 mm/yr (Wesson et al., 2007). For this study, the central slip rates of 1 mm/yr (Wesson et al., 2007) and 3.3 mm/yr (Carver et al., 2008) are selected for the Kodiak Island and Narrow Cape faults, respectively. A factor of 2 is applied to these central slip rate estimates to reflect the large uncertainty in the data and the resulting range in the combined slip rates from the Border Range, Kodiak Island and Narrow Cape faults. As indicated previously, this range is between 3.25 – 11.6 mm/yr and is slightly lower than the Carver et al. (2008) range of 5 – 15 mm/yr based on the GPS measurements. It is judged that this slightly smaller range is acceptable given the large uncertainties, the limited data, and or the potential for the regional GPS measurements to be representing other faults not included in the fault slip rate combination. The assigned slip rates for the Kodiak Island and Narrow Cape faults are listed in Table 3 along with the weights that are selected based on the limited data.

Based on the mapped length of 115 km for the Kodiak Island fault, an estimated maximum magnitude of 7.24 is computed based on the Wells and Coppersmith (1994) empirical relationship for magnitude and fault area. The Narrow Cape fault is characterized with a total length of 237 km based on a series of mapped fault traces, mainly off shore of Kodiak Island. For the maximum magnitude, ½ of the total fault length is used given the discontinuous nature of the fault, resulting in the same value of 7.24 as for the Kodiak Island fault. These faults are located at distances greater than 300 km from the Main TSF site location.

Denali Fault

The Denali fault is a major crustal fault in southern Alaska and is mapped from the western coast near Bristol Bay continuously to the Baranof Island region south of Juneau. Historically, larger earthquakes have occurred along this fault system with the largest most recent event being the 2002 Denali earthquake (**M**7.9). Given the significance of this large fault system, several investigations have been performed over the years (e.g., see Haeussler et al., 2016 and references therein); however, the level of investigations significantly decrease for the western sections of the fault system given the remoteness of its location.

The project site is located closest to the western segments of the Denali fault system (see Figure 10). Specifically, these segments are the Boss Holitna, Atsaksovluk and Togiak-Tikchik segments going from east to west. Geologic slip-rate estimates in the region of the Denali fault that ruptured during the 2002 earthquake fall within the range of 7 – 14 mm/yr (Koehler and Carver, 2018). The limited slip-rate estimates both to the east and west of this region are noted to be lower (Koehler and Carver, 2008). An estimate of about 5 mm/yr has been computed for a

location along the Denali fault at a longitude of -152 degrees. Further to the west, near longitude -154.5, a recent estimate of the slip rate was 3 mm/yr (Haeussler et al., 2016). The observed decrease of the slip rate in the western segments of the Denali fault system (Haeussler et al., 2016) is consistent with the tectonic model of rotation and internal deformation of the southern Alaska block and transfer of slip to faults north of the Alaska Range (Haeussler et al., 2014). As part of the USGS 2007 analysis (Wesson et al., 2007, 2008), the slip rate associated with the western segments of the Denali fault system were tapered down from the peak slip rate values in the central section to a slip rate value of zero at a longitude of -154.7. A recent geodetic study for the state of Alaska estimates slip rates for the western extension of the Denali fault to be 0.5+/-0.4 mm/yr range (Elliot and Freymueller, 2018). Given the observed decrease in the slip rates along the western segments of the Denali fault system, slip rates for the four segments considered in this analysis are assigned to be 0.1, 0.5, and 0.9 mm/yr given the recent geodetic study for the State of Alaska. The weights assigned to these values are 0.3, 0.4, and 0.3 given the limited data.

The Boss and Atsaksovluk segments have been classified as showing mid-Quaternary and Quaternary displacement, respectively (Koehler et al., 2013). The Holitna and Togiak-Titchik segments are classified as having pre-Quaternary displacements (Koehler et al., 2013). The Holitna segment is classified as being a northwest dipping reverse fault (Koehler and Carver, 2018), whereas the other faults are not classified and are assumed to be strike-slip in nature consistent with the other segments of the Denali fault system. The Holitna fault is assigned a dip angle of 60 degrees. This single value is selected as a representative value from reverse faults. No uncertainty is placed on this dip angle because of the large distance from the project site to this fault source and its relatively small contribution to the total hazard. All of these segments of the Denali fault system are approximately 200 km away from the Main TSF site location.

The individual fault lengths for each segment are listed in Table 3 along with the estimated maximum magnitude given the fault area.

Table 3. Seismic source characteristics for the crustal faults used in the analysis. Weights for multiple values are indicated in brackets.

Fault	Mechanism	Dip (Direction)	Vertical Thickness (km)[1]	Length (km)	Slip Rate (mm/yr)	Magnitude
Lake Clark	Oblique [0.5][2] Reverse [0.5][2]	55 [0.185] 70 [0.63] 85 [0.185] (NW)	15	262.0	0.67 [0.27] 0.715 [0.36] 0.76 [0.27] 0.14 [0.10]	7.42 [0.185] 7.62 [0.63] 7.82 [0.185]
Castle Mountain	Oblique [0.5] Strike-slip [0.5]	65 [0.185] 75 [0.63] 85 [0.185] (NW)	15	189.5	3.2 [0.5] 0.5 [0.5]	7.27 [0.185] 7.47 [0.63] 7.67 [0.185]
Telaquana	Strike-slip	90	15	134.5	0.25 [0.30] 0.285 [0.40] 0.32 [0.30]	7.11 [0.185] 7.31 [0.63] 7.51 [0.185]
Bruin Bay	Reverse	50 [0.185] 65 [0.63] 80 [0.185] (NW)	15	509.6	0.2 [0.30] 0.3 [0.40] 0.4 [0.30]	7.4 [0.185] 7.6[3] [0.63] 7.8 [0.185]
Border Ranges	Strike-slip	90	15	589.5	1.0 [0.30] 2.0 [0.40] 3.0 [0.30]	7.4 [0.185] 7.6[3] [0.63] 7.8 [0.185]
Kodiak Island	Strike-slip	90	15	114.9	0.5 [0.30] 1.0 [0.40] 2.0 [0.30]	7.04 [0.185] 7.24 [0.63] 7.44 [0.185]
Narrow Cape	Strike-slip	90	15	236.6	1.7 [0.30] 3.3 [0.40] 6.6 [0.30]	7.04 [0.185] 7.24[3] [0.63] 7.44 [0.185]
Denali – Boss	Strike-slip	90	15	223.3	0.1 [0.30] 0.5 [0.40]	7.32 [0.185] 7.52 [0.63]

					0.9 [0.30]	7.72 [0.185]
Denali - Holitna	Reverse	45 [0.30] 60 [0.40] 75 [0.30] (NW)	15	66.6	0.1 [0.30] 0.5 [0.40] 0.9 [0.30]	6.87 [0.185] 7.07 [0.63] 7.27 [0.185]
Denali - Atsaksovluk	Strike-slip	90	15	41.3	0.1 [0.30] 0.5 [0.40] 0.9 [0.30]	6.61 [0.185] 6.81 [0.63] 7.01 [0.185]
Denali – Togiak/Tikchik	Strike-slip	90	15	228.2	0.1 [0.30] 0.5 [0.40] 0.9 [0.30]	7.33 [0.185] 7.53 [0.63] 7.73 [0.185]

[1] All crustal faults are assumed to be surface rupturing faults with vertical thickness of 15 km.

[2] Reverse and oblique fault mechanism are treated the same in the NGA-West2 GMMs.

[3] Maximum magnitude computed based on ½ of total fault length.

2.4 Subduction Interface Sources

The main tectonic process that is occurring in region is the on-going subduction of the Pacific plate beneath the North American plate along the Aleutian trench. Convergence rates in the region are about 50 mm/yr (DeMets et al., 1990). However, all of this convergence is not translated directly into seismic displacement, as a poorly constrained amount of slip is being transferred aseismically (Wesson et al., 2007). Historically, several large interface earthquakes have occurred along this subduction zone including the large 1964 **M**9.2 Great Alaska earthquake. The estimated rupture areas for the large historical subduction earthquakes were shown previously in Figure 3.

The SSC model for the subduction interface events used in this study is primarily adopted from the USGS 2007 model (Wesson et al., 2007, 2008). Specific modifications from the USGS 2007 model are discussed. Given the historical seismicity, the modeling of the full Alaskan subduction zone for large interface events is segmented into seven segments as shown in Figure 11 (Wesson et al., 2008). Based on the location of the project site, the seismic hazard analysis will consider the three closest segments: Semidi, Kodiak, and Prince William Sound. The Prince William Sound and Kodiak segments approximate the rupture area from the 1964 Great Alaskan earthquake and are modeled as rupturing together in our model. In addition, the potential for the Kodiak segment to rupture independently from the Prince William Sound segment is considered. The Semidi segment is also modeled as separate rupture.

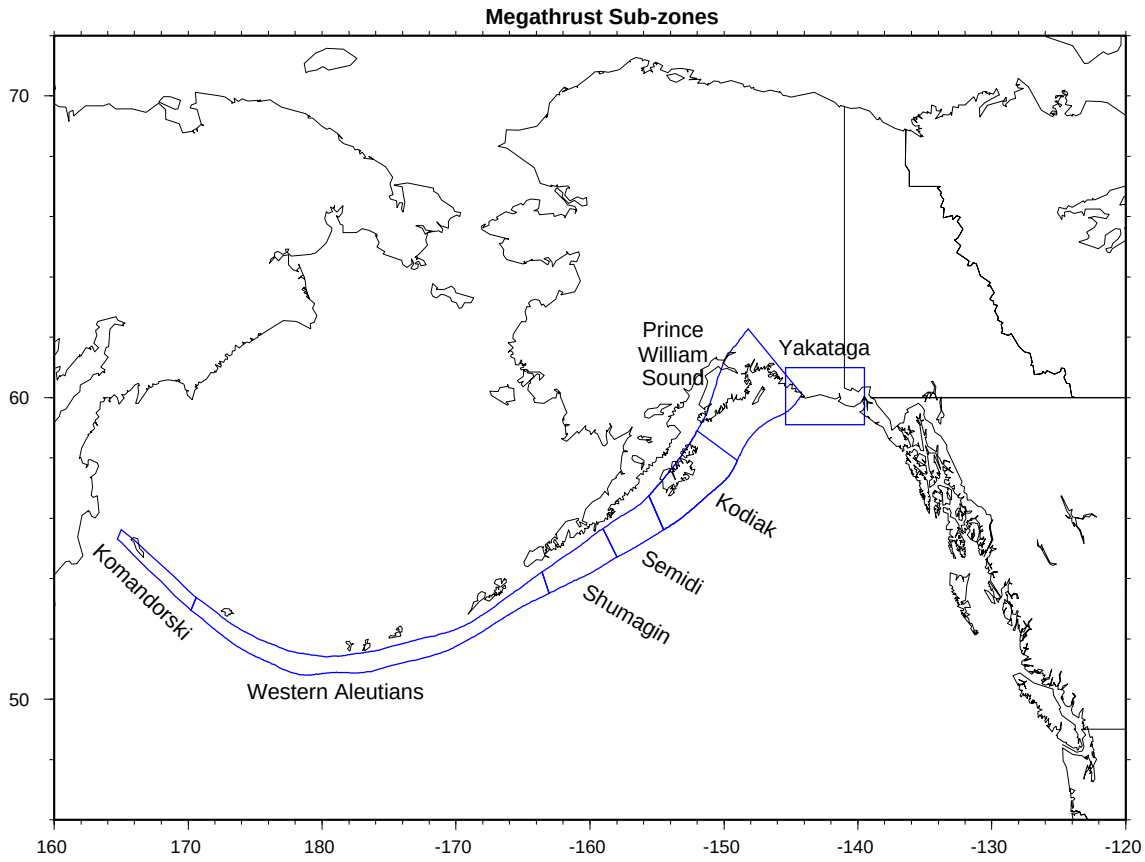

Figure 11. Segmentation of the Alaska-Aleutain subduction zone for large interface earthquakes (Source: Wessson et al., 2008).

Based on the rupture geometry of the subduction zone segments with a variable down-dip width (i.e., variable depth for the bottom of the segment), a singular rectangular fault plane with a constant dip angle would not adequately represent the rupture area. The PSHA program used in this analysis (HAZ45.2) can handle this variable down-dip thickness and has been applied for similar analyses in the Pacific Northwest to handle the variable geometry associated with the Cascadia subduction zone. To implement this geometry, the coordinates (latitude, longitude, and depth) of the top and bottom of the interface source are defined. The PSHA program will create the corresponding 3D shape for the rupture model and compute the necessary distance metrics needed for the ground-motion estimation. The geometry is adopted from the USGS model (Wesson et al., 2007, 2008), and the location of the top and bottom of the modeled interface are shown in Figure 12 for the three closest segments. The upper traces were all placed a depth of 20 km and the bottom traces vary over the range of 33 – 50 km. This upper depth of 20 km was selected based on the inferred rupture area from the 1964 Great Alaska earthquake rather than the shallower depth assumed with the subducting tectonic plate. Note that this shallower depth would be further away from the project site being located in a southeasterly direction. The closest distances from the project site region to the Kodiak segment and the Semidi segment are approximately 225 km and 350 km respectively.

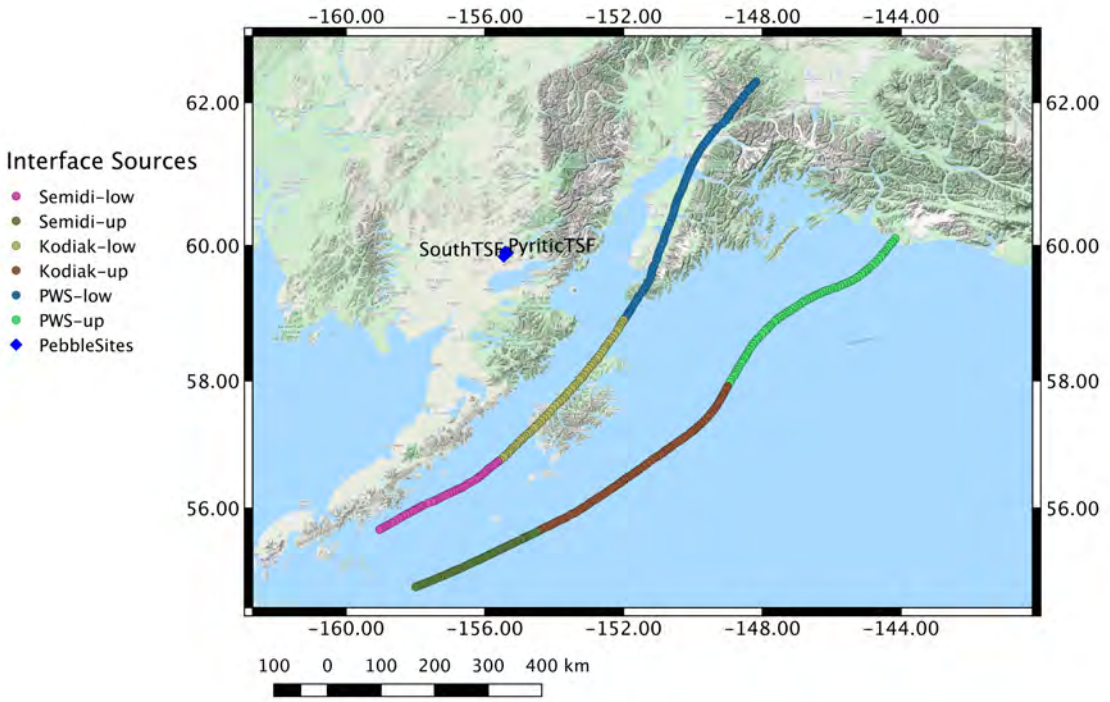

Figure 12. Top and bottom fault traces for the three closest segments of the Alaska-Aleutian subduction zone source model used in the analysis.

The maximum characteristic magnitudes adopted from the USGS 2007 model for the three closest segments are listed in Table 4. The Kodiak segment is modeled as rupturing both independently and with the Prince William Sound segment to replicate the 1964 Great Alaska earthquake. Differing estimates have been presented for the recurrence interval of great megathrust earthquakes in Southern Alaska. Koehler and Carver (2018) estimate a median recurrence interval for the 1964 event of 560 years based on a range between 333 – 875 years. This was based on the analysis of nine events over the last 5,000 years (Koehler and Carver, 2018). Note that the previous USGS 2007 hazard maps and the Knight-Piesold (2013) studies were based on a recurrence interval of 650 years (Wesson et al., 2007, 2008) based on the analysis of six events in the last 3,300 years. For this study, the more recent values from Koehler and Carver (2018) are adopted.

Separate estimates for the recurrence interval of independent rupture of the Kodiak segment have been estimated by Koehler and Carver (2018); however, it is difficult to estimate a robust median value. To account for this uncertainty, the characterization is developed in which the repeat of the 1964 Great Alaska earthquake includes rupture of both the Kodiak and Prince

William Sound segments and an alternative in which the Kodiak and Prince William Sound segments rupture independently. The assigned weights are 90% for the combined rupture and 10% for the separate independent ruptures. The assignment and value of the higher weight (90%) for the full rupture is based on the lack of definitive field investigations that would indicate the Kodiak segment ruptures independently of the combined segments as occurred in the 1964 event. Based on the smaller size associated with the Kodiak segment, a maximum magnitude of 8.8 is assigned which is consistent with the USGS model. Note that for the USGS model, only the combined rupture is considered for the Kodiak and Prince William Sound segments. For these two cases, the magnitude recurrence relationship is modeled as a purely characteristic model as represented by a normal distribution centered on the maximum magnitude and standard deviation of 0.12 magnitude units.

Recurrence interval estimates for the Semidi segment were not developed as part of the USGS 2007 model. Rather, the modeling of large magnitude events (magnitudes in the range of 8 – 8.5) was applied based on the analysis of the seismicity catalog (Wesson et al., 2007, 2008). A truncated Guntenberg-Richter (GR) relationship is used in this study and the parameters are listed in Table 4.

Following the USGS 2007 model and approach, events between magnitudes 7 – 8 are modeled using a truncated GR relationship. The recurrence parameters are listed in the last row in Table 4 and are taken directly from the USGS model. For magnitudes less than 7, the activity rate was based on the recurrence analysis of the seismicity catalog as applied through the smoothed gridded source file (Wesson et al., 2007, 2008). For this study, these smaller magnitude events associated with the distant interface sources (i.e., distances greater than about 300 km) are not expected to contribute significantly to the total hazard at the site and are not included in the SSC model or calculations.

Table 4. Seismic source parameters for Alaska-Aleutian subduction zone sources used in the analysis.

Segment	Largest Historical EQ (Mw, year)	Characteristic Magnitude[2]	Recurrence Interval (year)	a-value	b-value
Semidi	8.2 (1938)	8.5	---	2.4	0.710
Kodiak [0.1]	9.2 (1964)	8.8	560[1]	---	---
Kodiak + Prince William Sound [0.9]	9.2 (1964)	9.2	560[1]	---	---
Aleutian Zone (**M**7 – 8)	9.2 (1964)	8.0	---	3.54	0.689

[1] Median recurrence interval with estimate in the range between 333 – 875 years (Koehler and Carver, 2018). For the analysis three discrete recurrence intervals of 333 [0.185], 560 [0.63] and 875 [0.185] years are used.

[2] Additional epistemic uncertainty of +/-0.2 magnitude units is included in the SSC model with weights of 0.185, 0.63, and 0.185.

2.5 Subduction Slab Sources

The deeper seismicity associated with the subducting Pacific plate has also historically caused significant earthquakes in the region. Most recently, the November 30, 2018 Anchorage earthquake (**M**7.1) was located just north of Anchorage with a depth of 47 km. This epicenter was greater than 300 km from the project site locations. An older but closer (i.e., epicentral distance of approximately 117 km) large magnitude slab event occurred on January 24, 2016 (**M**7.1) and was also associated with the subducting slab. The 2016 event had a hypocentral depth of 129 km. It is also evident from the seismicity plots shown in Figures 5 and 6 that this deeper part of the subducting slab is highly active, and the overall seismic hazard at the project site locations can be expected to be influenced and controlled by these events.

Ratchkovski and Hasen (2002) performed an earthquake relocation methodology in the region which allows for the image of the subducting slab as shown in Figure 13. These relocated events in cross section C1 and C2 are the closest to the Pebble project site and indicate that the subducting slab is seismically active down to depth of approximately 200 km. This deeper section of the slab is about 30 km horizontally from the project site locations.

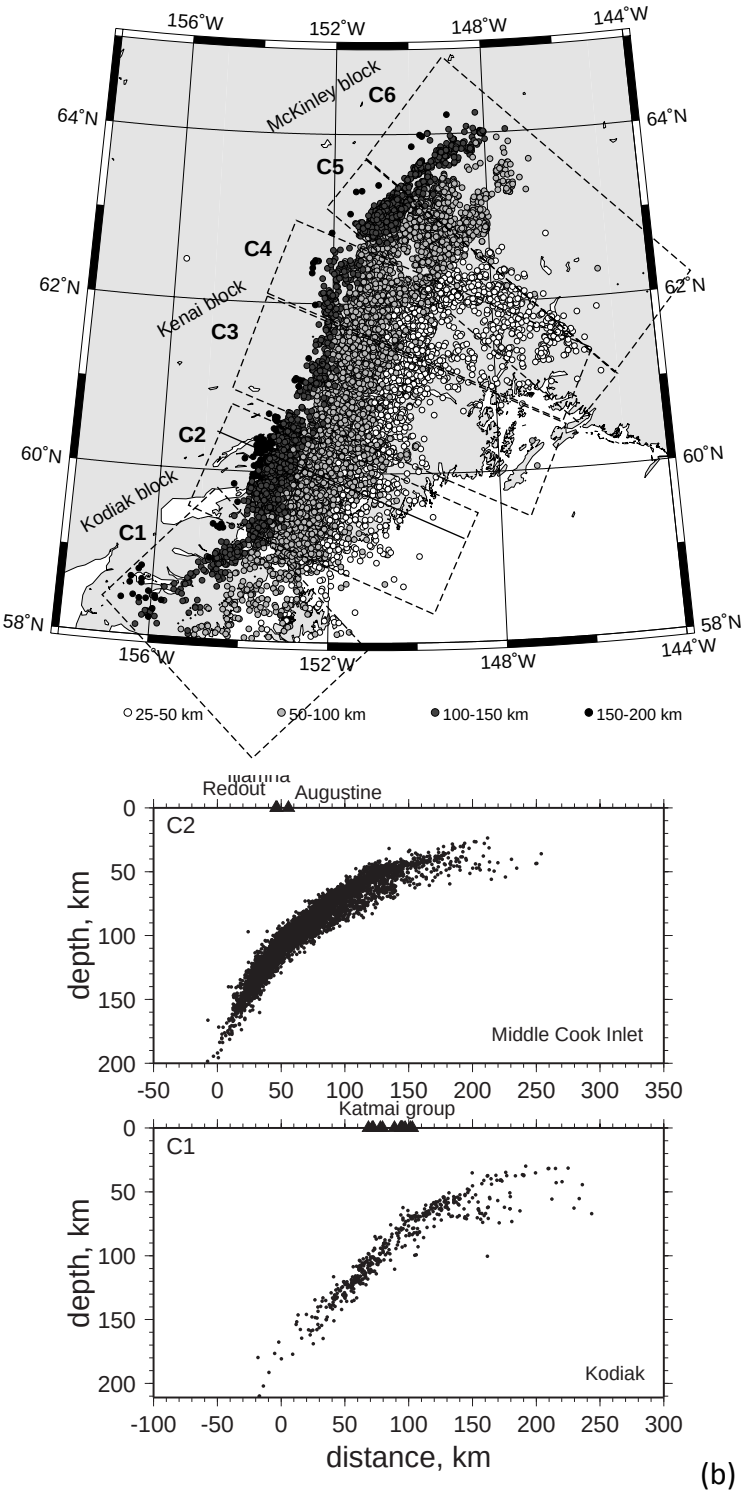

Figure 13. Relocated earthquakes from Ratchkovski and Hansen (2002) shown in map view (a) and cross sections closest to the project site (b).

The modeling and implementation of slab seismic sources within a given PSHA program has been observed to cause differences in the resulting hazard given the same characterization of a slab source (Hale et al., 2018). A more detailed presentation of these implementation choices and differences in the estimated hazard for the simple test case provided in Hale et al. (2018) and for the models used for Southern Alaska are presented in Appendix A.

The implementation differences are related to the geometrical representation of the subducting slab and the expected rupture plane for large slab events. Unlike large interface events that rupture along the top of the subducting plate, these deeper slab events are observed to rupture a cross section of the width of the subducting slab. The geometrical representation of the expected ruptures for slab events should be considered in the modeling of the slab seismic sources within any PSHA program. In addition, GMMs for deeper slab events have a noted strong dependence of increasing ground motions for deeper events for the same closest distance (e.g., Abrahamson et al., 2016).

For the USGS model which was also employed in the Knight-Piesold (2013) study, a gridded seismicity approach was implemented. Given the seismicity catalog for depths of 50 km and greater, a smoothing approach was applied to provide activity rates for grid points based on a 0.1x0.1 degree grid spacing. The smoothing distance was 50 km. Given that this approach is based on the occurrence of historical events in the catalog, the resulting variable activity rates are higher in areas in which historical events have occurred and lower in places with limited seismicity. For the USGS model, two separate depth ranges were computed: 50 – 80 km and 80 – 120 km. Based on the documentation, it is not clear if the events occurring with depths greater than 120 km in the area were included in the deeper layer or eliminated in the analysis. These smooth gridded files were then treated as areal points sources within the PSHA programs (i.e., Approach (a) described in Hale et al., 2018).

For the SSC model developed in this SHA study, virtual vertically dipping faults are placed at a series of depths ranging from 50 km to 200 km, every 25 km. These fault traces for the different depth range values are based on the depth contours of the subduction slab global model Version 2.0 (Hayes, 2018). The fault thickness is assigned to be 20 +/-5 km to represent the thickness of the subducting plate based on cross section plots shown in Figure 13 from Ratchkovski and Hansen (2002). The corresponding weights for this thickness variation is 0.185, 0.63 and 0.185 selected to represent the 5^{th}, 50^{th} and 95^{th} percentile. These virtual faults are plotted in Figures 14 and 15 along with the project seismicity catalog. One feature observed with the seismicity associated with the slab events is a non-uniform spatial distribution of events. To capture this feature in the SSC model, the seismicity catalog is separated first by depth ranges of 50 – 100km, 100 – 150 km, and 150 – 250 km. Next within a given depth range, subsections of seismicity based on the observed spatial distribution is selected. For the shallowest depth range of 50 – 100 km there are three selected subsections: SW, Central, and NE. The associated events with each of these subsections are plotted in Figure 14a with different colors.

For the next depth range, a total of six subsections are selected starting with SW01 at the southwestern end of the source through SW06 at the northeastern end of the source. This depth range shows a larger variability in the spatial distribution of events than the previous shallower depth range. The seismicity associated with the six different subsections are indicated in Figure 14b with the different colors. Finally in Figure 15, the seismicity from the deepest depth range of 150 – 250 km is plotted in separate colors indicating the three subsections, SW, Central, and NE.

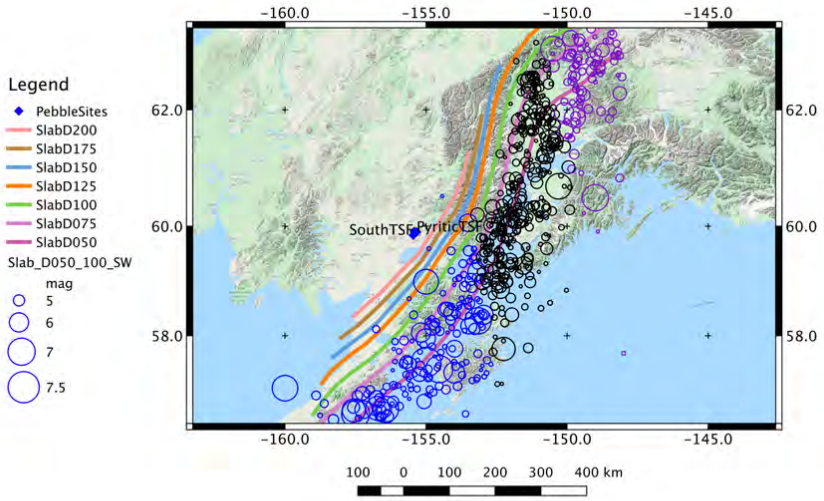

(a)

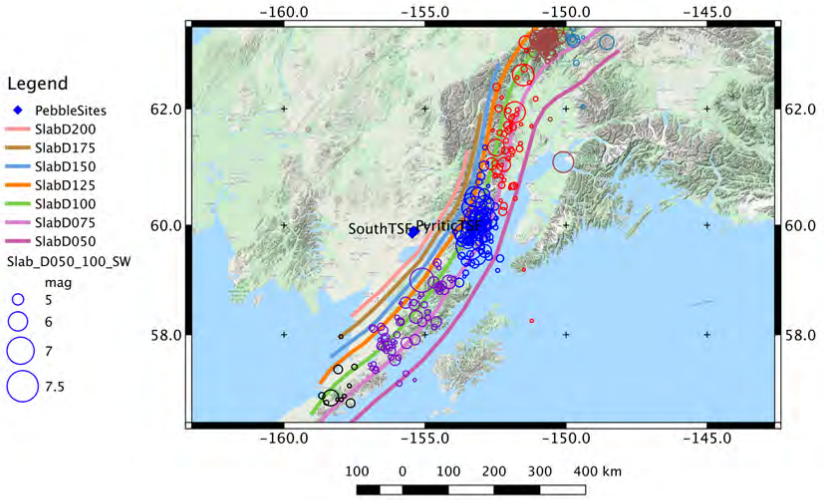

(b)

Figure 14. Virtual slab faults and seismicity from the project catalog for events separated by 50 – 100 km (a) and 100 – 150 km (b) with events from each subsection plotted with separate colors.

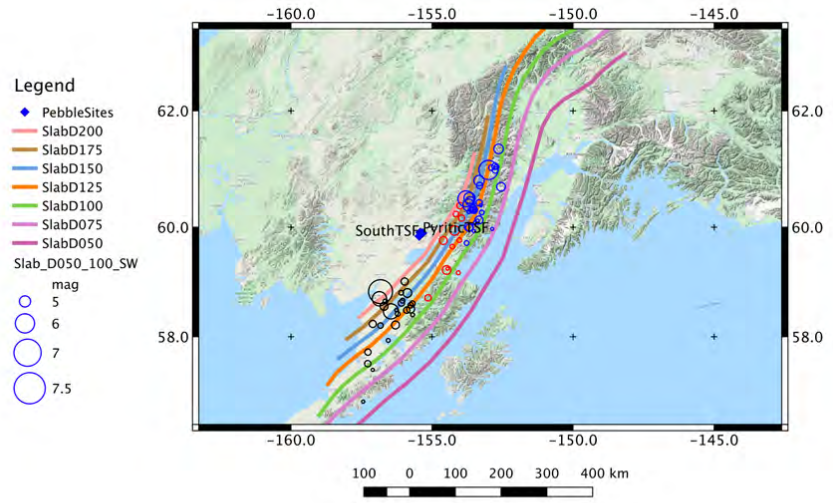

Figure 15. Virtual slab faults and seismicity from the project catalog for events separated by 150 – 200 km with events associated with each subsection plotted with different colors.

For the current SSC model, earthquake recurrence rates are estimated following the Weichert (1980) approach using the project earthquake catalog separated by depth and an additional selection criterion of having events located within the longitudes of -148 to -160 degrees. Although events outside of these longitudes are observed, their greater distance from the project site locations does not necessitate their inclusion for the SSC model development.

Recurrence parameters are estimated for the three specific depth ranges of 50 – 100 km, 100 – 150 km, and 150 – 250 km based on the full geographically sorted earthquake catalog. Based on these estimated recurrence parameters, the activity rates for a given depth range is assigned to the corresponding virtual fault for the associated depth range. A sensitivity analysis is performed on the full earthquake catalog where the recurrence parameters are estimated for the sorted earthquake catalog only using those events through 2004 and compared to the results from the full catalog. The same conclusion is observed that the full catalog including the more recent events does not change the recurrence parameters for the slab model. The additional partitioning of the activity rate within a given depth range is based on the fault lengths associated with each virtual fault and with the ratio of the number of events within a given subsection to the total number of events for all subsections. For the PSHA calculations, these subsection activity rates are assigned to the subsection part of each virtual fault. For the SSC model used in the analysis, the estimated uncertainty in the b-values is incorporated. These values are listed in Table 5.

The differences between this model and the USGS report can be summarized in the following topics. More additional details are discussed in Appendix A. This SSC model assumes that, for a given subsection of the fault (i.e., depth range), the occurrence of events is uniform along the virtual faults, whereas the USGS approach distributes the occurrence of events similar to the observed historical distribution. For the USGS approach, a simplified two-layer model is implemented to approximate the full down-dip extent of the slab whereas the current SSC model approximates the down-dip slab with a set of seven virtual faults. Although these deeper faults have lower activity rates consistent with the observed seismicity, the USGS model does not directly model these events. This deeper part of the slab is closer in horizontal distance to the project site locations, albeit at a deeper depth. Finally, the maximum magnitude assigned to these slab sources is 7.5 for the USGS and both 7.5 and 8.0 for the current SSC model. This increase for the maximum magnitude is consistent with global dataset of slab events (Bozorgnia and Stewart, 2020). The recent 2014 **M**7.96 slab earthquake occurred along the Aleutian slab section well to the west of the project site location. The largest historical event in the slab database for the Alaska subduction section is **M**7.15 and given these historical observations, the assigned weights for the two maximum magnitude values is 50% each.

Given these noted differences and the expected differences based on the implementation and representation of the slab within a PSHA program (Hale et al., 2018), it is expected that the contribution from the slab sources from the current SSC model will be greater than the simplified model used by the USGS. Additional details and discussion are provided in Appendix A to support this expectation.

Table 5. Seismic source parameters for slab subduction zone sources used in the analysis. Weights for multiple values are indicated in brackets.

Slab Fault	Depth Range (km)	Catalog Depth Range (km)	b-value	Act (N>=5) [Subsection]	Maximum Magnitude
Slab_D050	50 – 70	50 – 100	0.7403 [0.185] 0.7872 [0.63] 0.8341 [0.185]	0.41119 [SW] 0.69619 [Central] 0.20409 [NE]	7.5 [0.5] 8.0 [0.5]
Slab_D075	75 – 95	50 – 100	0.7403 [0.185] 0.7872 [0.63] 0.8341 [0.185]	0.42249 [SW] 0.71394 [Central] 0.20929 [NE]	7.5 [0.5] 8.0 [0.5]
Slab_D100	100 – 120	100 – 150	0.8217 [0.185] 0.8926 [0.63] 0.9635 [0.185]	0.01903 [SW01] 0.11418 [SW02] 0.18872 [SW03] 0.08881 [SW04] 0.14590 [SW05] 0.06978 [SW06]	7.5 [0.5] 8.0 [0.5]
Slab_D125	125 – 145	100 – 150	0.8217 [0.185] 0.8926 [0.63] 0.9635 [0.185]	0.01767 [SW01] 0.10601 [SW02] 0.17521 [SW03] 0.08245 [SW04] 0.13545 [SW05] 0.06478 [SW06]	7.5 [0.5] 8.0 [0.5]
Slab_D150	150 – 170	150 – 175	0.7417 [0.185] 0.9317 [0.63] 1.1217 [0.185]	0.02933 [SW] 0.01291 [Central] 0.03637 [NE]	7.5 [0.5] 8.0 [0.5]
Slab_D175	175 – 195	150 – 175	0.7417 [0.185] 0.9317 [0.63] 1.1217 [0.185]	0.02303 [SW] 0.01013 [Central] 0.02856 [NE]	7.5 [0.5] 8.0 [0.5]
Slab_D200	200 - 200	150 – 175	0.7417 [0.185] 0.9317 [0.63] 1.1217 [0.185]	0.01741 [SW] 0.00766[Central] 0.02159 [NE]	7.5 [0.5] 8.0 [0.5]

2.6 Crustal Host Zone

Given the lack of characterized faults in the immediate area around the project site location, the SSC model also considers the potential for events occurring and not associated with any fault. This areal crustal host zone is shown in Figure 16 along with the seismicity with depths less than 50 km. Note that only three of these events had depths greater than 21 km (see Figure 16) being from 1964, 1965, and 1968 and with depths of 33 km, these early hypocenter locations were likely based on a default depth of 33 km used for world-wide seismicity rather than an estimated instrumental depth location. The other remaining seven events have an

average depth of 10.6 km with the deepest being 21 km. The boundaries of this crustal host zone are selected to include the local seismicity in the area with the consideration of the general tectonics and other mapped features in the area. A total of 10 events are located within this crustal host zone and the recurrence parameters are estimated using the same Weichert (1980) methodology. These results are listed in Table 6. Given the limited number of events for this crustal host zone, the uncertainty associated with this source zone is large and taking an upper and lower value would lead to b-values inconsistent with general seismicity studies. Thus, a larger regional crustal catalog is processed to estimate the standard deviation for the b-value. This larger catalog had a total of 76 events. The computed b-value is 0.8981 with a standard deviation of 0.1295. This b-value is similar to the value of 0.9206 computed using the smaller catalog. Similar activity rates are also computed from these two earthquake catalogs. For the analysis, the base b-value of 0.9206 is selected along with an approximate standard deviation from the larger catalog of 0.12. These values are listed in Table 6.

The maximum magnitude for this source is assigned to be 7.25 with the additional epistemic uncertainty of +/-0.2 magnitude units. This maximum magnitude is consistent with the assigned maximum magnitude value of 7.3 used in the USGS SSC model and judgment in taking a slightly larger magnitude than has been historically observed. For the larger regional crustal earthquake catalog, the largest historical event occurred in 1903 and was a magnitude 6.9. The other difference, however, between the two SSC models is again the USGS model uses a smooth gridded approach with a smoothing distance of 75 km. Given the sparse events in the immediate region shown in Figure 16 and the smoothing distance of 75 km, it can be expected that the relative contribution from the crustal host zone in the current SSC model and the USGS gridded source zone would be similar. A sensitivity test run confirmed this expectation.

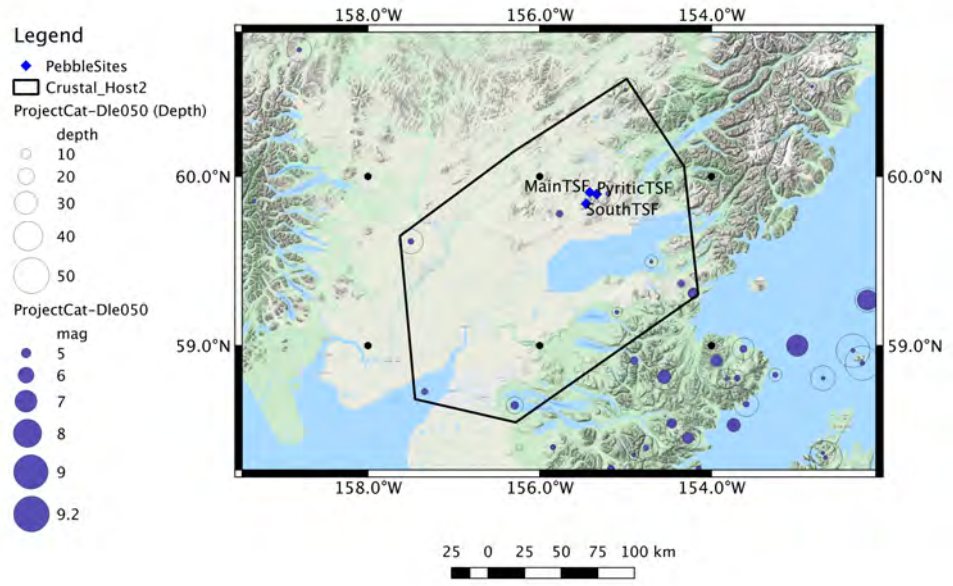

Figure 16. Crustal host areal source zone and all events with depths less than 50 km shown both with variable size for magnitude (purple circles) and depth (open circles).

Table 6. Seismic source parameters for crustal host zone. Weights for multiple values are indicated in brackets.

Source	b-value	Act (N>=5)	Thickness (km)	Maximum Magnitude
Crustal Host	0.72 [0.185] 0.92 [0.63] 1.12 [0.185]	0.02375	15.0	7.05 [0.185] 7.25 [0.63] 7.45 [0.185]

3. Ground-Motion Characterization

For both the PSHA and DSHA calculations, GMMs are required. Given the combination of crustal seismic sources and subduction seismic sources, available candidate GMMs are reviewed and ultimately selected for each of these two types of seismic sources. Based on the review of candidate GMMs, the GMC model is developed and is presented in this section of the report.

3.1 Crustal Ground-Motion Models

The development of GMMs for crustal earthquakes in active tectonic regions has significantly evolved during the last decade based on the large increase in the amount of empirical ground-

motion data. Given the history of the previous SHA studies discussed in this report, the suite of GMMs used for crustal events has also evolved. The USGS maps for the Alaska region were based on models from the late 1990s (Wesson et al., 2007). For the more recent Knight-Piesold (2013) study, an update to the GMMs used by the USGS was employed. These newer models were part of the NGA-West1 models that were published in 2008.

The current state of knowledge and practice for crustal GMMs is the more recent NGA-West2 models (Bozorgnia et al., 2014). This suite of GMMs are based on the increased database associated with the NGA-West2 project and GMMs were developed from the same developer teams that were involved in developing the GMMs from the NGA-West1 database. Specifically, five GMMs were developed: Abrahamson et al. (2014) (referred to as ASK14), Boore et al. (2014) (referred to as BSSA14), Campbell and Bozorgnia (2014) (referred to as CB14), Chiou and Youngs (2014) (referred to as CY14) and Idriss (2014) (referred to as ID14). All of these models were defined for the RotD050 component (Boore, 2010) and for spectral damping of 5%. The RotD050 ground-motion is a measure of the amplitude for the average horizontal component and corresponds to the 50^{th} percentile of the response spectra over all rotation angles.

One significant improvement in the GMMs from the 1990s to the current NGA-West2 models is in the classification and characterization of the site response aspect of ground motions. Previously, GMMs were classified based on either "rock" or "soil" site conditions given the limited site information contained in the database for the recording stations. With the improvement of the databases for the NGA-West1 (Chiou et al., 2008) and NGA-West2 (Ancheta et al., 2014) projects, a refined site response function was included based on the time-averaged shear-wave velocity in the top 30 m, defined as the V_{S30} value. Note that the Knight-Piesold (2013) study was for rock site conditions, however, the report does not indicate the V_{S30} value used in the analysis for this generic site condition. As noted earlier, the results presented in this study are for a defined reference site condition with a V_{S30} of 760 m/sec.

Certain NGA-West2 GMMs also include an additional site and basin response term associated with the depth to a shear-wave velocity of 1.0 km/sec (Z1) and 2.5 km/sec (Z2.5). If site-specific information is available for these parameters, they can be used. However, for this study, no site-specific information is available and the default values (i.e., Z1=0.034 km, Z2.5=0.608 km) given the V_{S30} value of 760 m/sec are used in the analysis.

For the ASK14 and CY14 models, the functional form of the models based on an "estimated V_{S30}" value was implemented in this study. Note that the differences between the estimated and measured V_{S30} flag only impact the aleatory standard deviation of two of the four GMMs (ASK14 and CY14) but does not impact the median ground-motion estimates.

Because the NGA-West2 GMPEs were developed in a collaborative effort with interactions and exchange of ideas among the developers, the NGA-West2 developers recommend that additional epistemic uncertainty be incorporated into the median ground-motion estimates from their GMPEs. The additional epistemic uncertainty model of Al Atik and Youngs (2014), developed as part of the NGA-West2 project is used in this study. This epistemic uncertainty

model is distance-independent but depends on magnitude, style-of-faulting, and spectral period. The logic tree for the ground-motion characterization model is shown in Figure 17.

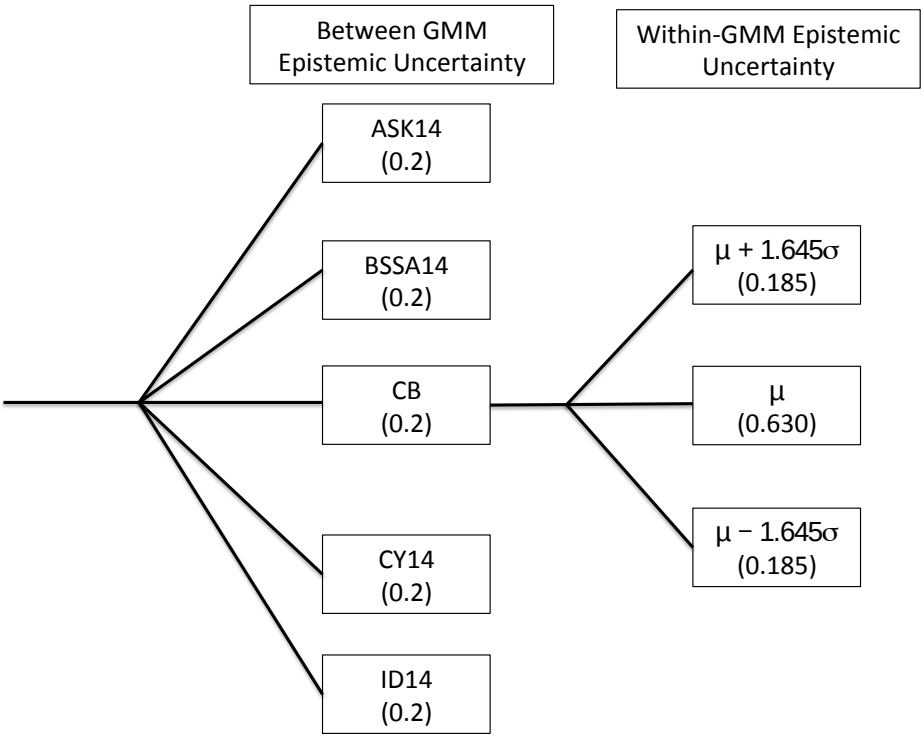

Figure 17. GMM logic tree for crustal events showing the different branches and associated weights; μ and σ are median predication and epistemic standard deviation of the natural-logarithmic values of the ground-motion parameter of interest.

3.2 Subduction Ground-Motion Models

The development of GMMs for subduction earthquakes has not followed the same rapid community-wide development as models for crustal earthquakes. Similar to the pre NGA-West community development of GMMs, subduction models were published based on developer teams working independently and based on different databases. One of the first large scale efforts to collect a global database of subduction ground motions was performed for the BC Hydro (2012) project. For this project, previous subduction databases (e.g., Youngs et al., 1997; Atkinson and Boore, 2003, 2008) were compiled with additional more recent data. Given this expanded database, a global GMM for subduction earthquakes was developed (Abrahamson et al., 2016).

This newly developed GMM for subduction earthquakes (referred to BCHydro) has several functional features which are similar to the functional form for crustal earthquakes. Included in

this was the functional model for the site response, which was based on the V_{S30} parameter similar to the crustal models. Following the time cutoff closure of the subduction database and during the development of the BCHydro GMM, two significant subduction interface events occurred: the 2008 Maule Chile **M**8.8 and the 2010 Tohoku Japan **M**9.0 events. Based on a residual analysis of the data and the initial model, period dependent adjustments were incorporated into the final model to account for these recent large interface events (Abrahamson et al., 2016). In addition, as part of these final adjustments, the magnitude scaling for slab events was modified to have a center magnitude scaling break point at 7.5. For the full BCHydro model, a full logic tree was developed for applications in which other subduction GMMs are not considered. For this study, since additional subduction GMMs are being used in the analysis, the full BCHydro logic is not used, but the epistemic uncertainty branches for the magnitude scaling break point is used.

Recently, the NGA-Subduction program (Bozorgnia et al., 2018) has followed the same community involvement approach successfully performed for crustal models. The database developed for this NGA-Subduction program represents the most current global subduction ground-motion database to date (Bozorgnia and Stewart, 2020). Subduction data was collected from numerous tectonic subduction zones around the world including Alaska. Both the 2008 Maule Chile and the 2010 Tohoku Japan ground-motion data are contained in this global database. In addition to the ground-motion data, the associated metadata for the events and the stations has been compiled although the quality of this additional data varies from region to region, especially for the station information.

Given this newly developed database for subduction earthquakes, several developer teams were involved with the development of GMMs for subduction earthquakes. Similar to the NGA-West program, these developer teams worked in a community environment allowing for the sharing of knowledge during the model development stage. To date, there are two models that have been developed and are in pre-publication: Kuehn et al. (2020) and Parker et al. (2020). These two models are referred to by the author's acronyms KBCG and PSHAB. Given the recent development of these models and their resulting limited use in ground-motion studies, an evaluation of the models in comparison with the BCHydro model (Abrahamson et al., 2016) is performed. The PSHAB model is initially considered as part of this analysis; however, a recent modification of the model is being performed (J. Stewart, personal communication) and based on the unresolved modifications of the model, it is dropped from consideration for this study.

Given the global subduction database, which is comprised of regional sub-datasets, the KBCG developer team constructed both a global model and regionalized models for different subduction zones, one of which is Alaska. The regionalization consists of a regional constant term, regional site amplification term, regionalized anelastic attenuation term, and regionalized magnitude scaling break point value. Both the global versions of this model and their respective Alaska versions are reviewed and considered for inclusion in this SHA study.

In reviewing the data contained in the NGA-Subduction database from Alaska, a large percentage (i.e., 95%) of the V_{S30} information for the stations was based on inferred values

rather than measured values. In addition, the majority of the measured values were for sites located in Anchorage and for stations located away from this large metropolitan area, the assigned V_{S30} values were not robust given the limited geologic and or general information for parts of Alaska (Bozorgnia and Stewart, 2020). It should also be noted that a large amount of the Alaska data is based on recordings from the Temporary Array at significant distances (i.e., several of hundreds of km away from the event) (Bozrognia and Stewart, 2020). Given this limitation in the data from Alaska, the regionalization of the models may not be robust and is considered as part of the evaluation of the regionalized Alaska models from this new NGA-Subduction model.

Another feature of these subduction GMMs being evaluated, including the BCHydro model, is the formulation of a magnitude scaling break point. For the new NGA-Subduction model, these magnitude scaling break points are defined as a function of the subduction region and specifically, the subducting plate. For example, for interface events for the global model, the value is 7.9 for the KBCG model. However, for the Alaska plate region which includes the Kodiak and Prince William Sound segments of the Alaska-Aleutian subduction zones, this value is 8.6. For the rest of the Alaska-Aleutian subduction zone, the value is 8.0. Given this larger magnitude scaling break value of 8.6 for the KBCG model, higher median ground motions are predicted for the representative **M**9.2 Great Alaska earthquake using the Alaska regional model than the global model with the smaller magnitude scaling break point value of 7.9. Additional differences are observed based on the differences between the regionalization of the other features of the model (i.e., constant term, site amplification, and anelastic attenuation).

Given the importance of these magnitude scaling break points, an assessment of their values is performed. The higher **M**8.6 value from the KBCG model is based on Campbell (2020) which is based on the age and geometry of the subducting plate in this region of Alaska. Median estimates of this magnitude value fall within the range of 8.3 to 8.9 with the recommended value of 8.6. Based on the limited large magnitude interface data from Alaska, the data does not allow for a better constraint on this value. As an example, the interface data selected for the KBCG model development in Alaska is shown in Figure 18. Additional data from Alaska is contained in the full NGA-Subduction database but the data shown in Figure 18 is the result of applying the selection criteria for the database (Kuehn et al., 2020). The Alaska sub-region (i.e, Kodiak and Prince William Sound segments) only has one earthquake of magnitude 5 (open blue diamonds) with only one station at distances less than 200 km. For the Aleutian segment there is more data but the largest event is a magnitude 7, which is below any magnitude scaling break point. Thus, the data cannot be used to constrain this magnitude break point for Alaska. Note that for the global version, the inclusion of data from events above the magnitude scaling break points allows for the data to constrain the model.

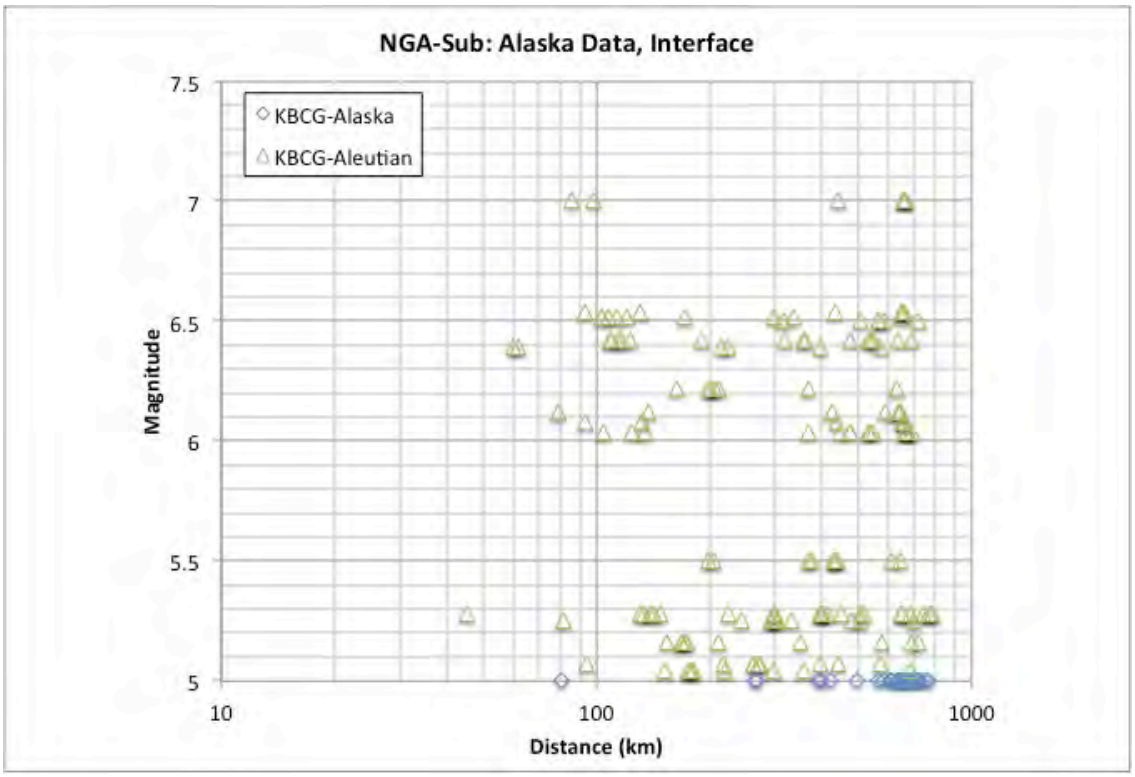

Figure 18. Selected interface data for the KBCG model from Alaska for the two sub-regions of Alaska (Kodiak+Prince William Sounds) and Aleutian.

To further evaluate the subduction interface GMMs, median ground-motion spectra are computed for a representative **M**9.2 earthquake at a distance of 250 km. These spectra are plotted in Figure 19 and are for the reference site condition V_{S30} value of 760 m/sec. The three models for the BCHydro (blue lines) are plotted along with the global and two regional models for the KBCG (red lines) model. As previously discussed, the larger magnitude scaling break point value of 8.6 for the Alaska KBCG model (red dashed line) is the cause of these larger median ground motions, especially at the longer spectral periods. In comparing the BCHydro model with the global KBCG model, the agreement is favorable for longer spectral periods, but the range is wider for short spectral periods. The new KBCG model has a very different spectral shape than the BCHydro model for this scenario. This may reflect regional differences in the ground motions. The BCHydro model is a global model from a data set that is dominated by data from Japan which has much stronger short-period ground motions than other regions.

In addition to the comparison for the median ground motions, a comparison of the total aleatory sigma from the evaluated interface models is shown in Figure 20. These sigma models are independent of magnitude, distance, V_{S30} etc. and the new model shows a significant increase in the total sigma relative to the BCHydro model for all spectral periods except long periods greater than about 5 – 6 sec.

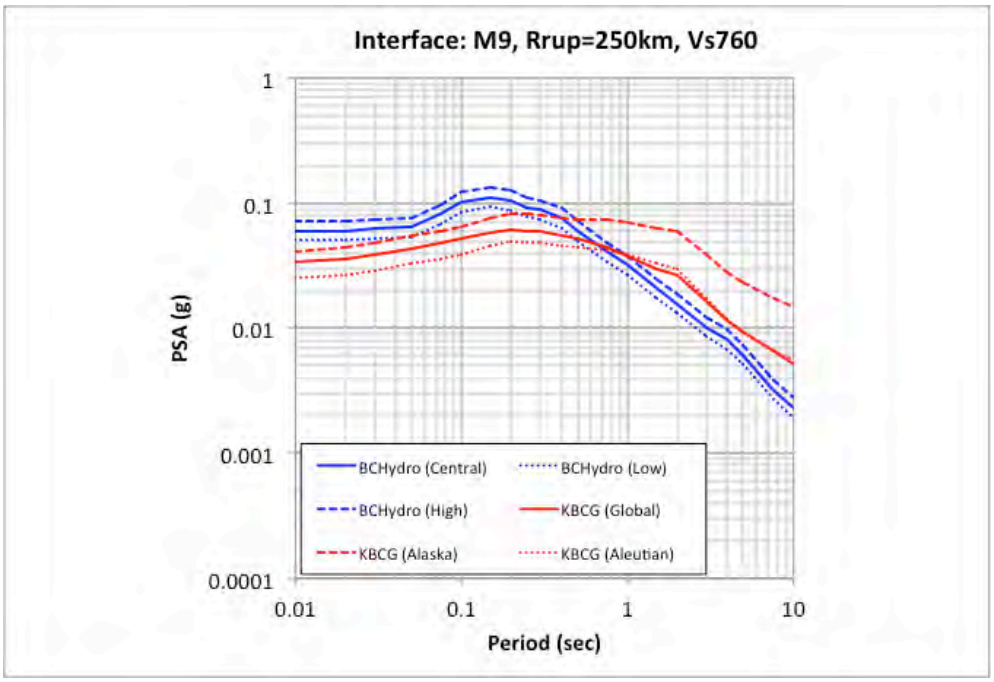

Figure 19. Median spectra for the suite of evaluated interface subduction models.

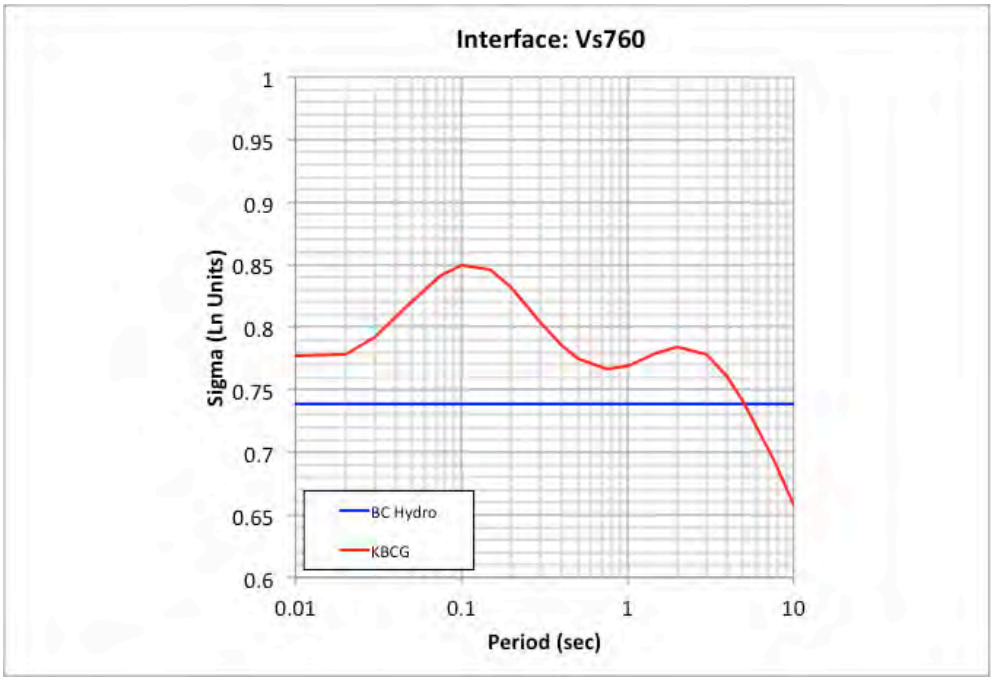

Figure 20. Total aleatory sigma from the evaluated interface subduction models.

Given these evaluations and the assessment of the Alaska data which went into the development of the regionalized models for the KBCG model, only the global versions of this new KBCG model is selected for inclusion in this SHA study.

A similar assessment of the slab models was conducted for this study. The magnitude scaling break points for the KBCG model is 7.6 for the global case, 7.2 for the Alaska case, and 8.0 for the Aleutian case. Note that for the BCHydro model, the recommended central value of the magnitude scaling break point was 7.5 for slab events. The selected slab data used in the KBCG model are plotted in Figure 21. Although there is more data than for the interface case, all of the data fall below the recommended magnitude scaling break point indicating that the data cannot assist in constraining the model.

Based on the preliminary sensitivity analyses of the PSHA, the controlling slab sources are associated with the shallower depths ranges (i.e., 50 – 100 and 100 – 150 km). As a result, four representative median spectra (i.e., two depth/distance values and magnitude 7 and 8) are computed to evaluate the slab subduction models. These spectra are shown in Figure 22 and 23.

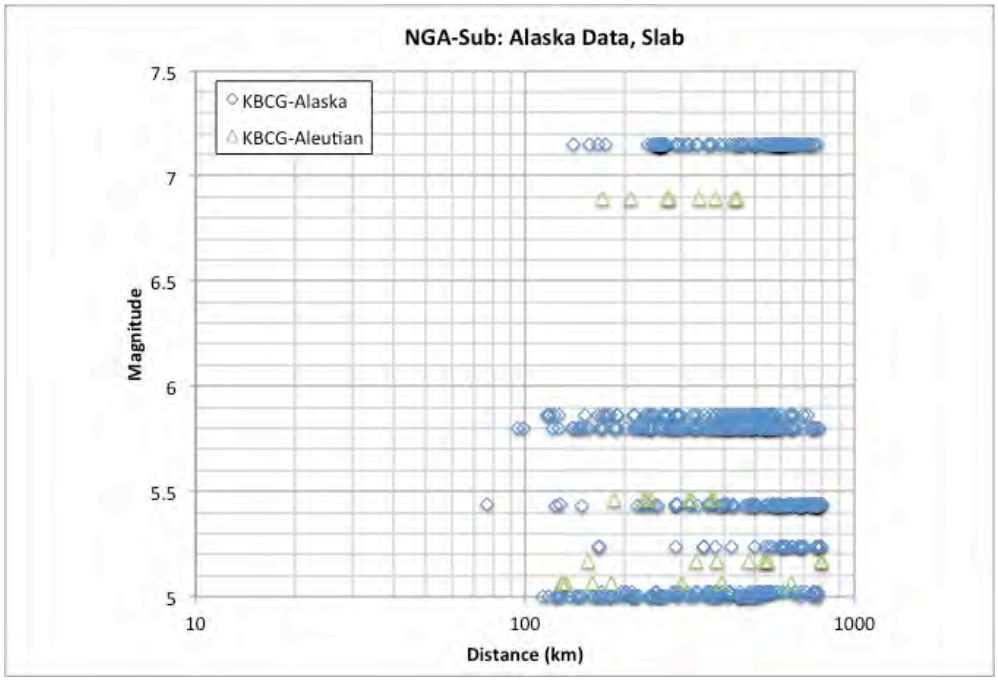

Figure 21. Selected slab data for the KBCG model from Alaska for the two sub-regions of Alaska (Kodiak+Prince William Sounds) and Aleutian.

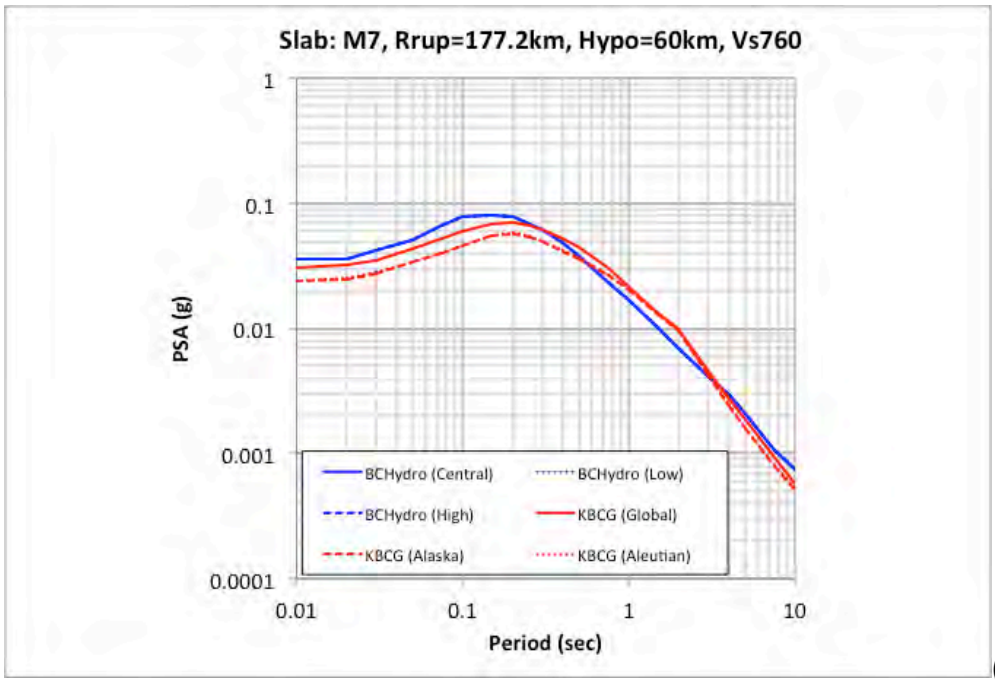

(a)

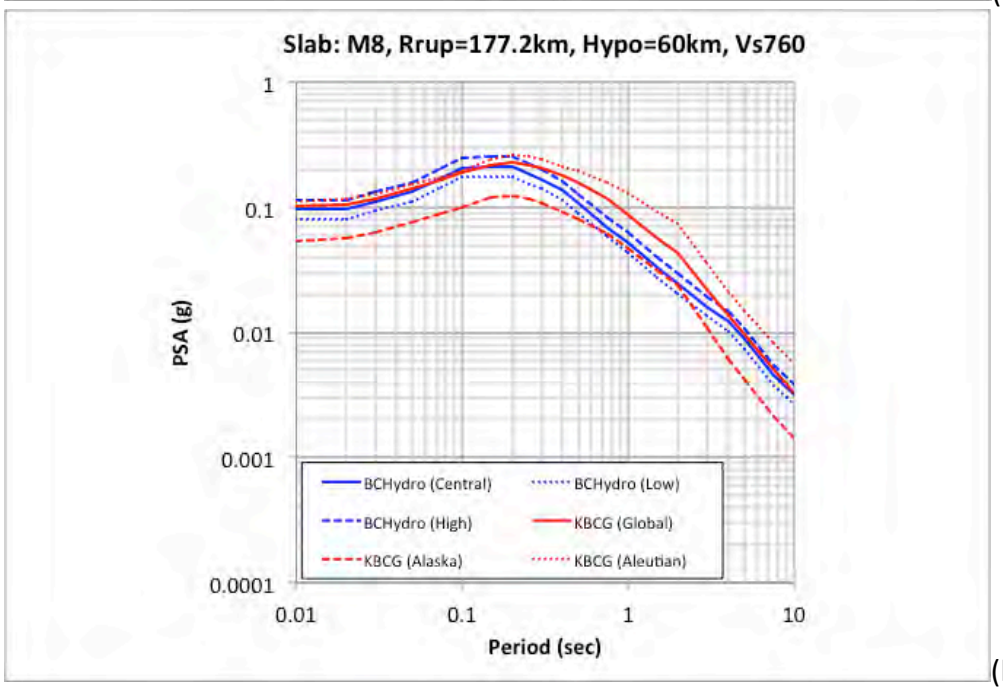

(b)

Figure 22. Median spectra for the suite of evaluated interface subduction models for hypocentral depth of 60 km and magnitude 7 (a) and 8 (b).

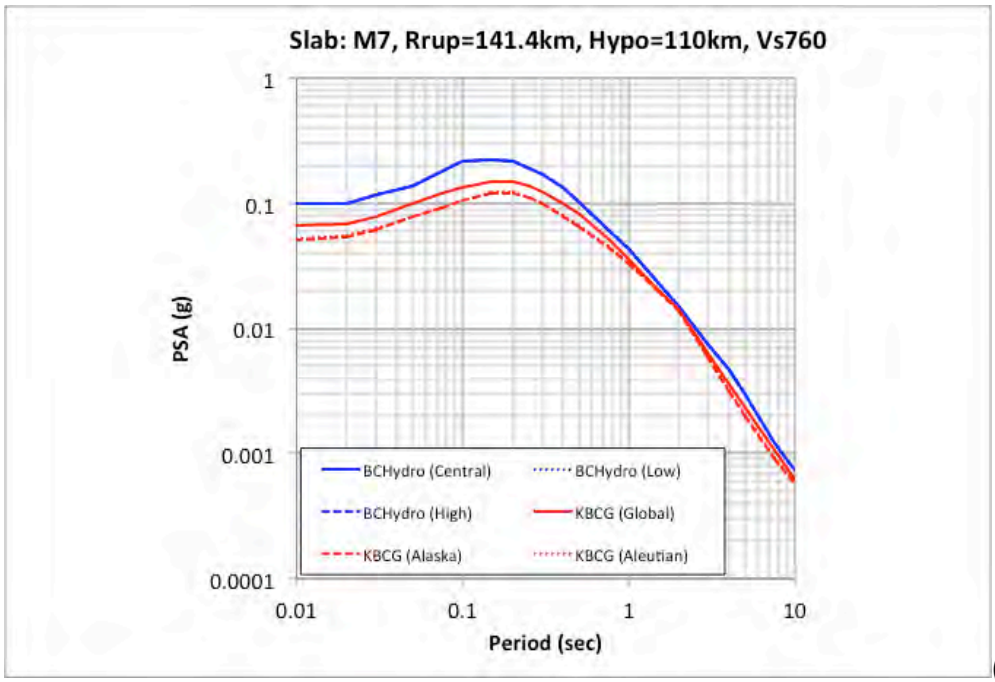

(a)

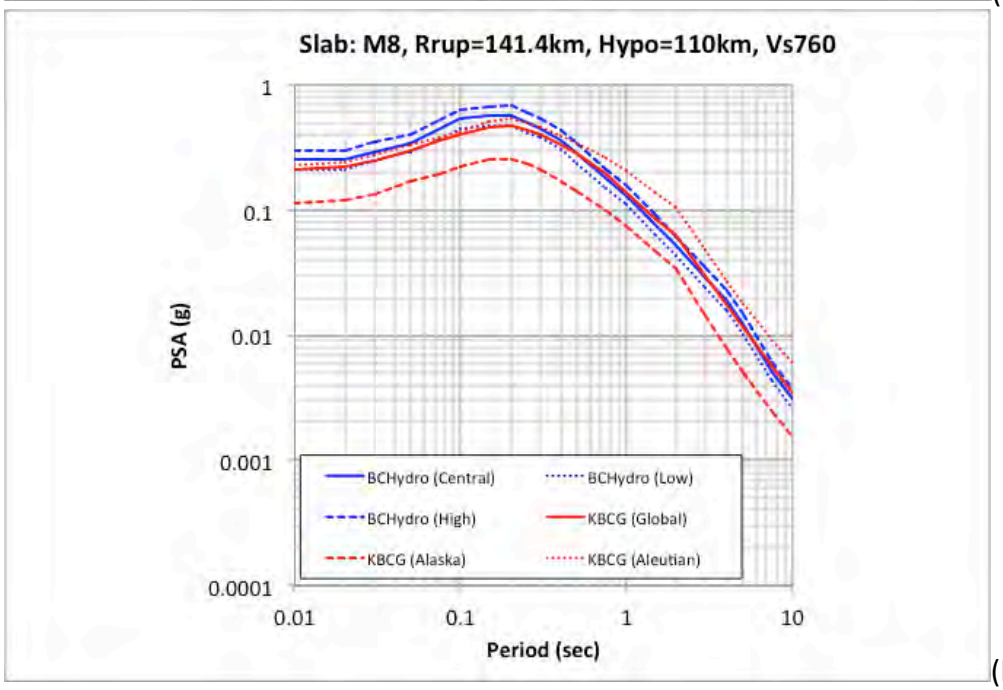

(b)

Figure 23. Median spectra for the suite of evaluated interface subduction models for hypocentral depth of 110 km and magnitude 7 (a) and 8 (b).

For the shallower depth case of 60 km, the agreement between the models is favorable for all spectral periods for the magnitude 7 case. For the larger magnitude 8 case, which is above the magnitude scaling break point, the models show a greater divergence for the regional versions but a similar ground-motion estimates for spectral periods up to about one second. For longer spectral periods, the global KBCG model and the BCHydro model show more divergence. For

the deeper cases plotted in Figure 23, a stronger depth dependence of the BCHydro model than modeled in the KBCG model is observed leading to higher ground motions for the BCHydro model. The other observations noted for the previous comparison are applicable for these deeper cases. For the application of the BCHydro GMM, the recommended hypocentral depth limit of 120 km (Abrahamson, et al., 2016) is implemented in the calculations.

The aleatory sigma models for slab events are plotted in Figure 24. Overall, the same observation as noted for the interface case is applicable for the slab case shown in Figure 24.

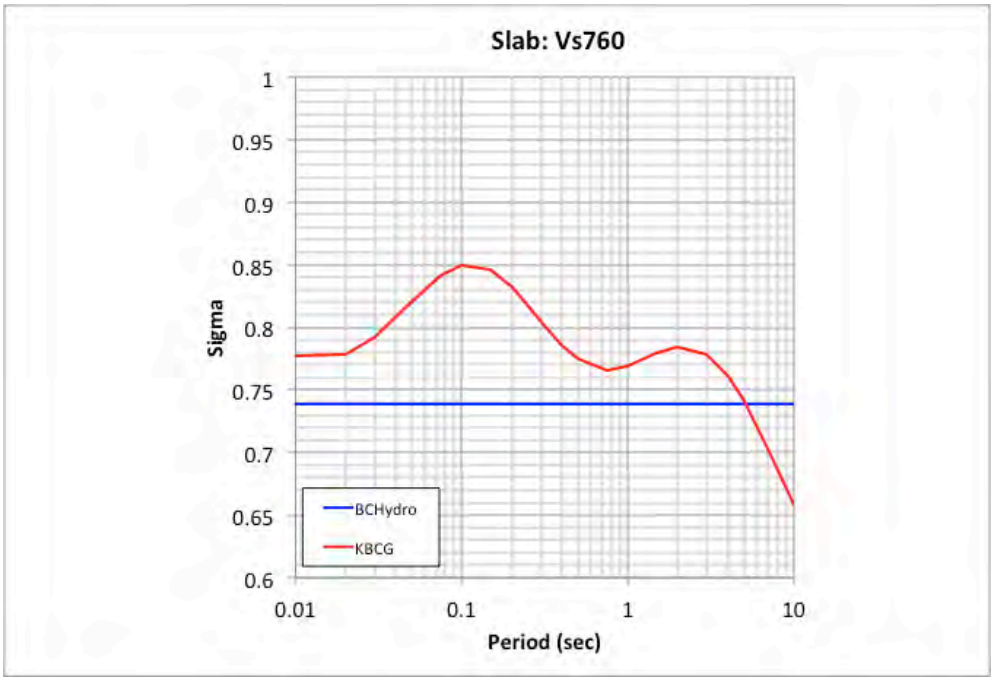

Figure 24. Total aleatory sigma from the evaluated slab subduction models.

Given these evaluations and the assessment of the Alaska data which went into the development of the regionalized slab model, only the global version of the new KBCG NGA-Subduction model is included in the SHA study consistent with the conclusion for the interface version.

The final logic tree for the subduction events (i.e., both interface and slab) is shown in Figure 25. These selected weights consisting of an increased weight for the BCHydro model relative to the new KBCG model is based on the stability and general use of the BCHydro model compared to the newly developed and released GMM and the evaluation observations presented in this report. This lower selected weight of 0.15 for the KBCG model is judged to be acceptable given the limited use of this model in engineering applications at the time of this study. This current study is one of the first studies to consider the new NGA-Subduction model for SHA studies and, as with any new GMM, caution should be used prior to its full adoption for use.

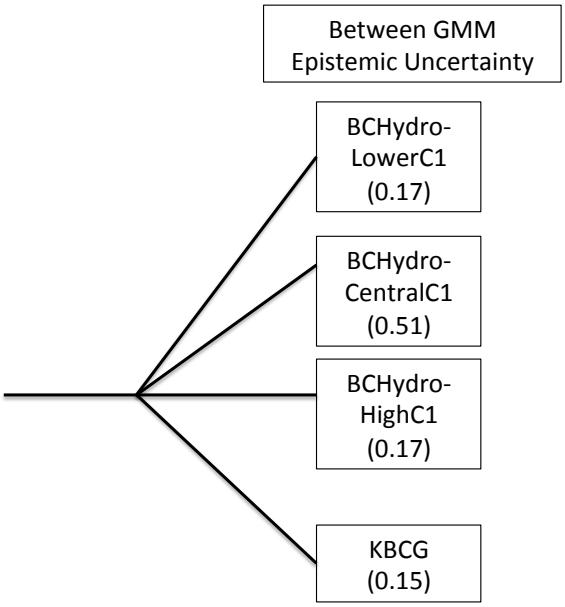

Figure 25. GMM logic tree for subduction events showing the different models and associated weights.

The previous USGS study used the Youngs et al. (1997) and Sadigh et al. (1997) crustal models for interface events with distances less than 70 km and only the Youngs et al. (1997) model for distances greater than 70 km (Wesson et al., 2007). For the slab events, the USGS used the Youngs et al. (1997) and Atkinson and Boore (2003, 2008) models. These older models represent one to two cycles of older GMMs than currently being recommended and used in this study.

For the Knight-Piesold (2013) study, the ground-motion models for interface events were based on the Youngs et al. (1997) and the Atkinson and Boore (2003, 2008) models, which represent an update from the USGS models. Also as noted in the Knight-Piesold (2013), complete saturation (i.e., no increase in the ground-motion estimates for magnitude greater than 8.5) for interface events with magnitude greater than 8.5 was applied for the Aktinson and Boore (2003, 2008) model. Thus in addition to using older GMMs, the estimated ground motions from the characteristic **M**9.2 Great Alaska earthquake would be relatively lower than from other GMMs as a result of the complete saturation magnitude of 8.5 in the Atkinson and Boore (2003, 2008) model.

The other notable difference from the GMMs used in the Knight-Piesold (2013) study and this current study is the classification of the applicable site conditions. For the Knight-Piesold (2013) study, the site condition was classified as “rock” which would be consistent with the classification of the Youngs et al. (1997) model. However, for the Atkinson and Boore (2003, 2008) model, the site classification is consistent with NEHRP site classes ranging from A – E. It is

not clear in the Knight-Piesold (2013) report which specific site classification version of the Atkinson and Boore (2003, 2008) model was used. As noted earlier, the GMMs used in this SHA study are all defined as a function of V_{S30} to capture the site response and a reference site condition of 760 m/sec was selected for this study.

Finally, the selected ground-motion models used in this SHA study are defined for the full broadband spectral period range of 0.01 sec (PGA) to 10 sec. The previous GMMs were more limited in their defined spectral period range with an upper limit of between 3 – 4 sec.

4. Probabilistic Seismic Hazard Analysis (PSHA)

4.1 Methodology

Probabilistic seismic hazard calculations are carried out using the computer program HAZ45.2 (Abrahamson, 2018). This PSHA program follows a standard state of practice approach for probabilistic seismic hazard analysis. It has successfully passed the validation test cases associated with the recent PEER PSHA Validation testing program (Hale et al., 2018).

An epsilon truncation value of 6.0 is used for the PSHA. The minimum magnitude used in the analysis is 5.0. Mean Hazard curves are computed for the three project site location (see Table 1) for the following suite of spectral periods: PGA (0.01 sec), 0.02, 0.03, 0.04, 0.05, 0.075, 0.1, 0.15, 0.2, 0.25, 0.3, 0.4, 0.5, 0.75, 1.0, 1.5, 2.0, 3.0, 4.0, 5.0, 7.5 and 10.0 sec. In addition, fractile hazard curves are computed for these same spectral periods. Based on this suite of mean hazard curves, uniform hazard spectra (UHS) are computed for the suite of five return from 475-yr to 10,000-yr. Estimates of the mean magnitude, distance and epsilon values associated with the set of five return periods are also computed and presented along with select deaggregation results for magnitude and distance bins.

Given the close proximity of the three sites, the general results from the PSHA calculations are similar and the representative plots are fully provided for the Main TSF site location. For the other two site locations (i.e., Pyritic and South TSF) a shorter presentation of the resulting UHS and fractile curves are presented. The deaggregation results are similar for these two sites compared to the results from the Main TSF site location.

4.2 PSHA Results – Main TSF Site Location

Given the input SSC and GMC model, the mean hazard curves for the Main TSF site location are shown in Figures 26 – 28 for the five spectral periods of PGA (0.01 sec), 0.2, 0.5, 1, and 3 sec. In these plots, the individual hazard curves from the Lake Clark fault, the other crustal faults, the crustal host zone, the Semidi segment of the interface zone, the Kodiak segment for the large magnitude 8.8 event, the full Kodiak and Prince William Sound segment and the various depth ranges for the slab model are plotted. The total mean hazard curve is also shown on these plots.

Based on these plots, it is observed that the controlling seismic source is a combination of the slab model for the depth range of 50 – 75 km and 100 – 125 km. For the shorter spectral periods, the stronger depth dependence of the BCHydro ground-motion model (i.e., see Figure 23) is causing the relatively higher contribution for the depth range of 100 – 125 km. For the longer spectral periods, the depth scaling between the BCHydro and KBCG models are more similar leading to the similar contribution from the two depth ranges of 50 – 75 and 100 – 125 km. The deeper slab sources do not contribute as significantly, mainly due to their relatively lower activity rate. At the 1 sec period, the relative contribution from the Kodiak and Prince William Sound source increases, and for spectral periods of 3 sec, its contribution is

approximately equal to the contribution from the two controlling slab sources. The other sources are not significant contributors to the total seismic hazard at the Main TSF site location.

Figures 29 – 31 show the fraction contribution to the total hazard separated by seismic sources. These curves are plotted as a function of mean annual probability of exceedance between the range of $1.0x10^{-2}$ to $1.0x10^{-4}$. These plots also show that the main contribution to the total hazard is coming from the slab sources with depths less than or equal to 125 km. For short periods up to 1 sec, this contribution is approximately 80% of the total hazard. At the longer spectral period of 3 sec, the contribution from slab source reduces to about 60%, the contribution from the interface sources stays constant at about 20%, and the contribution fro crustal sources increases to about 20%.

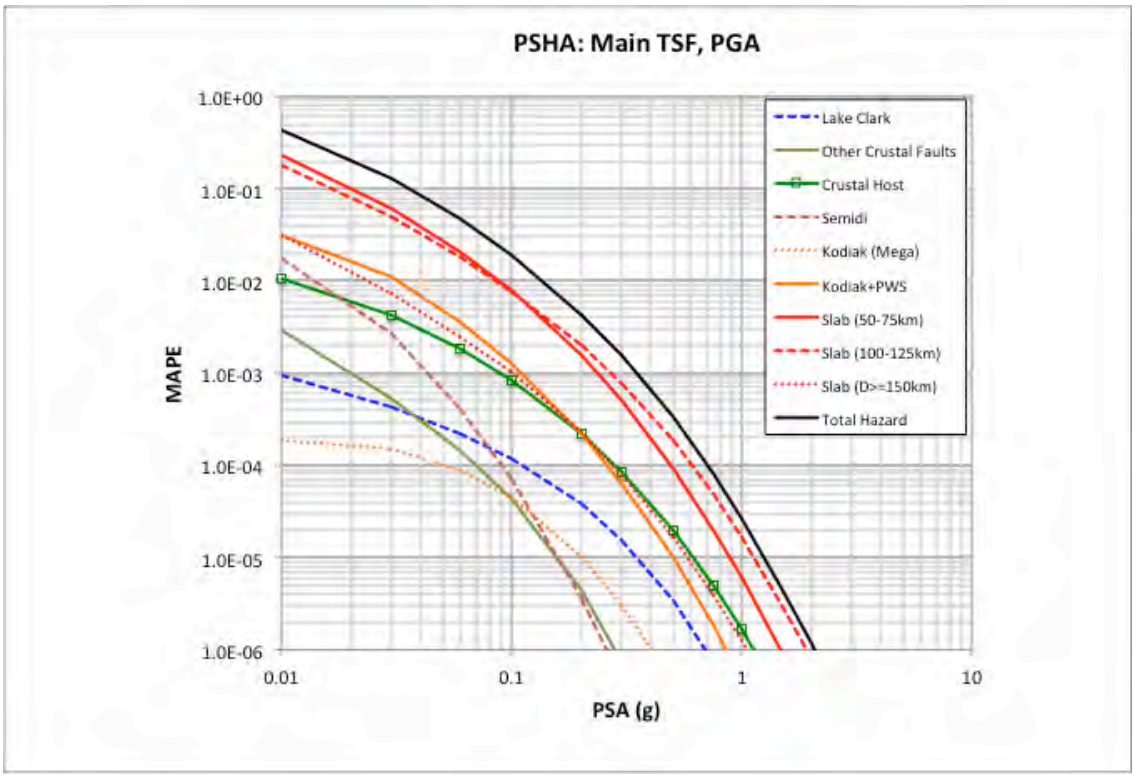

(a)

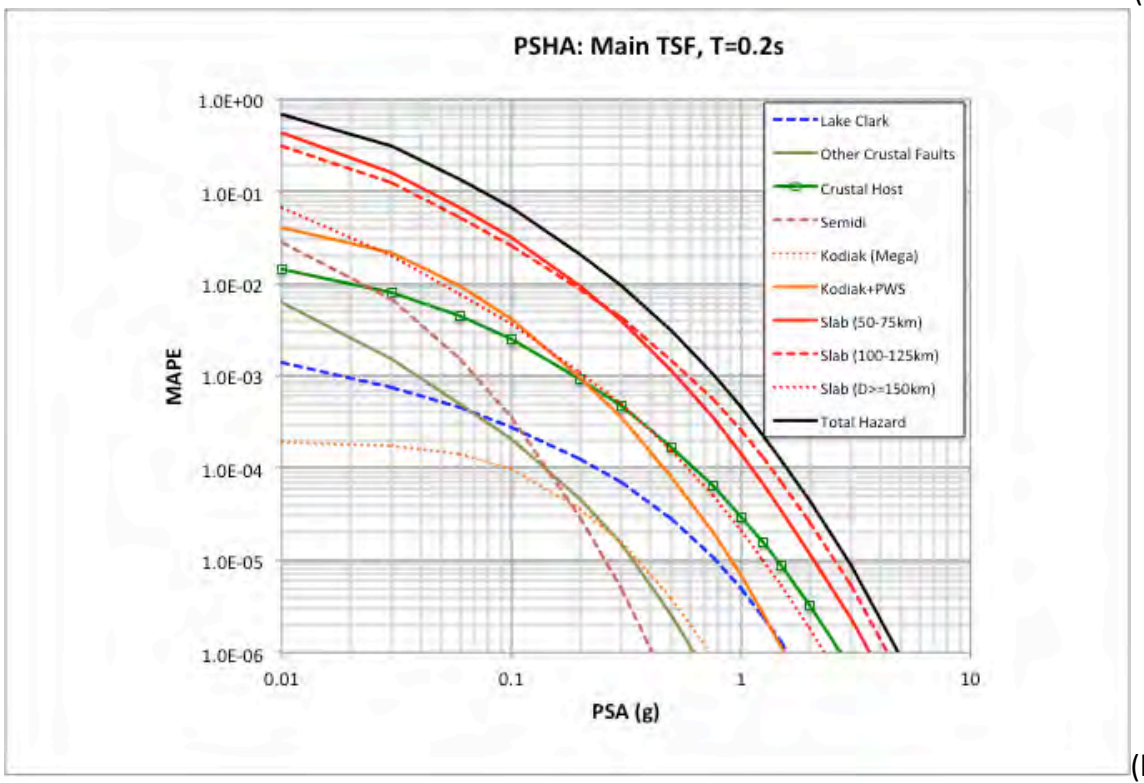

(b)

Figure 26. Mean hazard curves from the individual seismic sources and the total hazard curve for PGA (a) and 0.2 sec (b) for the Main TSF site location.

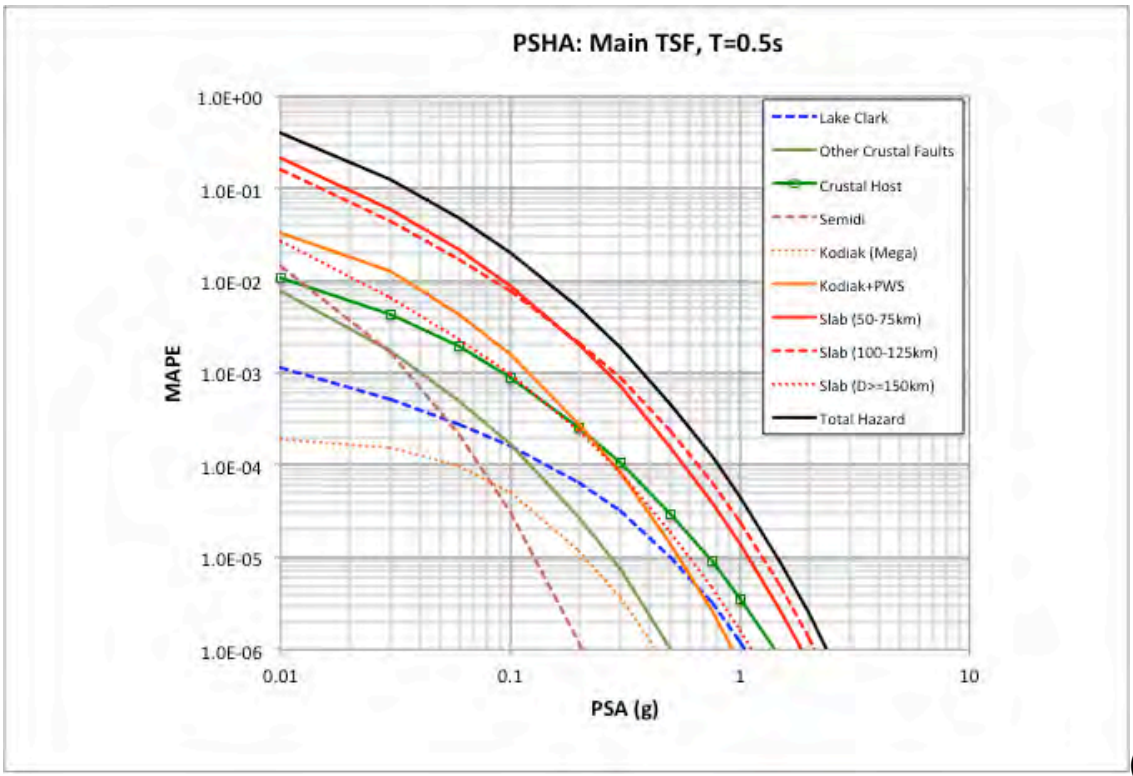

(a)

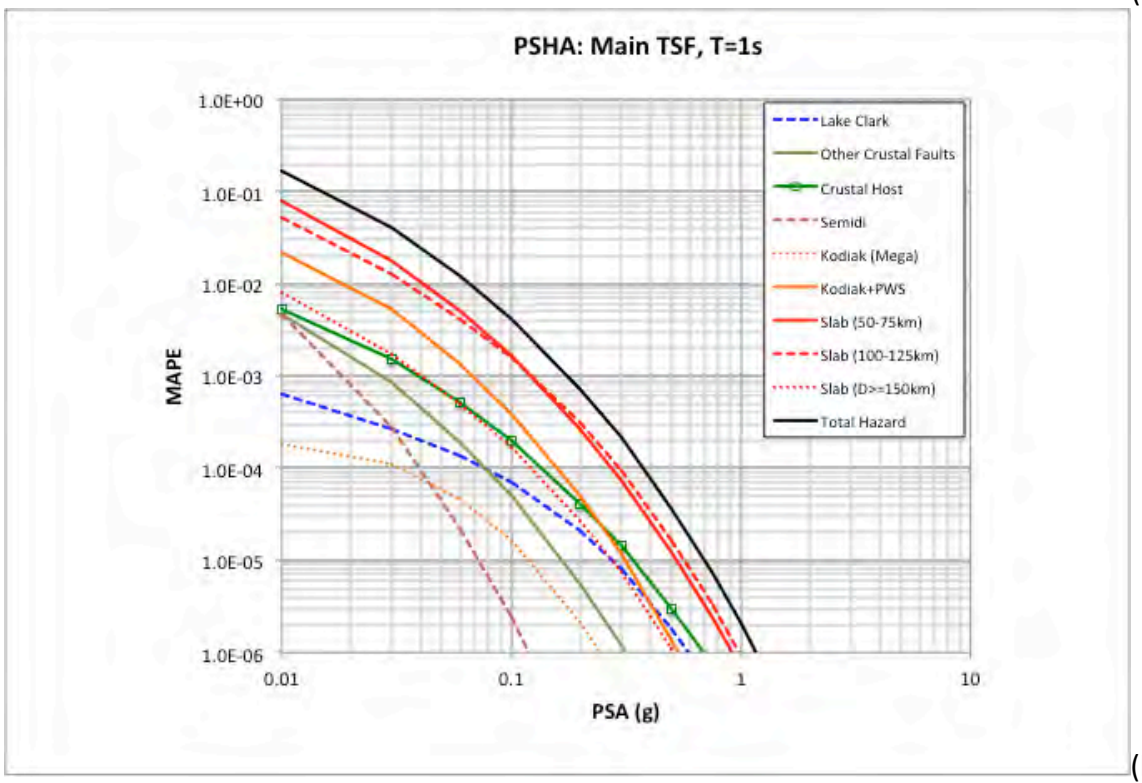

(b)

Figure 27. Mean hazard curves from the individual seismic sources and the total hazard curve for 0.5 (a) and 1 sec (b) for the Main TSF site location.

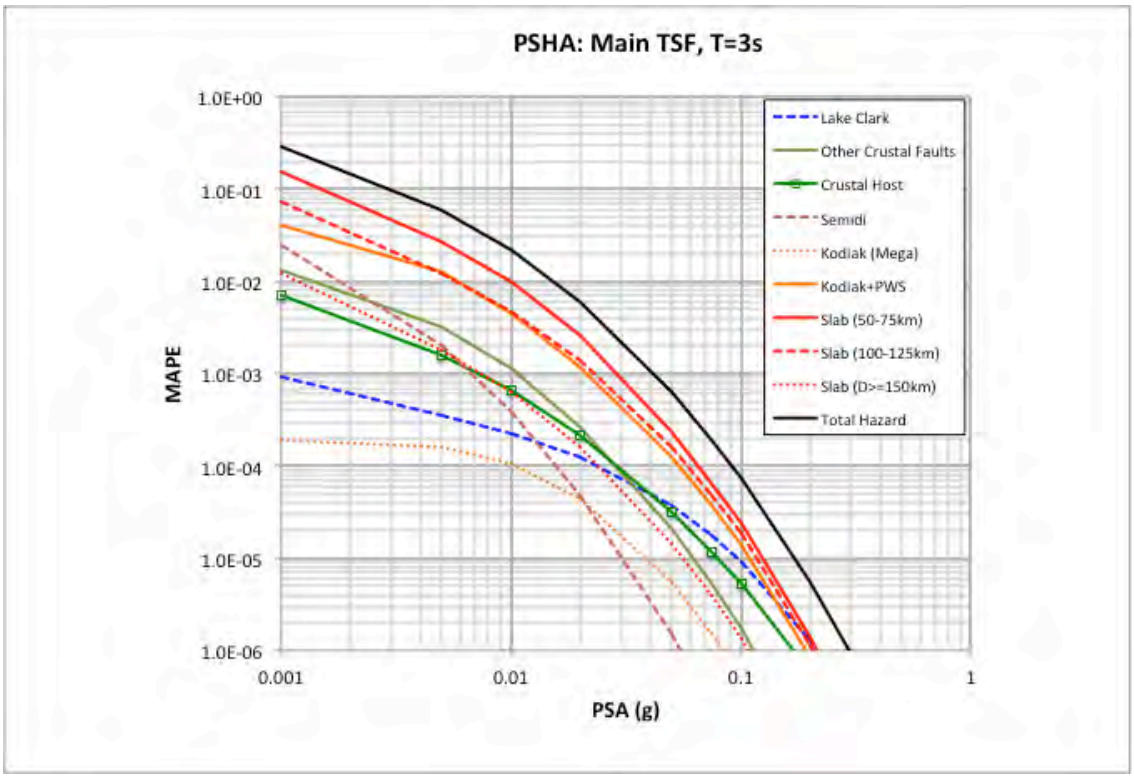

Figure 28. Mean hazard curves from the individual seismic sources and the total hazard curve for 3 sec for the Main TSF site location.

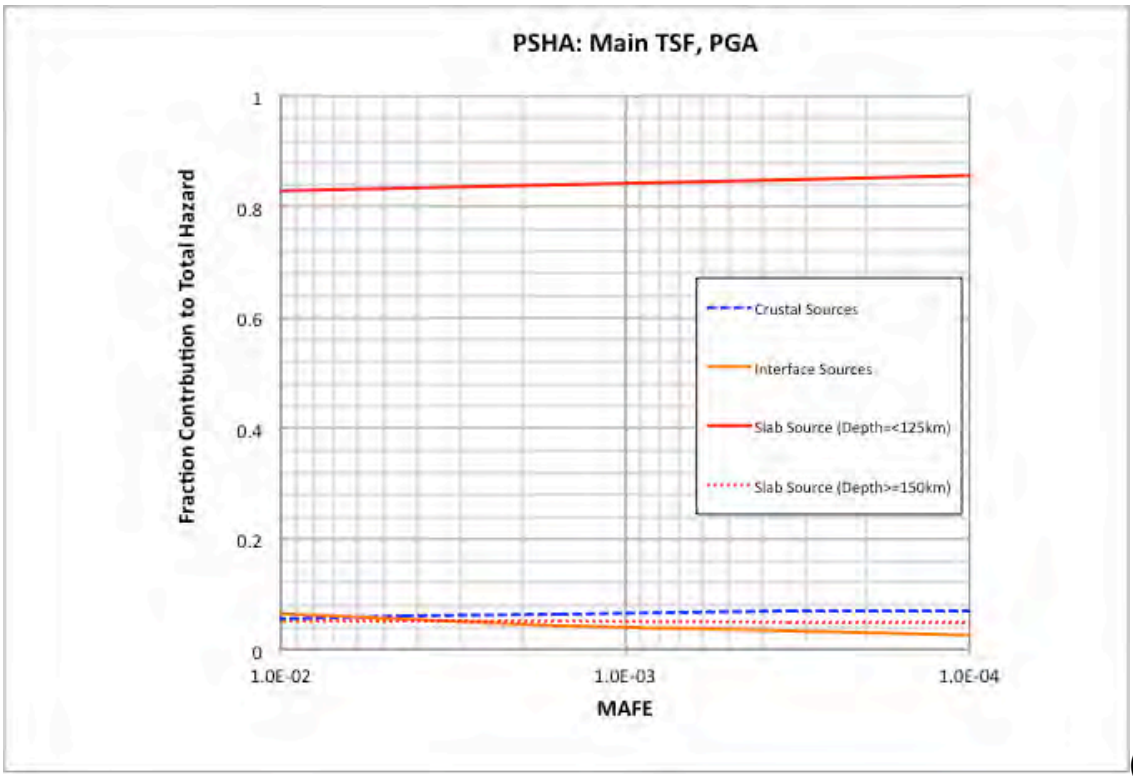

(a)

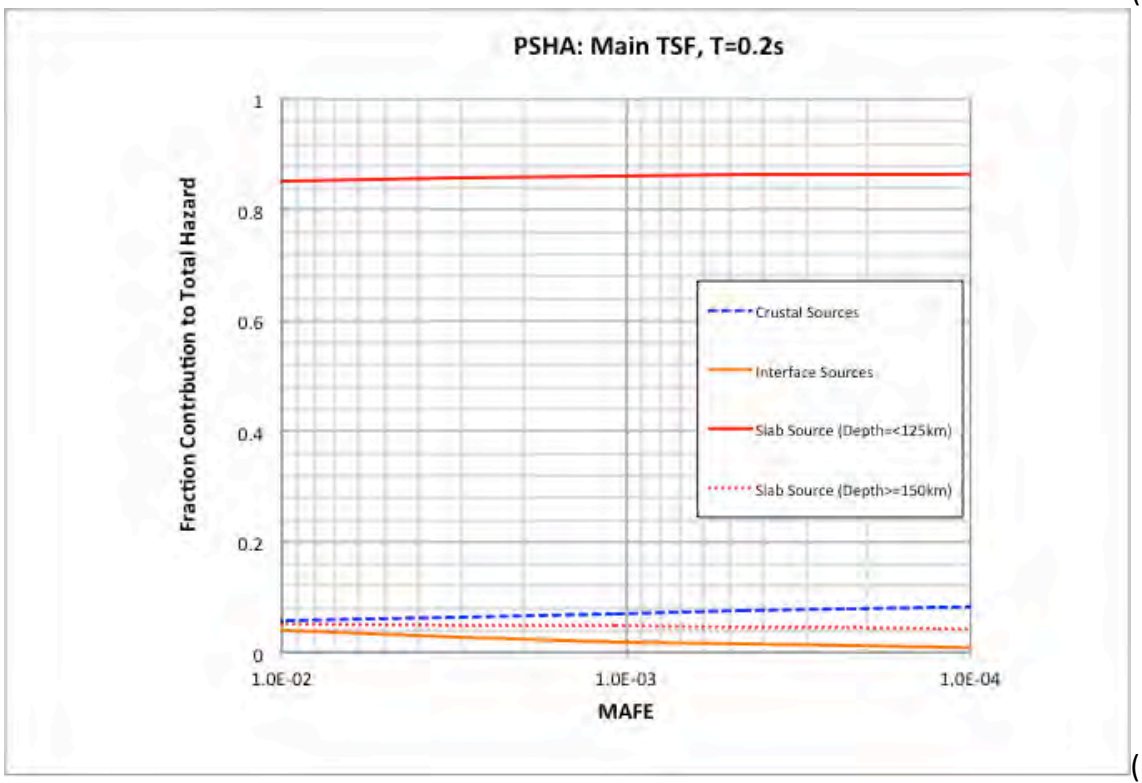

(b)

Figure 29. Fraction contribution to the total hazard from the individual seismic sources for PGA (a) and 0.2 sec (b) for the Main TSF site location.

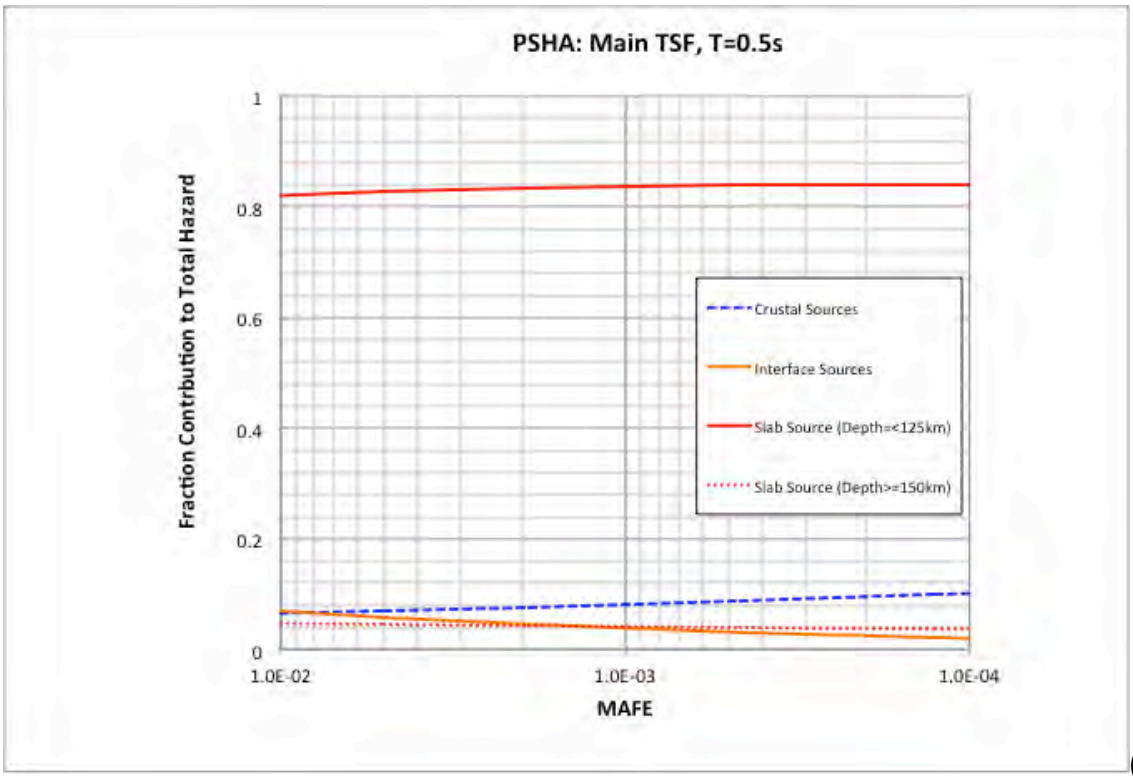

(a)

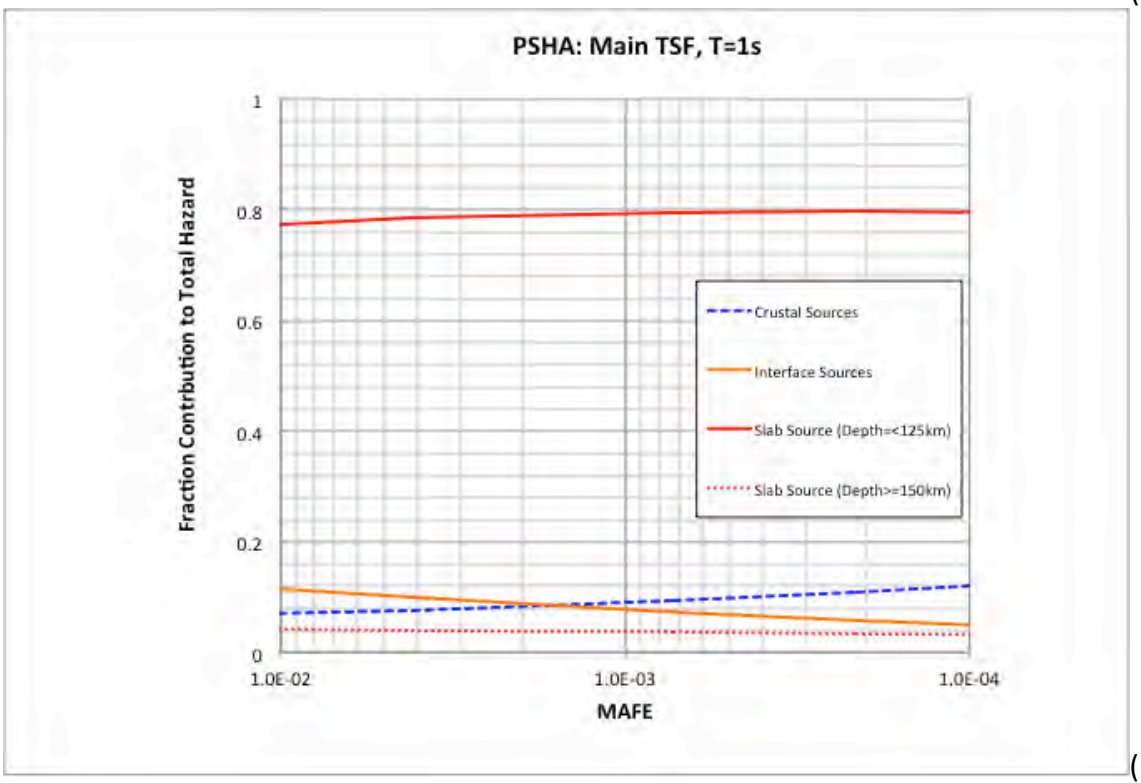

(b)

Figure 30. Fraction contribution to the total hazard from the individual seismic sources for 0.5 (a) and 1 sec (b) for the Main TSF site location.

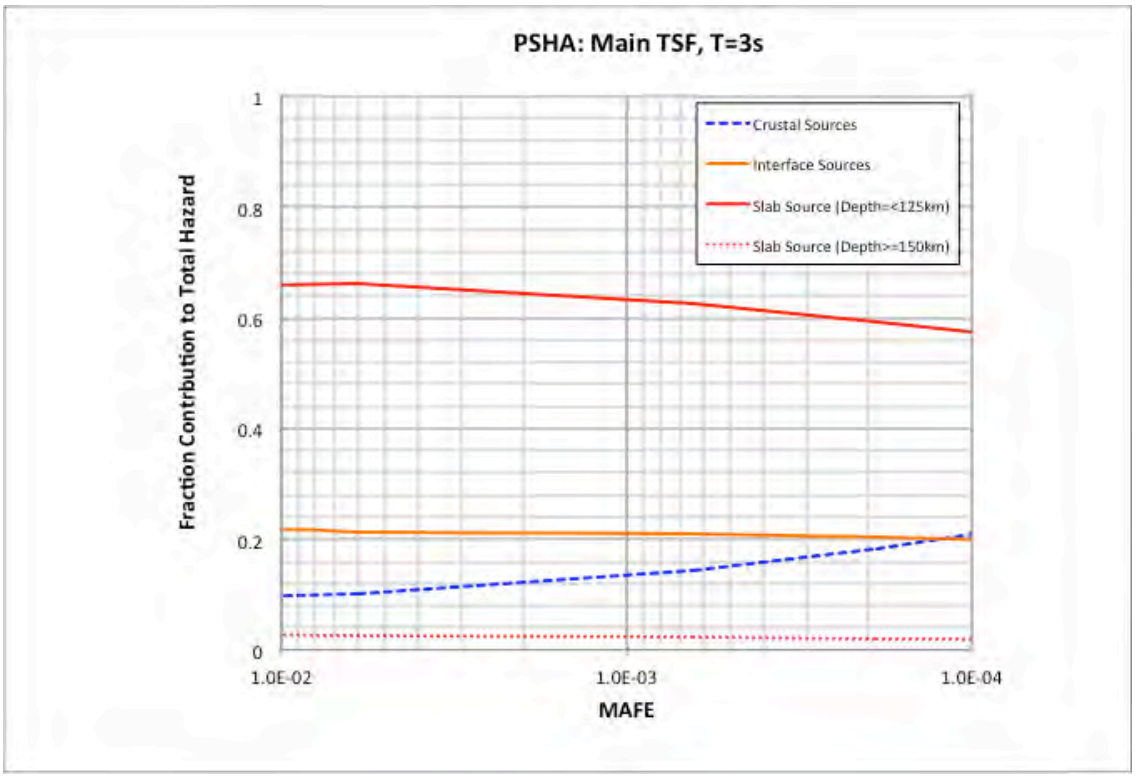

Figure 31. Fraction contribution to the total hazard from the individual seismic sources for 3 sec for the Main TSF site location.

Based on these mean hazard curves, the UHS is computed for return periods of 475, 1,000, 2,475, 5,000 and 10,000 years. These results for the Main TSF are shown in Figure 32 and listed in Table 7. Overall, the spectral shape of the UHS does not change as a function of hazard level which indicates that the controlling seismic source is similar across multiple spectral periods and the suite of return period levels. This observation is also supported by the deaggregation results that are presented later in this report.

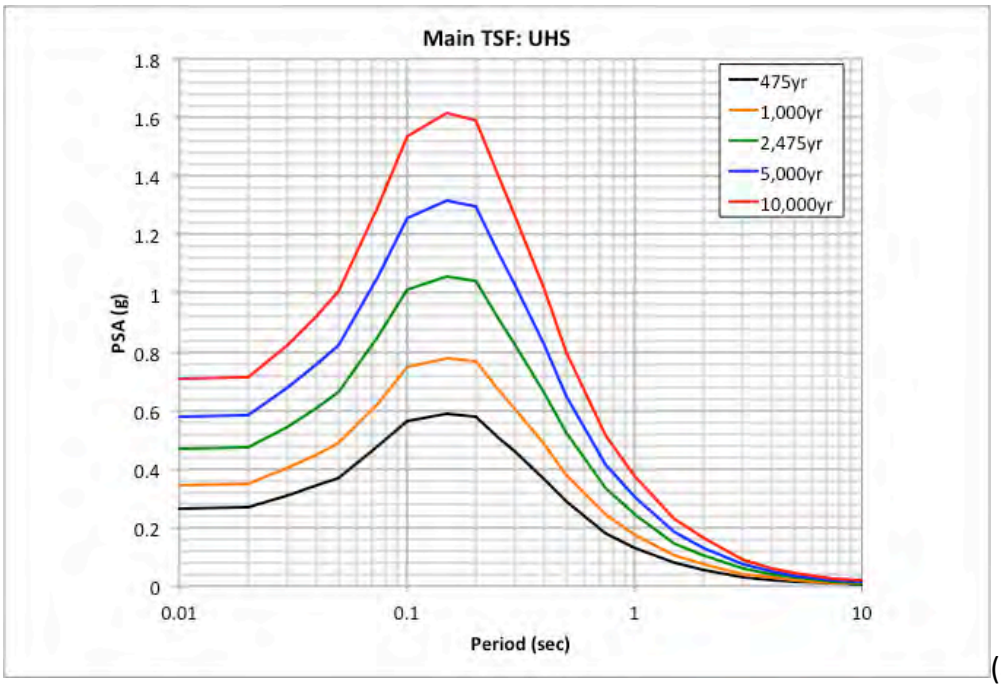

(a)

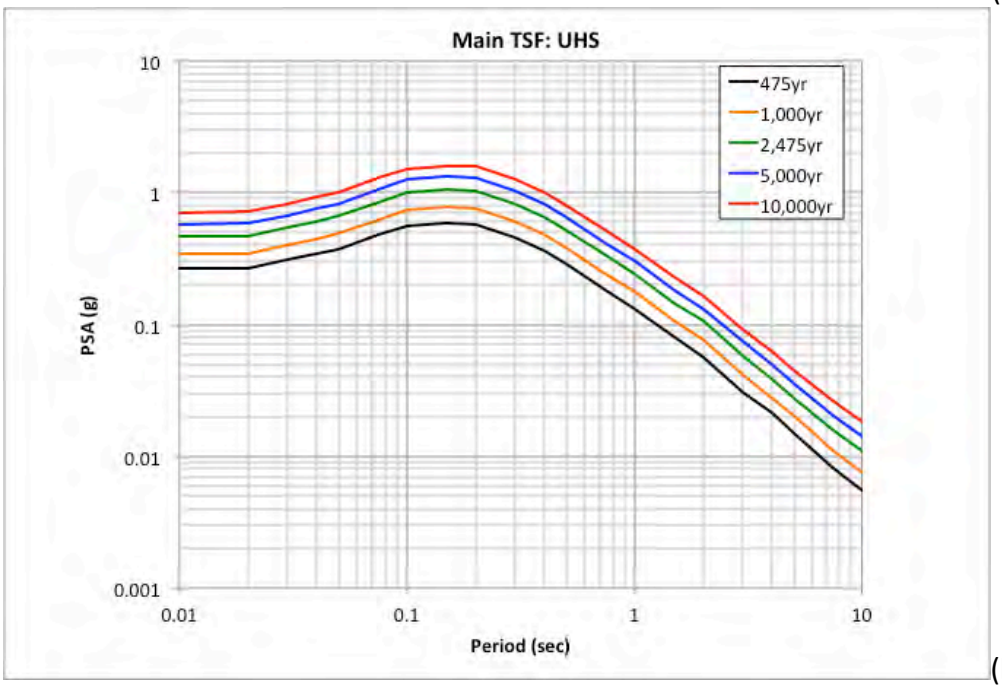

(b)

Figure 32. UHS spectra for the Main TSF site location (V_{S30} = 760 m/sec) plot log-linear (a) and log-log (b).

Table 7. UHS for the Main TSF site location for V_{S30} = 760 m/sec.

Period (sec)	475yr UHS (g)	1,000yr UHS (g)	2,475yr UHS (g)	5,000yr UHS (g)	10,000yr UHS (g)
0.010	0.2653	0.3461	0.4688	0.5790	0.7067
0.020	0.2673	0.3489	0.4735	0.5849	0.7148
0.030	0.3089	0.4017	0.5456	0.6757	0.8248
0.040	0.3417	0.4492	0.6078	0.7586	0.9237
0.050	0.3695	0.4898	0.6611	0.8234	1.0084
0.075	0.4776	0.6257	0.8508	1.0591	1.2955
0.100	0.5653	0.7466	1.0111	1.2561	1.5334
0.150	0.5880	0.7785	1.0583	1.3186	1.6132
0.200	0.5771	0.7655	1.0415	1.2983	1.5889
0.250	0.5100	0.6711	0.9167	1.1442	1.4040
0.300	0.4563	0.6022	0.8231	1.0279	1.2603
0.400	0.3649	0.4858	0.6592	0.8235	1.0108
0.500	0.2882	0.3785	0.5212	0.6486	0.7989
0.750	0.1817	0.2422	0.3322	0.4151	0.5148
1.000	0.1310	0.1756	0.2422	0.3051	0.3724
1.500	0.0799	0.1062	0.1447	0.1839	0.2276
2.000	0.0567	0.0765	0.1056	0.1319	0.1641
3.000	0.0307	0.0416	0.0583	0.0737	0.0910
4.000	0.0213	0.0279	0.0388	0.0500	0.0616
5.000	0.0150	0.0205	0.0279	0.0355	0.0450
7.500	0.0080	0.0110	0.0156	0.0204	0.0261
10.000	0.0055	0.0075	0.0109	0.0141	0.0182

The mean magnitude, distance and epsilon values as a function of spectral period and return period hazard levels are shown in Figures 33 – 35. Consistent with the slab events controlling the seismic hazard, the mean magnitude and distance parameters are in the magnitude 7.5 range at distances about 150 km. For the longer spectral periods, the increase in the mean magnitude and mean distance values are based on the increase of the relative contribution from the larger magnitude and more distant interface events associated with the Kodiak and Prince William Sound segments. The observed decrease in the mean distance for the spectral period of 7.5 sec at the longer return period hazard level is based on the relative increase in the contribution from the local Lake Clark fault. With this increase to the contribution from the closer local fault, the mean distance value is decreased. The mean epsilon values in the range of 1.5 to 2 are also consistent with the slopes of the hazard curves being approximately equal to -3.

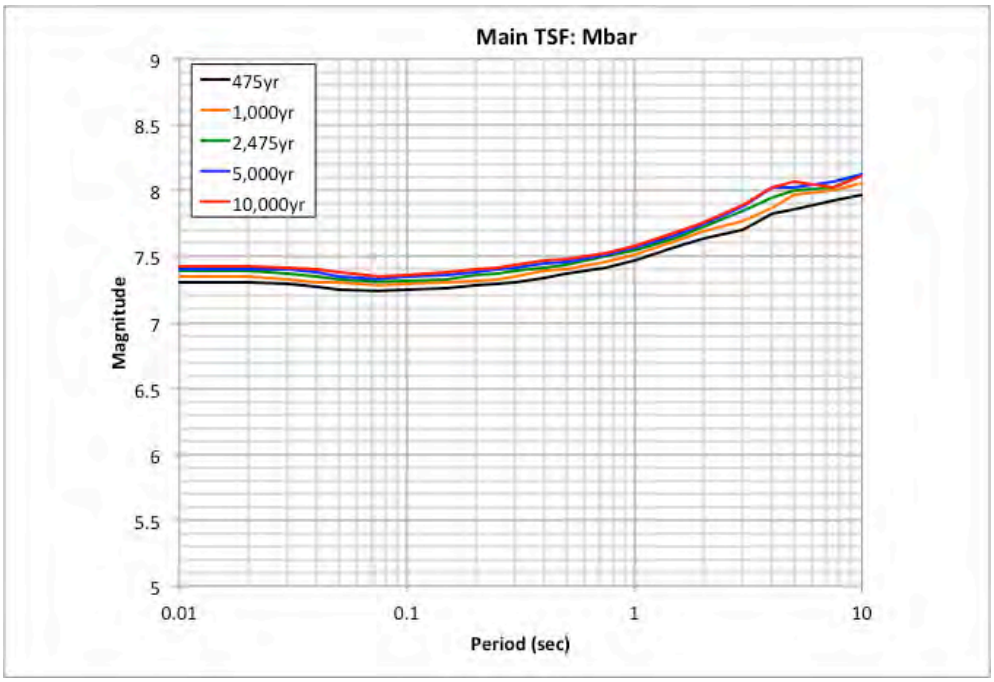

Figure 33. Mean magnitude values for the Main TSF site location (V_{S30} = 760 m/sec).

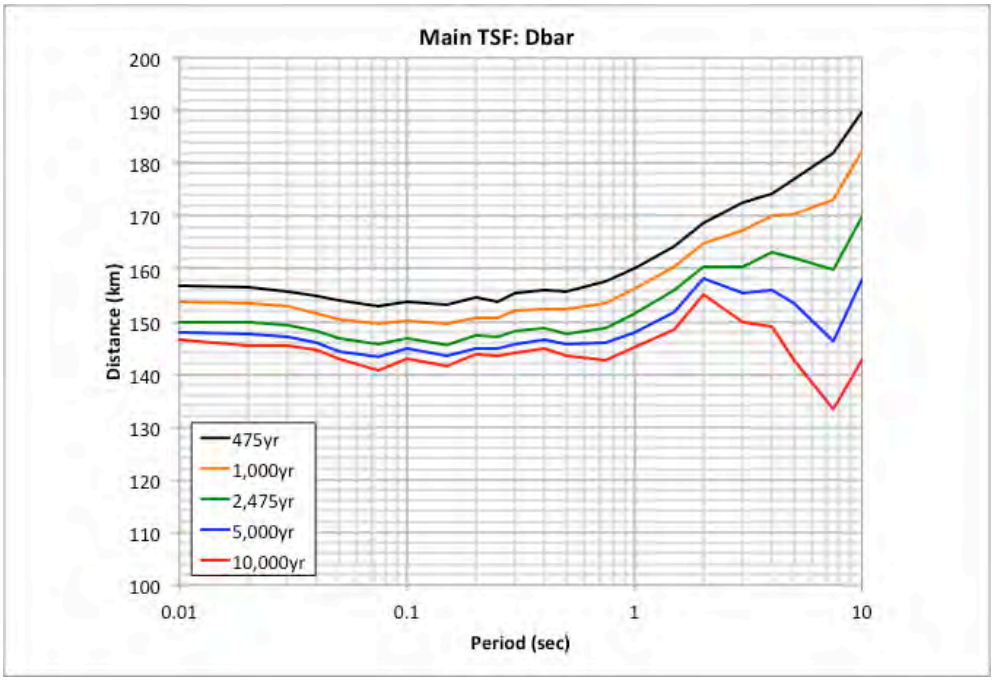

Figure 34. Mean distance values for the Main TSF site location (V_{S30} = 760 m/sec).

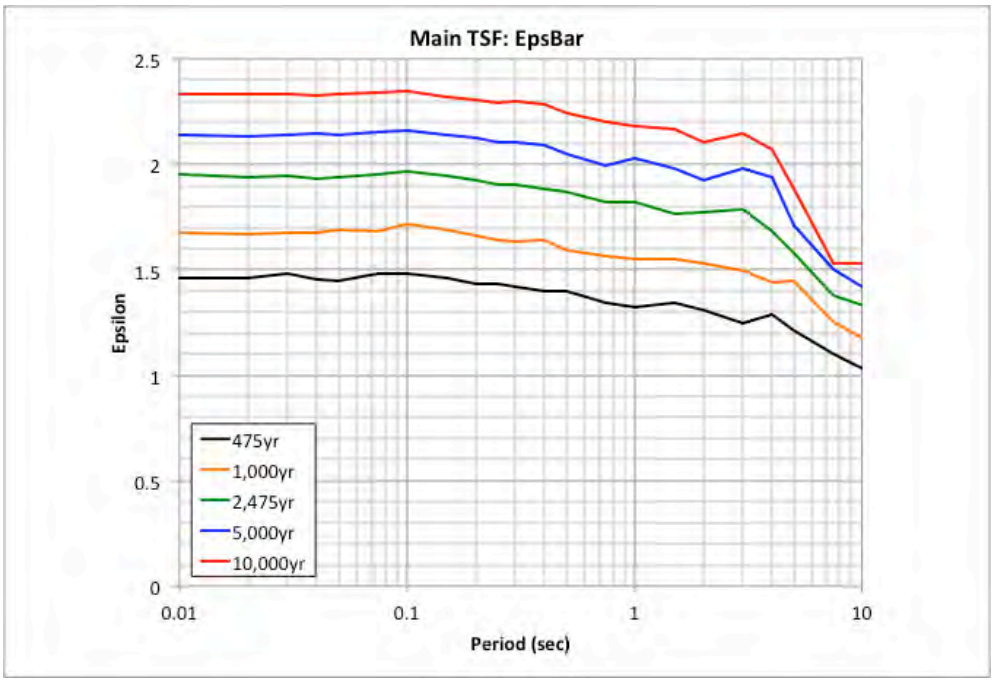

Figure 35. Mean epsilon values for the Main TSF site location (V_{S30} = 760 m/sec).

Given the controlling nature of the slab sources for the two depth ranges of 50 – 75 km and 100 – 125 km (i.e., see the hazard curve plots in Figures 26 – 28), the mean magnitude, distance, and epsilon values for each of these two seismic sources are presented. Figure 36 shows the mean magnitude values from the slab sources with the depth ranges of 50 – 75 km (a) and 100 – 125 km (b) for PGA and spectral periods of 0.2, 0.5, 1, and 3 seconds. The mean distance results are shown in Figure 37 and the mean epsilon values are plotted in Figure 38. These results are plotted as a function of the total hazard curve values. These results indicate that the mean events from these two controlling slab sources are rather consistent across the spectral period range with magnitudes in the 7.4 – 7.65 range, distances in the 150 – 170 km range and epsilon values in the 2 – 2.7 range for the 5,000-yr and 10,000-yr return period levels.

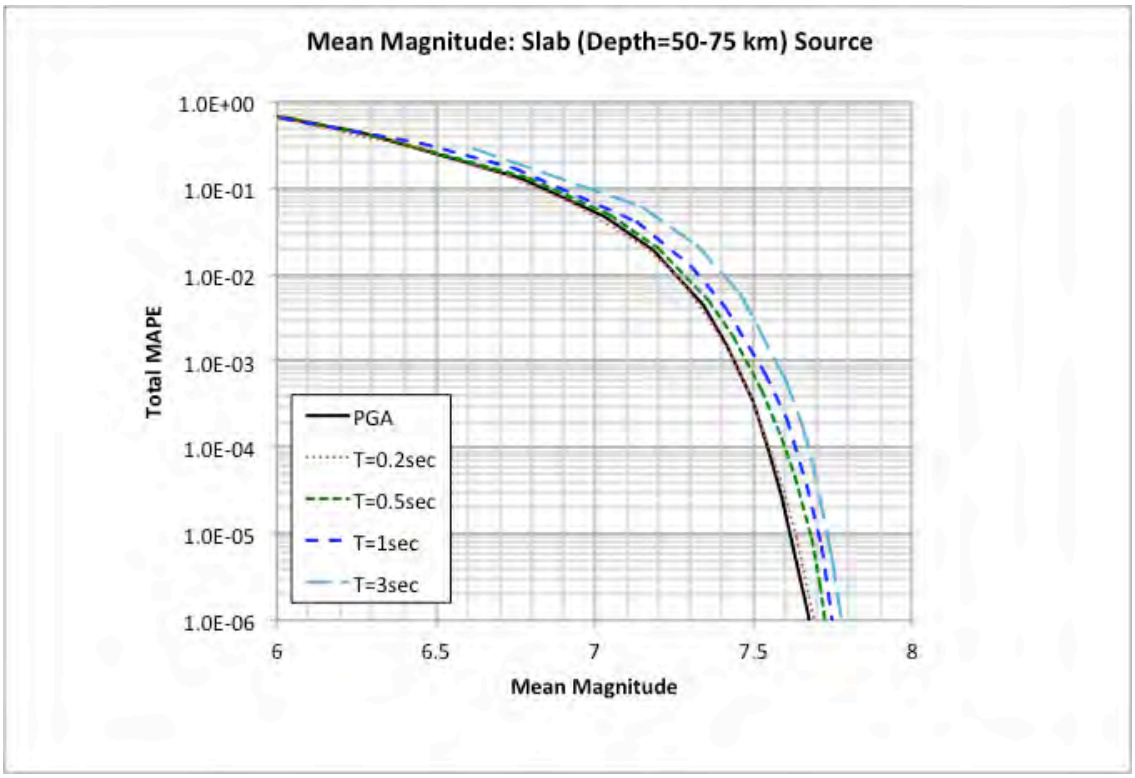

(a)

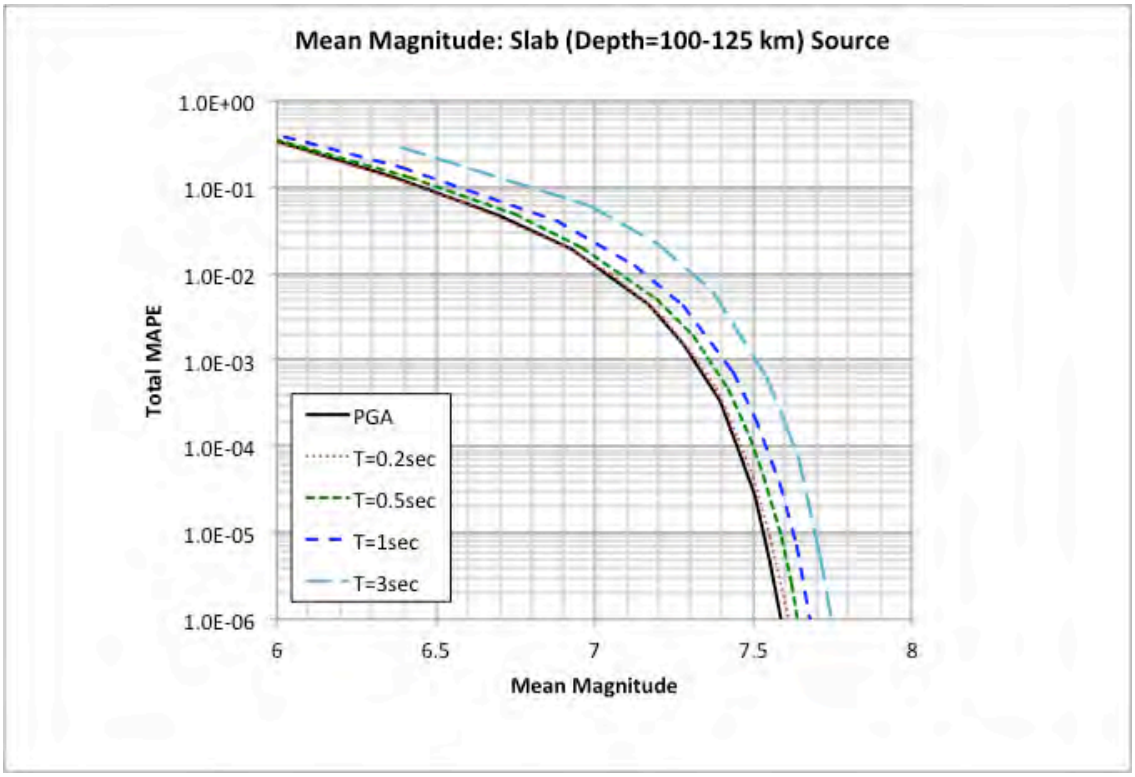

(b)

Figure 36. Mean magnitude values from the slab source for depth ranges of 50 – 75 km (a) and 100 – 125 km (b) for the Main TSF site location (V_{S30} = 760 m/sec).

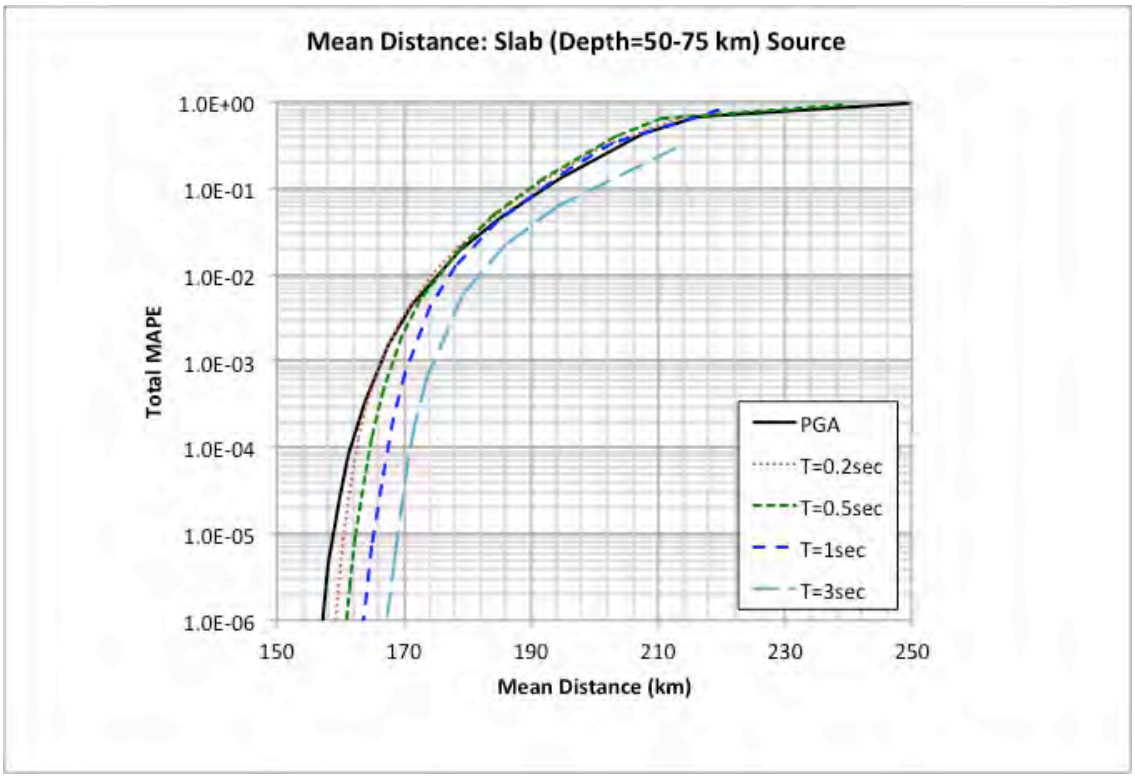

(a)

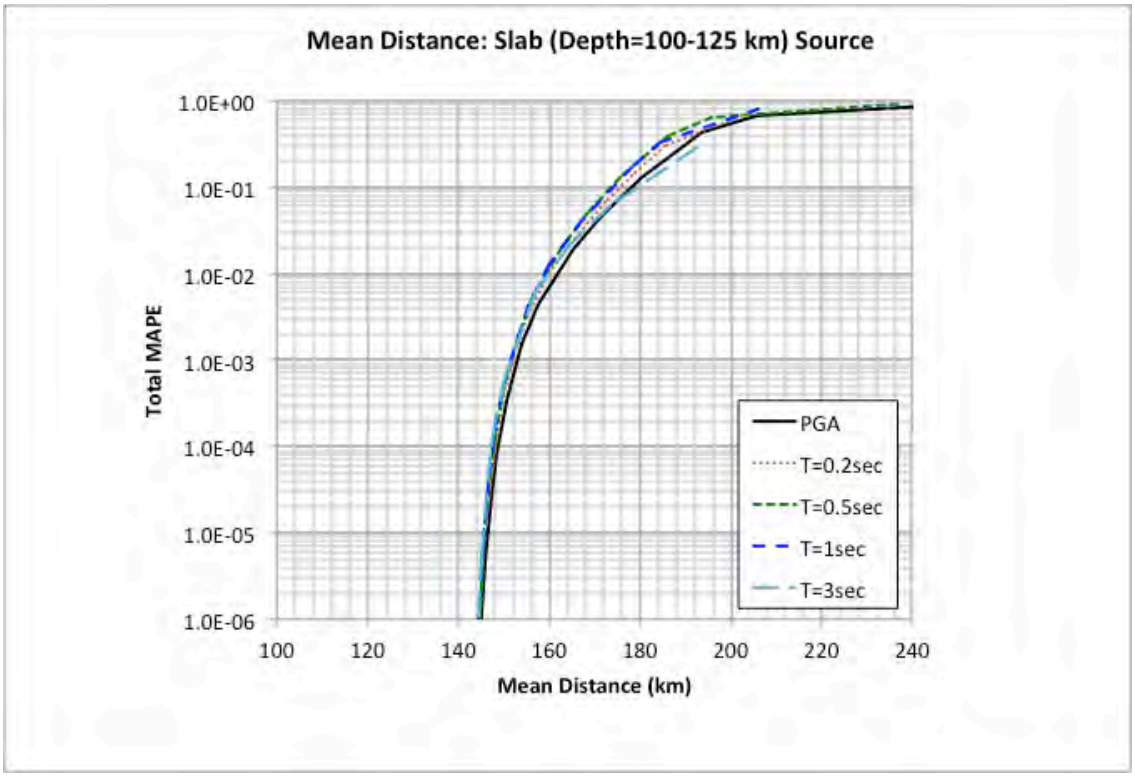

(b)

Figure 37. Mean distance values from the slab source for depth ranges of 50 – 75 km (a) and 100 – 125 km (b) for the Main TSF site location (V_{S30} = 760 m/sec).

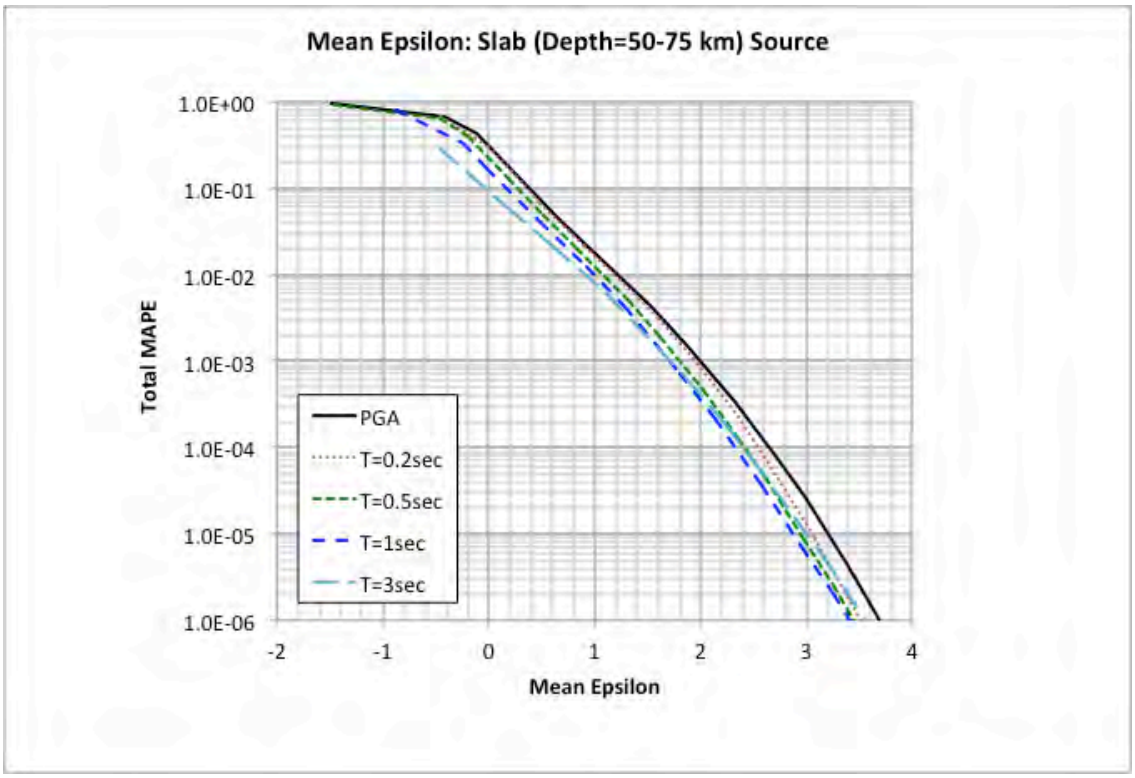

(a)

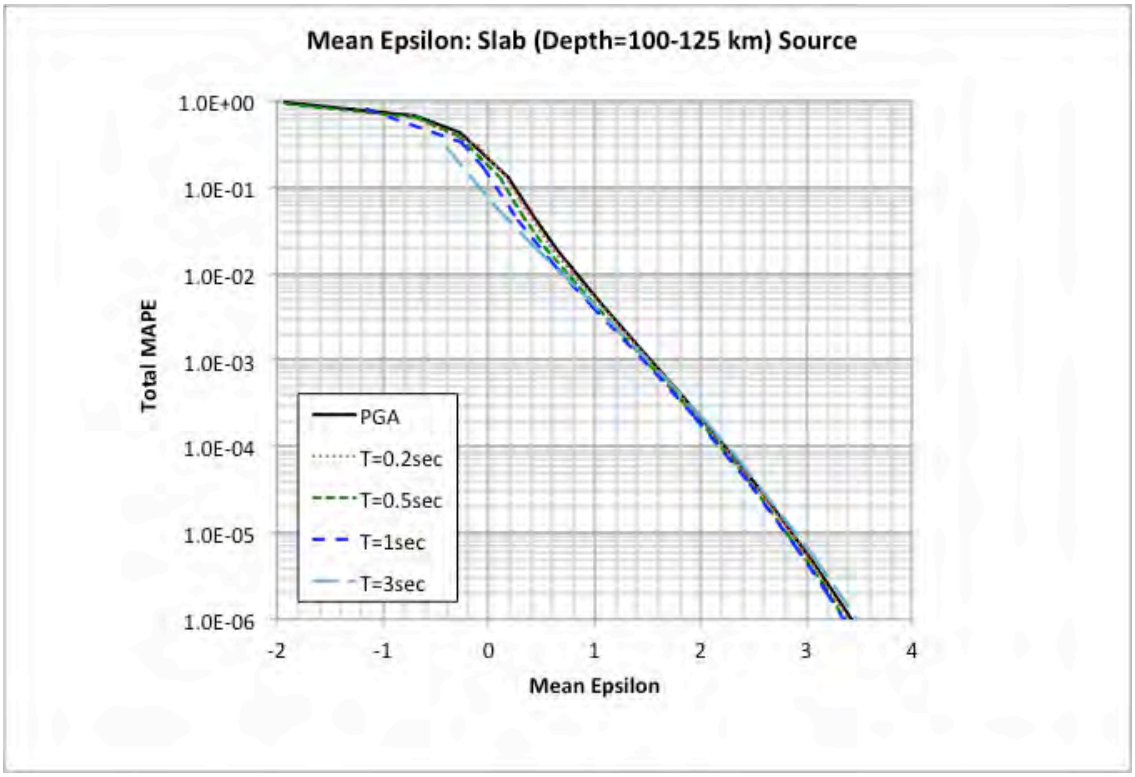

(b)

Figure 38. Mean epsilon values from the slab source for depth ranges of 50 – 75 km (a) and 100 – 125 km (b) for the Main TSF site location (V_{S30} = 760 m/sec).

The fractile hazard curves for the same five representative spectral periods are plotted in Figures 39 and 41. These observed fractile distributions are based on the uncertainty contained within the SSC and GMC models. The larger dispersion observed for the longer spectral periods is a result of the larger dispersion of the subduction GMMs at these longer spectral periods (e.g., see Figure 22 and 23). Fractile UHS are provided in Tables 8 and 9 for the longer return periods of 5,000-yr and 10,000-yr, respectively. These fractile UHS are also plotted in Figures 42 and 43. For the 95th percentile UHS, the increase at the 2 sec spectral period is a result of the feature of the KBCG GMM which shows an increase in the ground-motions for a spectral period of 2 sec relative to the 1.5 and 3 sec periods (e.g., see Figures 22, 23 and 19).

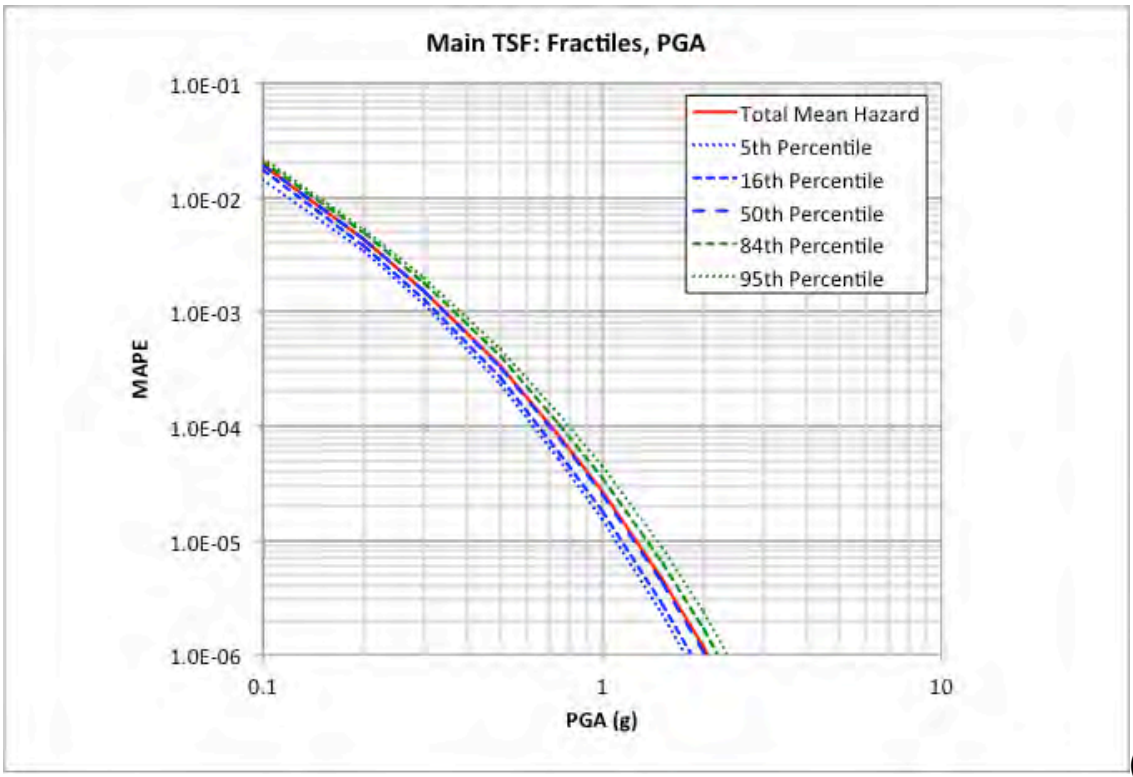

(a)

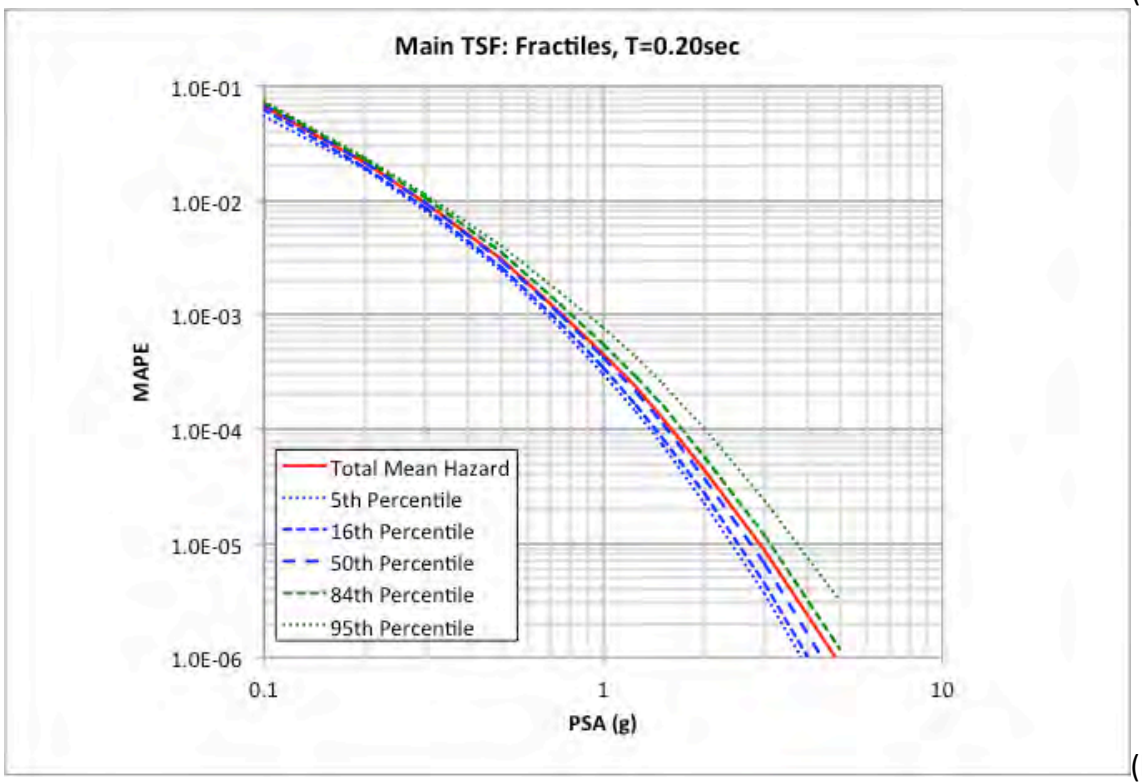

(b)

Figure 39. Fractile hazard curves for PGA (0.01 sec) (a) and 0.2 sec (b) for the Main TSF site location.

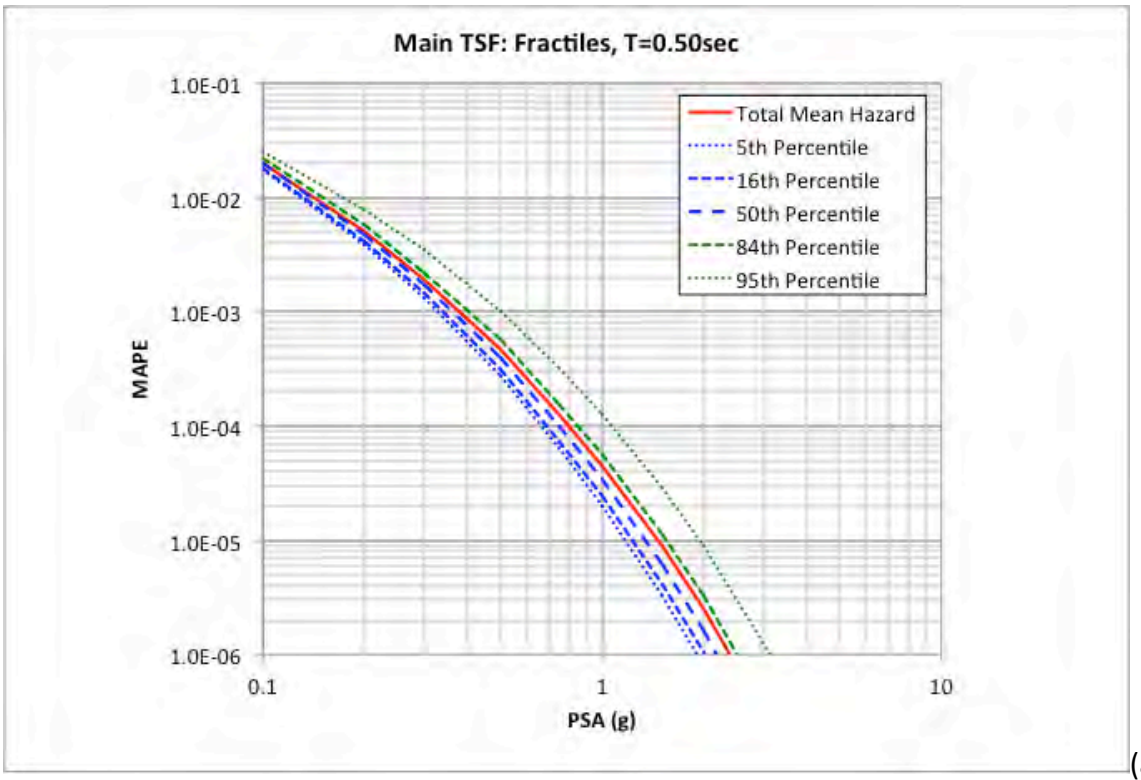

(a)

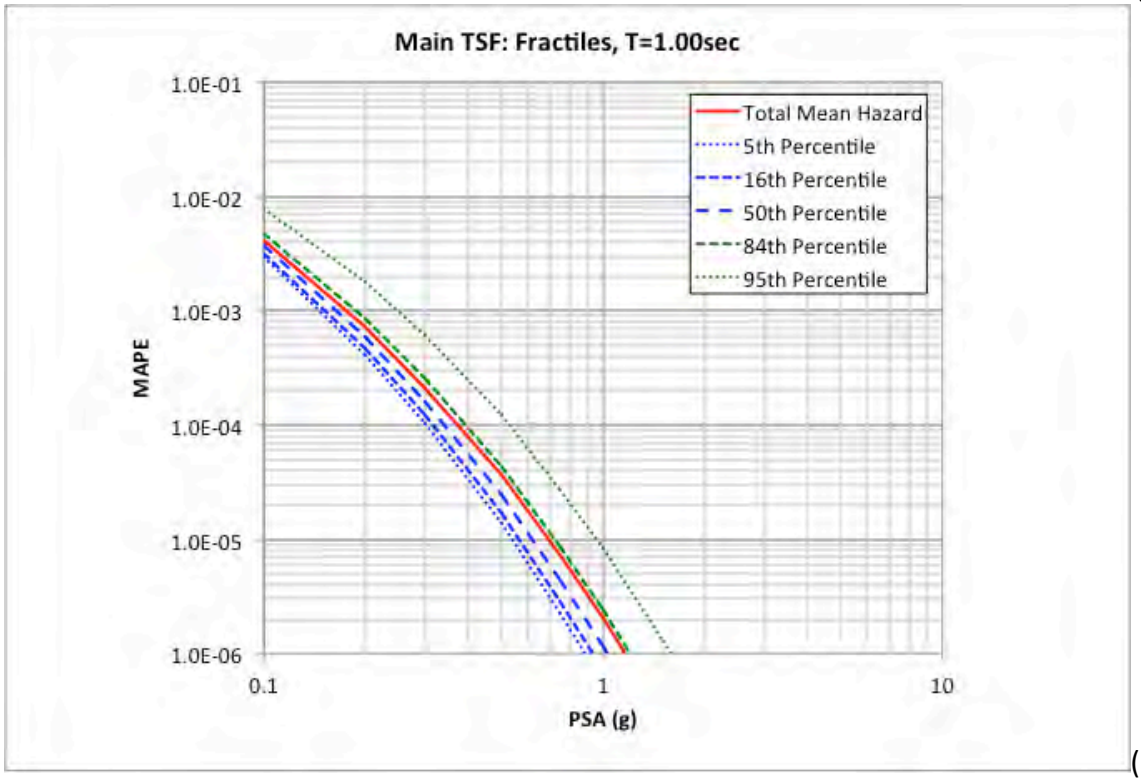

(b)

Figure 40. Fractile hazard curves for 0.5 sec (a) and 1 sec (b) for the Main TSF site location.

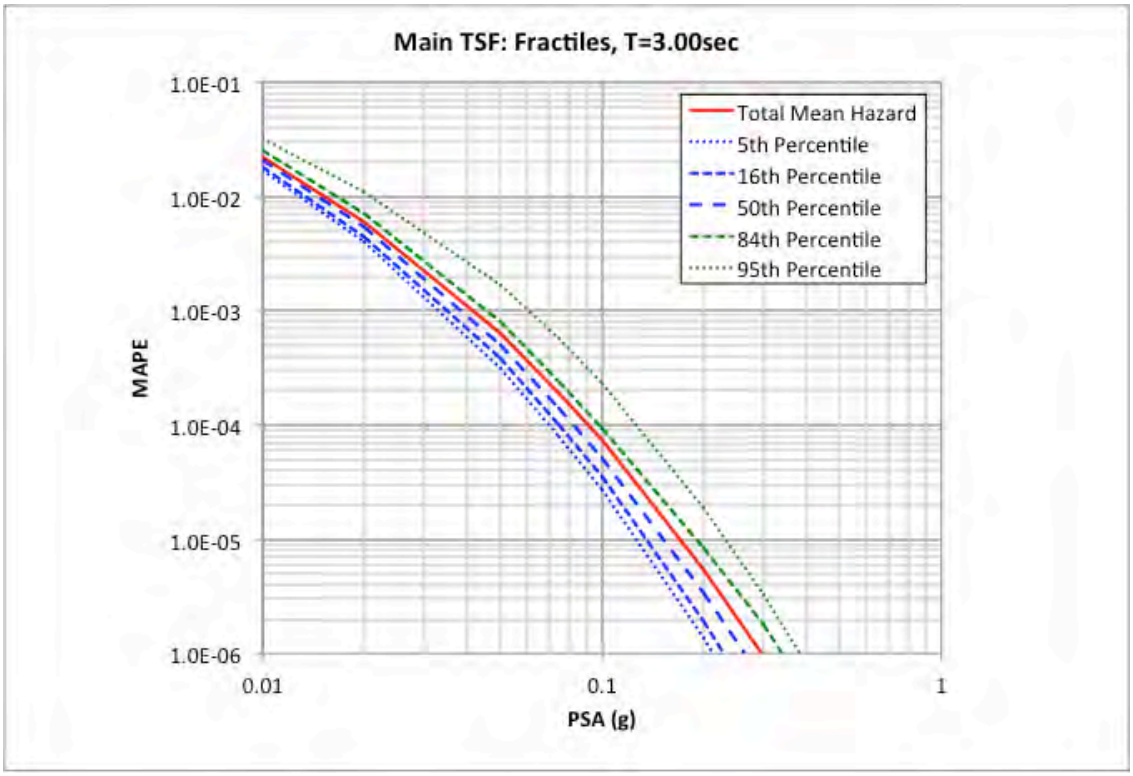

Figure 41. Fractile hazard curves for 3 sec for the Main TSF site location.

Table 8. Fractile UHS for the Main TSF site location for V_{S30} = 760 m/sec at the 5,000-yr return period level.

Period (sec)	Mean 5,000-yr UHS (g)	5th 5,000-yr UHS (g)	16th 5,000-yr UHS (g)	50th 5,000-yr UHS (g)	84th 5,000-yr UHS (g)	95th 5,000-yr UHS (g)
0.010	0.5790	0.5191	0.5383	0.5743	0.6159	0.6498
0.020	0.5849	0.5218	0.5407	0.5774	0.6231	0.6690
0.030	0.6757	0.6011	0.6235	0.6674	0.7213	0.7721
0.040	0.7586	0.6681	0.6934	0.7437	0.8075	0.8959
0.050	0.8234	0.7243	0.7522	0.8017	0.8786	1.0110
0.075	1.0591	0.9371	0.9718	1.0370	1.1290	1.2660
0.100	1.2561	1.1160	1.1570	1.2360	1.3370	1.4620
0.150	1.3186	1.1520	1.1960	1.2810	1.4120	1.6320
0.200	1.2983	1.1290	1.1740	1.2620	1.3930	1.6010
0.250	1.1442	0.9863	1.0260	1.1010	1.2300	1.4590
0.300	1.0279	0.8830	0.9187	0.9901	1.1030	1.3020
0.400	0.8235	0.7066	0.7368	0.7925	0.8832	1.0470
0.500	0.6486	0.5456	0.5673	0.6110	0.6939	0.8699
0.750	0.4151	0.3388	0.3527	0.3802	0.4380	0.5886
1.000	0.3051	0.2463	0.2575	0.2792	0.3210	0.4275
1.500	0.1839	0.1418	0.1489	0.1623	0.1910	0.2743
2.000	0.1319	0.0992	0.1042	0.1130	0.1316	0.2101
3.000	0.0737	0.0572	0.0606	0.0668	0.0791	0.1044
4.000	0.0500	0.0391	0.0421	0.0474	0.0557	0.0636
5.000	0.0355	0.0276	0.0297	0.0339	0.0407	0.0455
7.500	0.0204	0.0138	0.0153	0.0194	0.0245	0.0282
10.000	0.0141	0.0094	0.0104	0.0133	0.0170	0.0196

Table 9. Fractile UHS for the Main TSF site location for V_{S30} = 760 m/sec at the 10,000-yr return period level.

Period (sec)	Mean 10,000-yr UHS (g)	5th 10,000-yr UHS (g)	16th 10,000-yr UHS (g)	50th 10,000-yr UHS (g)	84th 10,000-yr UHS (g)	95th 10,000-yr UHS (g)
0.010	0.7067	0.6250	0.6500	0.6994	0.7560	0.7987
0.020	0.7148	0.6281	0.6530	0.7033	0.7650	0.8240
0.030	0.8248	0.7308	0.7593	0.8127	0.8802	0.9507
0.040	0.9237	0.8100	0.8398	0.9004	0.9903	1.1080
0.050	1.0084	0.8743	0.9078	0.9747	1.0750	1.2460
0.075	1.2955	1.1340	1.1770	1.2620	1.3850	1.5770
0.100	1.5334	1.3520	1.4020	1.5030	1.6360	1.8140
0.150	1.6132	1.3960	1.4500	1.5560	1.7270	2.0340
0.200	1.5889	1.3690	1.4250	1.5350	1.7060	1.9930
0.250	1.4040	1.1950	1.2460	1.3430	1.5100	1.8030
0.300	1.2603	1.0710	1.1160	1.2060	1.3540	1.6110
0.400	1.0108	0.8565	0.8924	0.9662	1.0820	1.2850
0.500	0.7989	0.6620	0.6910	0.7505	0.8519	1.0700
0.750	0.5148	0.4113	0.4301	0.4675	0.5400	0.7254
1.000	0.3724	0.3017	0.3147	0.3401	0.3924	0.5281
1.500	0.2276	0.1741	0.1836	0.2017	0.2345	0.3357
2.000	0.1641	0.1194	0.1257	0.1374	0.1621	0.2572
3.000	0.0910	0.0701	0.0747	0.0823	0.0977	0.1263
4.000	0.0616	0.0489	0.0526	0.0587	0.0694	0.0786
5.000	0.0450	0.0338	0.0368	0.0427	0.0522	0.0578
7.500	0.0261	0.0171	0.0191	0.0243	0.0320	0.0378
10.000	0.0182	0.0114	0.0126	0.0170	0.0222	0.0257

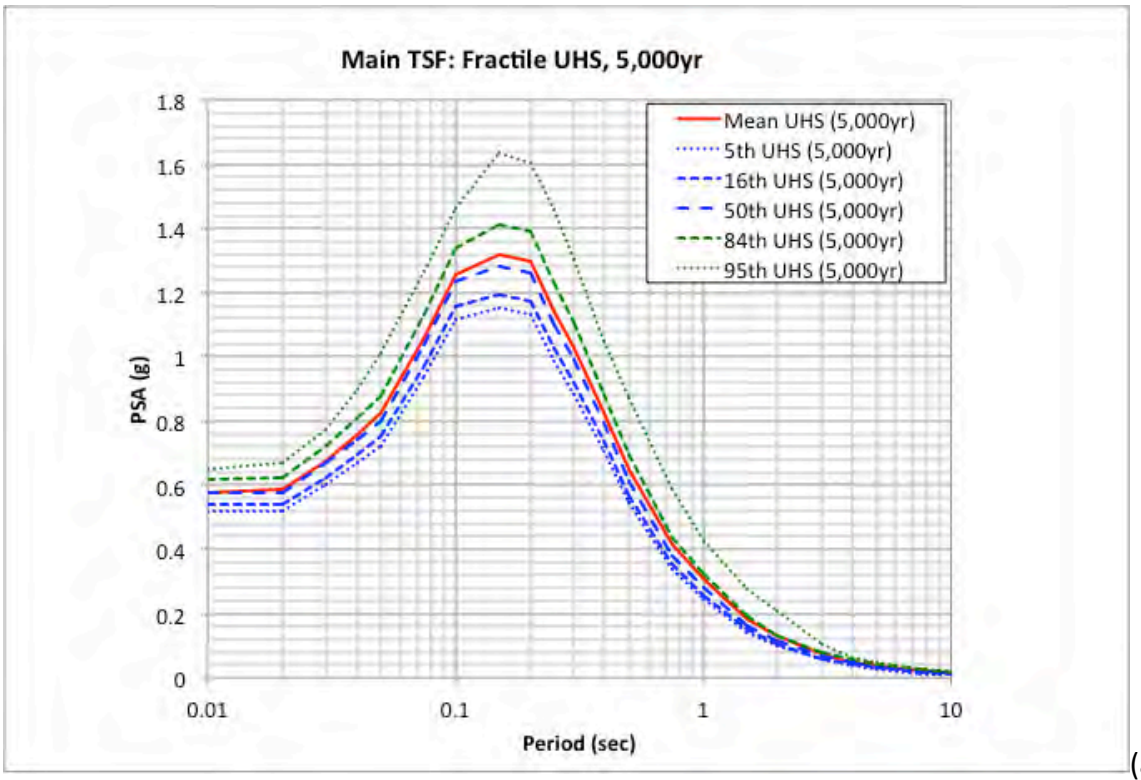

(a)

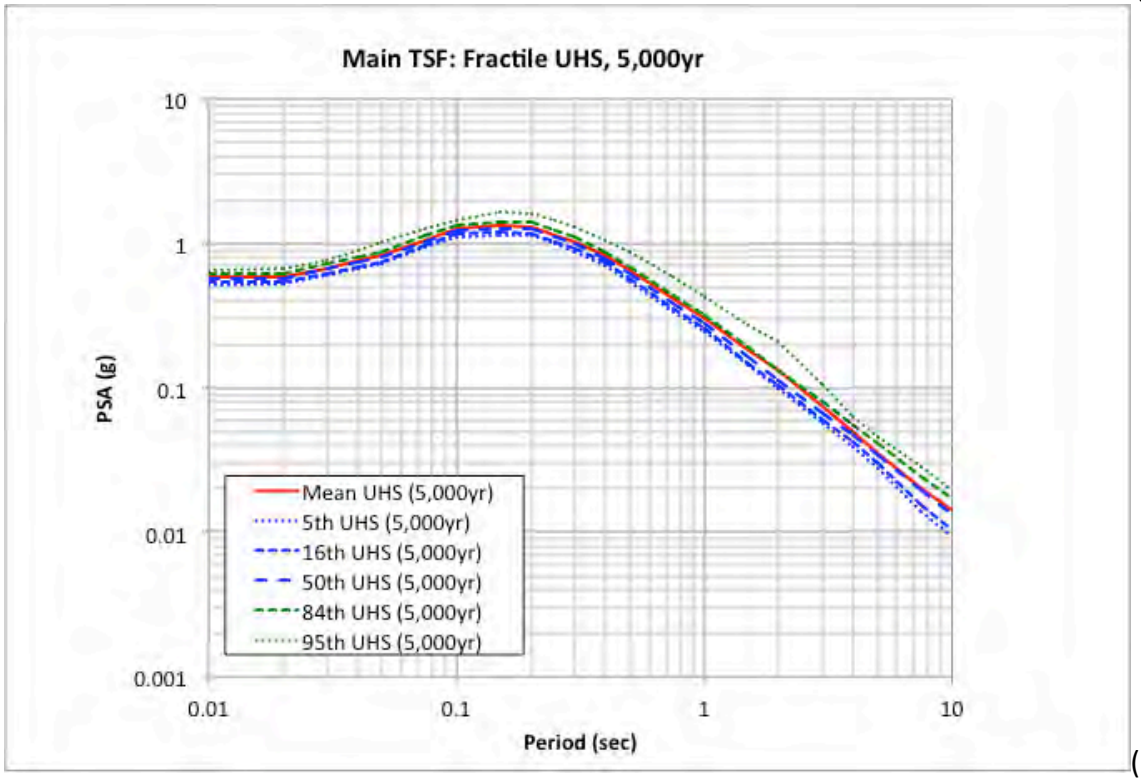

(b)

Figure 42. Fractile UHS for the Main TSF site location for 5,000-yr return period hazard level plotted log-linear (a) and log-log (b).

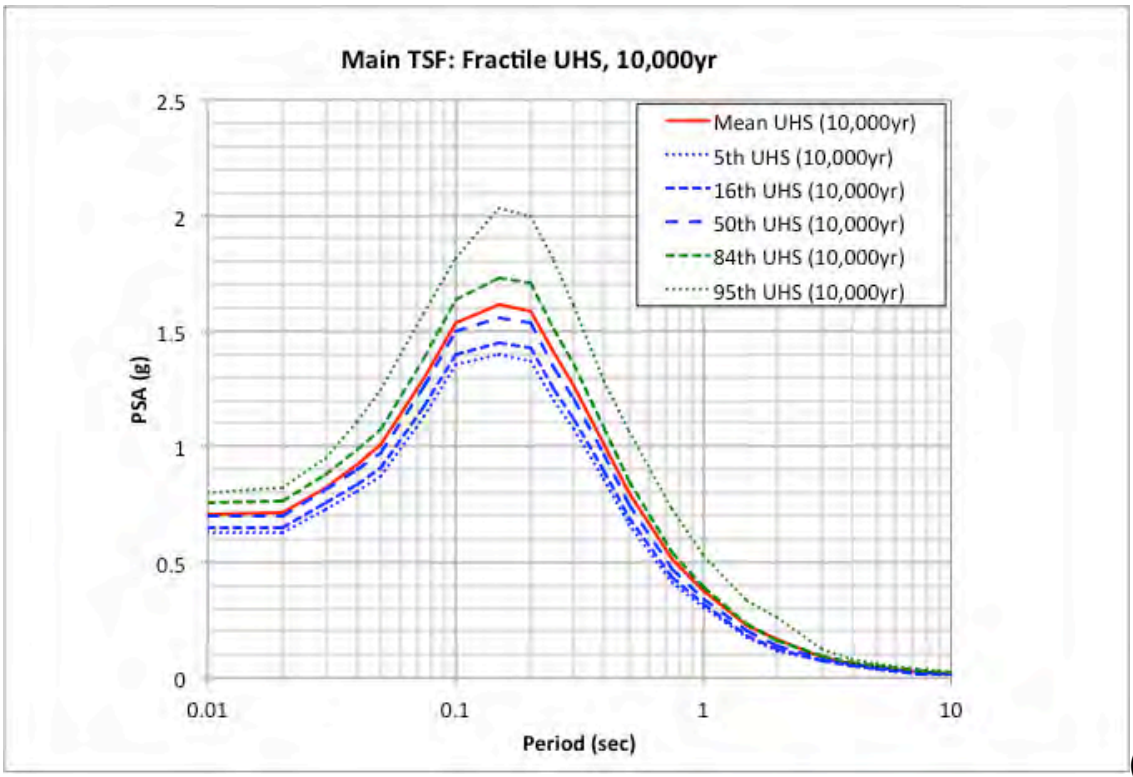

(a)

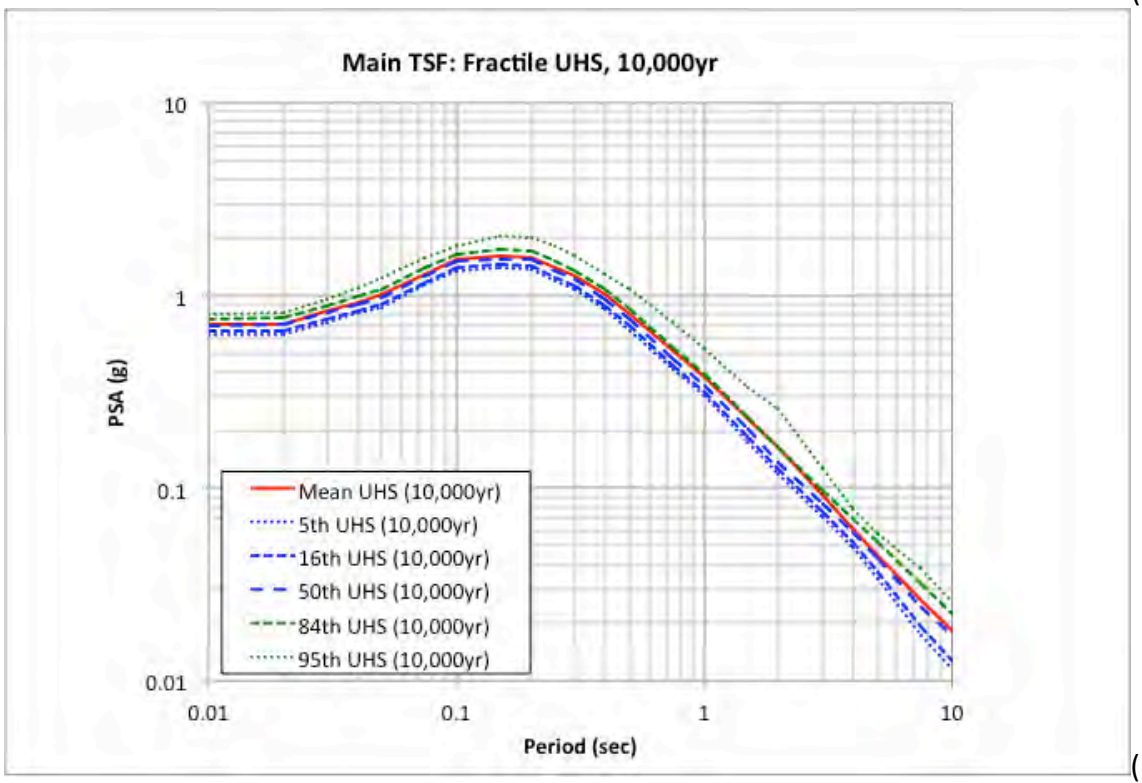

(b)

Figure 43. Fractile UHS for the Main TSF site location for 10,000-yr return period hazard level plotted log-linear (a) and log-log (b).

The binned deaggregation for the Main TSF site location for the hazard levels of 475, 5,000 and 10,000 years are plotted in Figures 44 – 52 for the representative five spectral periods of PGA (0.01 sec), 0.2, 0.5, 1, and 3 sec. These results are consistent with the previous hazard curve plots showing that the main contribution is from the slab seismic source with magnitudes in the 7 – 8 range and distances in the 100 – 200 km range. For the longer spectral periods of 1 and 3 sec, the relative contribution from the larger (M>8.5) and more distant (R>200 km) interface seismic source and the local Lake Clark fault (i.e., magnitudes 7.5 – 8.0 and distances 20 – 50 km) increases.

The modal peak bin values for the 5,000-yr and 10,000-yr cases are listed in Table 10. These results are also consistent with the previous plots and observations.

Table 10. Modal peak bin values (magnitude and distance) for the Main TSF site location for V_{S30} = 760 m/sec at the 5,000-yr and 10,000-yr return period levels.

Period (sec)	**5,000-yr Modal Deaggregation**	**10,000-yr Modal Deaggregation**
PGA (0.01)	Mag: 7.0 – 7.5 Distance: 110 – 150 km	Mag: 7.5 – 8.0 Distance: 110 – 150 km
0.2	Mag: 7.0 – 7.5 Distance: 110 – 150 km	Mag: 7.5 – 8.0 Distance: 110 – 150 km
0.5	Mag: 7.5 – 8.0 Distance: 110 – 150 km	Mag: 7.5 – 8.0 Distance: 110 – 150 km
1.0	Mag: 7.5 – 8.0 Distance: 150 – 200 km	Mag: 7.5 – 8.0 Distance: 150 – 200 km
3.0	Mag: 7.5 – 8.0 Distance: 150 – 200 km	Mag: 7.5 – 8.0 Distance: 150 – 200 km

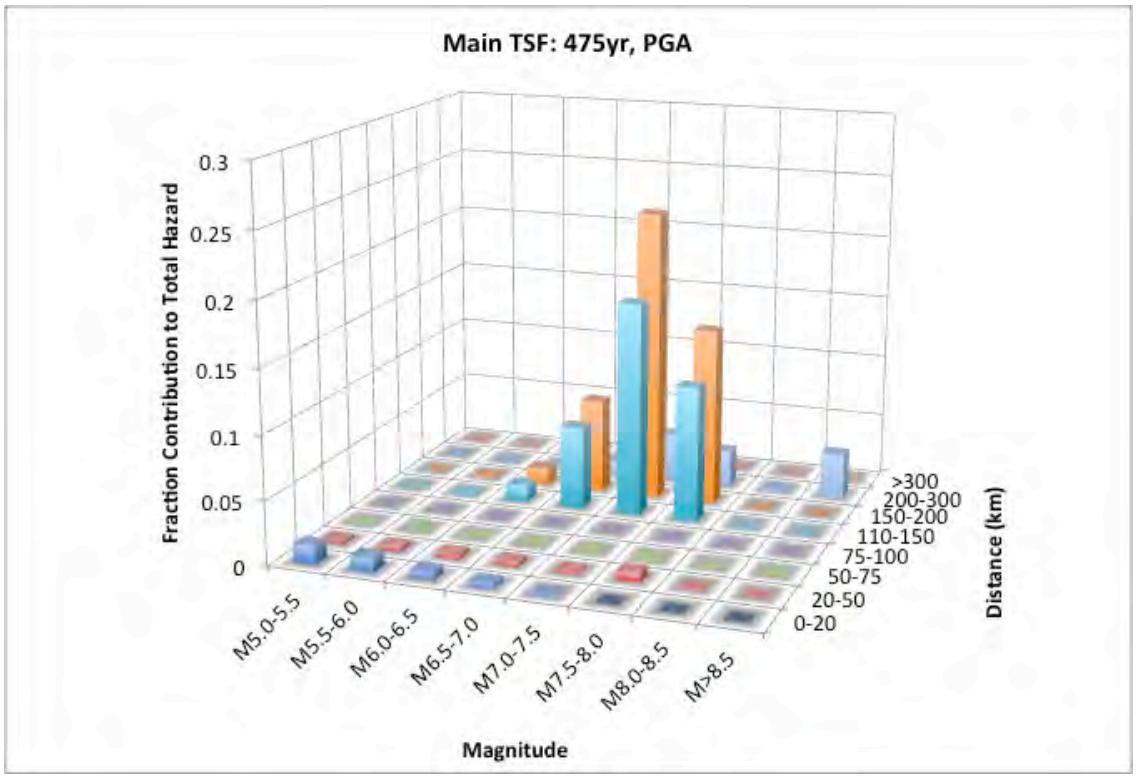

(a)

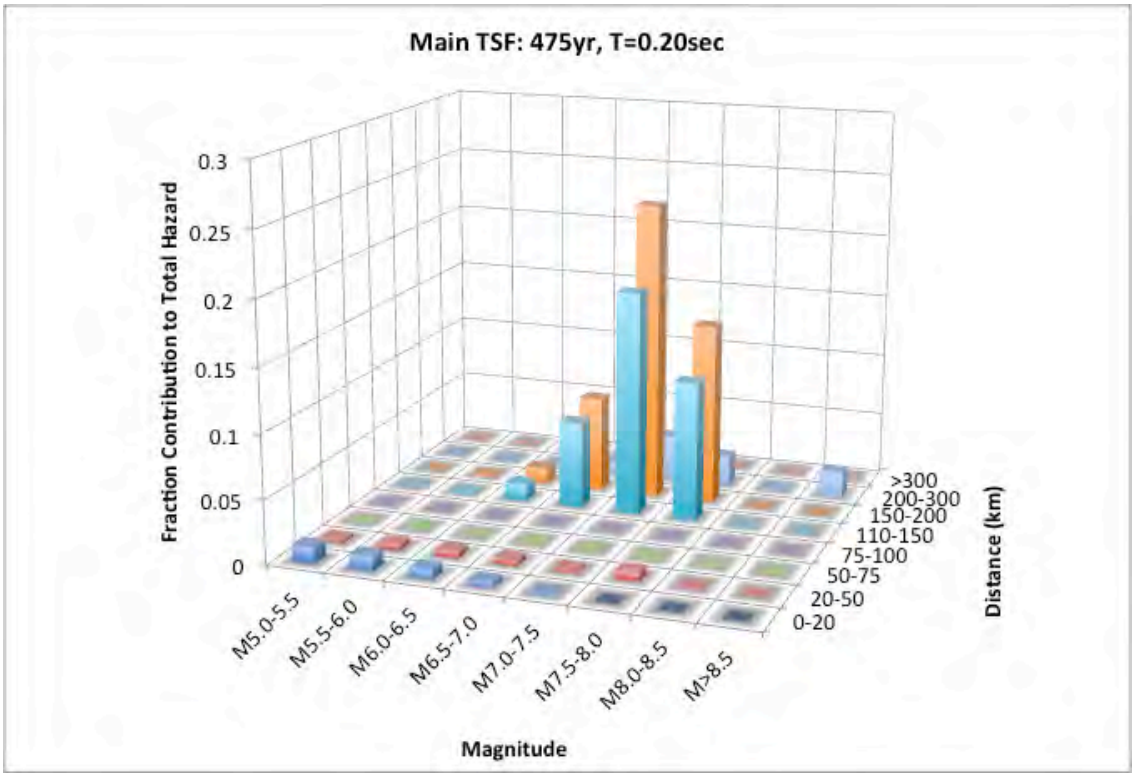

(b)

Figure 44. Deaggregation binned contribution as a function of magnitude and distance for the Main TSF site location, 475-yr hazard level and PGA (0.01 sec) (a) and 0.2 sec (b).

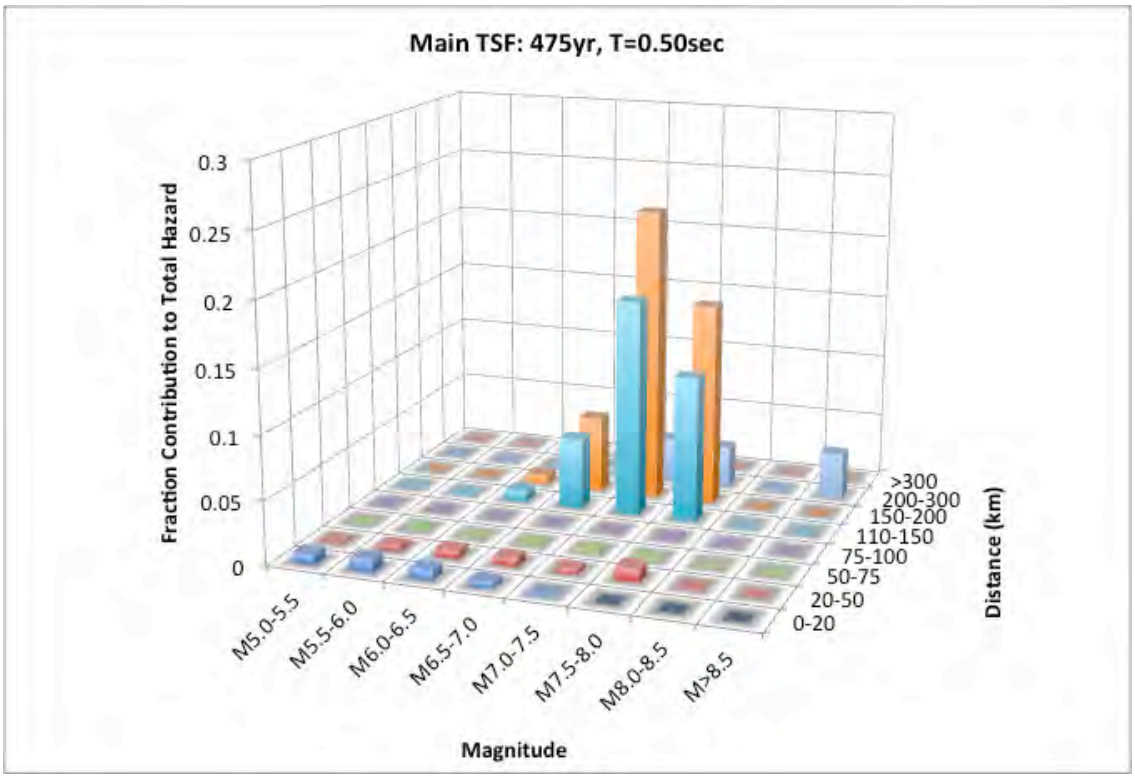

(a)

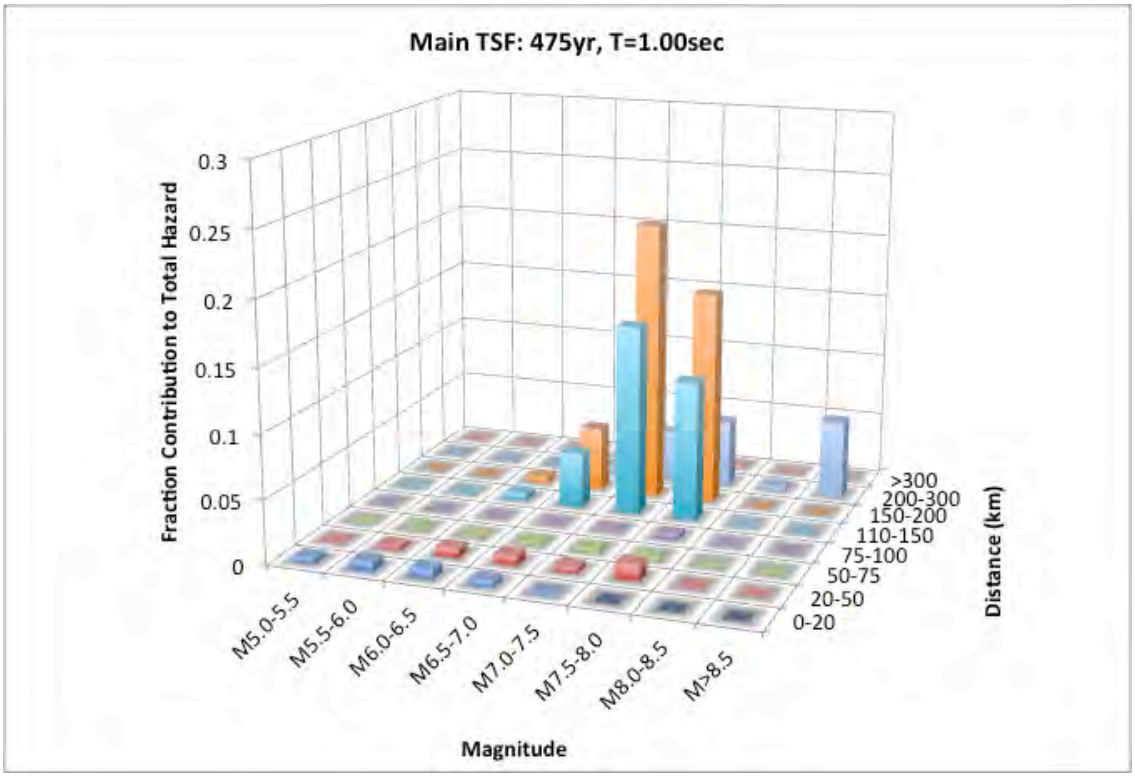

(b)

Figure 45. Deaggregation binned contribution as a function of magnitude and distance for the Main TSF site location, 475-yr hazard level and 0.5 sec (a) and 1 sec (b).

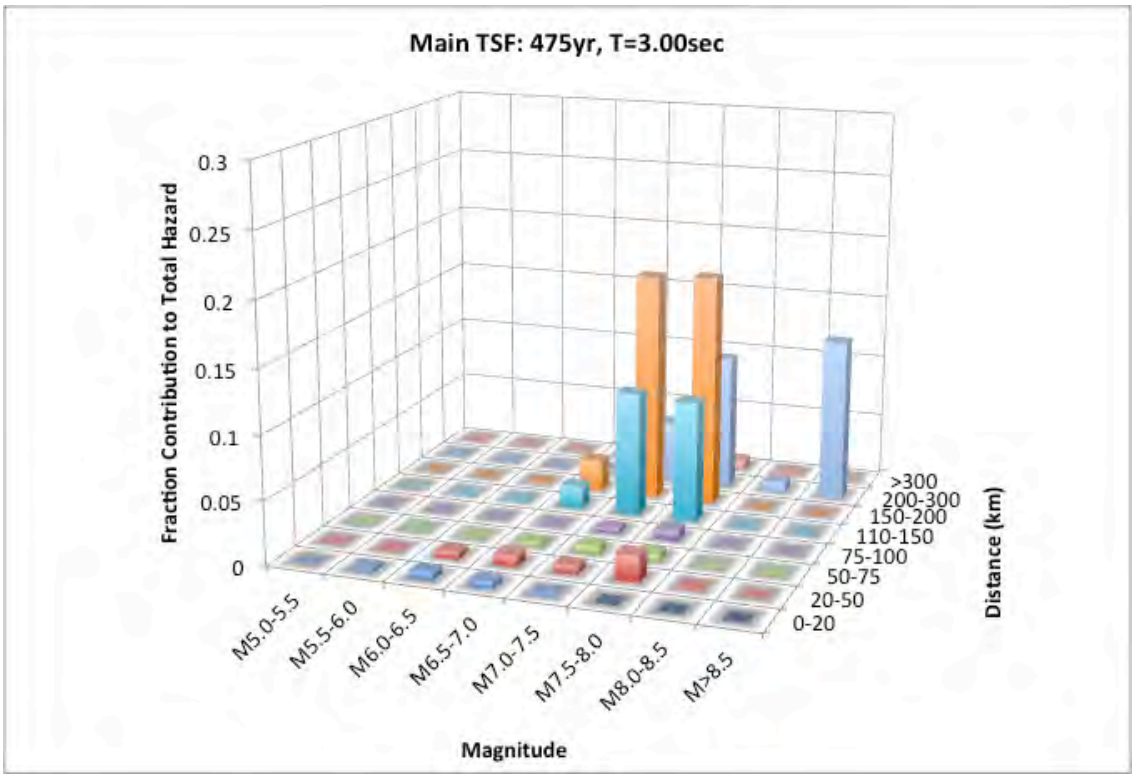

Figure 46. Deaggregation binned contribution as a function of magnitude and distance for the Main TSF site location, 475-yr hazard level and 3 sec.

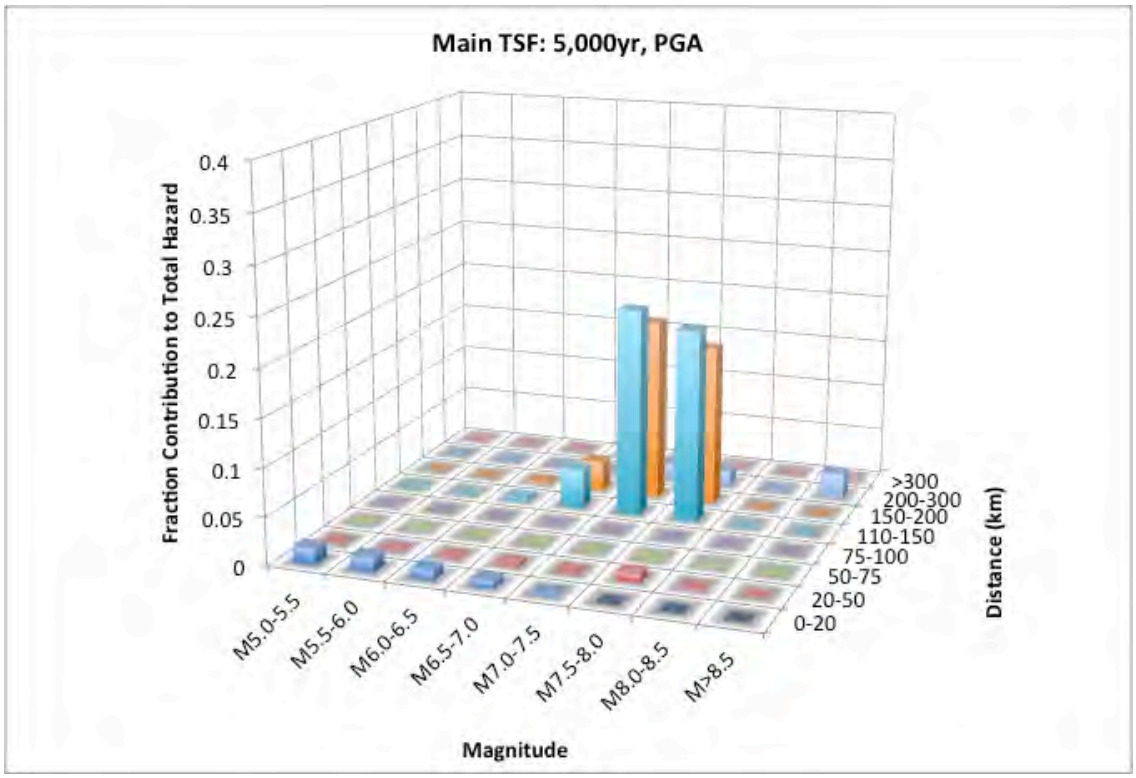

(a)

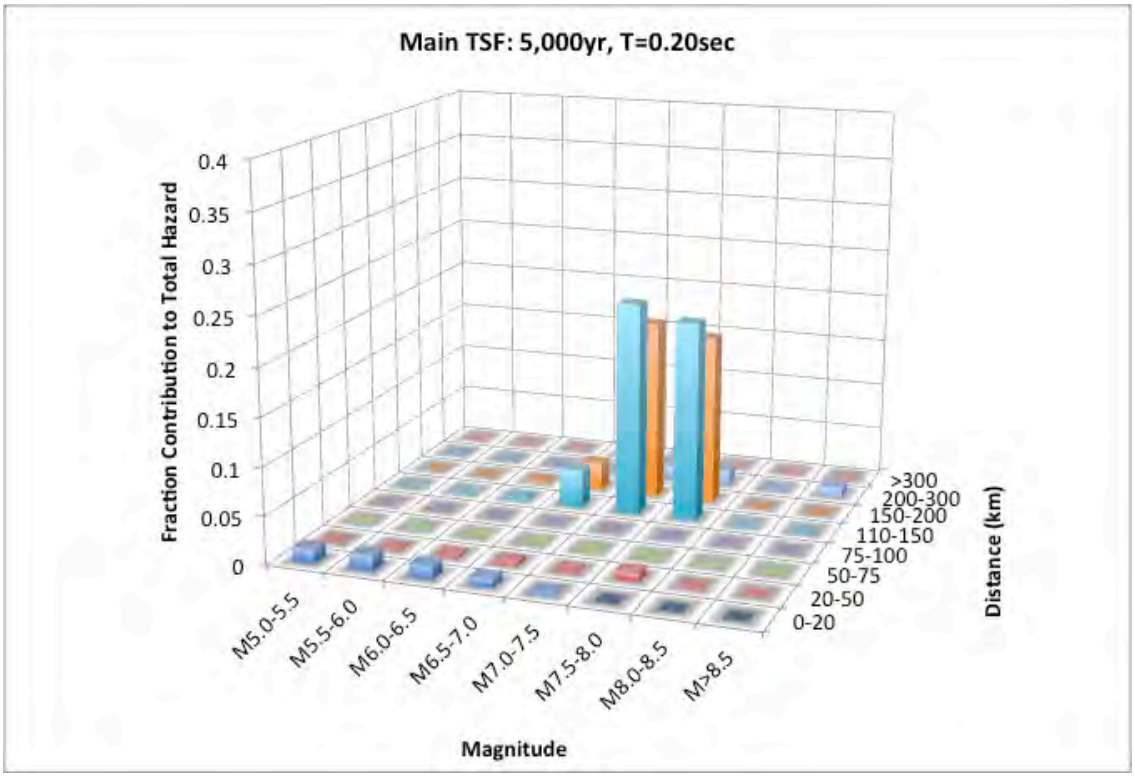

(b)

Figure 47. Deaggregation binned contribution as a function of magnitude and distance for the Main TSF site location, 5,000-yr hazard level and PGA (0.01 sec) (a) and 0.2 sec (b).

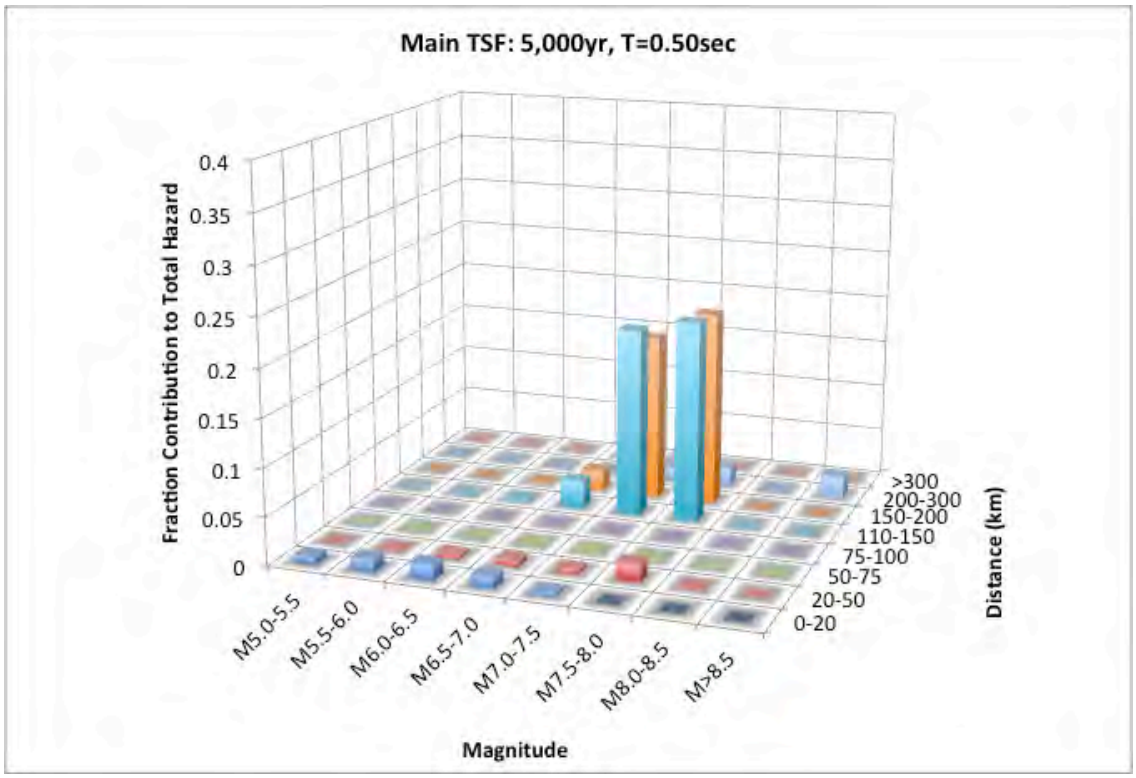

(a)

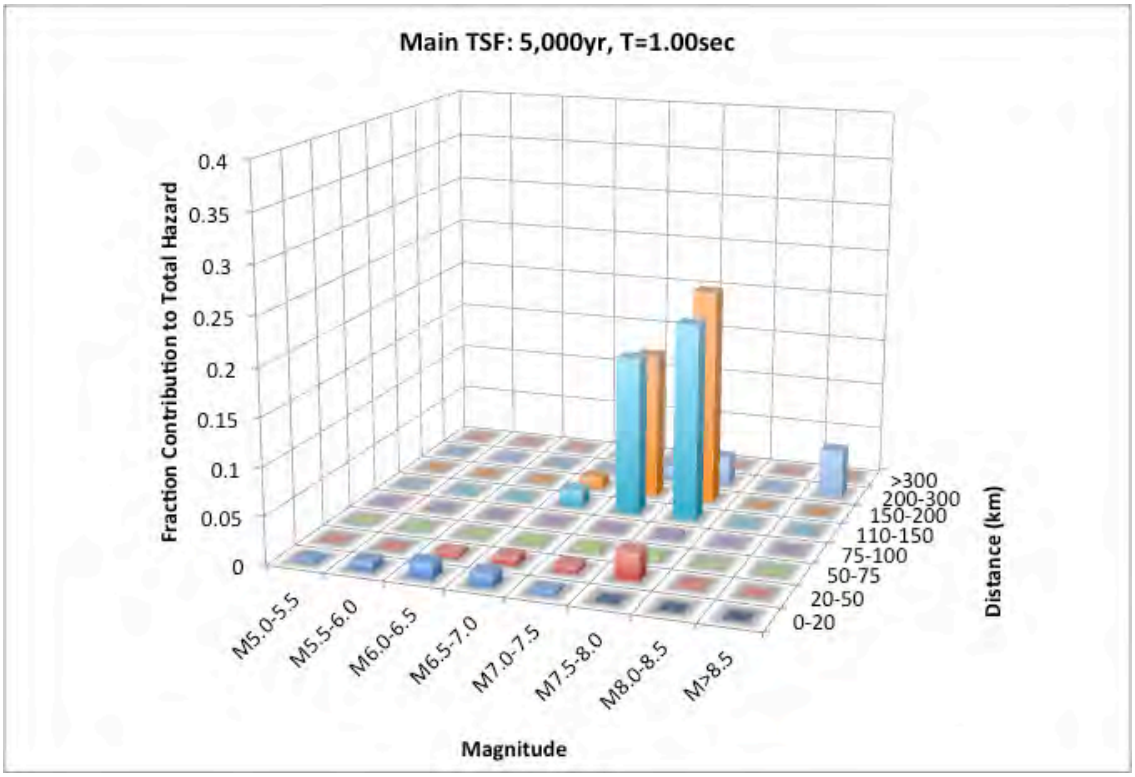

(b)

Figure 48. Deaggregation binned contribution as a function of magnitude and distance for the Main TSF site location, 5,000-yr hazard level and 0.5 sec (a) and 1 sec (b).

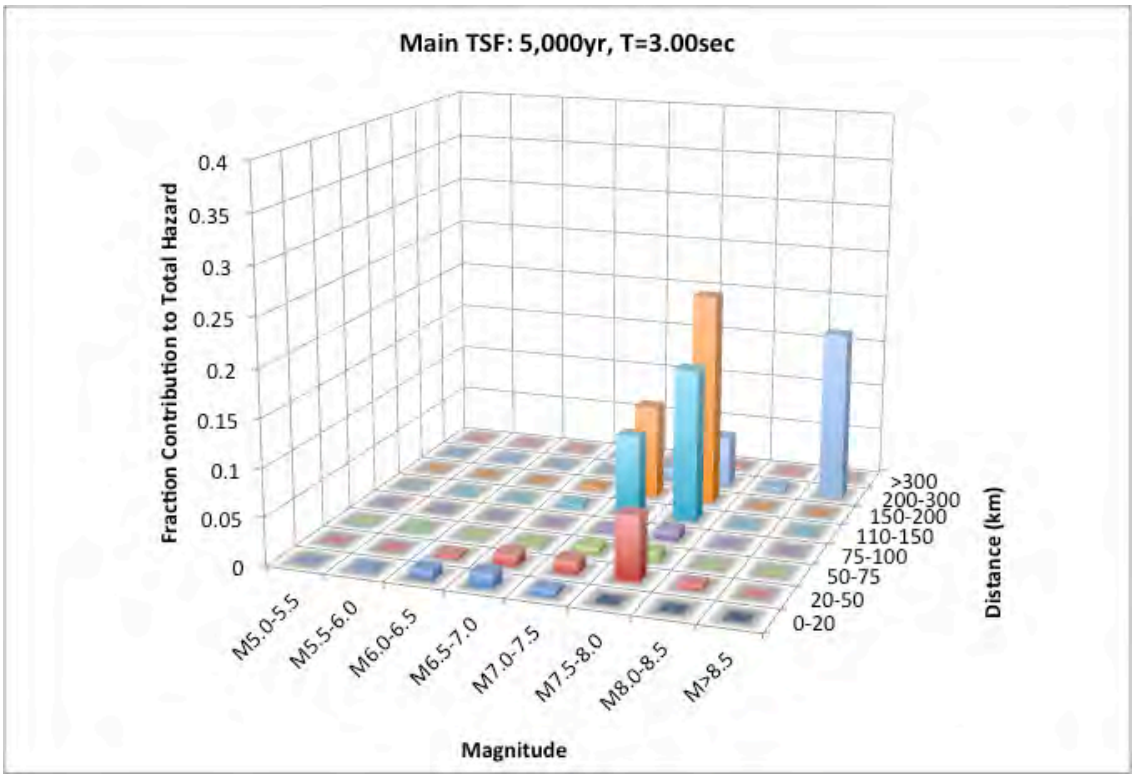

Figure 49. Deaggregation binned contribution as a function of magnitude and distance for the Main TSF site location, 5,000-yr hazard level and 3 sec.

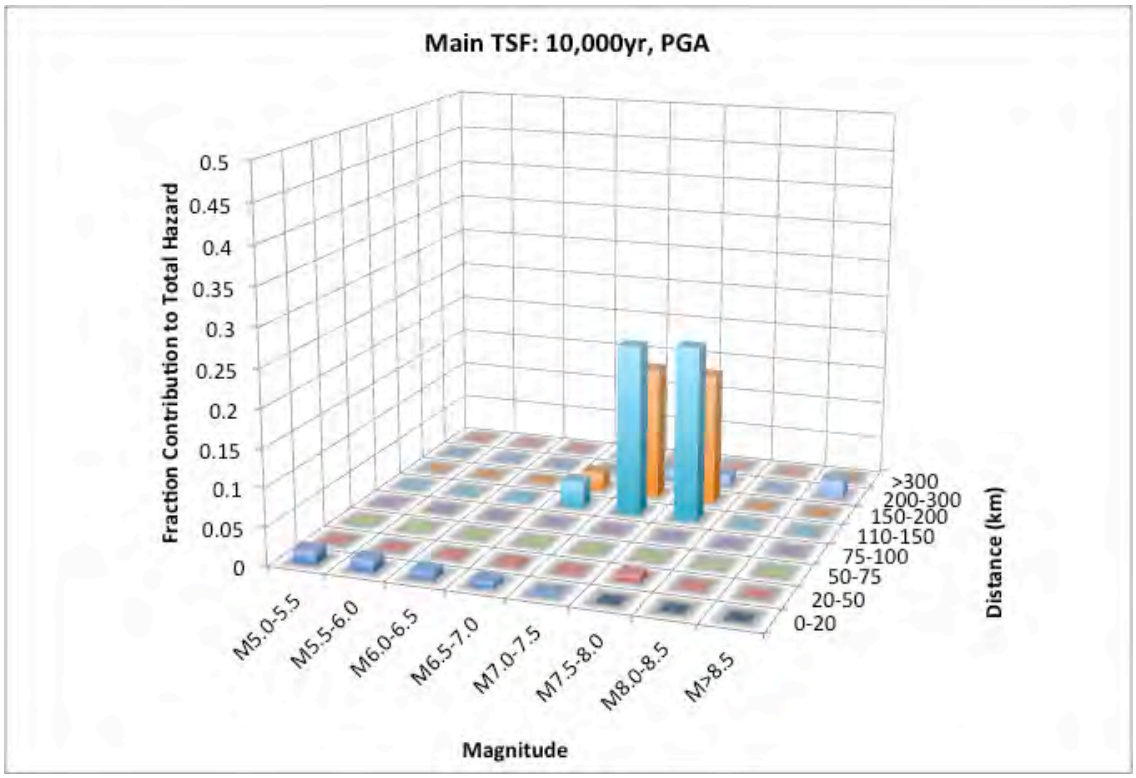

(a)

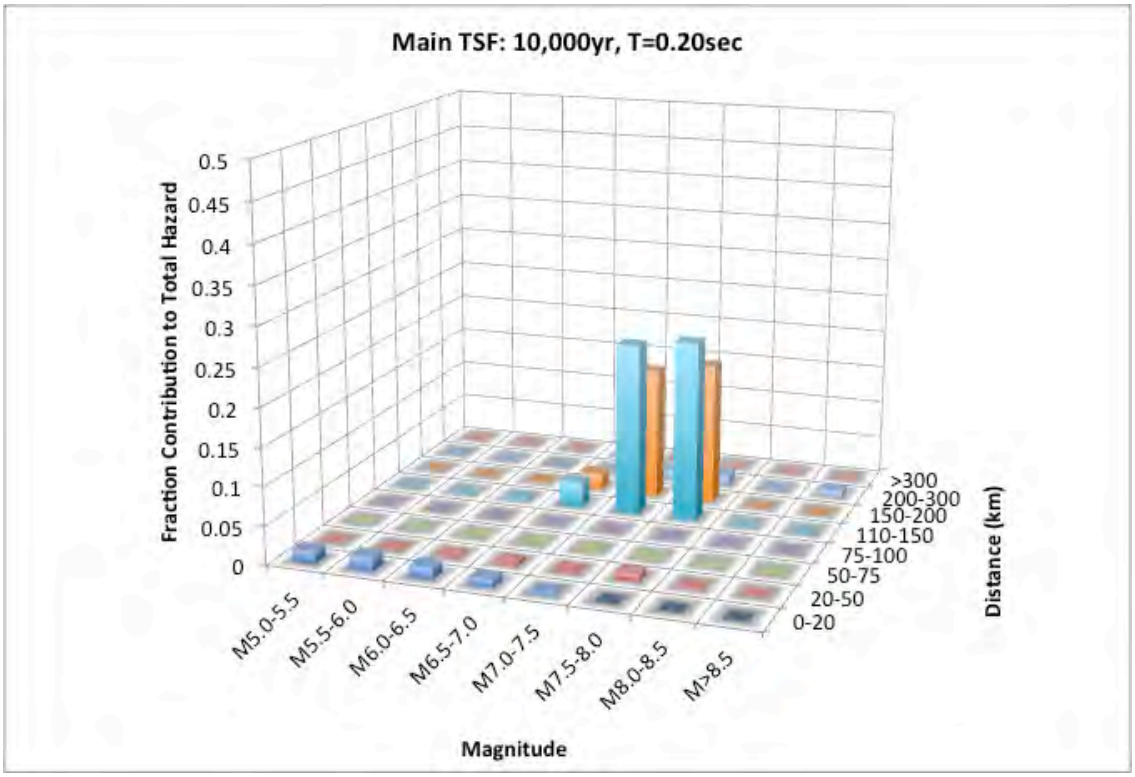

(b)

Figure 50. Deaggregation binned contribution as a function of magnitude and distance for the Main TSF site location, 10,000-yr hazard level and PGA (0.01 sec) (a) and 0.2 sec (b).

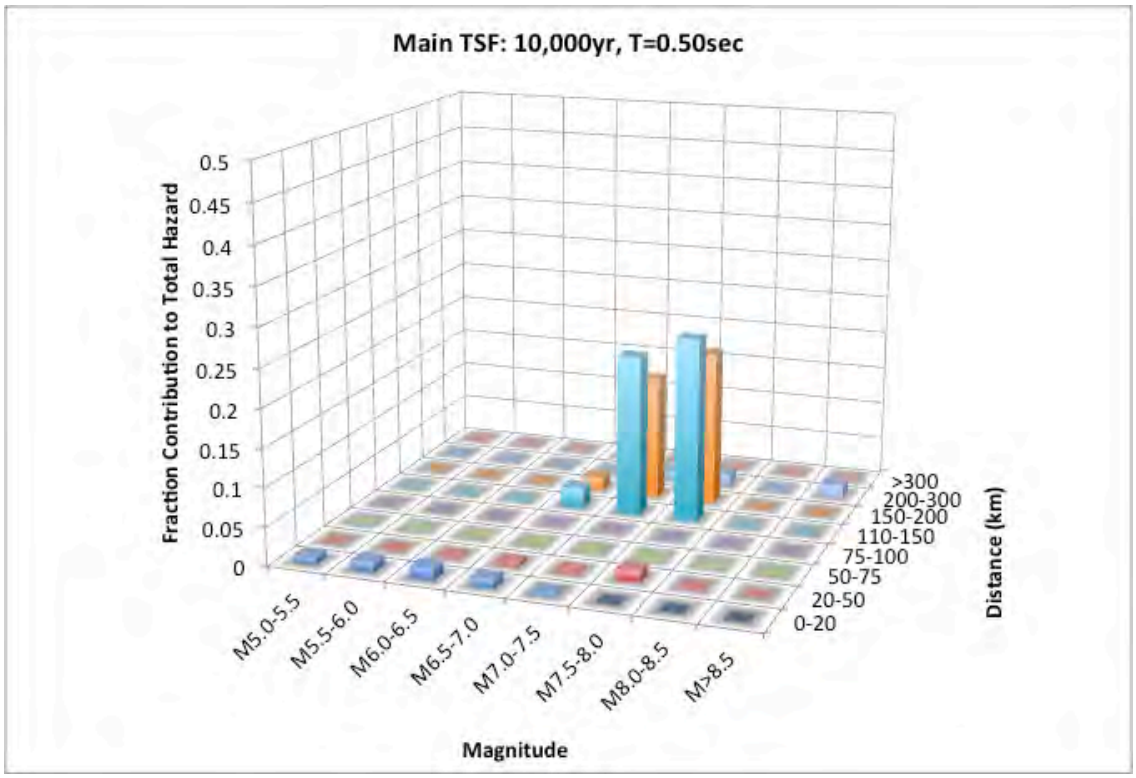

(a)

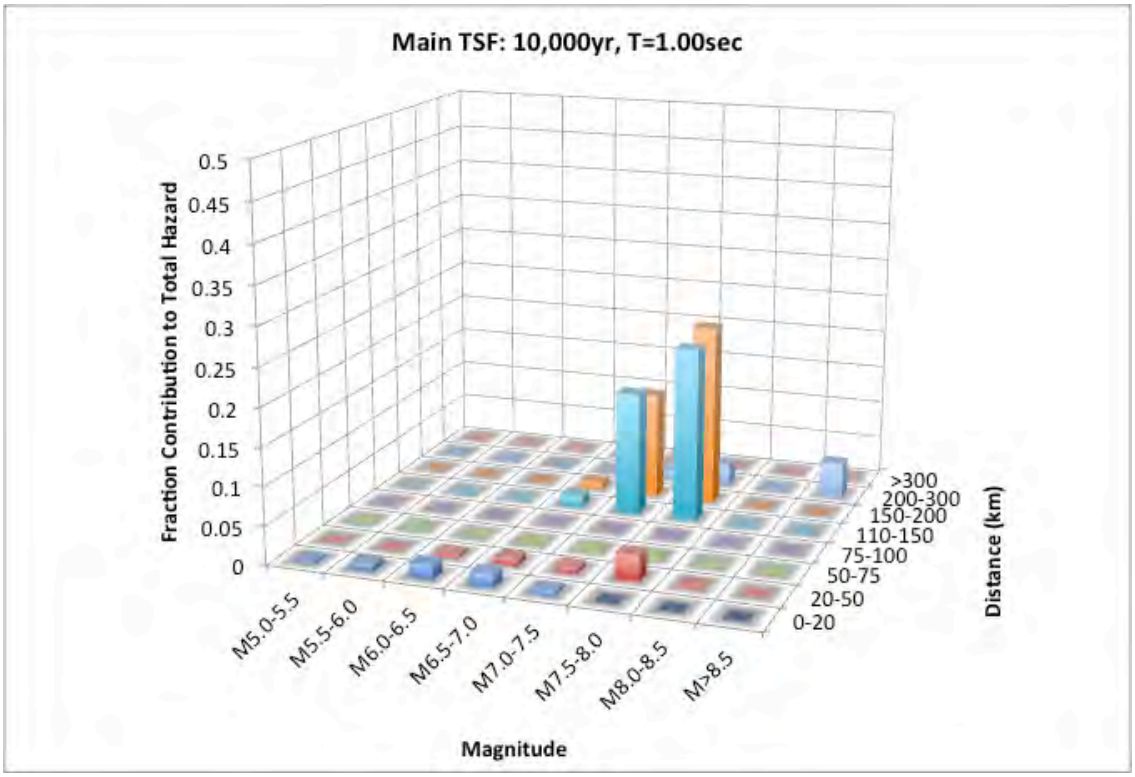

(b)

Figure 51. Deaggregation binned contribution as a function of magnitude and distance for the Main TSF site location, 10,000-yr hazard level and 0.5 sec (a) and 1 sec (b).

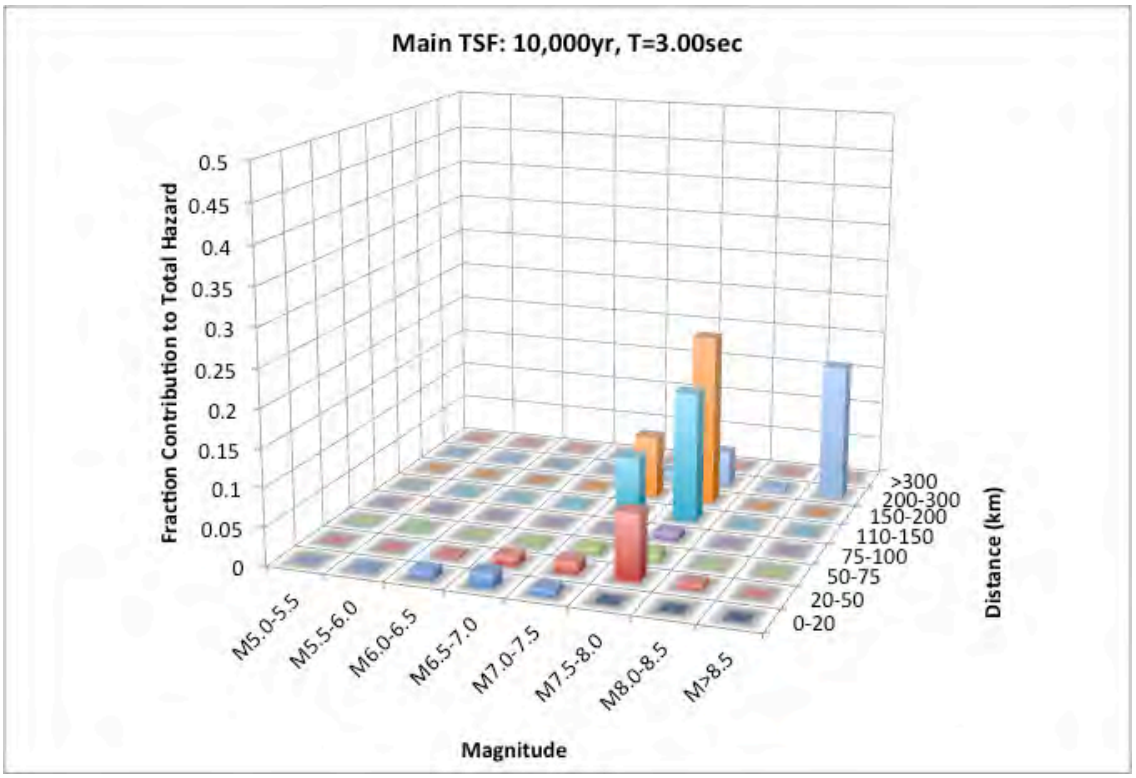

Figure 52. Deaggregation binned contribution as a function of magnitude and distance for the Main TSF site location, 10,000-yr hazard level and 3 sec.

4.3 PSHA Results – Pyritic TSF Site Location

As noted earlier and shown in Figure 1, the Pyritic TSF site location is located east of the Main TSF site location. This site is located slightly closer to the controlling slab seismic source and as such the UHS ground motions would be expected to be slightly larger (see Section 4.5 for the comparison). The overall contribution from the individual sources and the fractile distribution are expected to be similar to the results observed for the Main TSF site location.

The UHS based on the mean hazard curves are listed in Table 11 and plotted in Figure 53 for the Pyritic site location. The fractile UHS for the 5,000 and 10,000-yr return period hazard levels are listed in Tables 12 and 13 and plotted in Figures 54 and 55.

Table 11. UHS for the Pyritic TSF site location for V_{S30} = 760 m/sec.

Period (sec)	475-yr UHS (g)	1,000-yr UHS (g)	2,475-yr UHS (g)	5,000-yr UHS (g)	10,000-yr UHS (g)
0.010	0.2729	0.3555	0.4828	0.5949	0.7273
0.020	0.2751	0.3584	0.4878	0.6011	0.7360
0.030	0.3171	0.4132	0.5605	0.6954	0.8477
0.040	0.3511	0.4627	0.6252	0.7795	0.9507
0.050	0.3800	0.5043	0.6805	0.8467	1.0358
0.075	0.4925	0.6440	0.8753	1.0892	1.3323
0.100	0.5813	0.7675	1.0394	1.2913	1.5760
0.150	0.6054	0.8009	1.0895	1.3578	1.6607
0.200	0.5942	0.7876	1.0722	1.3368	1.6357
0.250	0.5245	0.6920	0.9450	1.1792	1.4470
0.300	0.4708	0.6202	0.8474	1.0580	1.2972
0.400	0.3756	0.5013	0.6794	0.8479	1.0396
0.500	0.2974	0.3900	0.5363	0.6688	0.8228
0.750	0.1878	0.2496	0.3420	0.4283	0.5300
1.000	0.1349	0.1814	0.2496	0.3137	0.3838
1.500	0.0821	0.1090	0.1490	0.1898	0.2344
2.000	0.0583	0.0786	0.1084	0.1357	0.1693
3.000	0.0316	0.0429	0.0599	0.0759	0.0939
4.000	0.0218	0.0287	0.0400	0.0515	0.0636
5.000	0.0154	0.0210	0.0287	0.0366	0.0466
7.500	0.0082	0.0112	0.0160	0.0209	0.0269
10.000	0.0056	0.0077	0.0111	0.0145	0.0187

Table 12. Fractile UHS for the Pyritic TSF site location for V_{S30} = 760 m/sec at the 5,000-yr return period level.

Period (sec)	Mean 5,000-yr UHS (g)	5th 5,000-yr UHS (g)	16th 5,000-yr UHS (g)	50th 5,000-yr UHS (g)	84th 5,000-yr UHS (g)	95th 5,000-yr UHS (g)
0.010	0.5949	0.5325	0.5521	0.5894	0.6332	0.6708
0.020	0.6011	0.5350	0.5545	0.5924	0.6410	0.6933
0.030	0.6954	0.6174	0.6404	0.6857	0.7430	0.7984
0.040	0.7795	0.6865	0.7126	0.7629	0.8300	0.9325
0.050	0.8467	0.7447	0.7711	0.8219	0.9034	1.0490
0.075	1.0892	0.9633	0.9989	1.0640	1.1620	1.3170
0.100	1.2913	1.1470	1.1890	1.2690	1.3760	1.5190
0.150	1.3578	1.1850	1.2300	1.3150	1.4540	1.6950
0.200	1.3368	1.1620	1.2070	1.2960	1.4340	1.6630
0.250	1.1792	1.0150	1.0540	1.1320	1.2660	1.5160
0.300	1.0580	0.9080	0.9448	1.0170	1.1350	1.3520
0.400	0.8479	0.7279	0.7581	0.8141	0.9094	1.0840
0.500	0.6688	0.5609	0.5834	0.6286	0.7149	0.9014
0.750	0.4283	0.3486	0.3630	0.3915	0.4517	0.6080
1.000	0.3137	0.2538	0.2654	0.2879	0.3300	0.4418
1.500	0.1898	0.1461	0.1534	0.1674	0.1973	0.2830
2.000	0.1357	0.1020	0.1070	0.1162	0.1355	0.2159
3.000	0.0759	0.0590	0.0624	0.0689	0.0815	0.1071
4.000	0.0515	0.0405	0.0436	0.0491	0.0574	0.0653
5.000	0.0366	0.0285	0.0307	0.0351	0.0421	0.0469
7.500	0.0209	0.0143	0.0158	0.0200	0.0252	0.0291
10.000	0.0145	0.0097	0.0107	0.0137	0.0174	0.0201

Table 13. Fractile UHS for the Pyritic TSF site location for V_{S30} = 760 m/sec at the 10,000-yr return period level.

Period (sec)	Mean 10,000-yr UHS (g)	5th 10,000-yr UHS (g)	16th 10,000-yr UHS (g)	50th 10,000-yr UHS (g)	84th 10,000-yr UHS (g)	95th 10,000-yr UHS (g)
0.010	0.7273	0.6420	0.6677	0.7187	0.7762	0.8240
0.020	0.7360	0.6450	0.6705	0.7225	0.7859	0.8537
0.030	0.8477	0.7515	0.7786	0.8336	0.9056	0.9868
0.040	0.9507	0.8309	0.8616	0.9240	1.0170	1.1510
0.050	1.0358	0.8973	0.9319	1.0010	1.1030	1.2960
0.075	1.3323	1.1650	1.2090	1.2940	1.4250	1.6380
0.100	1.5760	1.3880	1.4400	1.5410	1.6830	1.8870
0.150	1.6607	1.4350	1.4910	1.5970	1.7770	2.1110
0.200	1.6357	1.4080	1.4650	1.5760	1.7560	2.0680
0.250	1.4470	1.2300	1.2800	1.3790	1.5520	1.8740
0.300	1.2972	1.1010	1.1460	1.2400	1.3930	1.6710
0.400	1.0396	0.8807	0.9178	0.9941	1.1120	1.3330
0.500	0.8228	0.6817	0.7118	0.7709	0.8766	1.1070
0.750	0.5300	0.4239	0.4434	0.4823	0.5554	0.7514
1.000	0.3838	0.3102	0.3237	0.3500	0.4042	0.5442
1.500	0.2344	0.1797	0.1896	0.2074	0.2416	0.3456
2.000	0.1693	0.1229	0.1295	0.1416	0.1673	0.2649
3.000	0.0939	0.0724	0.0771	0.0849	0.1009	0.1298
4.000	0.0636	0.0507	0.0543	0.0607	0.0717	0.0808
5.000	0.0466	0.0350	0.0382	0.0443	0.0538	0.0597
7.500	0.0269	0.0178	0.0198	0.0250	0.0330	0.0391
10.000	0.0187	0.0118	0.0131	0.0176	0.0229	0.0264

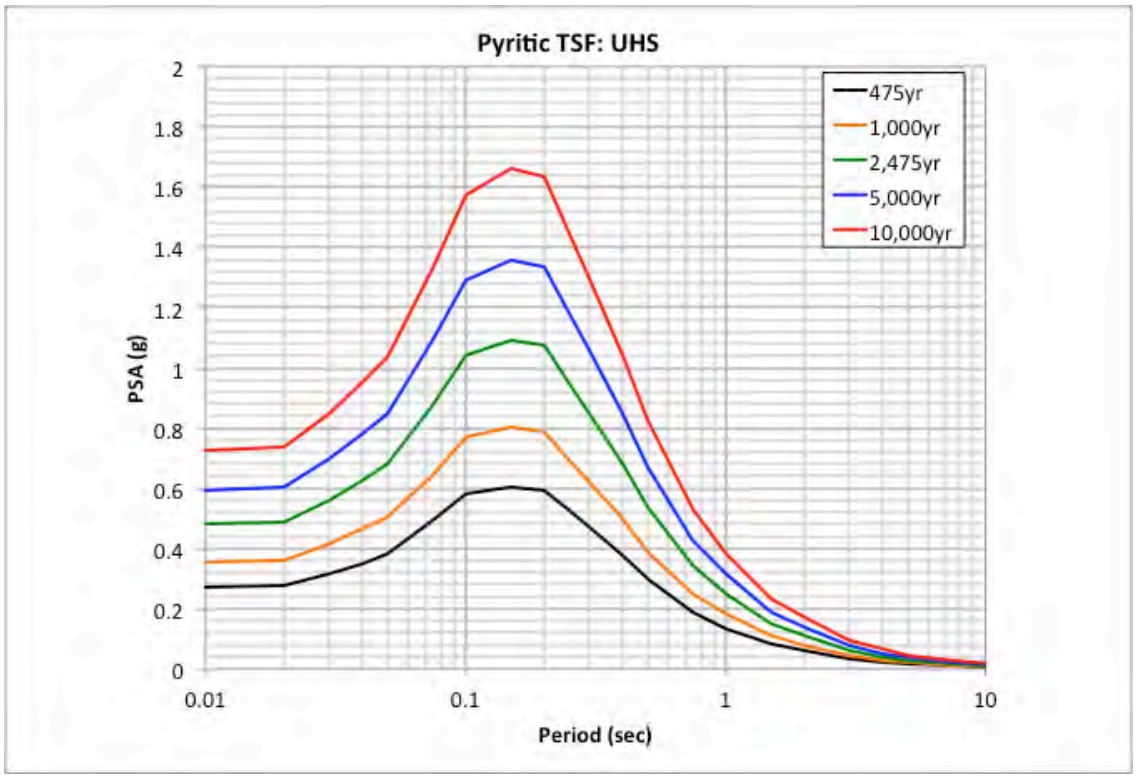

(a)

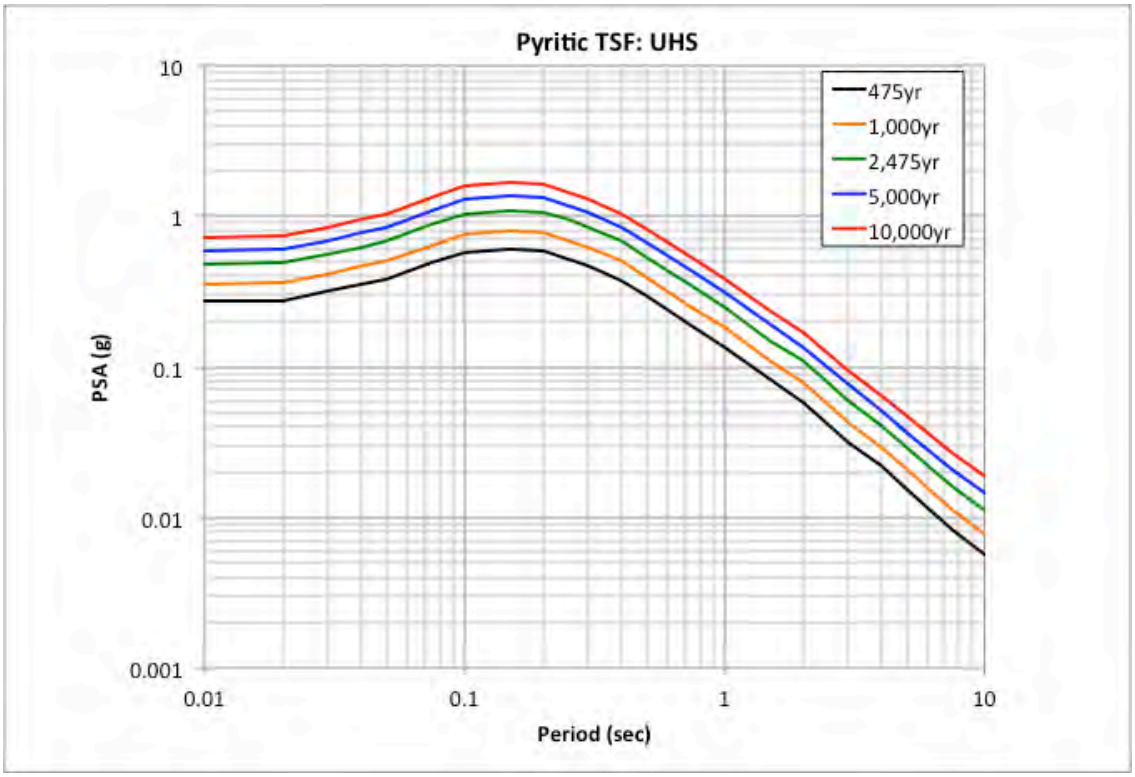

(b)

Figure 53. UHS spectra for the Pyritic TSF site location (V_{S30} = 760 m/sec) plot log-linear (a) and log-log (b).

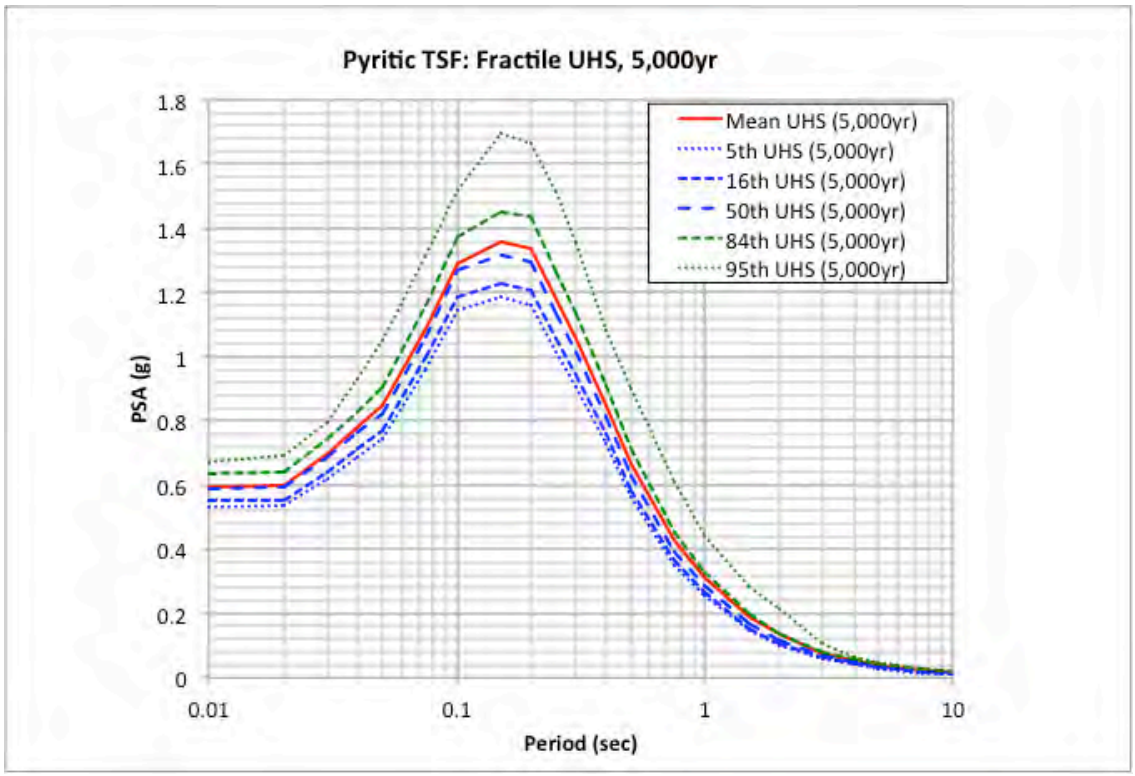

(a)

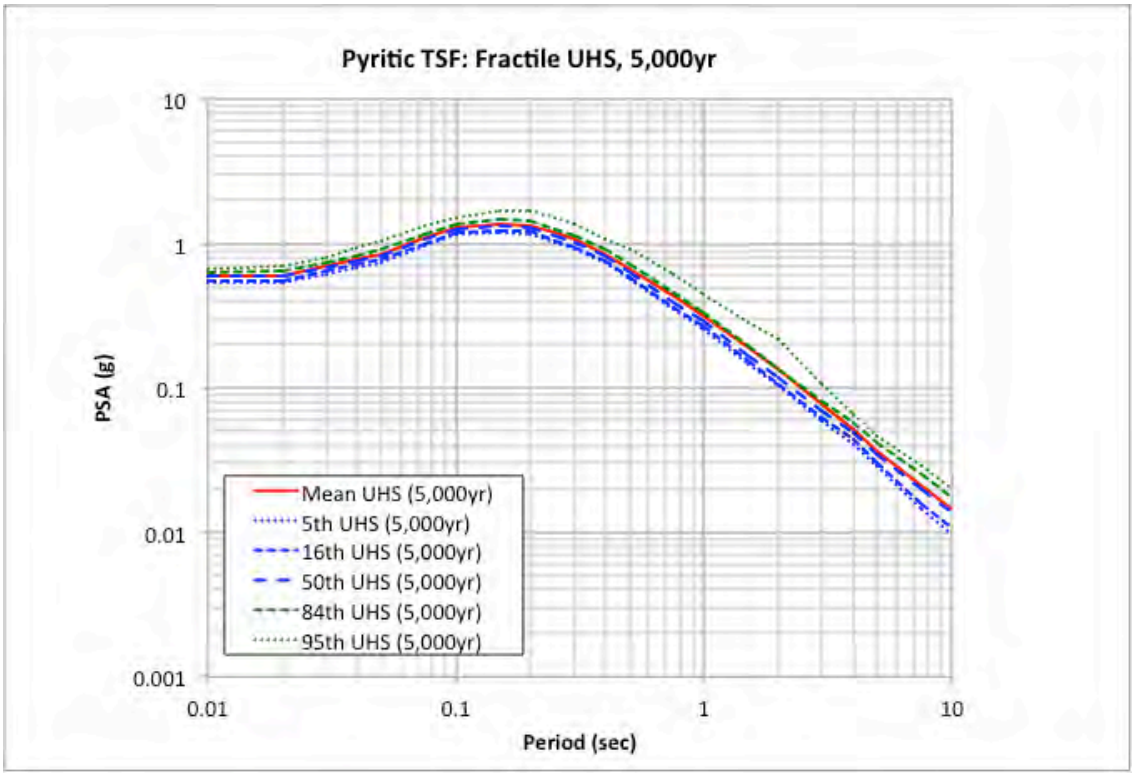

(b)

Figure 54. Fractile UHS for the Pyritic TSF site location for 5,000-yr return period hazard level plotted log-linear (a) and log-log (b).

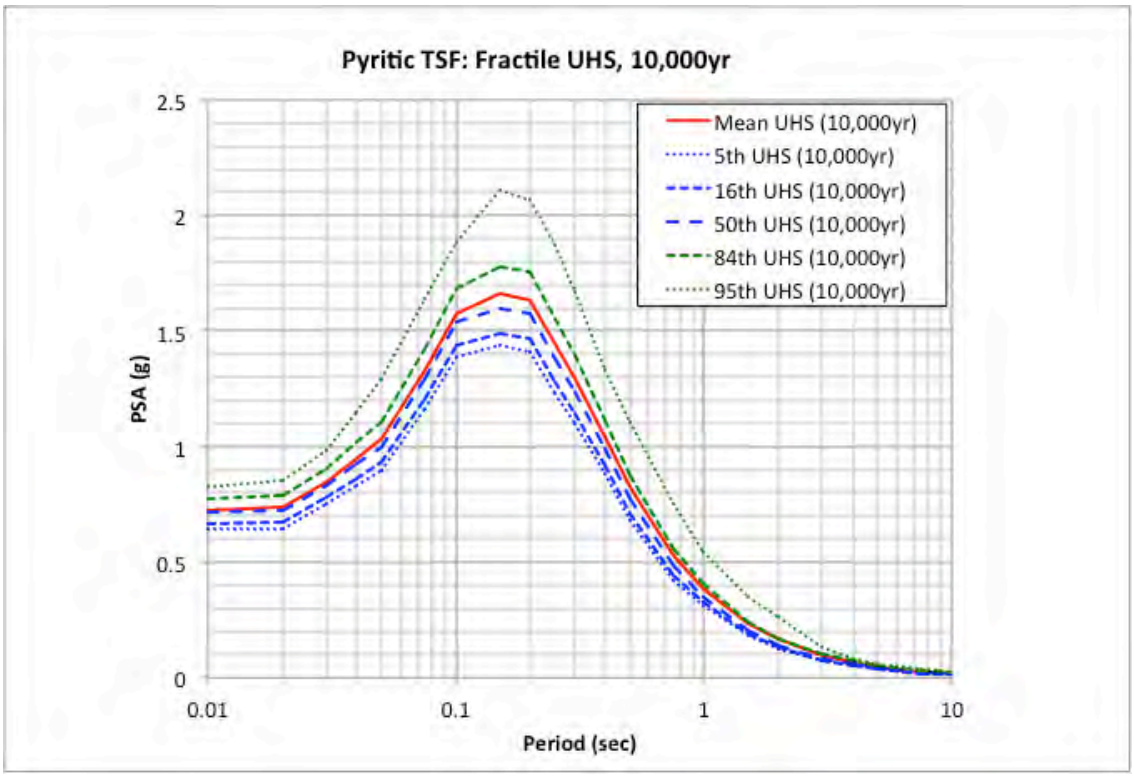

(a)

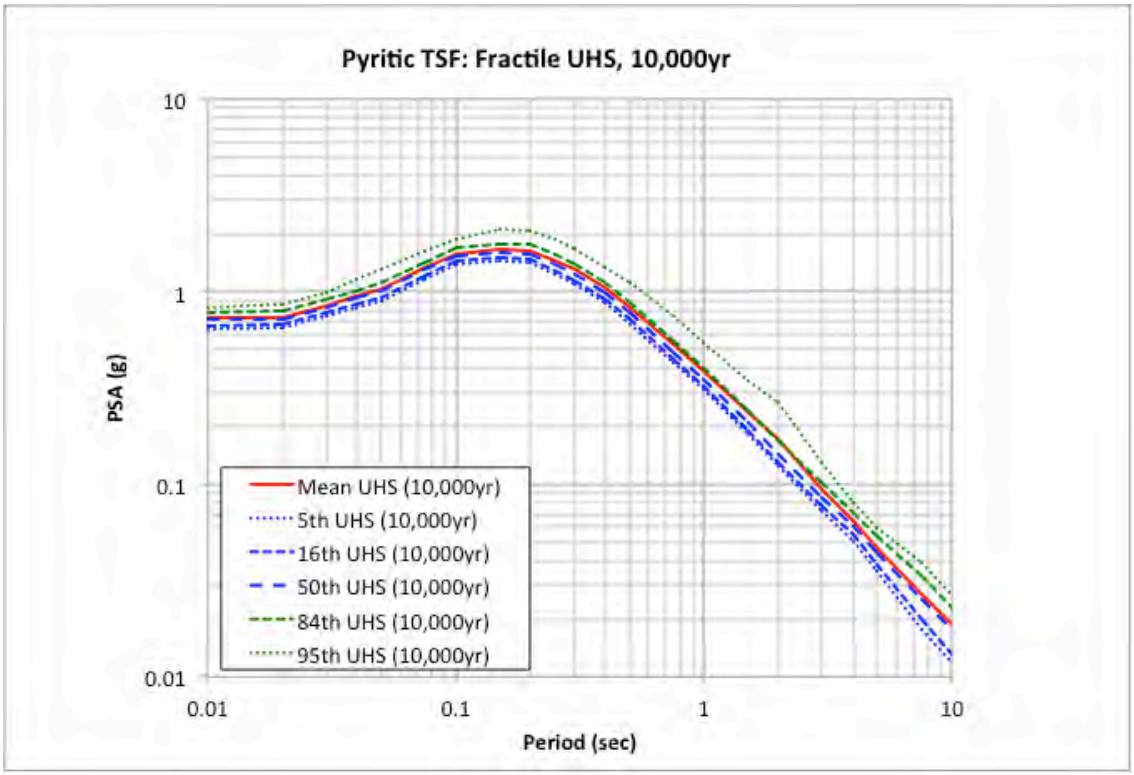

(b)

Figure 55. Fractile UHS for the Pyritic TSF site location for 10,000-yr return period hazard level plotted log-linear (a) and log-log (b).

4.4 PSHA Results – South TSF Site Location

As noted earlier and shown in Figure 1, the South TSF site is located southwest of the Main TSF site location. This site is located slightly closer to the controlling slab seismic source and as such the UHS ground motions would be expected to be slightly larger or similar (see Section 4.5 for the comparison). The overall contribution from the individual sources and the fractile distribution would be expected to be similar to the results observed for the Main TSF site location.

The UHS based on the mean hazard curves are listed in Table 14 and plotted in Figure 56 for the South site location. The fractile UHS for the 5,000 and 10,000-yr return period hazard levels are listed in Tables 15 and 16 and plotted in Figures 57 and 58.

Table 14. UHS for the South TSF site location for V_{S30} = 760 m/sec.

Period (sec)	475-yr UHS (g)	1,000-yr UHS (g)	2,475-yr UHS (g)	5,000-yr UHS (g)	10,000-yr UHS (g)
0.010	0.2646	0.3456	0.4684	0.5790	0.7072
0.020	0.2667	0.3484	0.4731	0.5849	0.7153
0.030	0.3082	0.4010	0.5452	0.6756	0.8254
0.040	0.3409	0.4483	0.6073	0.7585	0.9243
0.050	0.3686	0.4888	0.6604	0.8233	1.0089
0.075	0.4762	0.6245	0.8500	1.0590	1.2963
0.100	0.5639	0.7452	1.0103	1.2561	1.5343
0.150	0.5866	0.7773	1.0577	1.3188	1.6145
0.200	0.5757	0.7643	1.0409	1.2985	1.5904
0.250	0.5088	0.6699	0.9160	1.1443	1.4051
0.300	0.4551	0.6011	0.8223	1.0277	1.2610
0.400	0.3640	0.4848	0.6584	0.8231	1.0108
0.500	0.2873	0.3777	0.5205	0.6480	0.7985
0.750	0.1812	0.2417	0.3317	0.4145	0.5142
1.000	0.1307	0.1753	0.2418	0.3045	0.3717
1.500	0.0797	0.1060	0.1443	0.1833	0.2269
2.000	0.0566	0.0764	0.1054	0.1315	0.1635
3.000	0.0306	0.0415	0.0581	0.0733	0.0904
4.000	0.0213	0.0278	0.0386	0.0497	0.0611
5.000	0.0150	0.0204	0.0277	0.0351	0.0444
7.500	0.0080	0.0109	0.0155	0.0202	0.0256
10.000	0.0055	0.0075	0.0108	0.0140	0.0180

Table 15. Fractile UHS for the South TSF site location for V_{S30} = 760 m/sec at the 5,000-yr return period level.

Period (sec)	Mean 5,000-yr UHS (g)	5th 5,000-yr UHS (g)	16th 5,000-yr UHS (g)	50th 5,000-yr UHS (g)	84th 5,000-yr UHS (g)	95th 5,000-yr UHS (g)
0.010	0.5790	0.5192	0.5383	0.5743	0.6156	0.6496
0.020	0.5849	0.5217	0.5405	0.5773	0.6231	0.6700
0.030	0.6756	0.6012	0.6233	0.6672	0.7213	0.7730
0.040	0.7585	0.6679	0.6930	0.7433	0.8075	0.8984
0.050	0.8233	0.7237	0.7516	0.8010	0.8785	1.0130
0.075	1.0590	0.9365	0.9713	1.0360	1.1290	1.2690
0.100	1.2561	1.1160	1.1570	1.2360	1.3380	1.4650
0.150	1.3188	1.1520	1.1950	1.2800	1.4120	1.6350
0.200	1.2985	1.1290	1.1740	1.2620	1.3930	1.6040
0.250	1.1443	0.9862	1.0250	1.1010	1.2290	1.4610
0.300	1.0277	0.8827	0.9181	0.9892	1.1030	1.3040
0.400	0.8231	0.7060	0.7361	0.7917	0.8826	1.0480
0.500	0.6480	0.5448	0.5664	0.6099	0.6922	0.8706
0.750	0.4145	0.3380	0.3519	0.3792	0.4368	0.5887
1.000	0.3045	0.2457	0.2567	0.2784	0.3200	0.4277
1.500	0.1833	0.1412	0.1482	0.1616	0.1900	0.2743
2.000	0.1315	0.0987	0.1037	0.1125	0.1308	0.2101
3.000	0.0733	0.0569	0.0602	0.0663	0.0787	0.1044
4.000	0.0497	0.0388	0.0417	0.0470	0.0554	0.0633
5.000	0.0351	0.0274	0.0295	0.0335	0.0403	0.0452
7.500	0.0202	0.0137	0.0152	0.0192	0.0242	0.0277
10.000	0.0140	0.0093	0.0103	0.0131	0.0169	0.0194

Table 16. Fractile UHS for the South TSF site location for V_{S30} = 760 m/sec at the 10,000-yr return period level.

Period (sec)	Mean 10,000-yr UHS (g)	5th 10,000-yr UHS (g)	16th 10,000-yr UHS (g)	50th 10,000-yr UHS (g)	84th 10,000-yr UHS (g)	95th 10,000-yr UHS (g)
0.010	0.7072	0.6255	0.6504	0.6998	0.7562	0.7992
0.020	0.7153	0.6284	0.6532	0.7036	0.7654	0.8262
0.030	0.8254	0.7313	0.7596	0.8132	0.8808	0.9533
0.040	0.9243	0.8102	0.8398	0.9006	0.9909	1.1120
0.050	1.0089	0.8744	0.9076	0.9744	1.0750	1.2500
0.075	1.2963	1.1340	1.1770	1.2620	1.3860	1.5820
0.100	1.5343	1.3520	1.4030	1.5030	1.6380	1.8210
0.150	1.6145	1.3970	1.4510	1.5560	1.7280	2.0410
0.200	1.5904	1.3700	1.4260	1.5360	1.7080	2.0000
0.250	1.4051	1.1960	1.2460	1.3430	1.5100	1.8090
0.300	1.2610	1.0720	1.1160	1.2060	1.3530	1.6160
0.400	1.0108	0.8562	0.8920	0.9656	1.0820	1.2880
0.500	0.7985	0.6611	0.6900	0.7495	0.8500	1.0720
0.750	0.5142	0.4103	0.4289	0.4662	0.5387	0.7259
1.000	0.3717	0.3010	0.3138	0.3391	0.3912	0.5284
1.500	0.2269	0.1731	0.1825	0.2007	0.2333	0.3358
2.000	0.1635	0.1187	0.1249	0.1365	0.1609	0.2573
3.000	0.0904	0.0695	0.0740	0.0815	0.0969	0.1261
4.000	0.0611	0.0485	0.0521	0.0581	0.0687	0.0782
5.000	0.0444	0.0335	0.0364	0.0421	0.0515	0.0569
7.500	0.0256	0.0170	0.0189	0.0238	0.0313	0.0366
10.000	0.0180	0.0114	0.0126	0.0168	0.0218	0.0251

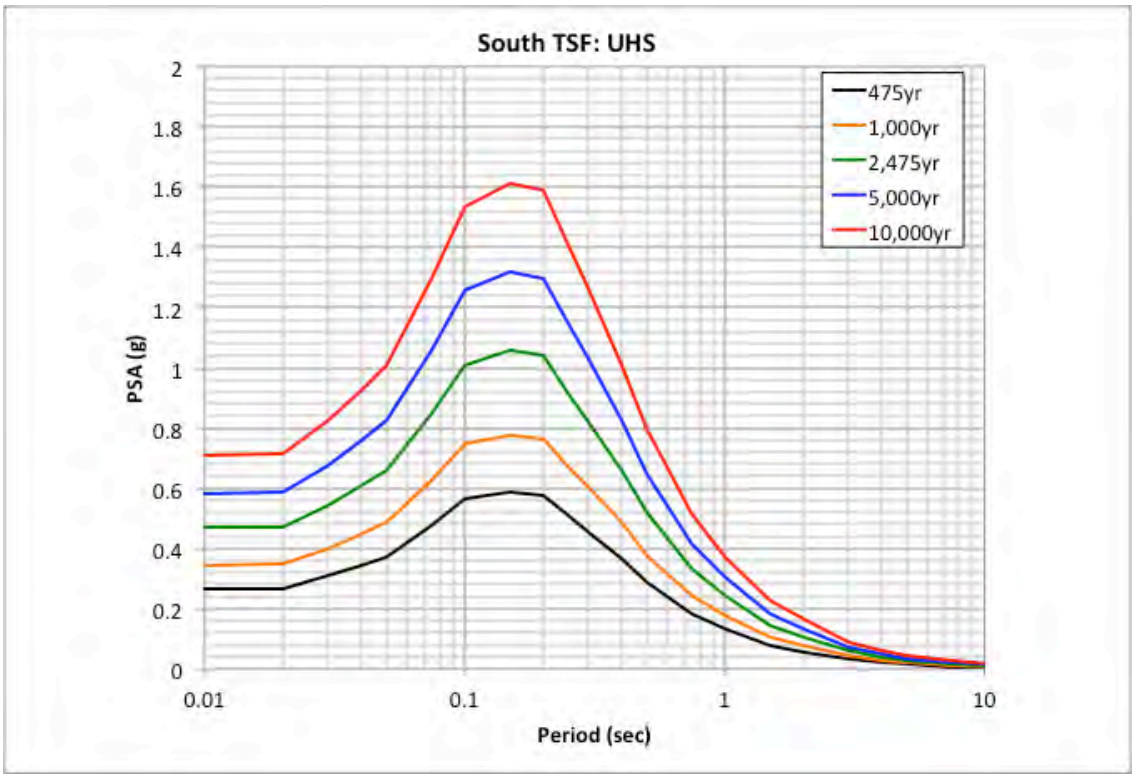

(a)

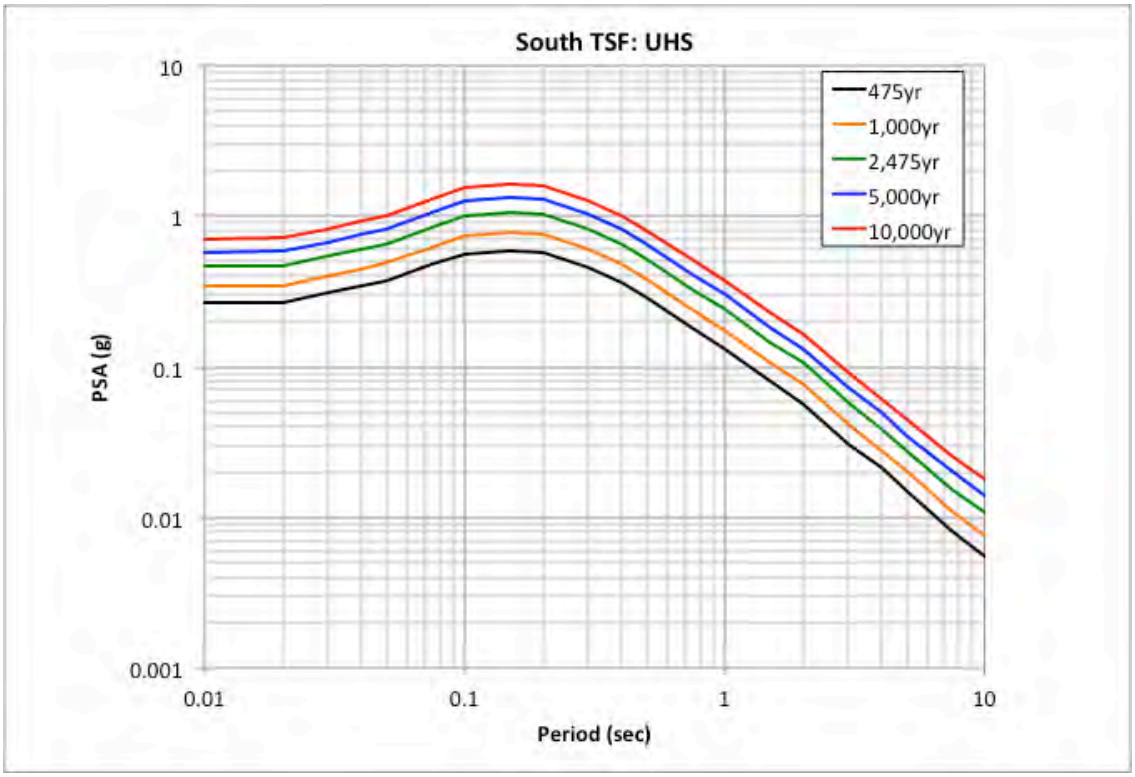

(b)

Figure 56. UHS spectra for the South TSF site location (V_{S30} = 760 m/sec) plot log-linear (a) and log-log (b).

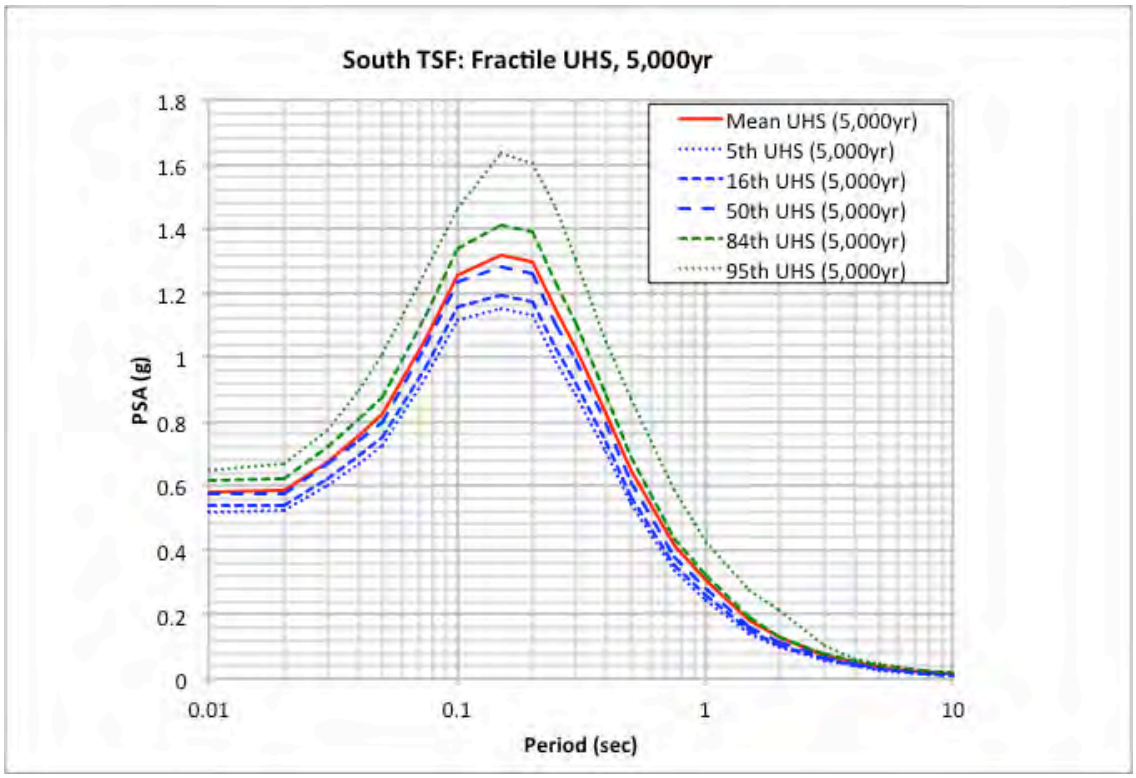

(a)

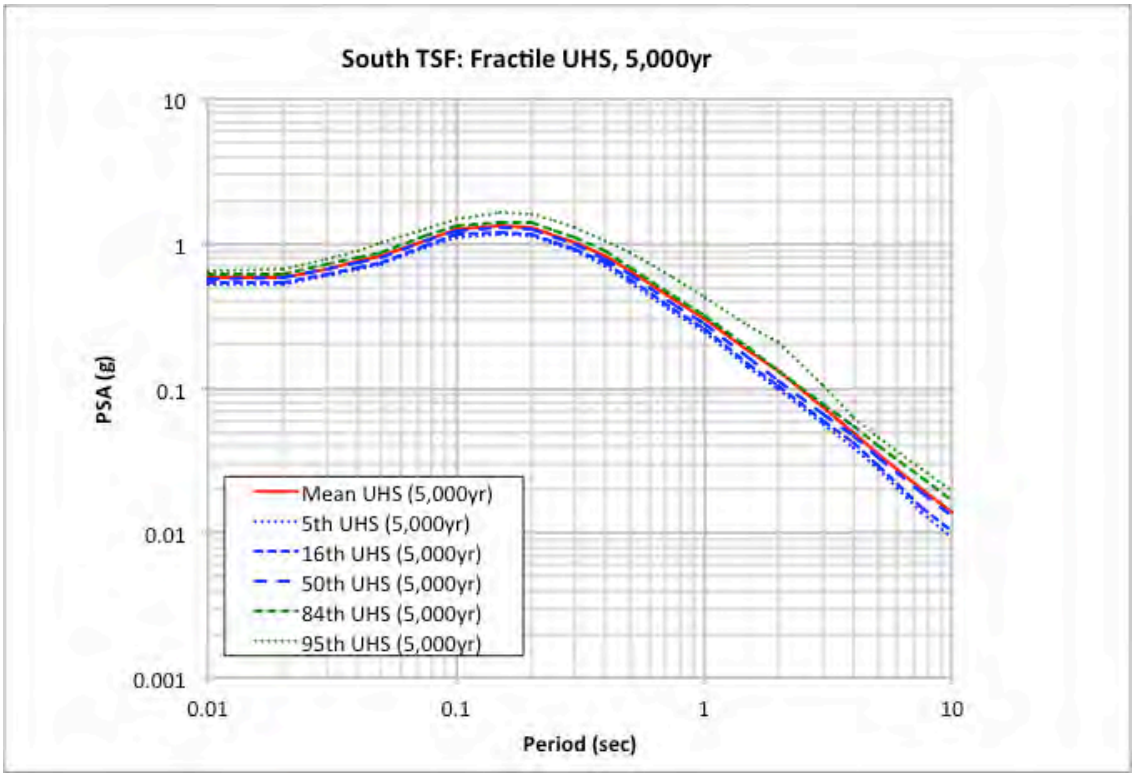

(b)

Figure 57. Fractile UHS for the South TSF site location for 5,000-yr return period hazard level plotted log-linear (a) and log-log (b).

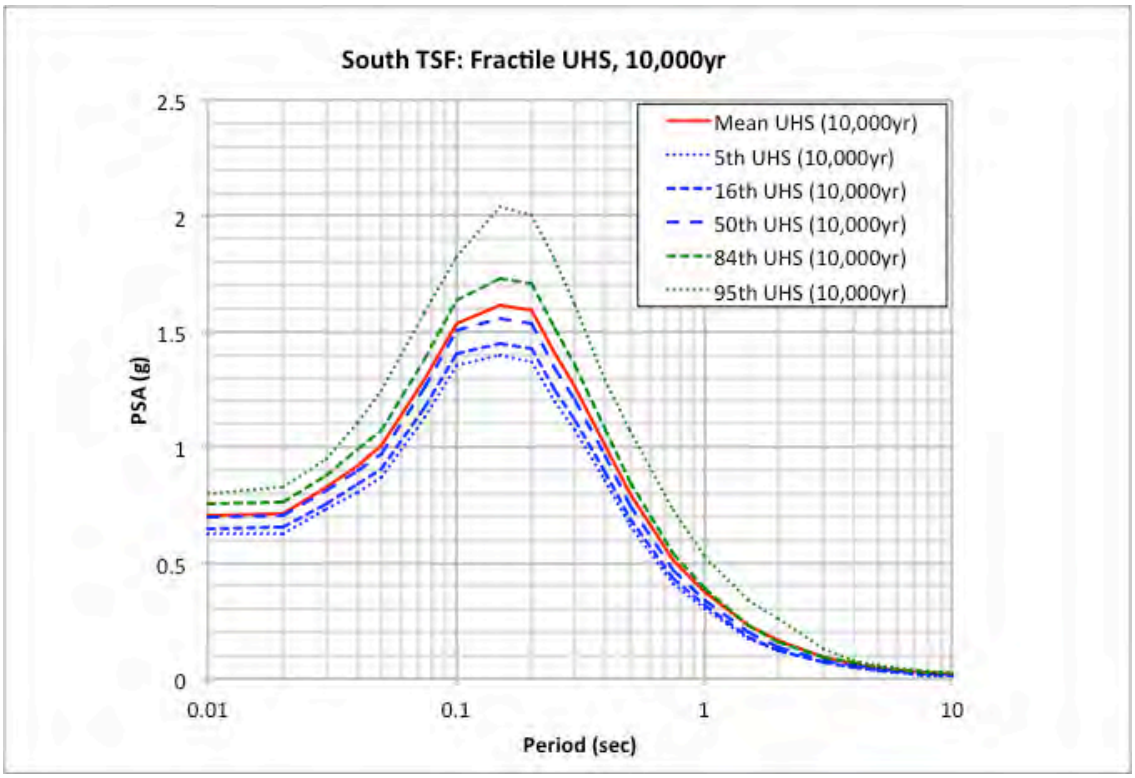

(a)

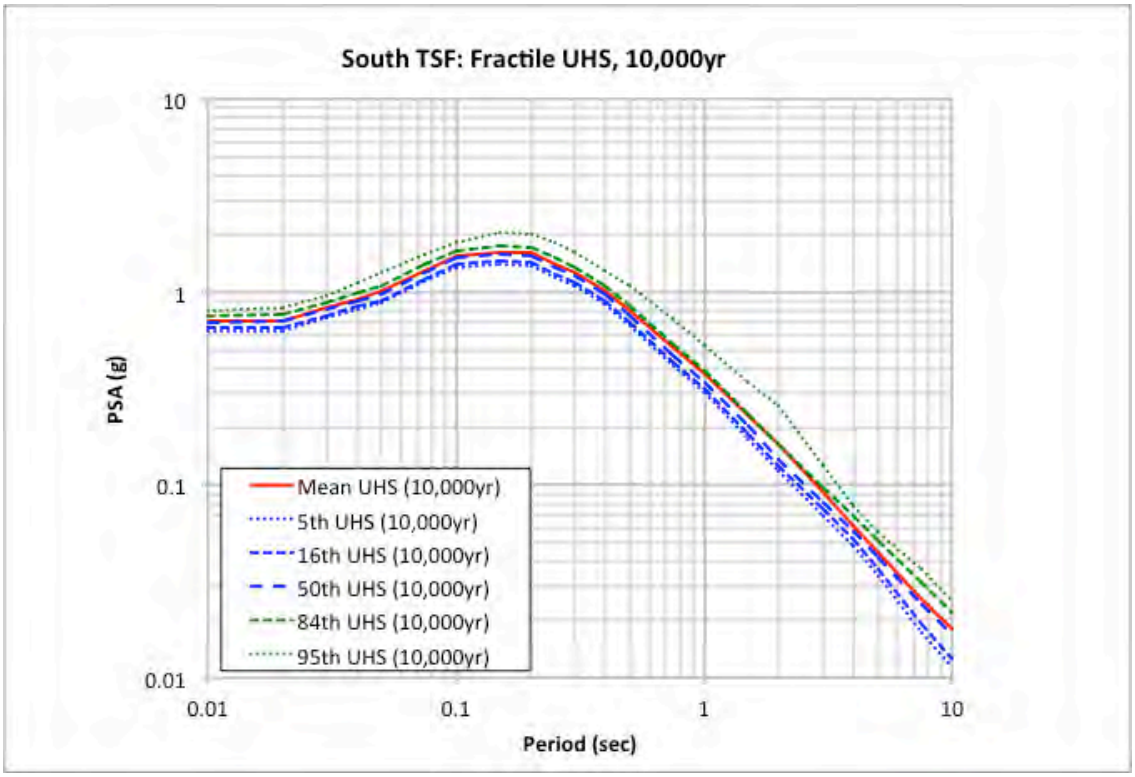

(b)

Figure 58. Fractile UHS for the South TSF site location for 10,000-yr return period hazard level plotted log-linear (a) and log-log (b).

4.5 PSHA Results Summary

Given the close proximity of the three TSF site locations, the calculated ground motions at the three sites are expected to be well within the uncertainty of any PSHA calculation. Individual results are given in Table 7 (Main TSF), Table 11 (Pyritic TSF) and Table 14 (South TSF) for the suite of five return period levels. A comparison of these spectra is plotted in Figure 59. The spectral ratio of the UHS from the three site locations relative to the ground motions from the Main TSF location is shown in Figure 60. Given the slightly closer location of the Pyritic TSF site to the controlling seismic sources, these ground motions are larger than the ground motions for the Main TSF site by approximately 3% or less. Thus, the results from the Pyritic TSF site location could be taken as the envelope ground motions for the three sites if the use of the three individual site-specific ground motions is not necessary for future analyses.

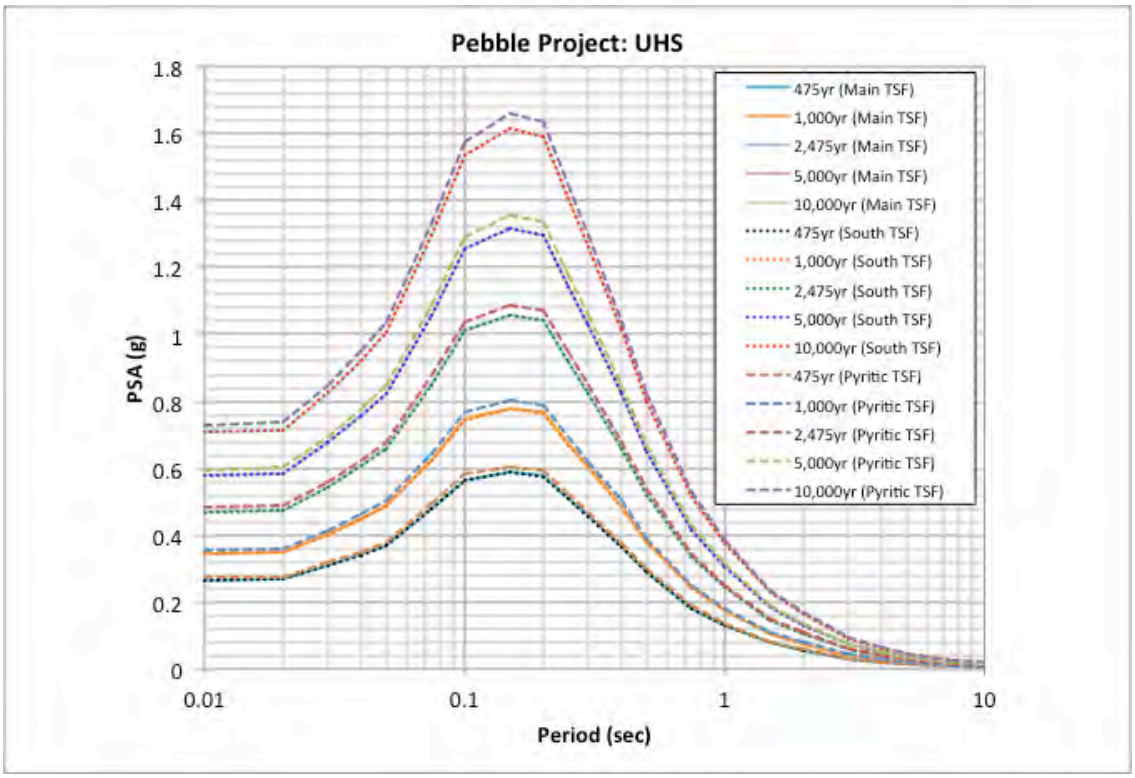

(a)

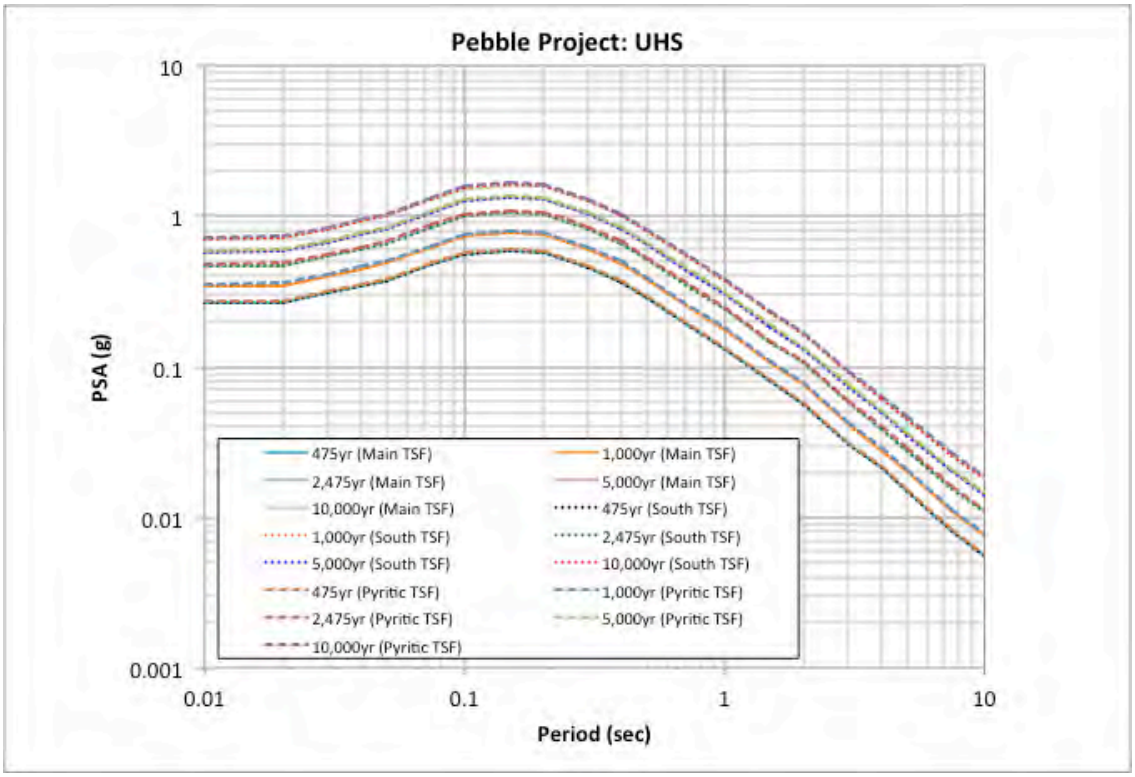

(b)

Figure 59. Comparison of mean UHS for the three site locations plotted log-linear (a) and log-log (b).

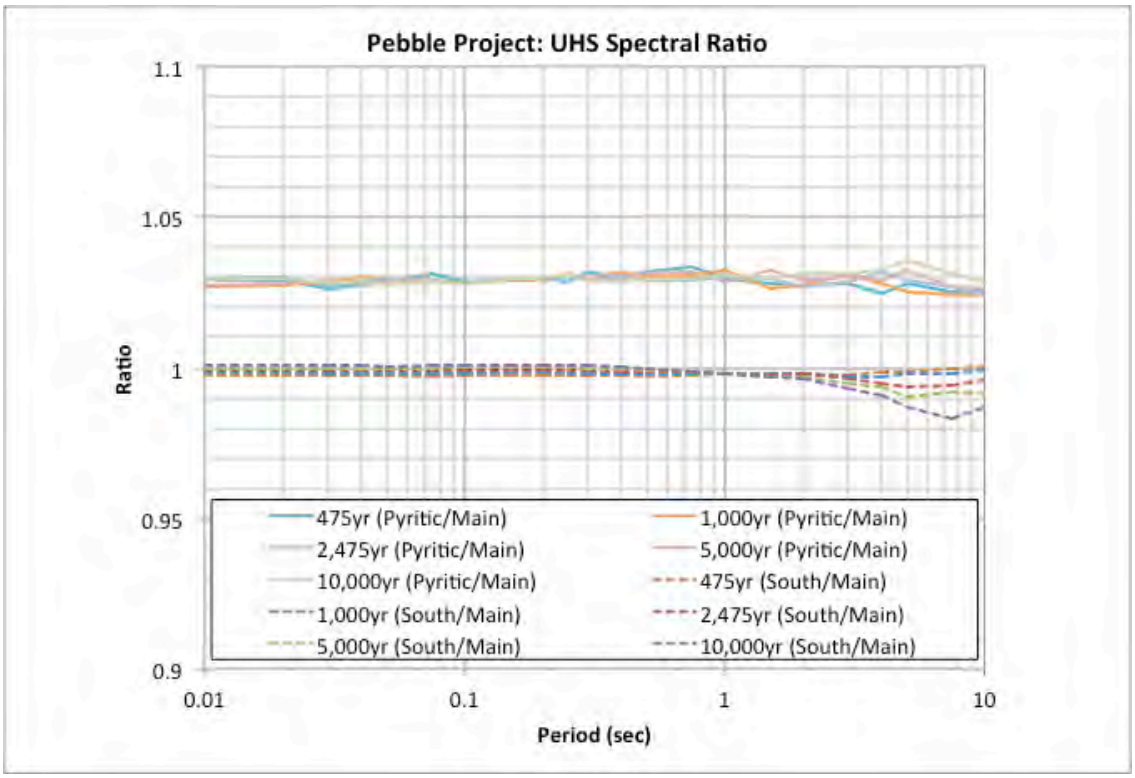

Figure 60. Spectral ratio of UHS from the two TSF site locations relative to the ground motions from the Main TSF site location.

An additional sensitivity analysis is performed to assess the impact of the new NGA-Subduction GMM on the hazard results. UHS are computed for the Main TSF site location using the same SSC model but assigning full weight to the BC Hydro ground-motion model. The same weighting for the crustal events is applied in both calculations. The comparison of the resulting spectra is shown in Figure 61 with the resulting spectral ratio plotted in Figure 62.

These results show that with the inclusion of the new KBCG GMM from the NGA-Subduction program with 15% weight, the resulting ground motions increase on the order of about 15% or less (i.e., spectral ratio of less than 1 in Figure 62). For spectral periods less than about 0.4 sec, the increase is on the order of 5% or less. This is a result of the BCHydro GMM having higher median ground motion estimates but lower aleatory sigma than the KBCG model (e.g., see Figures 22, 23, and 24). For longer spectral periods, the increase is larger, in the 10 – 15% range, with the largest occurring at 2 sec. As noted earlier, this peak difference between the results is driven by the increase from the KBCG GMM for the spectral period of 2 sec.

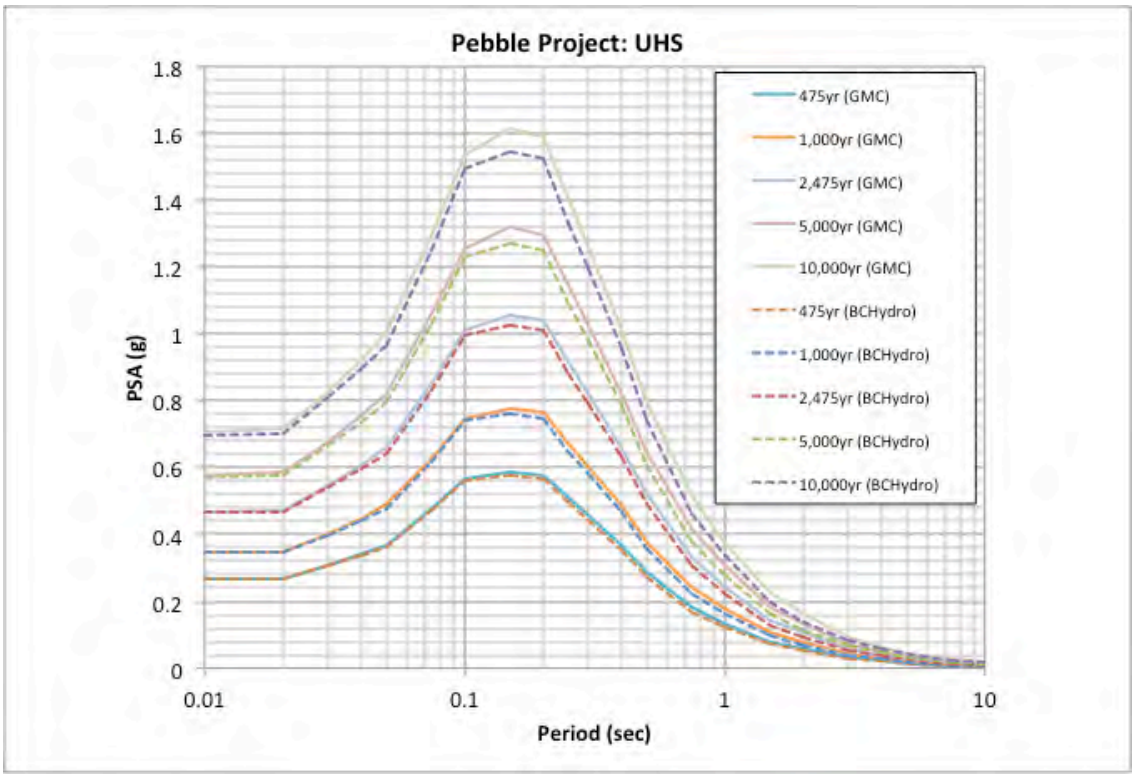

(a)

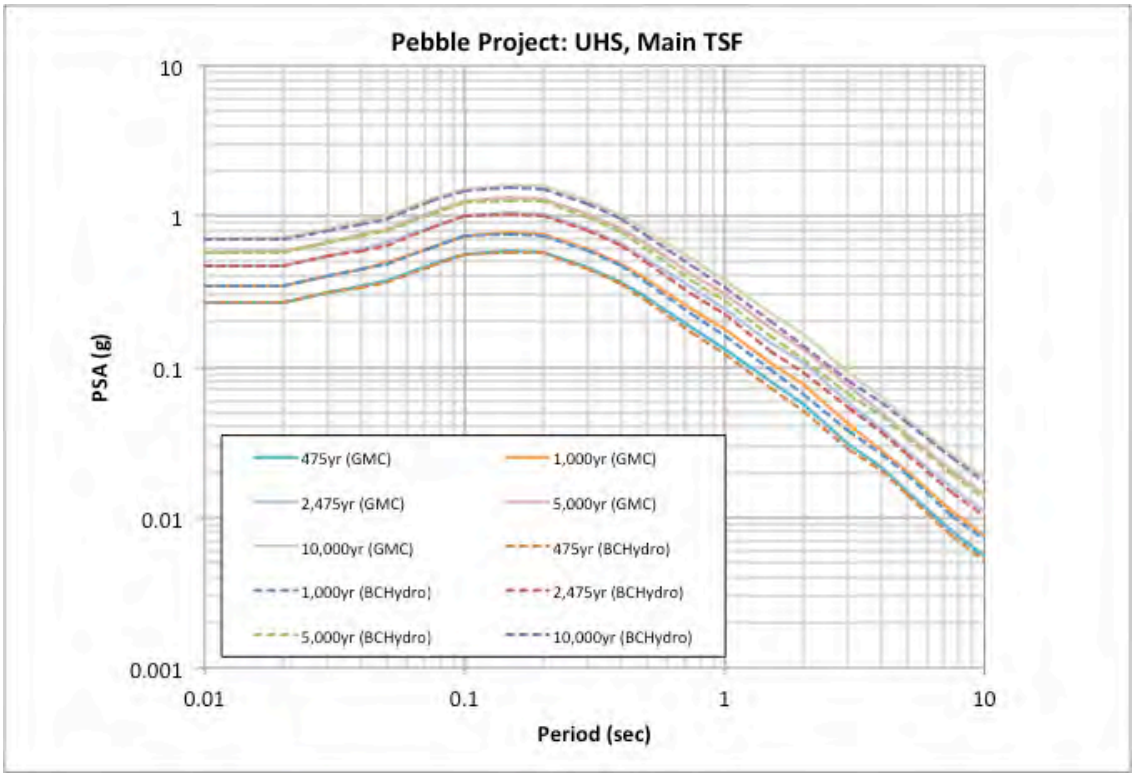

(b)

Figure 61. Comparison of mean UHS for the Main TSF site location only using the BCHydro GMM for the subduction events plotted log-linear (a) and log-log (b).

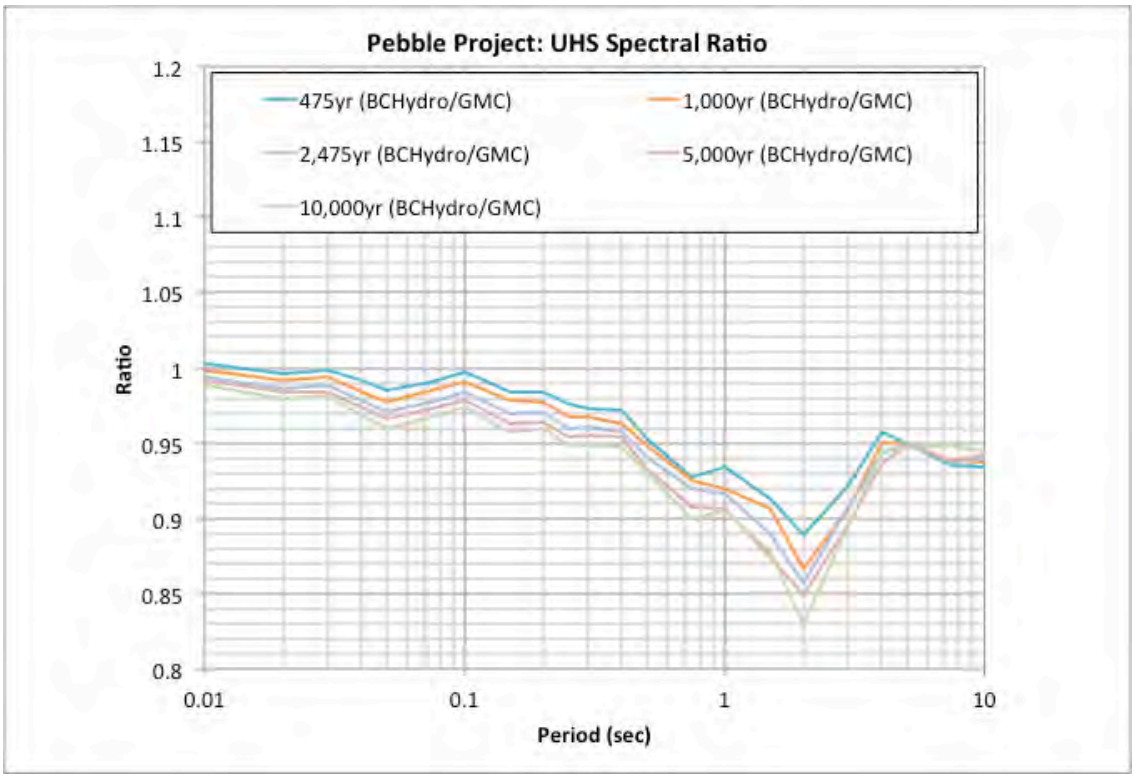

Figure 62. Spectral ratio (UHS with full BCHydro GMM divided by UHS with GMC model) of UHS for the Main TSF site location using only the BCHydro ground-motion model and the full GMC model for subduction events.

Only the PGA ground-motion values from the Knight-Piesold (2013) PSHA study are provided in their report. These values are listed in Table 17 along with the corresponding results from this study and the ratio of the ground motions. As listed, the ratio indicates an increase in the PGA values by a factor of slightly less than 2. Primarily, these observed differences can be attributed to several factors including the difference in ground-motion models and the difference in the slab source modeling used in the PSHA. A more detailed explanation of the causes for these differences is not possible based on the limited documentation provided in the Knight-Piesold (2013) report.

Table 17. Comparison of PGA ground-motion values from the Knight-Piesold (2013) study and this current SHA study.

Rerturn Period (yr)	KP (2013) PGA (g)	Main TSF PGA (g)	Ratio (Current/KP)
475	0.14	0.2653	1.89
1,000	0.19	0.3461	1.82
2,475	0.25	0.4688	1.88
5,000	0.31	0.5790	1.87
10,000	0.38	0.7067	1.86

5. Deterministic Seismic Hazard Analysis (DSHA)

5.1 Methodology

A standard DSHA methodology approach is used for the calculation that is consistent with the SSC and GMC models used in the PSHA. For the DSHA, the largest characteristic magnitude associated with each seismic source is considered along with the closest distance to the project site locations. Both median and 84th percentile ground-motion spectra are computed for the controlling DSHA cases. Specifically, DSHA spectra are computed for the Lake Clark fault, the slab events and the repeat of the 1964 **M**9.2 Great Alaska earthquake. For each of the three site locations, a DSHA calculation is performed given the slightly different distances for each controlling seismic source.

For the Lake Clark fault, the DSHA magnitude is 7.62 with a reverse mechanism. Note that the NGA-West2 GMMs do not differentiate between oblique and reverse mechanism ground motions. All three TSF site locations are identified as being on the hanging wall of the Lake Clark fault and off the end of the fault. Following the FERC recommendations (Idriss et al., 2018), the ground motions for these hanging wall sites are computed not including the two GMMs (i.e., BSSA14 and ID14) that do not explicitly account for the effects of being located on the hanging wall. The remaining three crustal GMMs are assigned equal weights. For the Knight-Piesold (2013) study, a slightly smaller magnitude of 7.5 was used for the DSHA calculation.

For the slab seismic source, ground motions were computed for each of the virtual faults used to represent the down going slab. Given these virtual faults, the median and 84th percentile ground motions are controlled by the slab virtual faults at the depths of 100 and 125 km. For both cases, a maximum magnitude of 8.0 is used based on the SSC model. This is the same DSHA magnitude assigned in the Knight-Piesold (2013) study. For the BCHydro GMM, the recommended maximum hypocentral depth of 120 km is used.

For the interface event, a repeat of the 1964 **M**9.2 Great Alaska earthquake is selected. The distances are computed based on the closest distance to Kodiak segment of the subduction zone. Both the BCHydro and KBCG subduction GMMs contain a magnitude scaling break point where the scaling of ground motion (i.e., increase of ground motions with increasing magnitudes) decreases above the magnitude scaling point leading to an effect of saturation in the estimation of ground motions from large earthquakes. This scenario **M**9.2 event is above the two magnitude scaling break points. For complete saturation, the magnitude scaling above the break point is assumed to be flat (i.e., no increase in ground motions for larger magnitude events). The two empirical models have a reduction in the magnitude scaling but not complete saturation. For the Knight-Piesold (2013) study, a complete saturation maximum magnitude of 8.5, rather than the **M**9.2 associated with this historical event, was used in calculated the DSHA ground motions (i.e., following this approach, the same ground motions would be estimated for a magnitude 8.5 event as a magnitude 9.2 event given the same distance).

5.2 DSHA Results – Main TSF Site Location

For the Main TSF site location, the necessary GMM parameters for the four DSHA scenario cases are listed in Table 18. The same suite of GMMs and their assigned weights that were used for the PSHA are applied for the DSHA calculation. The resulting weighted average median and 84th percentile (i.e., median plus one sigma) response spectra are listed in Table 19 and plotted in Figures 63 and 64. Also for comparison, the UHS for the suite of return periods are plotted in these figures. For spectral periods equal to or less than 2 sec, the controlling DSHA spectra is from the slab events. For longer spectral periods, the Lake Clark spectrum is the controlling event. The median spectra from the slab events is approximately equal to the 475-yr UHS for spectral periods up to 2 sec. At periods beyond 2 sec, the Lake Clark median spectrum increases relative to the UHS return period levels.

For the comparison plot of the 84th percentile spectra, the UHS for return periods of 2,475, 5,000 and 10,000 years are also plotted in Figure 64. The controlling DSHA spectra from the slab events are approximately equal to the 5,000-yr UHS for spectral periods up to 2 sec. For the longer spectral periods, the Lake Clark DSHA spectrum is similar to the 10,000-yr UHS.

Table 18. Event parameters for the DSHA scenario events for the Main TSF site location.

Parameter	Lake Clark Fault	Slab Fault (Depth=100 km)	Slab Fault (Depth=125km)	Interface Event
Magnitude	7.62	8.0	8.0	9.2
Rupture Distance (km)	25.3	138.1	143.4	226.5
R_x Distance (km)	6.38	---	---	---
R_{jb} Distance (km)	24.7	---	---	---
R_{hypo} (km)	---	145.5	152.2	---
Ry0 (km)	23.7	---	---	---
Hypocenter Depth (km)	7.5	110	135[1]	30
Top of Rupture (km)	0	100	125	20
Dip	70	---	---	---
Fault Width (km)	16.0	---	---	---
Hanging Wall/Foot Wall	Hanging Wall	---	---	---
V_{S30} (m/sec)	760	760	760	760
Z_1 (km)	0.034	---	---	---
Z_{25} (km)	0.608	---	---	---
Mechanism	Reverse	Slab	Slab	Interface

[1] Maximum recommended hypocentral depth of 120 km is used for the BCHydro GMM.

DSHA spectra were computed and listed in the Knight-Piesold (2013) report. Spectra were computed for the Lake Clark fault, slab and interface events as well as a maximum background earthquake located directly beneath the site. This background event was assigned a magnitude of 6.5 and assumed to be located directly beneath the project site. The corresponding spectrum

controls the Knight-Piesold (2013) DSHA spectra for periods up to 1.5 sec. At longer spectral periods, the ground motions from the slab sources control the results. The selection of this background event would not be supported based on the deaggregation results from the current PSHA study. Note that given the suite of ground-motion models used in the Knight-Piesold (2013) study, the spectra were only computed up to a spectral period of 3 sec.

A comparison of the 84th percentile DSHA spectra from the Knight-Piesold (2013) study and the DSHA and UHS from this current study is provided in Figure 65. The controlling 84th percentile DSHA spectra from Knight-Piesold (2013) study (i.e., background source event) envelopes the results from this study and is approximately equal to the 5,000-yr UHS for spectral periods less than about 0.2 sec and the 10,000-yr UHS for longer spectral periods. As listed in the Knight-Piesold (2013) report (i.e., see Table 3.3), two slab events are modeled – shallow and deep. The hypocentral depth for these two events are listed as 40 and 80 miles respectively which converts to depths of 64 and 129 km. In addition, the epicentral distances assigned to these two events are 177 and 80 km. These assigned distances and depths are consistent with the general geometry and location of the project site and the typical depths for slab earthquakes.

One critical observation of the Knight-Piesold (2013) results for the slab spectra is that the spectral shapes for the slab and interface events are not consistent with the empirical spectral shape of subduction ground motions given the current empirical database. For the slab events, the unfavorable behavior of the Atkinson and Boore (2003) model for these large magnitude deep earthquakes is contributing to the uncharacteristic spectral shapes. The Atkinson and Boore (2003) model was assigned 50% of the total weight in the Knight-Piesold (2013) study with the other 50% being assigned to the Youngs et al. (1997) model. Similarly the behavior of the Atkinson and Boore (2003) model for the large distance interface event is contributing to observed results with the shift in the spectral peak to longer spectral periods.

Table 19. Median and 84th percentile ground motions from the DSHA scenarios for the Main TSF site location.

Period (sec)	Lake Clark Median (g)	Lake Clark 84th (g)	Slab (D=100km) Median (g)	Slab (D=100km) 84th (g)	Slab (D=125km) Median (g)	Slab (D=125km) 84th (g)	Interface Median (g)	Interface 84th (g)
0.010	0.1775	0.3209	0.2570	0.5403	0.2671	0.5614	0.0724	0.1520
0.020	0.1813	0.3285	0.2587	0.5443	0.2688	0.5651	0.0727	0.1527
0.030	0.2011	0.3675	0.2975	0.6269	0.3087	0.6499	0.0757	0.1593
0.040	0.2291	0.4218	0.3278	0.6922	0.3395	0.7165	0.0777	0.1638
0.050	0.2563	0.4743	0.3516	0.7439	0.3638	0.7690	0.0789	0.1666
0.075	0.3196	0.6013	0.4488	0.9517	0.4638	0.9823	0.0992	0.2099
0.100	0.3553	0.6747	0.5354	1.1356	0.5538	1.1732	0.1222	0.2583
0.150	0.3884	0.7434	0.5720	1.2137	0.5915	1.2533	0.1348	0.2850
0.200	0.3793	0.7284	0.5800	1.2285	0.6009	1.2711	0.1290	0.2725
0.250	0.3507	0.6738	0.5130	1.0851	0.5312	1.1224	0.1156	0.2441
0.300	0.3192	0.6185	0.4622	0.9759	0.4786	1.0097	0.1109	0.2337
0.400	0.2704	0.5282	0.3747	0.7892	0.3879	0.8165	0.0973	0.2047
0.500	0.2315	0.4569	0.2953	0.6213	0.3048	0.6409	0.0793	0.1668
0.750	0.1627	0.3283	0.1884	0.3960	0.1936	0.4067	0.0567	0.1192
1.000	0.1213	0.2471	0.1376	0.2892	0.1409	0.2960	0.0452	0.0951
1.500	0.0797	0.1633	0.0804	0.1693	0.0816	0.1719	0.0305	0.0642
2.000	0.0593	0.1215	0.0556	0.1172	0.0558	0.1177	0.0237	0.0501
3.000	0.0379	0.0773	0.0300	0.0632	0.0295	0.0621	0.0152	0.0322
4.000	0.0277	0.0558	0.0192	0.0403	0.0185	0.0388	0.0119	0.0251
5.000	0.0212	0.0428	0.0125	0.0263	0.0119	0.0248	0.0091	0.0190
7.500	0.0121	0.0246	0.0054	0.0111	0.0049	0.0102	0.0050	0.0104
10.000	0.0079	0.0159	0.0032	0.0067	0.0029	0.0060	0.0037	0.0075

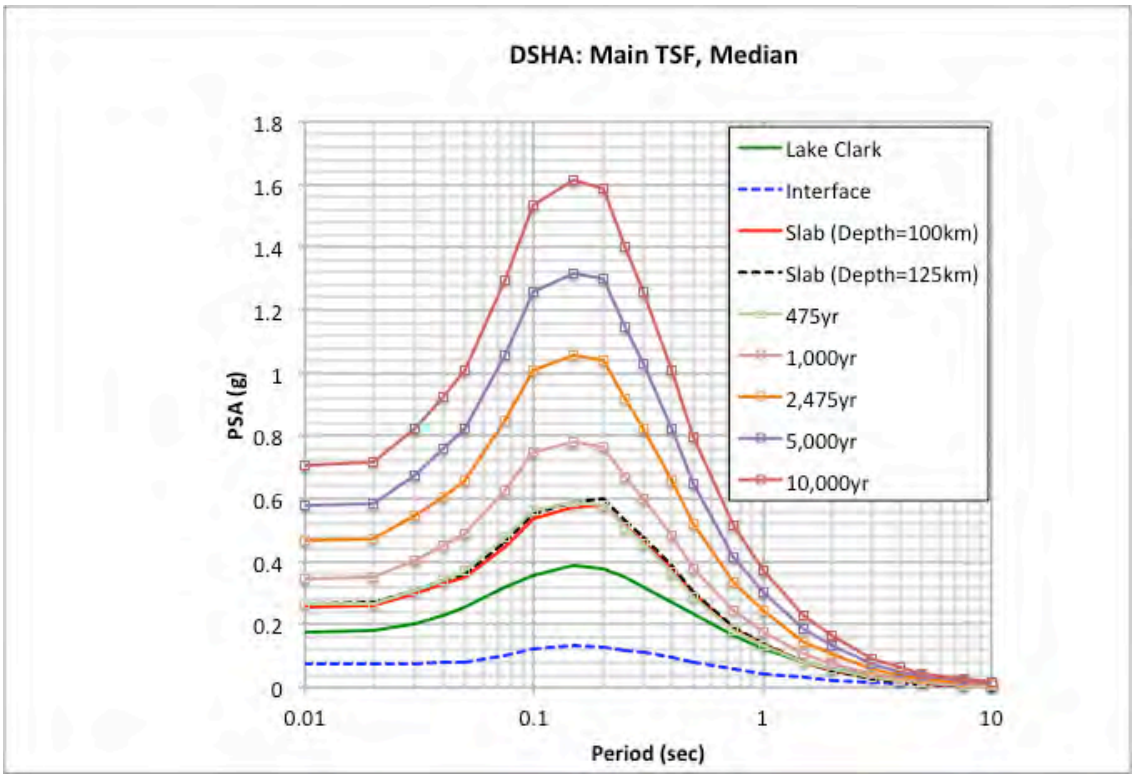

(a)

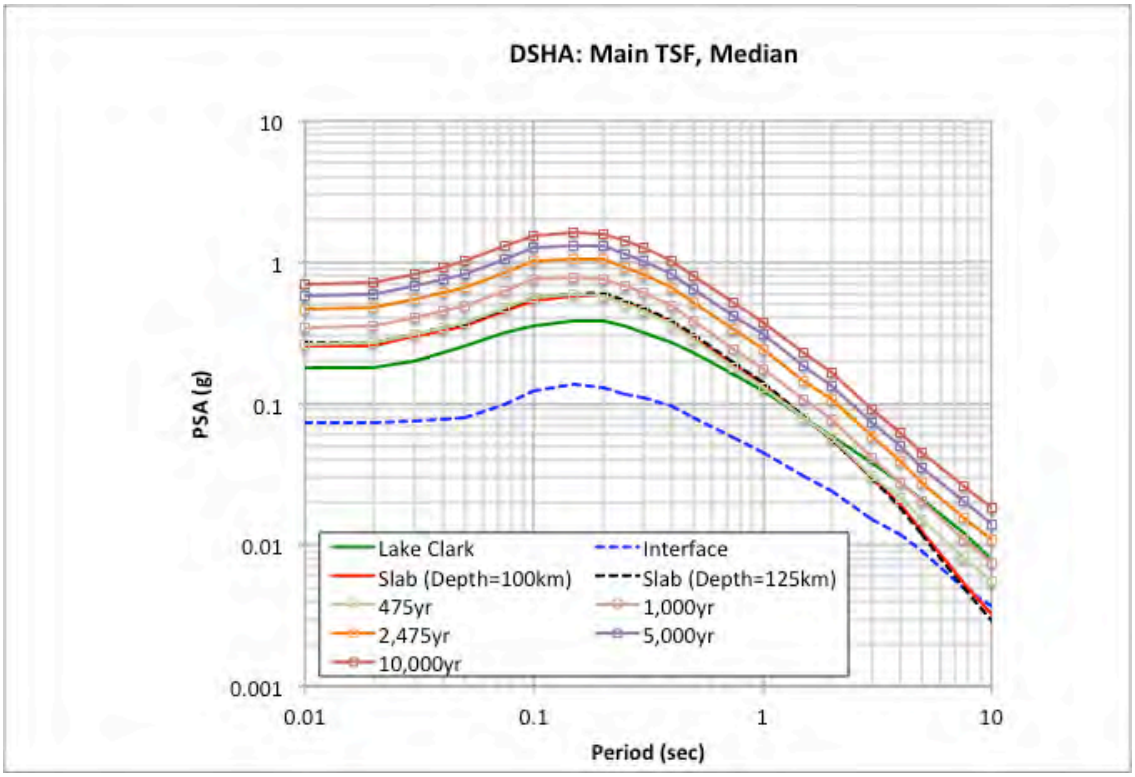

(b)

Figure 63. Median DSHA scenario events (Main TSF) spectra plotted log-linear (a) and log-log (b).

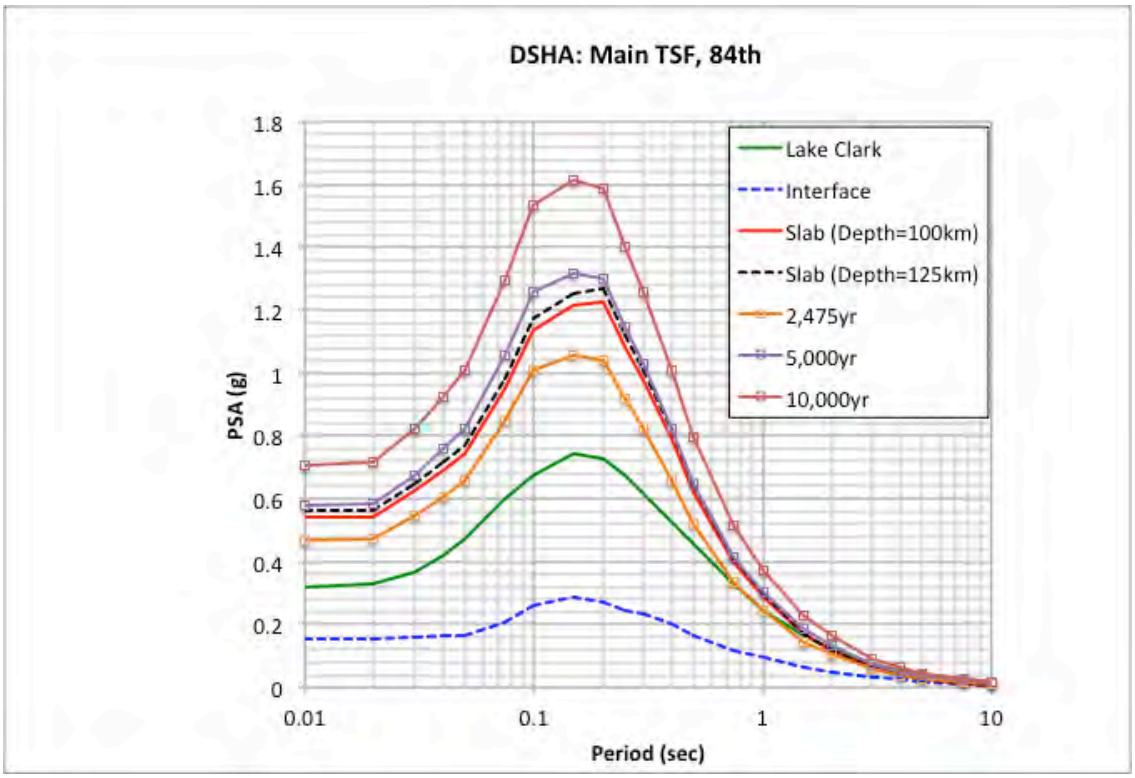

(a)

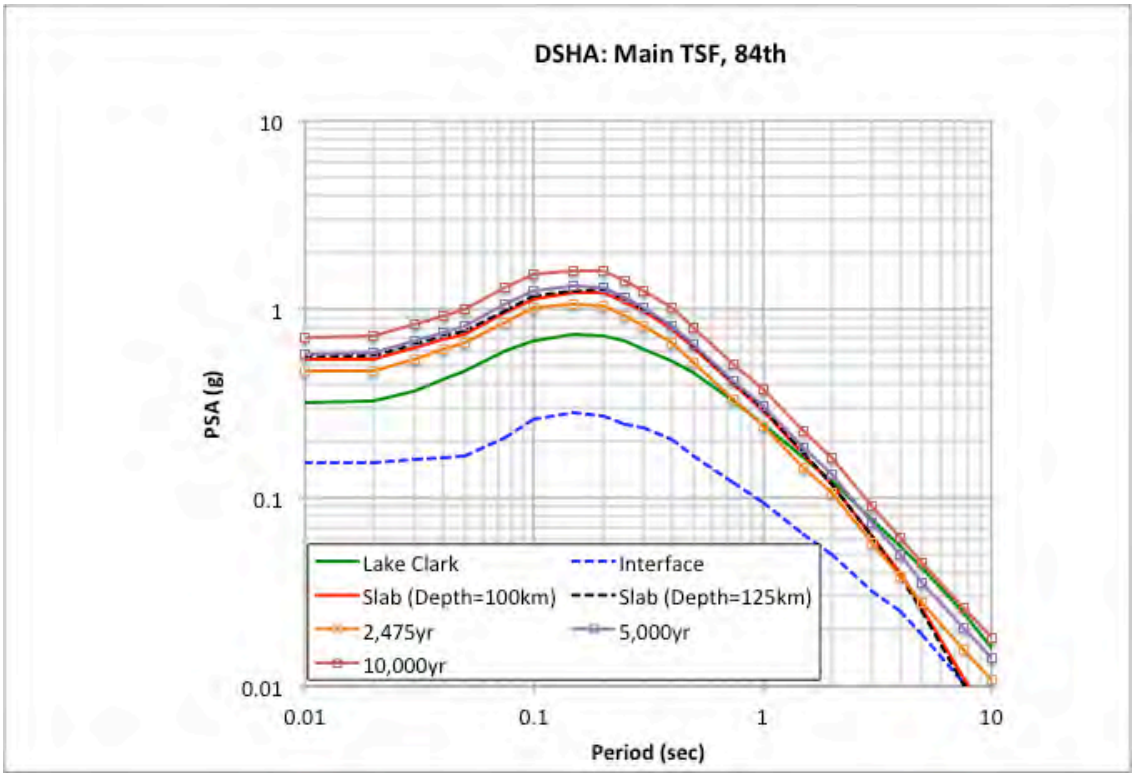

(b)

Figure 64. 84th percentile DSHA scenario events (Main TSF) spectra plotted log-linear (a) and log-log (b).

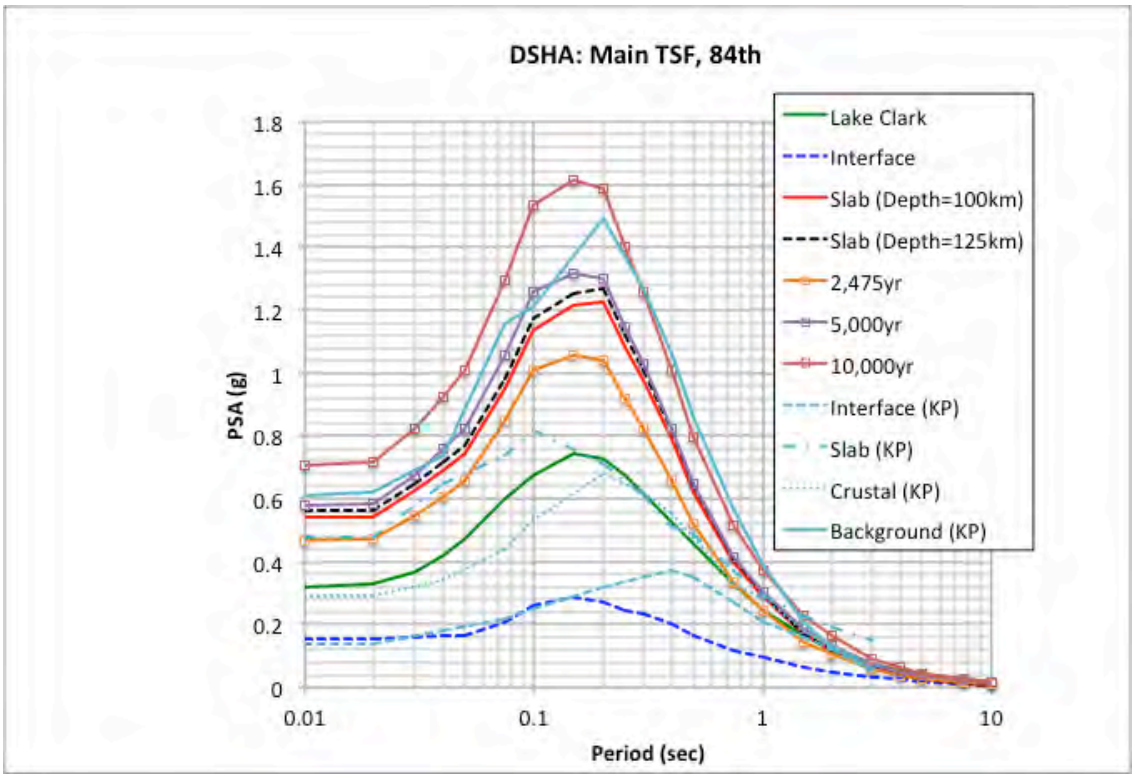

(a)

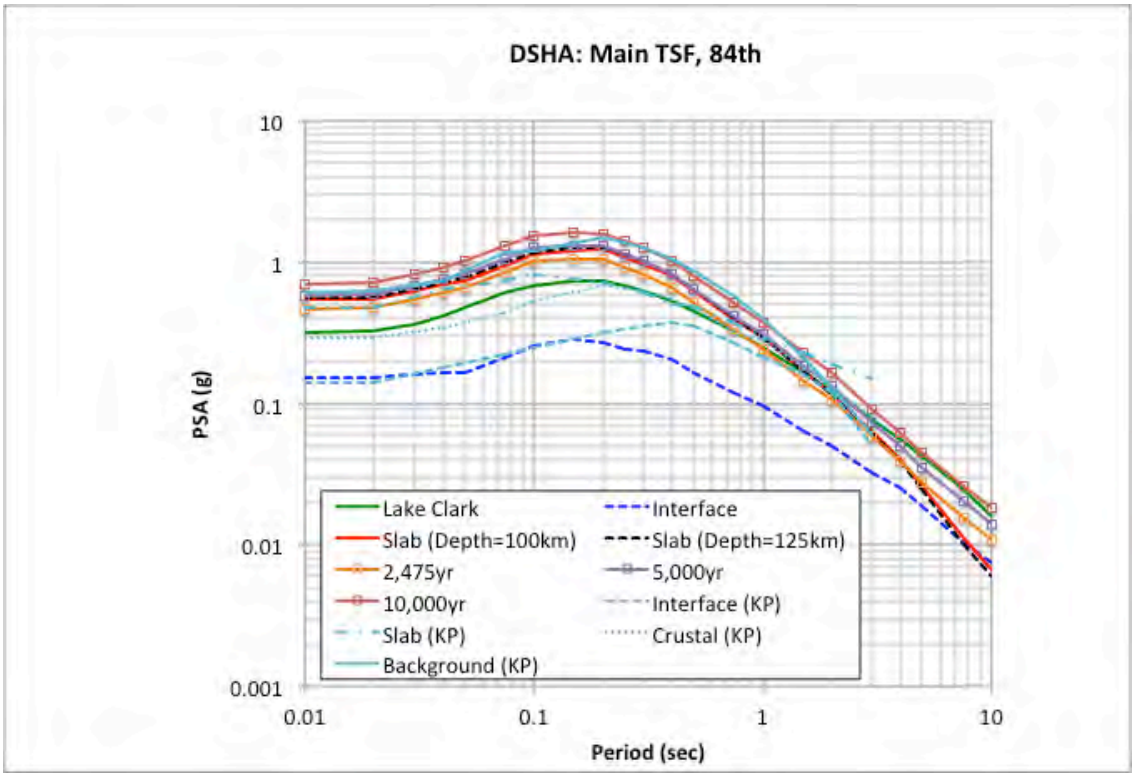

(b)

Figure 65. 84th percentile DSHA scenario events (Main TSF) spectra from the Knight-Piesold (2013) study and the current study plotted log-linear (a) and log-log (b).

5.3 DSHA Results – Pyritic TSF Site Location

For the Pyritic TSF site location, the necessary GMM parameters for the four DSHA scenario cases are listed in Table 20. The same suite of GMMs and their assigned weights that were used for the PSHA are applied for the DSHA calculation. The resulting weighted average median and 84th percentile (i.e., median plus one sigma) ground-motion spectra are listed in Table 21. Given the close proximity of the three TSF locations, these spectral values are similar to the previous results presented for the Main TSF site location. A summary comparison of these 84th percentile spectra for the Pyritic TSF site location from this study and the Knight-Piesold (2013) study is shown in Figure 66 with the UHS for this Pyritic TSF site location. The same observations as noted for the Main TSF site location are applicable to the results for the Pyritic TSF site location.

Table 20. Event parameters for the DSHA scenario events for the Pyritic TSF site location.

Parameter	Lake Clark Fault	Slab Fault (Depth=100 km)	Slab Fault (Depth=125km)	Interface Event
Magnitude	7.62	8.0	8.0	9.2
Rupture Distance (km)	21.8	135.0	141.3	222.1
R_x Distance (km)	2.7	---	---	---
R_{jb} Distance (km)	21.7	---	---	---
R_{hypo} (km)	---	142.6	150.2	---
Ry0 (km)	21.0	---	---	---
Hypocenter Depth (km)	7.5	110	135[1]	30
Top of Rupture (km)	0	100	125	20
Dip	70	---	---	---
Fault Width (km)	16.0	---	---	---
Hanging Wall/Foot Wall	Hanging Wall	---	---	---
V_{S30} (m/sec)	760	760	760	760
Z_1 (km)	0.034	---	---	---
Z_{25} (km)	0.608	---	---	---
Mechanism	Reverse	Slab	Slab	Interface

[1] Maximum recommended hypocentral depth of 120 km is used for the BCHydro GMM.

Table 21. Median and 84th percentile ground motions from the DSHA scenarios for the Pyritic TSF site location.

Period (sec)	Lake Clark Median (g)	Lake Clark 84th (g)	Slab (D=100km) Median (g)	Slab (D=100km) 84th (g)	Slab (D=125km) Median (g)	Slab (D=125km) 84th (g)	Interface Median (g)	Interface 84th (g)
0.010	0.1979	0.3578	0.2658	0.5589	0.2732	0.5741	0.0743	0.1561
0.020	0.2023	0.3664	0.2676	0.5631	0.2749	0.5780	0.0747	0.1569
0.030	0.2246	0.4102	0.3077	0.6484	0.3156	0.6646	0.0778	0.1637
0.040	0.2561	0.4711	0.3389	0.7159	0.3471	0.7326	0.0798	0.1683
0.050	0.2867	0.5302	0.3635	0.7693	0.3719	0.7861	0.0811	0.1713
0.075	0.3586	0.6738	0.4642	0.9845	0.4743	1.0045	0.1021	0.2160
0.100	0.3990	0.7571	0.5538	1.1749	0.5663	1.1998	0.1256	0.2657
0.150	0.4375	0.8371	0.5926	1.2576	0.6055	1.2831	0.1389	0.2936
0.200	0.4267	0.8194	0.6013	1.2736	0.6154	1.3020	0.1330	0.2809
0.250	0.3935	0.7558	0.5317	1.1247	0.5440	1.1494	0.1193	0.2519
0.300	0.3572	0.6920	0.4787	1.0107	0.4899	1.0336	0.1145	0.2413
0.400	0.3023	0.5904	0.3879	0.8170	0.3970	0.8357	0.1006	0.2118
0.500	0.2585	0.5102	0.3057	0.6431	0.3119	0.6559	0.0822	0.1728
0.750	0.1813	0.3657	0.1950	0.4098	0.1980	0.4161	0.0589	0.1238
1.000	0.1355	0.2758	0.1422	0.2990	0.1441	0.3028	0.0469	0.0987
1.500	0.0888	0.1820	0.0829	0.1747	0.0834	0.1756	0.0316	0.0666
2.000	0.0661	0.1354	0.0573	0.1208	0.0570	0.1201	0.0246	0.0519
3.000	0.0423	0.0864	0.0309	0.0651	0.0301	0.0633	0.0158	0.0333
4.000	0.0310	0.0624	0.0197	0.0415	0.0188	0.0395	0.0123	0.0259
5.000	0.0237	0.0479	0.0129	0.0270	0.0121	0.0253	0.0094	0.0196
7.500	0.0134	0.0272	0.0055	0.0114	0.0050	0.0104	0.0052	0.0107
10.000	0.0086	0.0175	0.0033	0.0069	0.0030	0.0061	0.0038	0.0077

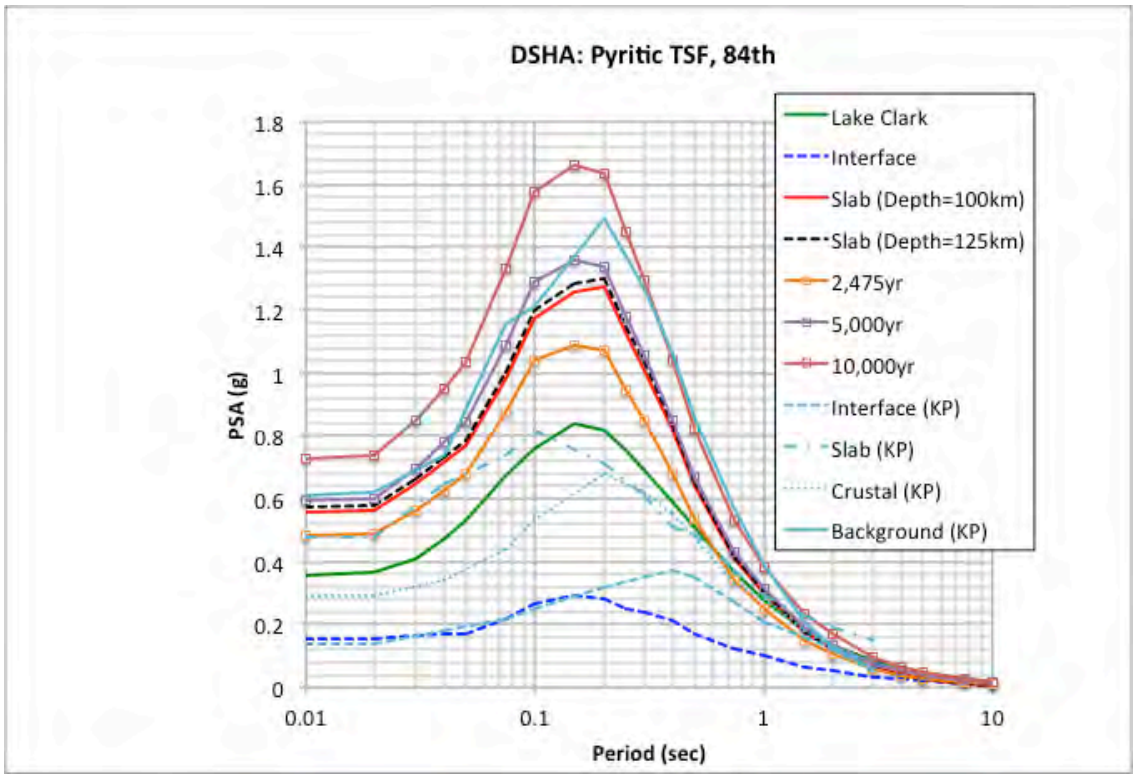

(a)

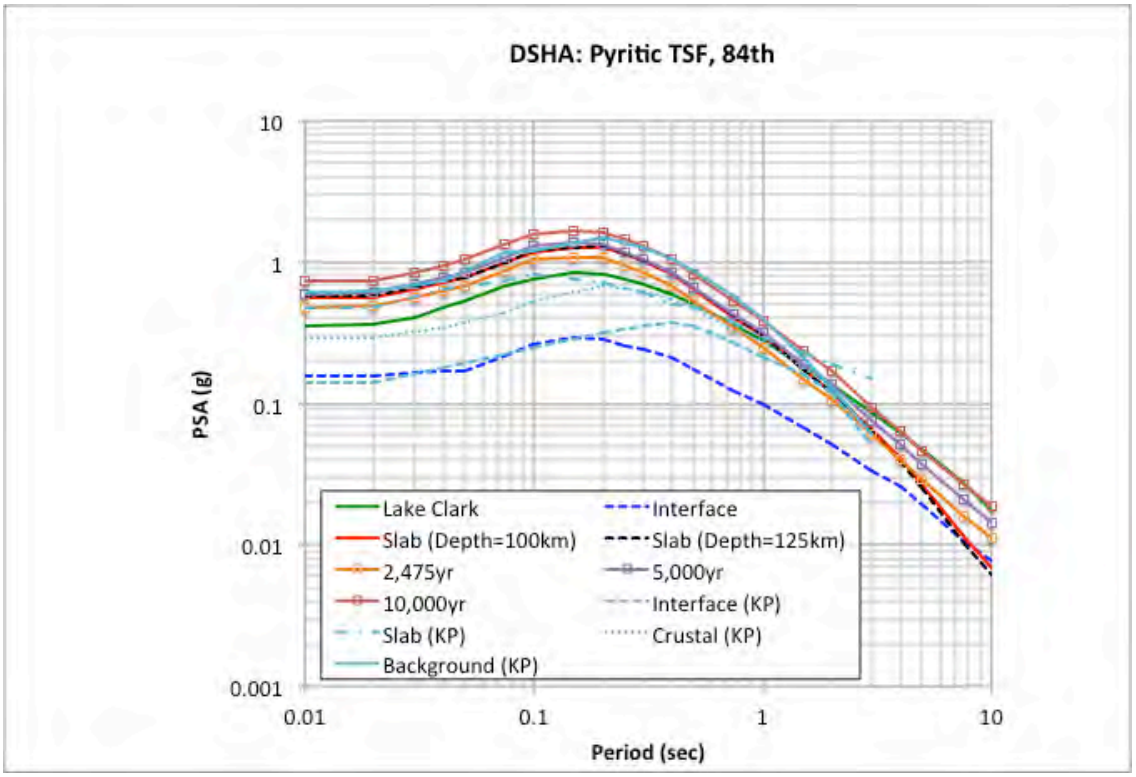

(b)

Figure 66. 84th percentile DSHA scenario events (Pyritic TSF) spectra from the Knight-Piesold (2013) study and the current study plotted log-linear (a) and log-log (b).

5.4 DSHA Results – South TSF Site Location

For the South TSF site location, the necessary GMM parameters for the four DSHA scenario cases are listed in Table 22. The same suite of GMMs and their assigned weights that were used for the PSHA are applied for the DSHA calculation. The resulting weighted average median and 84th percentile (i.e., median plus one sigma) ground-motion spectra are listed in Table 23. Given the close proximity of the three TSF locations, these spectral values are similar to the previous results presented for the Main TSF site location. A summary comparison of these 84th percentile spectra for the South TSF site location from this study and the Knight-Piesold (2013) study is shown in Figure 67 with the UHS for this South TSF site location. The same observations as noted for the Main TSF site location are applicable to the results for the South TSF site location with one exception. For the longer spectral periods (i.e., greater than about 2 seconds), the 84th percentile DSHA spectrum from the Lake Clark fault is approximately equal to the 5,000-yr UHS rather than the 10,000-yr UHS for the other two sites. This reduction in the comparison is based on the slightly larger distance for the South TSF site location than the other two TSF site locations from the Lake Clark fault.

Table 22. Event parameters for the DSHA scenario events for the South TSF site location.

Parameter	Lake Clark Fault	Slab Fault (Depth=100 km)	Slab Fault (Depth=125km)	Interface Event
Magnitude	7.62	8.0	8.0	9.2
Rupture Distance (km)	30.8	136.7	142.2	224.9
R_x Distance (km)	1.8	---	---	---
R_{jb} Distance (km)	30.8	---	---	---
R_{hypo} (km)	---	144.2	151.1	---
Ry0 (km)	30.0	---	---	---
Hypocenter Depth (km)	7.5	110	135[1]	30
Top of Rupture (km)	0	100	125	20
Dip	70	---	---	---
Fault Width (km)	16.0	---	---	---
Hanging Wall/Foot Wall	Hanging Wall	---	---	---
V_{S30} (m/sec)	760	760	760	760
Z_1 (km)	0.034	---	---	---
Z_{25} (km)	0.608	---	---	---
Mechanism	Reverse	Slab	Slab	Interface

[1] Maximum recommended hypocentral depth of 120 km is used for the BCHydro GMM.

Table 23. Median and 84th percentile ground motions from the DSHA scenarios for the South TSF site location.

Period (sec)	Lake Clark Median (g)	Lake Clark 84th (g)	Slab (D=100km) Median (g)	Slab (D=100km) 84th (g)	Slab (D=125km) Median (g)	Slab (D=125km) 84th (g)	Interface Median (g)	Interface 84th (g)
0.010	0.1504	0.2721	0.2609	0.5485	0.2704	0.5684	0.0646	0.1381
0.020	0.1535	0.2783	0.2627	0.5526	0.2722	0.5722	0.0651	0.1395
0.030	0.1700	0.3107	0.3020	0.6364	0.3125	0.6580	0.0676	0.1452
0.040	0.1932	0.3560	0.3327	0.7027	0.3437	0.7253	0.0694	0.1501
0.050	0.2156	0.3996	0.3568	0.7552	0.3682	0.7783	0.0709	0.1545
0.075	0.2678	0.5045	0.4556	0.9663	0.4696	0.9945	0.0879	0.1929
0.100	0.2971	0.5650	0.5435	1.1530	0.5607	1.1878	0.1059	0.2315
0.150	0.3239	0.6204	0.5812	1.2332	0.5992	1.2697	0.1180	0.2568
0.200	0.3171	0.6093	0.5895	1.2485	0.6088	1.2880	0.1158	0.2516
0.250	0.2948	0.5667	0.5213	1.1026	0.5382	1.1372	0.1064	0.2315
0.300	0.2694	0.5222	0.4695	0.9914	0.4848	1.0229	0.1036	0.2246
0.400	0.2288	0.4472	0.3806	0.8016	0.3929	0.8270	0.0925	0.1996
0.500	0.1964	0.3878	0.2999	0.6309	0.3087	0.6491	0.0774	0.1667
0.750	0.1387	0.2799	0.1913	0.4021	0.1961	0.4119	0.0576	0.1244
1.000	0.1033	0.2104	0.1397	0.2936	0.1426	0.2998	0.0464	0.0998
1.500	0.0681	0.1397	0.0815	0.1717	0.0826	0.1739	0.0324	0.0698
2.000	0.0508	0.1040	0.0563	0.1188	0.0564	0.1190	0.0257	0.0554
3.000	0.0325	0.0663	0.0304	0.0641	0.0298	0.0628	0.0164	0.0352
4.000	0.0238	0.0478	0.0194	0.0408	0.0187	0.0392	0.0126	0.0267
5.000	0.0182	0.0367	0.0127	0.0266	0.0120	0.0251	0.0096	0.0203
7.500	0.0106	0.0214	0.0054	0.0112	0.0050	0.0103	0.0055	0.0114
10.000	0.0069	0.0141	0.0033	0.0068	0.0029	0.0061	0.0040	0.0080

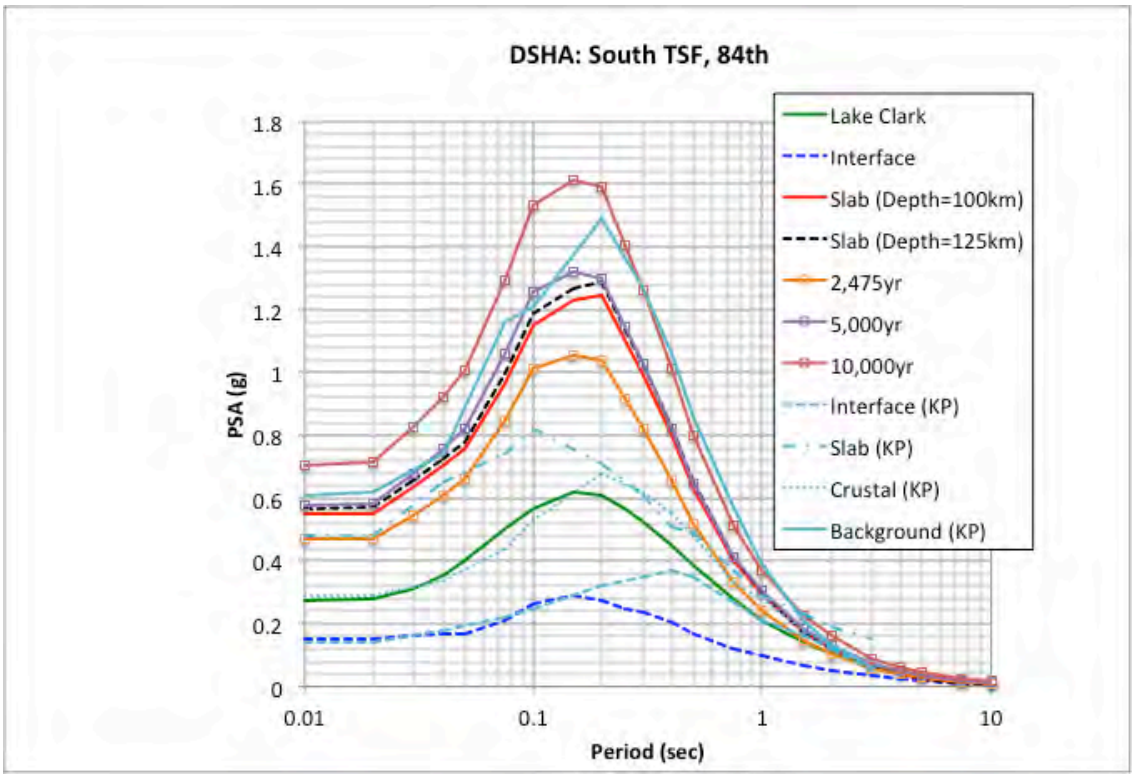

(a)

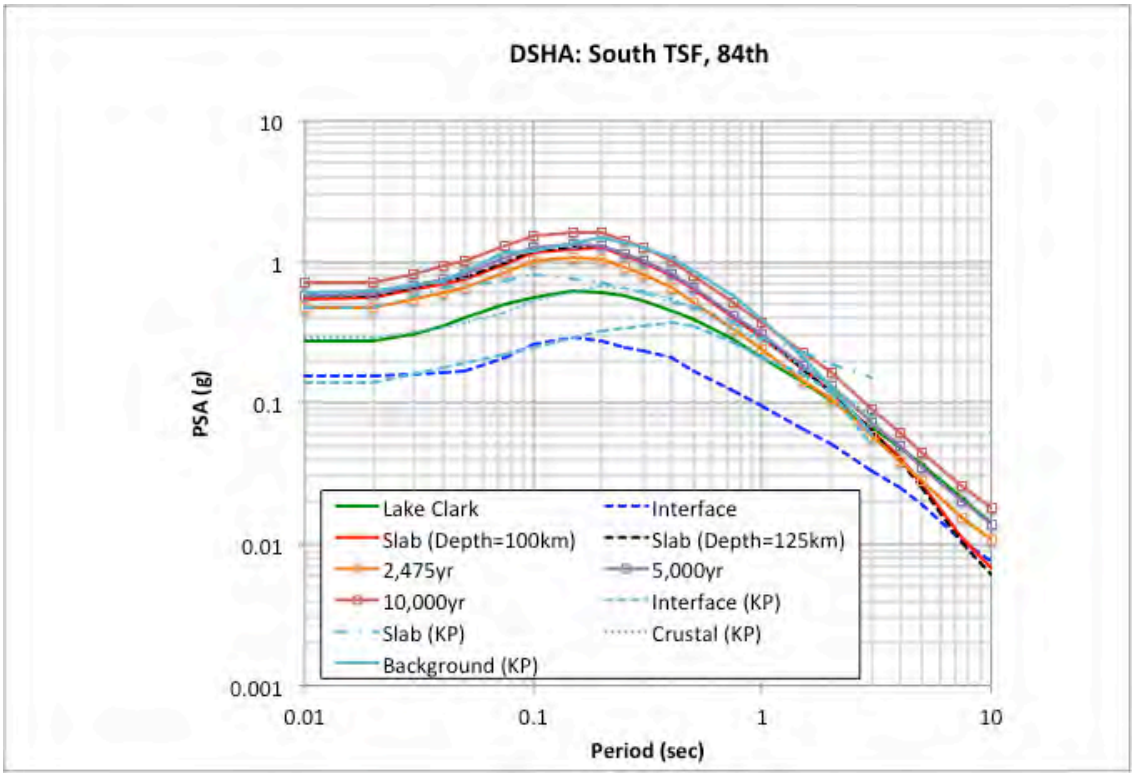

(b)

Figure 67. 84th percentile DSHA scenario events (South TSF) spectra from the Knight-Piesold (2013) study and the current study plotted log-linear (a) and log-log (b).

5.5 DSHA Summary

Given the close proximity of the three TSF site locations, the calculated DSHA are similar with variations for individual scenario events based on the relative distances from each site location to the source. For the controlling slab events, the ground motions from the Pyritic TSF site location are larger than the ground motions at the Main TSF site location by approximately 3% or less. As shown of the Main TSF site location, the 84th percentile DSHA spectra from the controlling slab seismic sources from this study are approximately equal to the 5,000-yr UHS from the PSHA calculations for spectral periods from PGA to approximately 1 sec. For longer spectral periods, the slab spectra falls closer to the 2,475-yr UHS and the deterministic spectra from the Lake Clark fault exceeds the slab spectra and is approximately equal to the 10,000-yr UHS for the Main and Pyritic TSF site locations and the 5,000-yr UHS for the South TSF site location.

The enveloping DSHA 84th percentile spectrum from this study is lower than the controlling DSHA 84th percentile spectrum from the Knight-Piesold (2013) study which was based on a background **M**6.5 event directly at the site location. The background event 84th percentile spectral ground-motion values from the Knight-Piesold (2013) study are more similar to the 5,000-yr UHS from this current study for spectral periods up to about 0.15 sec and closer to the 10,000-yr UHS for spectral periods greater than 0.2 sec and less than 1.5 sec. For longer spectral periods, the slab 84th percentile spectrum from the Knight-Piesold (2013) study is similar to the 10,000-yr UHS from this study.

In comparing the reported 84th percentile PGA value from the slab source between the results of this study and the values provided in the Knight-Piesold (2013) report (i.e., 0.48g), the current PGA value is greater by about 15%. For intermediate periods, this difference increases to about 80% peaking about 0.2 sec and then reduces to about 2% at 1 sec. For longer spectral periods, the ground-motion values from this current study are lower than the values from the Knight-Piesold (2013) report, and as discussed earlier, these observed differences are expected to primarily be a result from the different ground-motion models and their respective modeling features. The two subduction GMMs used in this study are consistent in their empirical shapes with modern empirical databases from subduction events.

Similar to the results from the PSHA, the results from the Pyritic TSF site location could be taken as the envelop ground motions for the three sites if the use of the three individual site-specific ground motions is not necessary for future analyses.

6. Summary and Conclusions

A SHA study is performed for three TSF site locations for the Pebble Mine project in Southwest Alaska. Both PSHA and DSHA studies are performed using approaches and methodologies consistent with the international state of practice. As part of this SHA study, a regional SSC model is developed based on published literature and previous SHA studies that have been performed in Southwestern Alaska. This SSC model represents an update given more current information than the model implemented in the previous Knight-Piesold (2013) study and the USGS regional seismic hazard map for Alaska (Wesson et al., 2007, 2008). As part of this update, an evaluation of the recent seismicity since 2004 is captured and incorporated into the SSC model. No site-specific geologic mapping was conducted as part of this study and if potential seismic sources in the project region are identified and characterized in the future, the hazard results and response spectra presented in this study should be re-evaluated.

In addition to the update of the SSC model, the GMC model is updated to include more current GMMs than were used in the previous studies. These newer models are incorporated for both crustal and subduction seismic events. All of the ground-motion results presented in this study are for the assumed reference site conditions with a V_{S30} value of 760 m/sec. The resulting 475-yr, 5,000-yr and 10,000-yr UHS and the envelop of the two controlling slab events (i.e., depths of 100 and 125 km) median and 84^{th} percentile deterministic spectra are listed in Table 24 for the Main TSF site location. The results for the Pyritic TSF and South TSF site locations are listed in Tables 25 and 26. Before application of these computed ground-motion results as design spectra, the site conditions at the Pebble Mine project sites should be determined and the hazard results adjusted to the site-specific site condition if needed. Commonly, this is performed through the use of analytical site response modeling and should follow a standard state of practice in its methodology and application.

Table 24. PSHA UHS and controlling slab 84th percentile spectra for the reference site conditions of V_{S30} = 760 m/sec for the Main TSF site location.

Period (sec)	475-yr UHS (g)	5,000-yr UHS (g)	10,000-yr UHS (g)	Slab, Median (g)	Slab, 84th (g)
0.010	0.2653	0.5790	0.7067	0.2671	0.5614
0.020	0.2673	0.5849	0.7148	0.2688	0.5651
0.030	0.3089	0.6757	0.8248	0.3087	0.6499
0.040	0.3417	0.7586	0.9237	0.3395	0.7165
0.050	0.3695	0.8234	1.0084	0.3638	0.7690
0.075	0.4776	1.0591	1.2955	0.4638	0.9823
0.100	0.5653	1.2561	1.5334	0.5538	1.1732
0.150	0.5880	1.3186	1.6132	0.5915	1.2533
0.200	0.5771	1.2983	1.5889	0.6009	1.2711
0.250	0.5100	1.1442	1.4040	0.5312	1.1224
0.300	0.4563	1.0279	1.2603	0.4786	1.0097
0.400	0.3649	0.8235	1.0108	0.3879	0.8165
0.500	0.2882	0.6486	0.7989	0.3048	0.6409
0.750	0.1817	0.4151	0.5148	0.1936	0.4067
1.000	0.1310	0.3051	0.3724	0.1409	0.2960
1.500	0.0799	0.1839	0.2276	0.0816	0.1719
2.000	0.0567	0.1319	0.1641	0.0558	0.1177
3.000	0.0307	0.0737	0.0910	0.0300	0.0632
4.000	0.0213	0.0500	0.0616	0.0192	0.0403
5.000	0.0150	0.0355	0.0450	0.0125	0.0263
7.500	0.0080	0.0204	0.0261	0.0054	0.0111
10.000	0.0055	0.0141	0.0182	0.0032	0.0067

Table 25. PSHA UHS and controlling slab 84th percentile spectra for the reference site conditions of V_{S30} = 760 m/sec for the Pyritic TSF site location.

Period (sec)	475-yr UHS (g)	5,000-yr UHS (g)	10,000-yr UHS (g)	Slab, Median (g)	Slab, 84th (g)
0.010	0.2729	0.5949	0.7273	0.2732	0.5741
0.020	0.2751	0.6011	0.7360	0.2749	0.5780
0.030	0.3171	0.6954	0.8477	0.3156	0.6646
0.040	0.3511	0.7795	0.9507	0.3471	0.7326
0.050	0.3800	0.8467	1.0358	0.3719	0.7861
0.075	0.4925	1.0892	1.3323	0.4743	1.0045
0.100	0.5813	1.2913	1.5760	0.5663	1.1998
0.150	0.6054	1.3578	1.6607	0.6055	1.2831
0.200	0.5942	1.3368	1.6357	0.6154	1.3020
0.250	0.5245	1.1792	1.4470	0.5440	1.1494
0.300	0.4708	1.0580	1.2972	0.4899	1.0336
0.400	0.3756	0.8479	1.0396	0.3970	0.8357
0.500	0.2974	0.6688	0.8228	0.3119	0.6559
0.750	0.1878	0.4283	0.5300	0.1980	0.4161
1.000	0.1349	0.3137	0.3838	0.1441	0.3028
1.500	0.0821	0.1898	0.2344	0.0834	0.1756
2.000	0.0583	0.1357	0.1693	0.0573	0.1208
3.000	0.0316	0.0759	0.0939	0.0309	0.0651
4.000	0.0218	0.0515	0.0636	0.0197	0.0415
5.000	0.0154	0.0366	0.0466	0.0129	0.0270
7.500	0.0082	0.0209	0.0269	0.0055	0.0114
10.000	0.0056	0.0145	0.0187	0.0033	0.0069

Table 26. PSHA UHS and controlling slab 84th percentile spectra for the reference site conditions of V_{S30} = 760 m/sec for the South TSF site location.

Period (sec)	475-yr UHS (g)	5,000-yr UHS (g)	10,000-yr UHS (g)	Slab, Median (g)	Slab, 84th (g)
0.010	0.2646	0.5790	0.7072	0.2704	0.5684
0.020	0.2667	0.5849	0.7153	0.2722	0.5722
0.030	0.3082	0.6756	0.8254	0.3125	0.6580
0.040	0.3409	0.7585	0.9243	0.3437	0.7253
0.050	0.3686	0.8233	1.0089	0.3682	0.7783
0.075	0.4762	1.0590	1.2963	0.4696	0.9945
0.100	0.5639	1.2561	1.5343	0.5607	1.1878
0.150	0.5866	1.3188	1.6145	0.5992	1.2697
0.200	0.5757	1.2985	1.5904	0.6088	1.2880
0.250	0.5088	1.1443	1.4051	0.5382	1.1372
0.300	0.4551	1.0277	1.2610	0.4848	1.0229
0.400	0.3640	0.8231	1.0108	0.3929	0.8270
0.500	0.2873	0.6480	0.7985	0.3087	0.6491
0.750	0.1812	0.4145	0.5142	0.1961	0.4119
1.000	0.1307	0.3045	0.3717	0.1426	0.2998
1.500	0.0797	0.1833	0.2269	0.0826	0.1739
2.000	0.0566	0.1315	0.1635	0.0564	0.1190
3.000	0.0306	0.0733	0.0904	0.0304	0.0641
4.000	0.0213	0.0497	0.0611	0.0194	0.0408
5.000	0.0150	0.0351	0.0444	0.0127	0.0266
7.500	0.0080	0.0202	0.0256	0.0054	0.0112
10.000	0.0055	0.0140	0.0180	0.0033	0.0068

Based on the close proximity of the three site locations, the resulting ground-motion spectra are similar with the results from the Pyritic TSF site location being slightly higher given its closer distance to the controlling seismic sources. The observed differences are within the uncertainty of the ground-motion calculations. If a single representative set of PSHA and DSHA ground motions are requested from the project for analyses in the Pebble Mine project are, the results from Pyritic TSF site can be selected as representative for the ground motions given their enveloping level when compared to the results from the other two sites. If however, more site-specific analyses are requested for the three TSF site locations, the specific results provided in this report can be used.

7. References

Abers, G.A. and M.E. Mann (2018). Earth Structure Effects on Wave Propagation of the Damaging 2016 M7.1 Iniskin Alaska Earthquake and other in-slab Earthquakes, Final Technical Report, USGS NEHRP award G17AP00065.

Abrahamson, N.A. (2018). Seismic Hazard Software HAZ45.2, Piedmont, California.

Abrahamson, N.A., N. Gregor and K. Addo (2016). BC Hydro Ground Motion Prediction Equations for Subduction Earthquakes, Earthquake Spectra, Vol. 32, No. 1, p. 23-44.

Abrahamson, N.A., Silva, W.J., and R. Kamai (2014). Summary of the ASK14 ground motion relation for active crustal regions, Earthquake Spectra, Vol. 30, No. 3, p. 1025-1055.

Ancheta, T.D., Darragh, R.B., Stewart, J.P., Seyhan, E., Silva, W.J., Chiou, B.S.-J., Wooddell, K.E., Graves, R.W., Kottke, A.R., Boore, D.M., Kishida, T., and Donahue, J.L. (2014). NGA-West2 database, Earthquake Spectra, Vol. 30, No. 3, p. 989–1005.

Al Atik, L. and R.R. Youngs (2014). Epistemic uncertainty for NGA-West2 Models. Earthquake Spectra, Vol. 30, No. 3, p. 1301-1318.

Amato, J.M., M.J. Bogar, G.E. Gehrels, G.L. Farmer and W.C. McIntosh (2007). The Tlikakila complex in southern Alaska: A suprasubduction-zone ophiolite between the Wrangellia Composite Terrane and North America, Geological Society of America, Special Paper 431.

Atkinson, G.M., and Boore, D.M. (2003). Empirical ground-motion relationships for subduction-zone earthquakes and their application to Cascadia and other regions, Bull. Seism. Soc. Am., Vol. 93, p. 1703–1729.

Atkinson, G.M., and Boore, D.M. (2008). Erratum to empirical ground-motion relationships for subduction-zone earthquakes and their application to Cascadia and other regions, Bull. Seism. Soc. Am., Vol. 98, p. 2567–2569.

Barnes, F.F. (1966). Geology and coal resources of the Beluga–Yentna region, Alaska: U.S. Geological Survey Bulletin 1202-C, 54 p., 2 sheets, scale 1:250,000 and 1:63,360.

Bazzurro, P., and C. A. Cornell (1999). Disaggregation of seismic hazard, Bull. Seism. Soc. Am., Vol. 89, p. 501–520.

BC Hydro (2012). Probalistic Seismic Hazard Analysis (PSHA) Model, Engineering Report E658, November, 2012.

Betka, P.M., R.J. Gillis and J.A. Benowitz (2017). Cenozoic sinistral transpression and polyphase slip within the Bruin Bay fault system, Iniskin-Tuxedni region, Cook Inlet, Alaska, Geosphere, Vol. 13, No. 6, p. 1806-1813.

Boore, D.M. (2010). Orientation-independent, non geometric-mean measures of seismic intensity from two horizontal components of motion, Bull. Seism. Soc. Am., Vol. 100, pp. 1830-1835.

Boore, D.M, Stewart, J.P., Seyhan, E. and G.M. Atkinson (2014). NGA-West2 equations for predicting PGA, PGV, and 5% damped PSA for shallow crustal earthquakes. Earthquake Spectra, Vol. 30, No. 3, p. 1057-1085.

Bozorgnia, Y., N. Abrahamson, L. Al Atik, T. D. Ancheta, G.M. Atkinson, J.W. Baker, A. Baltay, D.M. Boore, K.W. Campbell, B.S-J. Chiou, R. Darragh, S. Day, J. Donahue, R.W. Graves, N. Gregor, T. Hanks, I.M. Idriss, R. Kamai, T. Kishida, A. Kottke, S.A. Mahin, S. Rezaeian, B. Rowshandel, E. Seyhan, S. Shahi, T. Shantz, W. Silva, P. Spudich, J.P. Stewart, J. Watson-Lamprey, K. Wooddell, R. Youngs (2014). NGA-West2 Research Project, Earthquake Spectra, Vol. 30, No. 3, p. 973-987.

Bozorgnia, Y., T. Kishida, N.A. Abrahamson, S.K. Ahdi, T.D. Ancheta, R.J. Archuleta, G. Atkinson, D.M. Boore, K.W. Campbell, B. Chiou, V. Contreras, R. Darragh, N. Gregor, Z. Gulerce, I.M. Idriss, C. Ji, R. Kamai, N. Kuehn, D.Y. Kwak, A. Kwok, P.S. Lin, H. Magistrale, S. Mazzone, S. Muin, S. Midorikawa, G. Parker, H. Si, W.J. Silva, J.P. Stewart, M. Walling, K.E. Wooddell, and R.R. Youngs (2018). NGA-Subduction Research Program, Proceedings of the 11th US National Conference on Earthquake Engineering, Paper 001705, Los Angeles, CA.

Bozorgnia, Y. and J. P. Stewart (2020). Data Resources for NGA-Subduction Project, PEER Report 2020/02.

Campbell, K.W. (2020). Proposed Methodology for Estimating the Magnitude at Which Subduction Megathrust Ground Motions and Source Dimensions Exhibit a Break in Magnitude Scaling: Example for 79 Global Subduction Zones, Earthquake Spectra, in press.

Campbell, K.W. and Y. Bozorgnia (2014). NGA-West2 ground motion model for the average horizontal components of PGA, PGV, and 5% damped linear acceleration response spectra. Earthquake Spectra, Vol. 30, No. 3, p. 1087-1115.

Carver, G., J. Sauber, W. Lettis, R. Witter, and B. Whitney (2008). Active Faults on Northeastern Kodiak Island, Alaska, American Geophysical Union, Active Tectonics and Seismic Potential of Alaska, Geophysical Monograph Series 179, p. 167-184.

Chiou, B.S.-J., and R.R. Youngs (2014). Update of the Chiou and Youngs NGA model for the average horizontal component of peak ground motion and response spectra. Earthquake Spectra, Vol. 30, No. 3, p. 1117-1153.

Chiou, B., R. Darragh, N. Gregor and W. Silva (2008). NGA Project Strong-Motion Database, Earthquake Spectra, Vol. 24, No. 1, p. 23-44.

Decker, J., S.C. Bergman, R.B. Blodgett, S.E. Box, T.K. Bundtzen, J.G. Clough, W.L. Coonrad, W.G. Gilbert, M.L. Miller, J.M. Murphy, M.S. Robinson, and W.K. Wallace (1994). Geology of southwestern Alaska, The Geology of North America, Vol. G-1, The Geology of Alaska.

Detterman, R.L.T. Hudson, G. Plakfer, R.G. Tysdal and J.M. Hoare (1976). Reconnaissance Geology Map along Bruin Bay and Lake Clark Faults in Kenai and Tyonek Quadangles, Alaska, USGS Open File Report 76-477.

Detterman, R.L., and Reed, B.L. (1980). Stratigraphy, structure, and economic geology of the Iliamna Quadrangle, Alaska: U.S. Geological Survey Bulletin 1368-B, 86 p.

DeMets, C., Gordon, R.G., Argus, D.F., and Stein, S. (1990). Current plate motions: Geophysical Journal International, v. 101, no. 2, p. 425–478.

Doser, D.I., N.A. Ratchkovski, P.J. Haeussler, and R. Saltus (2004). Changes in Crustal Seismic Deformation Rates Associated with the 1964 Great Alaska Earthquake, Bull. Seism. Soc. Am., Vol. 94, No. 1, p. 320-325.

Earthquake Engineering Research Institute (1989). The basics of seismic risk analysis, Earthquake Spectra, Vol. 5, pp. 675–699.

Elliot, J. and J. Freymueller (2018). Geodetic contributions to the Alaska Hazard Maps: Collaborative Research between the University of Alaska Fairbanks and Purdue University, USGS External Grants, Final Report, https://earthquake.usgs.gov/cfusion/external_grants/reports/G15AP00056.pdf.

Field, E.H, G.P. Biasi, T.E. Dawson, K.R. Felzer, D.D. Jackson, K.M. Johnson, T.H. Jordan, C. Madden, A.J. Michael, K.R. Milner, M.T. Page, T. Parsons, P.M. Powers, B.E. Shaw, W.R. Thatcher, R.J. Weldon and Y. Zeng (2013). Uniform California Earthquake Rupture Forecast, Version 3 (UCERF3) – The Time-Independent Model, USGS Open File Report 2013-1165.

Fugro (2012). Seismic Hazard Characterization and Ground Motion Analyses for the Susitna-Watana Dam Site Area, Report prepared for Alaska Energy Authority, February 24, 2012.

Gardner, J.K. and L. Knopoff (1974). Is the sequence of earthquakes in Southern California with aftershocks removed, Poissonian?, Bull. Seism. Soc. Am., Vol. 64, No. 5, p. 1363-1367.

Gillis, R. J., D.L. LePain, K.D. Ridgway and E.S. Finzel (2009). A reconnaissance view of an unnamed fault near Capps Glacier, northwestern Cook Inlet Basin, and its potential as a regional-scale, basin-controlling structure, State of Alaska Division of Geological and Geophysical Surveys, Preliminary Interpretive Report 2009-03.

Hale, C., N. Abrahamson, and Y. Bozorgnia (2018). Probabilistic Seismic Hazard Analysis Code Verification, PEER Report, Pacific Earthquake Engineering Research Center, University of California, Berkeley, California, PEER Report 2018/03.

Hartstock, J. K. (1954). Geologic map and structure sections of the Iniskin Peninsula and adjacent area of Alaska, U.S. Geological Survey Open File Report 54-118.

Haeussler, P.J., A. Matmon, D.P. Schwartz and G.G. Seitz (2016). Neotectonics of Interior Alaska and the late Quaternary slip rate along the Denali fault system, Geosphere, Vol. 13, No. 5., p. 1445 – 1463.

Haeussler, P.J., Matmon, A., Schwartz, D.P., Seitz, G. (2014). The Denali fault slip rate and models of interior Alaska active deformation [abs.]: Seismological Society of America Annual Meeting, Anchorage, Alaska, April 30–May 2, 2014, Abstracts with Programs, v. 85, no. 2, p. 474.

Haeussler, P.J., Bruhn, R.L., and Pratt, T.L. (2000). Potential seismic hazards and tectonics of the upper Cook Inlet basin, Alaska, based on analysis of Pliocene and younger deformation: Geological Society of America Bulletin, Vol. 112, No. 9, p. 1,414–1,429.

Haeussler, P.J., Best, T.C., and Waythomas, C.F. (2002). Paleo- seismology at high latitudes; seismic disturbance of upper Quaternary deposits along the Castle Mountain Fault near Houston, Alaska: Geological Society of America Bulletin, Vol. 114, No. 10, p. 1296–1310.

Haeussler, P. and R.W. Saltus (2004). 26 km of Offset on the Lake Clark Fault Since Late Eocene Time, U.S. Geological Survey Professional Paper 1709-A.

Haeussler, P. and R.W. Saltus (2011). Location and Extent of Tertiary Structures in Cook Inlet Basin, Alaska, and Mantle Dynamics that Focus Deformation and Subsidence, U.S. Geological Survey, Professional Paper 1776-D.

Hayes, G. (2018). Slab2 – A Comprehensive Subduction Zone Geometry Model, USGS data release, https://doi.org/10.5066/F7PV6JNV.

Idriss, I.M. (2014). An NGA-West2 empirical model for estimating the horizontal spectral values generated by shallow crustal earthquakes. Earthquake Spectra, Vol. 30, No. 3, p. 1155-1177.

Idriss, I.M., R.J. Archuleta, and N.A. Abrahamson (2018). Engineering Guidelines for the Evaluation of Hydropower Projects, Chapter 13 – Evaluation of Earthquake Ground Motions, Federal Energy Regulatory Commission (FERC), Washington D.C..

Ktenidou, O.J. and N. A. Abrahamson (2016). Empirical Estimation of High-Frequency Ground Motion on Hard Rock, Seism. Res. Letters, Vol. 87, No. 6, p. 1465 – 1478.

Knight-Piesold Ltd. (2013). Report on Seismicity Assessment and Seismic Design Parameters, Report prepared for Pebble Limited Partnership, August 14, 2013.

Koehler, R.D. (2010). Technical Review of a Trench Across a Potential Fault Scarp Feature East of Lower Talarik Creek, Lake Iliamna Area, Southwestern Alaska, State of Alaska Division of Geological and Geophysical Surveys, Miscellaneous Publication 139.

Koehler, R.D. and R.D. Reger (2011). Reconnaissance Evaluation of the Lake Clark Fault, Tyonek Area, Alaska, State of Alaska Division of Geological and Geophysical Surveys, Preliminary Interpretive Report 2011-1.

Koehler, R.D., R.E. Farrell, P.A.C. Burns and R.A. Combellick (2012). Quaternary Faults and Folds in Alaska: A Digital Database, State of Alaska Division of Geological and Geophysical Surveys, Miscellaneous Publication 141.

Koehler, R.D., P.A.C. Burns and J.R. Weakland (2013). Digitized Faults of the Neotectonic Map of Alaska (Plafker and Others, 1994), State of Alaska Division of Geological and Geophysical Surveys, Miscellaneous Publication 150.

Koehler, R.D. and G.A. Carver (2018). Active faulting and seismic hazards in Alaska, State of Alaska Division of Geological and Geophysical Surveys, Miscellaneous Publication 160.

Kuehn, N., Y. Bozorgnia, K. Campbell, and N. Gregor (2020). Partially Nonergodic Ground-Motion Model for Subduction Regions using the NGA-Subduction Database PEER Report 2020/XX, in press.

Labay, K. and P.J. Haeussler (2001). GIS Coverages of the Castle Mountain Fault, South Central Alaska, USGS Open File Report 01-504.

McGuire, R.K. (2004). Seismic Hazard and Risk Analysis, Monograph NMO-10, Earthquake Engineering Research Institute, Oakland, California.

Parker, G.A., J.P. Stewart, D.M. Boore, G. Atkinson and B. Hassani (2020). NGA-Subduction Global Ground Motion Models with Regional Adjustment Factors, PEER report 2020/XX, in press.

Parkington, T. (2018). Technical memorandum to Bill Craig, AECOM for the Pebble Project Review of Seismic Hazard Analysis, Letter dated September 17, 2018.

Pavlis, T.L. and S.M. Roeske (2007). The Border Ranges Fault System, Southern Alaska, Geological Society of America, Special Paper 341.

Pebble Partnership (2018). The Pebble Project, Project Description, December 2018.

Plafker, G., R.L. Detterman, and T. Hudson (1975). New Data on Displacement History of the Lake Clark Fault, in Yount, M.E. ed., USGS Alaska Program, USGS Circular 722, p. 44-45.

Plafker, G., Gilpin, L.M., and Lahr, J.C., (1994). Neotectonic map of Alaska, in Plafker, G., and Berg, H.C., eds., Geology of Alaska, Geology of North America, in Decade of North American Geology: Boulder, Geological Society of America, v. G-1, plate 12, 1 sheet, scale 1:2,500,000.

Ratchkovski, N.A. and R.A. Hansen (2002). New Evidence for Segmentation of the Alaska Subduction Zone, Bull. Seism. Soc. Am., Vol. 92, No. 5, p. 1754-1765.

Ruppert, N.A. and R.C. Witter (2020). Preface to the Focus Section on he 30 November 2018 Mw 7.1 Anchorage, Alaska, Earthquake, Seism. Res. Letters, Vol. 91, No. 1, p. 16 – 18.

Sadigh, K., C.Y. Chang, J.A. Egan, F. Makdisi and R.R. Youngs (1997). Attenuation Relationships for Shallow Crustal Earthquakes Based on California Strong Motion Data, Seism. Res. Letters, Vol. 68, No. 1, p. 180-189.

Schmoll, H.R., and Yehle, L.A. (1987). Surficial geologic map of the northwestern quarter of the Tyonek, A-4 Quadrangle, south-central Alaska: U.S. Geological Survey Miscellaneous Field Studies Map, MF-1934, scale 1:31,680, 1 sheet.

Silwal, V., C. Tape, and A. Lomax (2018). Crustal earthquakes in the Cook Inlet and Susitna region of southern Alaska, Tectonophysics, p. 245-263.

Sipkin, S.A. (2003). A Correction to Body-Wave Magnitude mb based on Moment Magnitude Mw, Seism. Res. Letters, Vol. 74, No. 6, p. 739-742.

Stevens, D.S.P. and P.A. Craw (2003). Geologic hazards in and near the Northern Portion of the Bristol Bay Basin, Alaska Division of Geological and Geophysical Surveys, Miscellaneous Publication 132.

Utsu, T. (2002). Relationships between Magnitude Scales, in International Handbook of Earthquake and Engineering Seismology, Part A, IASPEI Handbook, edited by Lee, W. H. K., H. Kanamori, P. C. Jennings, and C. Kisslinger, Academic Press, New York, p. 733-746.

Weichert, D.H. (1980). Estimation of the Earthquake Recurrence Parameters for unequal Observation Periods for Different Magnitude, Bull. Seism. Soc. Am., Vol. 70, No. 4, p. 1337-1346.

Wells, D.L. and K.J. Coppersmith (1994). New Empirical Relationships Among Magnitude, Rupture Length, Rupture Width, Rupture Area and Surface Displacement, Bull. Seism. Soc. Am., Vol. 84, No. 4, p. 974-1002.

Wesson, R.L., A.D. Frankel. C.S. Mueller and S. Harmsen (1999). Probabilisitic Seismic Hazard Maps of Alaska, USGS Miscellaneous Investigation Series, I-2679.

Wesson, R.L., O.S. Boyd, C.S. Mueller, C.G. Bufe, A.D. Frankel, and M.D. Petersen (2007). Revision of Time-Independent Probabilistic Seismic Hazard Maps for Alaska, USGS Open File Report 2007-1043.

Wesson, R.L., O.S. Boyd, C.S. Mueller, and A.D. Frankel (2008). Challenges in Making a Seismic Hazard Map for Alaska and the Aleutians, in Active Tectonics and Seismic Potential of Alaska, Geophysical Monograph Series 179, American Geophysical Union.

Willis, J.B., Haeussler, P.J., Bruhn, R.L., and Willis, G.C., (2007). Holocene slip rate for the western segment of the Castle Mountain fault, Alaska, Bull, Seism. Soc. Am., Vol. 97, p. 1019-1024.

Woodward-Clyde Consultants (1978). Offshore Alaska Seismic Exposure Study, Woodward-Clyde Consultants, San Francisco, CA.

Youngs, R.R. and K.J. Coppersmith (1985). Implications of Fault Slip Rates and Earthquake Recurrence Models to Probabilistic Seismic Hazard Estimates, Bull. Seism. Soc. Am., Vol. 75, No. 4, p. 939-964.

Youngs, R., Chiou, S., Silva, W., and Humphrey, J., 1997. Strong ground motion attenuation relationships for subduction zone earthquakes, Seismic Research Letters Vol. 68, p. 58–73.

Appendix A – Modeling the Slab Seismic Source in Southern Alaska for PSHA programs

A-1. Introduction

The project region in Southern Alaska is located in the tectonically active Alaska-Aleutian subduction zone. Historically, seismic events have occurred along the shallow and deep parts of the subduction slab. The characterization of these seismic sources is presented in detail in the main part of this report. Typically for PSHA studies, the interface seismic source zone is geometrically represented by a planar fault source. This is consistent with the understanding of the rupture mechanism of these interface events, which tend to rupture along the subducting plate following the general down dip angle of the plate. However, the typical understanding of the rupture process for the deeper slab events is a normal mechanism event that ruptures through the cross section of the subducting plate rather than along the subducting plate.

Given this difference in the rupture process and the capabilities and limitations of PSHA programs, a wide range in the modeling approaches are currently used in practice. Hale et al. (2018) showed that these different approaches can lead to significant differences in the resulting hazard curves for a simple example. The main cause for these observed differences is in the distance metrics estimated from the different approaches. This is also accentuated given the strong depth dependence contained in slab ground motion models. This appendix summarizes the different approaches described in Hale et al. (2018) and also compares and discusses the approach used in this PSHA study and the USGS approach (Wesson et al., 2007), which was also applied in the Knight-Piesold (2013) study.

A-2. Slab Seismic Source Modeling Approaches

Given the current suite of available PSHA programs, four basic approaches are used for the modeling of slab subduction seismic sources. These are illustrated in Figure A-1 (from Hale et al., 2018). In approach (a) the slab source is modeled with multiple sub-source areal sources, each with a point source representation within a given areal sub-source. Together the collection of areal sub-sources attempts to represent the geometry of the subduction slab by varying the depth of these sources following the subducting plate geometry. The next approach (b) is similar to the representation for the shallower interface sources in which a planar fault source is used. This fault source can be assigned with the upper, middle (as shown in Figure A-1), or bottom part of the subduction slab. For the third approach (c), virtual faults are placed within the subducting slab to represent cross sections of the plate. Earthquakes are then defined on these virtual faults and this is the approach used in this current seismic hazard study. Finally, the last approach (d) is a variation on the first approach where the areal sub-source zones are represented by virtual faults centered on the point source locations within each area sub-zone.

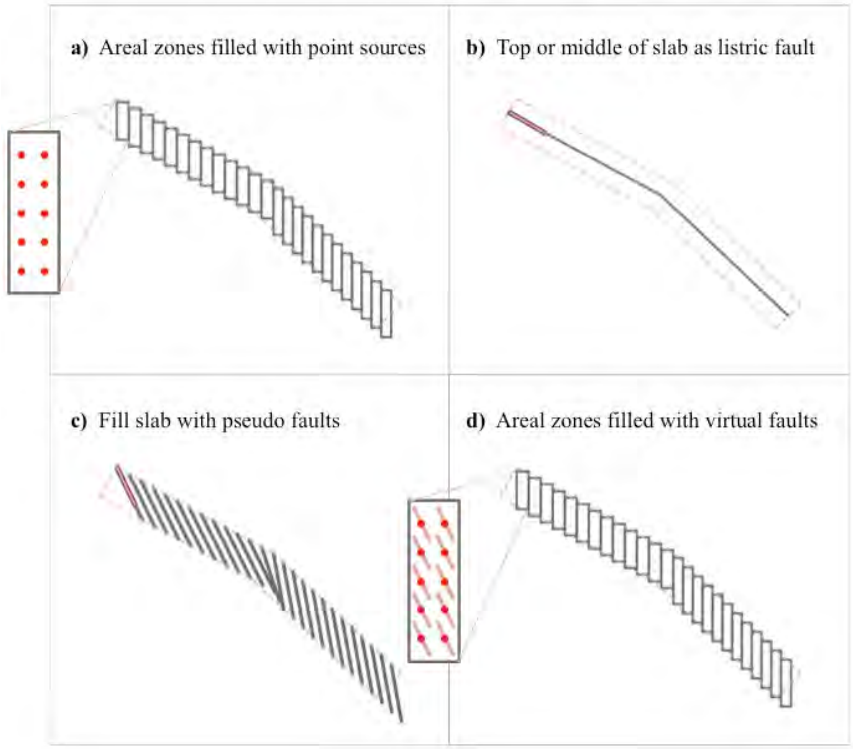

Figure A-1. Four representative approaches for the modeling of slab events in PSHA programs (Source: Hale et al., 2018).

Given these four modeling approaches, a simple example calculation using the same GMM model and with a **M**6.5 characteristic event assigned to the slab source was performed as part of the Hale et al. (2018) study. Three PSHA programs computed a hazard curve for approach (a), two for approach (b), seven for approach (c) and two for approach (d). The results of these calculations are shown in Figure A-2. As noted in Hale et al. (2018) a comparison of the results for a given approach (i.e., (a) through (d)) was favorable with differences between the results from different PSHA programs within 5%. However, it is observed in Figure A-2 and noted in Hale et al. (2018), that the differences in approach (a) relative to the other three approaches are more significant and lower than the other three approaches which are similar. Given that these differences are understood to be caused mainly by the different distance metrics computed using points sources (i.e., approach (a)) rather than virtual faults, it is expected that these differences would potentially increase for larger magnitudes given their larger rupture area and hence extended fault ruptures when compared to a point source. As is noted for the Hale et al. (2018) example calculation, the characteristic magnitude assigned to the sources was 6.5 whereas for this seismic hazard study the maximum magnitude assigned for the slab source is 7.5 and 8.0 and the differences observed in the Hale et al. (2018) example can be expected to be larger for this current study given the larger maximum magnitudes.

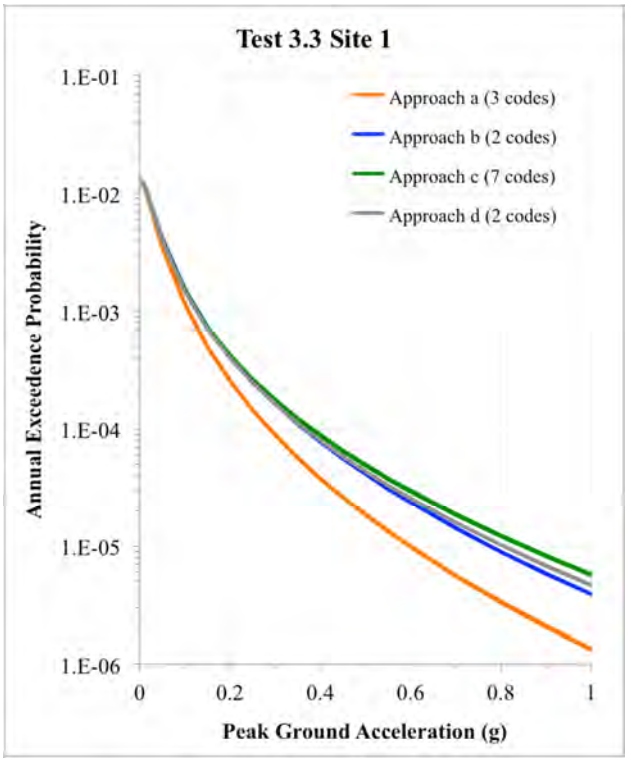

Figure A-2. Comparison of hazard curves from the four different slab modeling approaches presented in Hale et al. (2018). (Source: Hale et al., 2018).

A-2. Application for Southern Alaska

The slab seismic source is shown in the main report to be the controlling seismic source from the PSHA calculations for high to intermediate spectral periods. For longer spectral periods, this slab source still contributes, but is equal in its contribution to the interface source. Thus, given its importance, the approach used in modeling the slab source can have strong impacts on the ground motions, especially given the sensitivity results presented in Hale et al. (2018).

The subduction slab associated with the Alaska-Aleutian subduction zone in the project region is a highly active seismic source with slab events occurring down to a depth of approximately 200 km which is about 30 km east of the project site locations. Ratchkovski and Hasen (2002) performed an earthquake relocation methodology in the region which allows for the image of the subducting slab as shown in Figure A-3. These relocated events in cross section C1 and C2 are the closest to the Pebble project site.

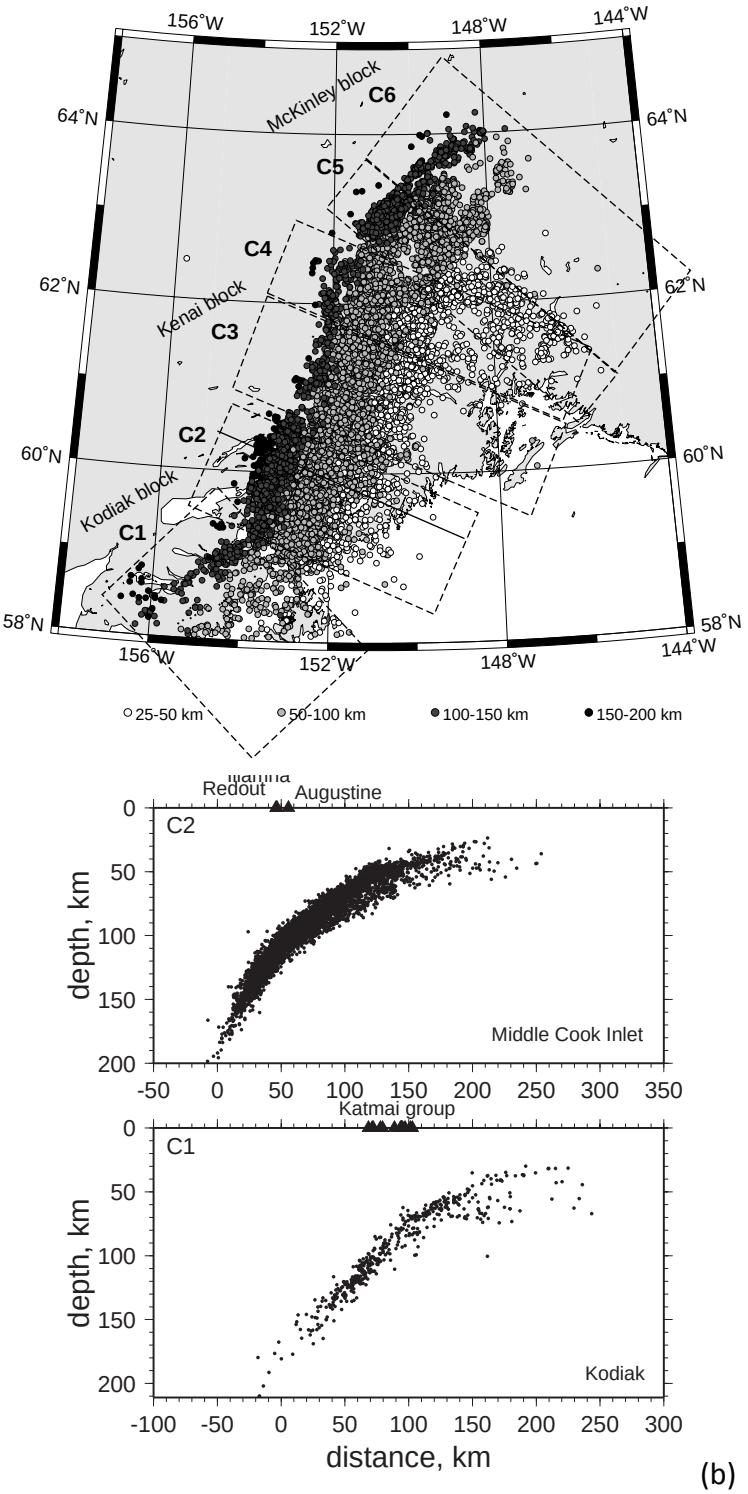

Figure A-3. Relocated earthquakes from Ratchkovski and Hansen (2002) shown in map view (a) and cross sections closest to the project site (b).

For the SSC model developed in this SHA study, virtual vertically dipping faults are placed at a series of depths ranging from 50 km to 200 km, every 25 km. This follows approach (c) from Hale et al. (2018). These virtual fault traces for the different depth range values are based on the depth contours of the subduction slab global model Version 2.0 (Hayes, 2018). The fault thickness is assumed to be 20 +/- 5 km to represent the thickness of the subducting plate given the cross sections from Ratchkovsi and Hansen (2002) shown in Figure A-3. These virtual faults are plotted in Figures A-4 through A-6 along with the project seismicity catalog for three depth ranges: 50 – 100 km (Figure A-4), 100 – 150 km (Figure A-5) and 150 – 250 km (Figure A-6). One feature observed with the seismicity associated with the slab events is a non-uniform spatial distribution of events. To capture this feature in the SSC model, the seismicity catalog is separated first by the three depth ranges. Next within a given depth range, subsections of seismicity based on the observed spatial distribution is selected. For the shallowest depth range of 50 – 100 km there are three selected subsections: SW, Central, and NE. The associated events with each of these subsections are plotted in Figure A-4 with different colors.

For the next depth range, a total of six subsections are selected starting with SW01 at the southwestern end of the source through SW06 at the northeastern end of the source. This depth range shows a larger variability in the spatial distribution of events than the previous shallower depth range. The seismicity associated with the six different subsections are indicated in Figure A-5 with the different colors. Finally in Figure A-6, the seismicity from the deepest depth range of 150 – 250 km is plotted in separate colors indicating the three subsections, SW, Central, and NE.

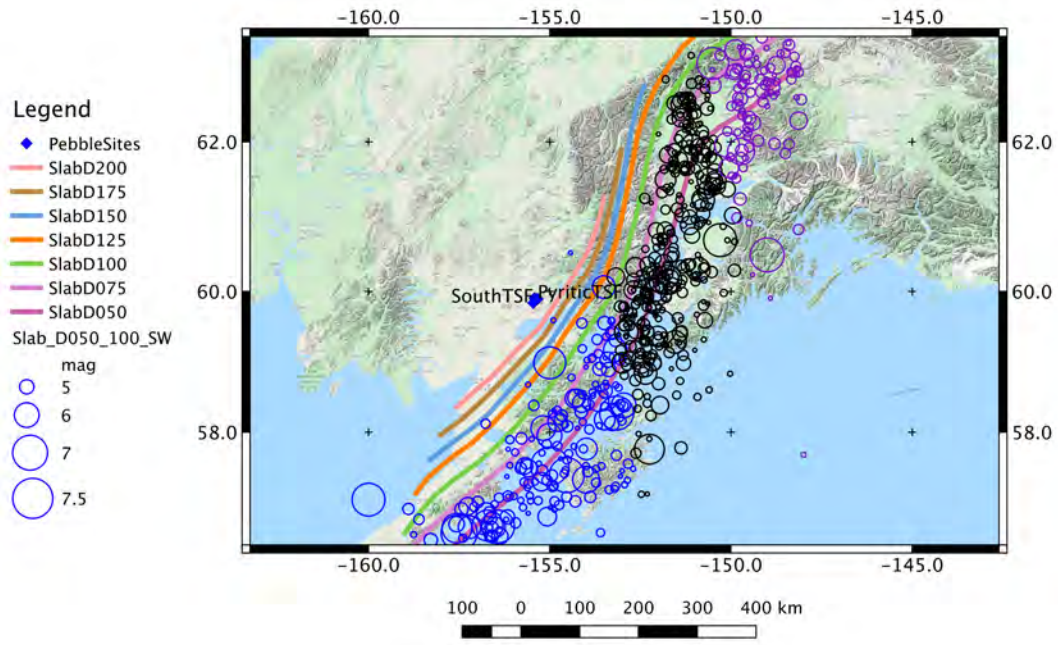

Figure A-4. Virtual slab faults and seismicity from the project catalog for events in the depth range of 50 – 100 km with color symbols separated based on geographical grouping.

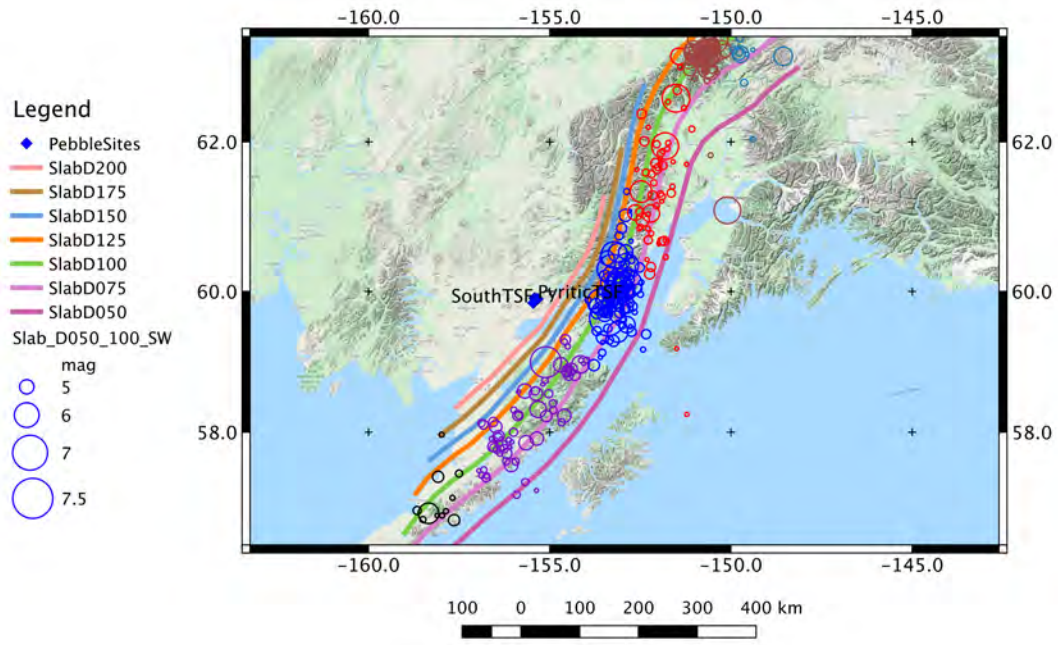

Figure A-5. Virtual slab faults and seismicity from the project catalog for events in the depth range of 100 – 150 km with color symbols separated based on geographical grouping.

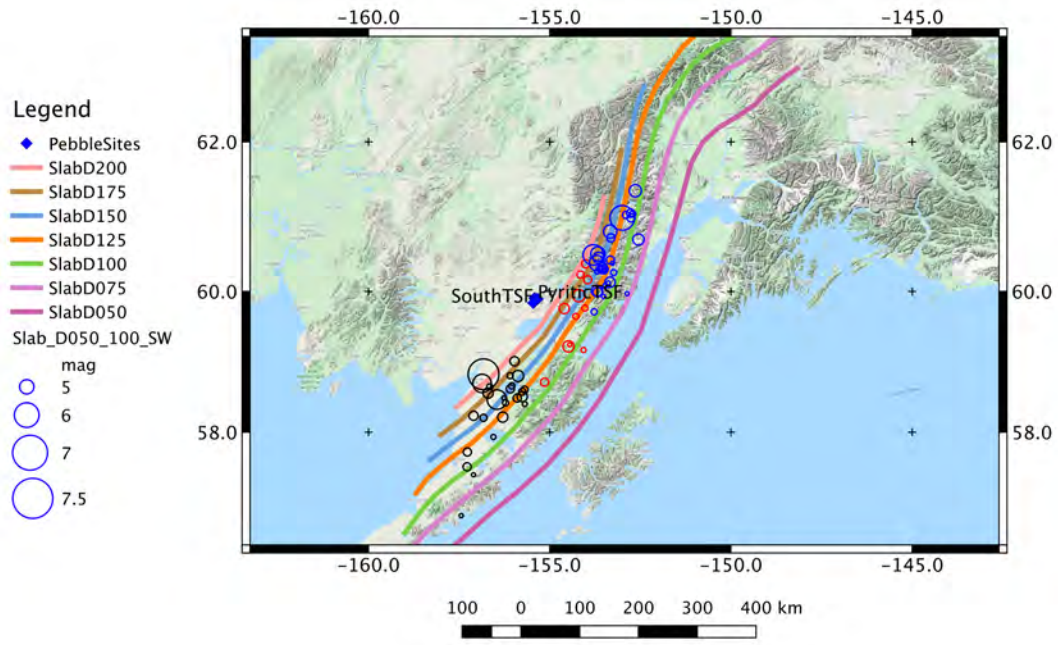

Figure A-6. Virtual slab faults and seismicity from the project catalog for events in the depth range of 150 – 250 km with color symbols separated based on geographical grouping.

For the current SSC model, earthquake recurrence rates are estimated following the Weichert (1980) approach using the project earthquake catalog separated by depth and an additional selection criterion of having events located within the longitudes of -148 to -160 degrees. Although events outside of these longitudes are observed, their greater distance from the project site locations does not necessitate their inclusion for the SSC model development.

Recurrence parameters are estimated for the three specific depth ranges of 50 – 100 km, 100 – 150 km, and 150 – 250 km based on the sorted earthquake catalog. Based on these estimated recurrence parameters, the activity rates for a given depth range were assigned to the corresponding virtual fault and partitioned based on the respective fault lengths for the associated depth range and number of events in each sub-source.

In contrast to the modeling approach used in this SHA study, the USGS modeling (Wesson et al., 2007), which was also used in the Knight-Piesold (2013) study, was a variation and simplification of approach (a) presented in Hale et al. (2018). Rather than model the subducting slab with sub-areal source zones, two regional areal source zones were developed for the depth ranges of 50 – 80 km and 80 – 120 km. Thus, the deeper part of the slab is not being modeled

within the USGS approach nor is the deepening of the slab in a northwesterly direction (i.e., toward the project sites) being directly modeled. This two-layer approximation is a simplified representation of the true geometry of the subducting slab in the region of Southern Alaska.

Within each of these two depth ranges, the seismicity catalog was processed to compute a smoothed grid of activity rates based on a 0.1x0.1 degree grid point spacing. The smoothing distance was 70 km (Wesson et al. 2007). Following this smoothing approach, the activity rate distribution is not uniform and more closely follows the historical seismicity in a similar approach that is implemented for this study.

The normalized activity rates for the two USGS grid files are plotted in Figure A-7 (50 – 80 km depth) and Figure A-8 (80 – 120 km). Also plotted are the virtual slab faults from the current SSC model. The shallow layer was placed at a depth of 60 km and the deeper depth at 90 km in the USGS analysis.

Based on a visual comparison of the normalized activity rates in Figure A-7 and the virtual slab faults which correlate with the top of the subducting plate, the highest activity from the USGS model is located slightly east of the 50 km depth virtual fault. This is assumed to be an artifact of the smoothing process implemented in the USGS methodology and the historical seismicity location distributions shown in Figure A-4. However, this relative eastern shift would result in lower ground motions at the project site locations given the larger distances from the sites to the source.

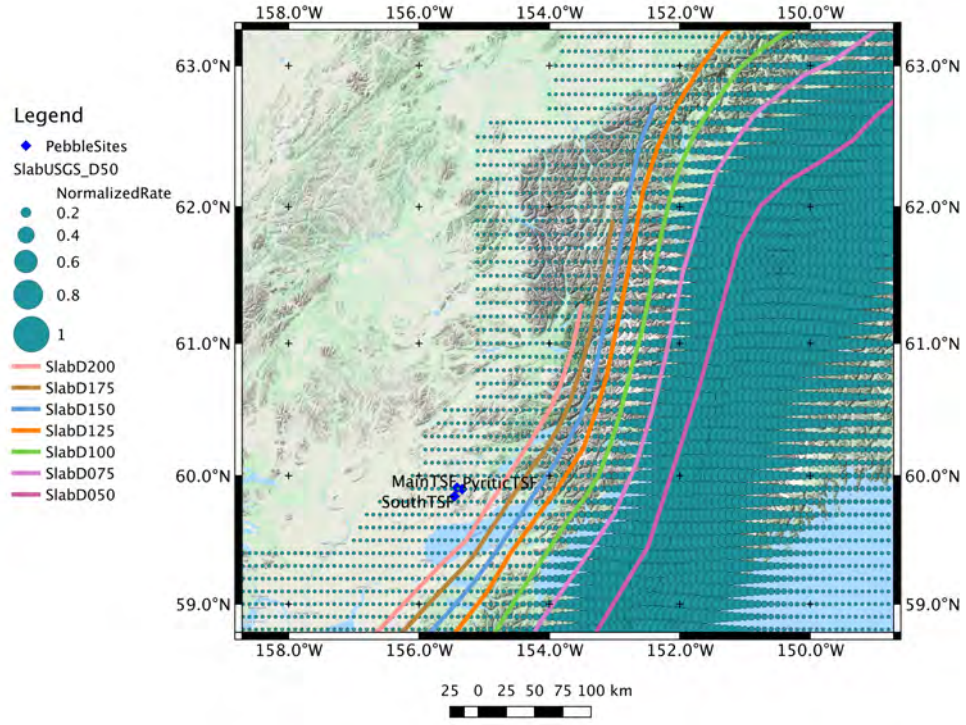

Figure A-7. Virtual slab faults and normalized seismicity activity rates from the USGS source model for events in the 50 – 80 km depth range.

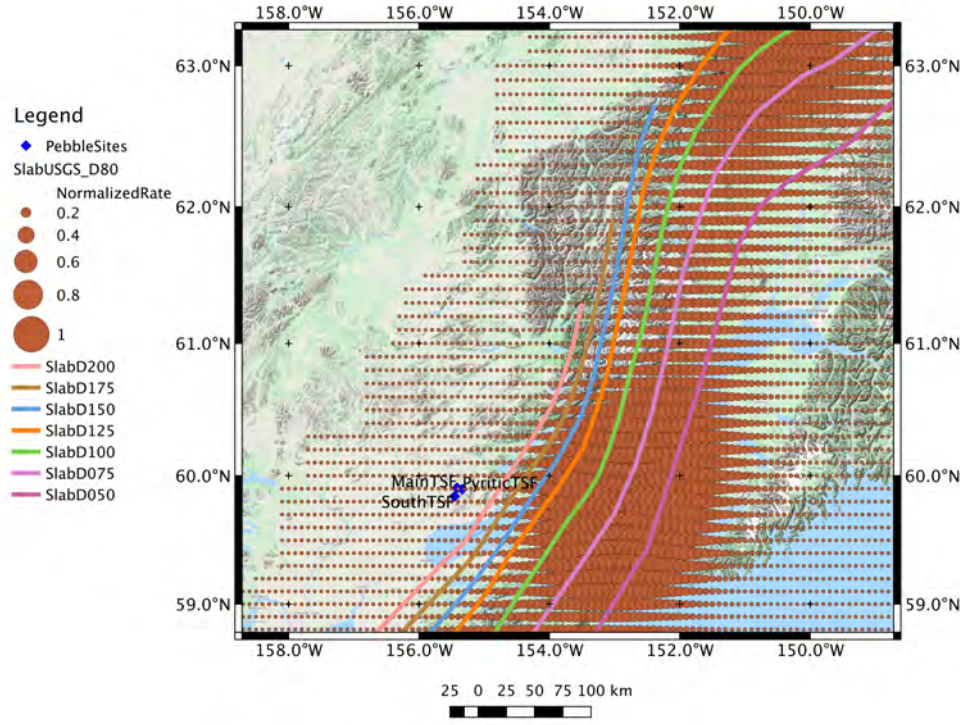

Figure A-8. Virtual slab faults and normalized seismicity activity rates from the USGS source model for events in the 80 – 120 km depth range.

For the deeper layer (80 – 120 km) there is a strong concentration of normalized activity rates east of the project site locations. This is in agreement with the observed seismicity shown in Figure A-5. However, similar to the previous shallow layer, the concentration of the normalized activity rates for the depth range of 80 – 120 km is slightly east of the faults associated with the 75 – 125 km depths. This observed shift would also have the expected impact of producing lower ground motions at the project site locations from the USGS model based on the larger separation distance. In addition, the depth of this layer was placed at 90 km and given the strong correlation of increasing ground motions as a function of depth, this shallower assigned depth would also be expected to cause lower ground motions at the project site location.

Given these noted differences and the expected differences based on the implementation and representation of the slab within a PSHA program (Hale et al., 2018), it is expected that the contribution from the slab sources from the current SSC model would be greater than the simplified model used by the USGS. However, given the observations and recommendations from Hale et al. (2018) for the modeling of slab sources, the current model, which follows approach (c), provides a better representation than the USGS model, which follows a variation of approach (a) from Hale et al. (2018). These differences in the implementation choices used in the two seismic hazard studies, indicates that the lower calculated ground motions from the Knight-Piesold (2013) study compared to the current study can be attributable to the

implementation methodology used for the slab seismic source and the inherent bias introduced by that representation.

A-3. References

Hale, C., N. Abrahamson, and Y. Bozorgnia (2018). Probabilistic Seismic Hazard Analysis Code Verification, PEER Report, Pacific Earthquake Engineering Research Center, University of California, Berkeley, California, PEER Report 2018/03.

Hayes, G. (2018). Slab2 – A Comprehensive Subduction Zone Geometry Model, USGS data release, https://doi.org/10.5066/F7PV6JNV.

Knight-Piesold Ltd. (2013). Report on Seismicity Assessment and Seismic Design Parameters, Report prepared for Pebble Limited Partnership, August 14, 2013.

Ratchkovski, N.A. and R.A. Hansen (2002). New Evidence for Segmentation of the Alaska Subduction Zone, Bull. Seism. Soc. Am., Vol. 92, No. 5, p. 1754-1765.

Weichert, D.H. (1980). Estimation of the Earthquake Recurrence Parameters for unequal Observation Periods for Different Magnitude, Bull. Seism. Soc. Am., Vol. 70, No. 4, p. 1337-1346.

Wesson, R.L., O.S. Boyd, C.S. Mueller, C.G. Bufe, A.D. Frankel, and M.D. Petersen (2007). Revision of Time-Independent Probabilistic Seismic Hazard Maps for Alaska, USGS Open File Report 2007-1043.